Failure of thin-walled structures under impact loading

Salar Mostofizadeh

FAILURE OF THIN-WALLED STRUCTURES UNDER IMPACT LOADING

FAILURE OF THIN-WALLED STRUCTURES UNDER IMPACT LOADING

Proefschrift

ter verkrijging van de graad van doctor
aan de Technische Universiteit Delft,
op gezag van de Rector Magnificus prof. dr. ir. T.H.J.J. van der Hagen,
voorzitter van het College voor Promoties,
in het openbaar te verdedigen op maandag 15 juni 2020 om 15:00 uur

door

Salar MOSTOFIZADEH

Licentiate Engineer in Mechanical Engineering,
Chalmers University of Technology, Göteborg, Sweden,
geboren te Tehran, Iran.

Dit proefschrift is goedgekeurd door de promotoren

Promotor: Prof. dr. ir. L. J. Sluys
Promotor: Prof. dr. R. Larsson
Copromotor: Dr. M. Fagerström

Samenstelling promotiecommissie:

Rector Magnificus,	voorzitter
Prof. dr. ir. L. J. Sluys,	Technische Universiteit Delft
Prof. dr. R. Larsson,	Technische Universiteit Chalmers
Dr. M. Fagerström,	Technische Universiteit Chalmers
Onafhankelijke leden:	
Prof. dr. A. Combescure,	INSA de Lyon
Prof. dr. S. Bordas,	Universiteit Luxembourg
Prof. dr. ir. A. van Keulen,	Technische Universiteit Delft
Dr. J.J.C. Remmers,	Technische Universiteit Eindhoven
Prof. dr. ir. M. Veljkovic,	Technische Universiteit Delft, reservelid

The doctoral research has been carried out in the context of an agreement on joint doctoral supervision between Chalmers University of Technology, Sweden and Delft University of Technology, the Netherlands.

Keywords: XFEM; Phantom node method; shells; Continuum damage; ductile fracture; cohesive zone; rate dependence

Printed by: Ipskamp printing

ISBN 978-94-028-2079-9

An electronic version of this dissertation is available at
http://repository.tudelft.nl/.

To Shabnam and Elena,
the two greatest loves of my life.

CONTENTS

SUMMARY

Increase in computational power during recent years contributed to a significant development in numerical methods in mechanics. There are many methods developed that address various complex problems, yet modelling of initiation and propagation of failure in thin-walled structures requires further development. Among numerous challenges involved, one main complexity is to capture the behaviour of the material at the failure process zone, where the underlying micro-structure governs the macroscopic process. Accounting for all details in a model will increase the computational cost, which thereby requires finding a balance between the level of details and the cost incurred. The research in the present thesis aims at developing a framework capable of analysing ductile fracture in terms of initiation and propagation of cracks, which is applicable to thin-walled steel structures subjected to high strain rates. Of particular importance is to address the application to large scale structures for which capturing the accurate response of the structure calls for an efficient numerical procedure.

First, a method is developed to analyse and predict the crack propagation in thin-walled structures subjected to large plastic deformation under high strain rate loading. In order to represent crack propagation independent of the finite element discretisation, the extended finite element method (XFEM) based on a 7-parameter shell formulation with extensible directors is employed. For the temporal discretisation, as typically used in high speed events and high strain rates, an explicit time integration is used which is observed to be prone to generate unphysical oscillations upon crack propagation. To remedy this problem, two possible solutions are proposed. To verify and validate the proposed model, various numerical examples are presented. It is shown that the results correlate well with the experiments.

Second, to capture the fine scale nature of the ductile fracture process, a new XFEM based enrichment of the displacement field is proposed that allows for a crack tip and/or kink to be represented within an element. It concerns refining the crack tip element locally yet retaining the macroscale node connectivity unchanged. This in turn results in a better representation of the discontinuous kinematics, however, unlike regular mesh refinement, this requires no change to the macroscale solution procedure. To show the accuracy of the proposed method, a number of examples are presented. It is shown that the proposed method enhances the analyses of the ductile fracture of the thin-walled large scale structures under high strain rates.

Third, in line with the previous developments, a new Phantom node based approach for analyses of the ductile fracture of thin-walled large scale structures is proposed. It concerns subscale refinement of the elements through which the crack progresses. As compared to the XFEM approach, the Phantom node method is more

efficient implementation-wise and computationally. It allows for a detailed representation of the crack tip and kink, which leads to a more smooth progression of the crack. The proposed approach is applicable to both low and high order elements of different types. In order to show the accuracy of the new approach a number of examples are presented and compared to the conventional approach.

Finally, a new approach to analyse ductile failure of thin-walled structures based on the continuum damage theory is developed. For this, a Johnson-Cook visco-plasticity formulation coupled to continuum damage is developed, whereby the total response is obtained from a damage enhanced effective visco-plastic material model. Production of the fracture area is governed by a rate dependent damage evolution law, where the damage-visco-plasticity coupling is realised via the inelastic damage driving dissipation. In addition, a local damage enhanced model (without damage gradient terms) is used, which contributes to the computational efficiency. A number of examples are presented to investigate the accuracy of the proposed model and it is shown that the model provides good convergence properties.

SAMENVATTING

De toename in computer rekensnelheid gedurende de afgelopen jaren heeft significant bijgedragen aan de ontwikkeling van nieuwe numerieke methodes in de mechanica. Er zijn vele technieken ontwikkeld die verschillende complexe problemen aanpakken, echter vereist het modelleren van initiatie en voortplanting van breuk mechanismen in dunwandige constructies verdere ontwikkeling. Een specifieke uitdaging is het beschrijven van het materiaalgedrag rondom de breuk, waar de onderliggende micro structuur van het materiaal het macroscopisch proces bepaalt. Het meenemen van alle details in het rekenmodel leidt tot een noemenswaardige toename in de berekeningsgrootte en dus zal er hier een goede afweging tussen rekensnelheid en nauwkeurigheid gevonden moeten worden. Het doel van dit onderzoek is om een methode te ontwikkelen die ertoe in staat is om in dunwandige constructies, onderworpen aan hoge reksnelheden, de initiatie en uitbreiding van taaie breuken te analyseren. Het is van belang dat de methode worden toegepast op grootschalige constructies, omdat een efficiente numerieke procedure hier gewenst is voor het bepalen van een nauwkeurige respons van de constructie zelf.

Als eerste is er een methode ontwikkeld om scheurgroei te analyseren in dunwandige constructies die grote plastische deformaties ondergaan en met hoge reksnelheden belast worden. Om de scheur uitbreiding onafhankelijk van de eindige elementen discretisatie te kunnen representeren, is de extended finite element method (XFEM) gebruikt. Deze methode is gebaseerd op een 7-parameter schaal formulering en neemt de verandering van de schaal directors mee. Voor de tijdsdiscretisatie is een expliciete tijdsintegratie toegepast, die niet-fysische oscillaties teweeg brengt tijdens het groeien van de scheur. Als remedie voor dit probleem zijn er twee oplossingen voorgesteld. Een aantal numerieke voorbeelden zijn gepresenteerd om het voorgestelde model te verifieren en valideren. Deze voorbeelden bewijzen dat de resultaten overeenkomen met de experimenten.

Ten tweede is een nieuwe verfijning van het verplaatsingsveld voorgesteld om het taaie breukproces dat zich op kleine schaal afspeelt mee te nemen in het model. Deze verfijning is gebaseerd op XFEM en laat het toe om de tip van de scheur en de scheur richting weer te geven in een enkel element. Hiermee kan de scheur lokaal verfijnd worden, terwijl de connectiviteit van de knopen op de macroschaal onveranderd blijft. Dit zorgt er dan weer voor dat de discontinue kinematica beter beschreven wordt terwijl er, in tegenstelling tot reguliere mesh verfijning, geen verandering nodig is in de oplossingsprocedure op de macroschaal. Opnieuw zijn er een aantal voorbeelden opgenomen om de nauwkeurigheid van deze methode te laten zien. De voorbeelden laten zien dat de voorgestelde methode inderdaad de analyse van het ductiel falen van dunwandige constructies belast met hoge reksnelheden verbetert.

In lijn met de eerdere ontwikkelingen is als derde een nieuwe techniek voorgesteld om het ductiel falen in grootschalige dunwandige constructies te analyseren. Deze aanpak is gebaseerd op een Phantom node, waar de elementen waarin de scheur groeit, verfijnd worden. Vergeleken met de XFEM methode is de Phantom node aanpak efficienter qua berekeningen, maar ook in de implementie ervan. Een gedetailleerde weergave van de tip van de scheur is hier mogelijk, wat zorgt voor een geleidelijke groei van de scheur. De voorgestelde methode is toepasbaar voor verschillende typen elementen van zowel lage en hogere orde. Om de nauwkeurigheid van deze nieuwe aanpak weer te geven zijn er een aantal voorbeelden gepresenteerd en zijn er vergelijkingen gemaakt met de conventionele aanpak.

Als laatste is er een nieuwe methode ontwikkeld om het ductiel falen van dunwandige constructies te analyseren. Deze methode gebruikt een Johnson-Cook viscoplastische formulering die dan gekoppeld is aan continuum schade theorie. De totale respons wordt hier verkregen door een, met schade verrijkt, visco-plastisch materiaal model. De productie van nieuw scheur oppervlak wordt bepaald door een snelheidsafhankelijke schade evolutie wet, waar koppeling tussen schade en viscoplasticiteit is gerealiseerd via een inelastische schade gedreven dissipatie. Ook is er een lokaal schade verrijkt model (zonder afgeleide schade termen) gebruikt, wat bijdraagt aan de efficientie van het model. Een aantal voorbeelden zijn uitgewerkt om de nauwkeurigheid van het voorgestelde model te onderzoeken en de resultaten laten goede convergentie eigenschappen zien.

1

INTRODUCTION

1.1. MOTIVATION AND BACKGROUND

Increasing computational power during the last years has led to a huge advance in numerical modelling. Many methods has been developed to address many interesting subjects. Yet, there are many others that need to be explored, among which dynamic ductile fracture in thin-walled structures is of significance in the current study. Thin-walled structures are widely used for various civilian and defense applications such as maritime and off-shore structures, aircraft fuselage, vehicles and ship hulls just to name a few. These applications call for an increase in the efficiency as well as the safety of the structures. Therefore, it is desired to employ better materials and to improve the design of the structures so that they can withstand these loads to a certain degree.

Of particular interest here is to investigate the behaviour of the large-scale thin-walled structures under impact and high-strain rate loads. Due to high cost of experimental approaches, numerical simulations of dynamic ductile fracture are of great interest. Therefore, a numerical tool that represents a physically-based description of the material and its failure process will allow a realistic simulation at a fraction of the cost incurred in experiments. For that, the numerical tool should predict crack initiation and propagation, its path, as well as the stress states in the vicinity of the failure process zone. One challenge to address is to specify the behaviour of the material at the failure process zone based on the underlying microstructure that governs the macroscopic process. Although accounting for such details in developing a representative modelling framework is necessary, it will add to the complexity and the computational cost. Hence, finding a balance between the level of details included in the model and the computational cost of that is of significance.

This work is intended to investigate the process of dynamic ductile failure in order to provide a tool for numerical simulations. Employing such a tool can improve the design of thin-walled structures to make them withstand high strain rate loads.

For that, advanced numerical methods are employed to develop an efficient numerical tool that provides an accurate response for the structures at a reasonable cost.

1.2. OBJECTIVE OF THE RESEARCH

This research aims at investigating the dynamic ductile fracture process. Given that, an accurate and efficient modelling approach that can predict and represent failure and its progressive process in terms of its initiation and progression in thin-walled structures is addressed. Considering the main application of this development, that is large-scale thin-walled structures, finding a balance between the level of details accounted for and the computational cost incurred is of significance. The research questions addressed to accomplish the aforementioned goal are as follows:

- How to develop an accurate and representative simulation method to investigate dynamic ductile fracture at low cost ?
- Which are the different modelling approaches to consider ?
- How to model dynamic ductile fracture in large-scale thin-walled structures ?
- How to predict the onset and progression of dynamic ductile fracture ?

1.3. DYNAMIC DUCTILE FRACTURE

Ductile fracture refers to the fracture process during which the material at the process zone undergoes large plastic deformation which eventually leads to formation of fracture surfaces. Formation of these surfaces is a function of the underlying microscopic fracture mechanisms and the localisation of deformation eventually (e.g. necking formation) leading to the fracture.

In general, once material suffers plastic deformation, the reduced cross-section of the material results in an increase in the stress. At the same time, the plastic hardening effect increases the stress the material can bear. In case the reduction in the cross-section of the material cannot be compensated by the strain hardening effect it leads to formation of a neck. Necking in its early stages is governed by the slip of atoms. Once plastic deformation becomes large enough, voids, if not pre-existing, start to nucleate at the material defects. Further plastic deformation leads to an increase in the stress triaxiality which makes the material susceptible to void growth. Once voids are large enough they coalesce and form microcracks. These microcracks eventually lead to macrocracks and cause the material to fail, cf. Figure 1.1 [1].

Dynamic ductile fracture is a fracture for which the role of inertia cannot be ignored. In general, it concerns a structure loaded at high rates. As a consequence of that, the evolution of the process zone and the stress field at high progression speeds is influenced by the inertial resistance of the material at the crack tip [2].

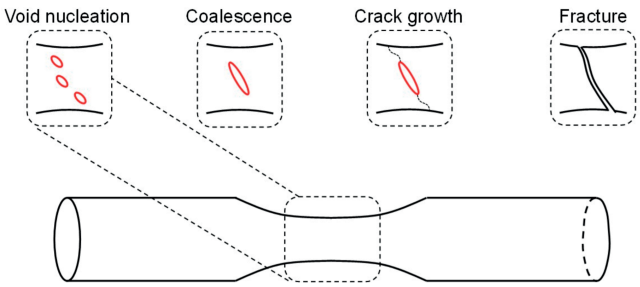

Figure 1.1: Evolution of ductile failure from the void nucleation to the fracture. Image reproduced from [3]. Printed with permission.

1.4. DIFFERENT SHELL FORMULATIONS

Shell structures due to their lightweight character are among the most efficient load-carrying structures have ever existed. The increasing complexity of the shell structures necessitated employing a reliable an accurate shell formulation to perform numerical simulations. Although there are plenty of different shell formulations available, many of them fail for certain classes of problems while some formulations perform perfectly.

In case of classical shell theories, it is noted that change in the thickness is disregarded. Two examples of classical shell theory are Kirchhoff-Love and Mindlin-Reissner. One main deficiency of the Kirchhoff-Love theory is its straight and normal to mid-surface representation of the cross section of the shell. This limitation together with inextensibility of the director leads to an incompatibility in representation of the shear deformation through the thickness of the shell. Alternatively, Mindlin-Reissner theory allows for an improved representation of the shear deformation given that it does not require the cross section of the shell to remain normal to the mid-surface of the shell, yet it lacks representation of the thickness strain. Therefore to address lack of thickness strain in these theories assumption of plane stress through the thickness of the shell is required. However, application of non-linear constitutive laws to represent large strains and plasticity makes a plane stress assumption more complicated to consider. Therefore, to employ a three-dimensional constitutive law, representing the transverse normal strain in the shell formulation is a necessity [4, 5].

In recent years, solid-shell formulations have been extensively investigated. Using an extensible director they allow for three-dimensional stress state representation, yet they suffer from thickness-locking effect. This deficiency is shown to be resolved in [6, 7] using the Enhanced Assumed Strain method.

In the current work the shell formulation employed is in line with the developments in [8, 9]. It is a 7-parameter shell formulation which incorporates a second order expansion along the director field to prevent the Poisson locking effect caused by the incompatible representation of the thickness strain.

1.5. APPROACHES TO MODELLING OF DYNAMIC DUCTILE FRACTURE

The displacement discontinuity incurred during the failure process makes it a complicated phenomenon to model using traditional finite element methods. This is due to the fact that most of the traditional approaches depend on the evolution of the continuous state variables within a finite discretised domain to specify the response. Therefore, modelling of the failure process requires a more detailed approach.

Modelling of dynamic ductile failure is generally categorised under two approaches, namely continuum and discrete methodologies. Continuum methods provide a volume representation of the degradation where there is no discontinuity in the displacement field under consideration. These methods are similar to constitutive models in which failure is specified in terms of a damage variable in each integration point of the discretised domain. Continuum damage models are typically phenomenological models which represent the degradation process taking place at the micro-level scale governed by a set of state variables specified at the macro-level scale, cf. [10–15]. Apart from the simplicity of the continuum damage models in terms of their implementation, one main advantage of these models is their progressive damage representation unlike approaches as mesh deletion which results in an abrupt unloading of the failure zone. This characteristic makes continuum damage models an interesting choice to model non-catastrophic loss of strength in structures. However, continuum damage models are prone to strain localisation and lack of reliability. Once the stiffness at an integration point decreases to nearly zero, mesh distortion may increase to an unacceptable value. This problem can be avoided using complementary approaches such as mesh deletion, mesh adaptivity schemes, and non-local damage models [16–19]. More details on continuum damage modelling can be found in chapter 5 where a damage enhanced effective material model is presented.

Alternatively, discrete methods allow for presence of discontinuities in the displacement field which in turn prevents excessive mesh distortion as in the continuum methods. These methods represent the process zone on a surface via remeshing or employing additional kinematics to represent the discontinuity. The onset and direction of this surface/crack is described using various criteria available, cf. 1.5.2. Discrete methods usually represent the degradation at the process zone using cohesive zone methods. Cohesive theory assumes that material adhesion in front of the crack tip decreases progressively which results in a lower traction along the crack surface. This traction eventually decreases to zero once the crack opening reaches a certain limit which results in an irreversible energy loss [20, 21]. Xu and Needleman [22] employed Cohesive zone elements by inserting them between all elements assuming a traction-separation law. However, it resulted in introduction of spurious compliance to the finite element model. Camacho and Ortiz [23] improved it later by utilising an adaptive insertion of the cohesive zone elements. In this approach, connectivity between all elements is as in the regular finite element method until traction along an element boundary exceeds the critical limit, at which connectiv-

ity is modified and a cohesive element is inserted between the elements along the boundary. One main drawback for this method is its mesh dependency in describing the crack direction which can be improved by employing remeshing techniques. In order to represent the discontinuity in the displacement field independent of the discretisation of the domain, the extended finite element method (XFEM), cf. [24, 25], and phantom node method, cf. [26–29] are extensively employed in the current work, cf. Chapter 2, 3, and 4. The XFEM and phantom node method employ enriched nodes and overlapping elements respectively to describe the crack independent of the mesh alignment. Therefore, they require no significant mesh refinement which is of high significance from the computational point of view.

1.5.1. MATERIAL MODELLING

A reliable simulation of thin-walled shell structures requires employing a proper material modelling framework to describe the development of the visco-plastic response of the structure at high loading rates. In the current research, in order to represent the material behaviour in a computationally efficient, yet accurate way, it is opted to employ a hypoelastic-inelastic framework. A downside to employ hypoelastic-plastic models is that they suffer from lack of energy conservation in a closed deformation cycle. However, the discrepancy in conservation of the energy is found to be negligible provided that the elastic strains remain small compared to the plastic strains [30].

In line with the developments in [31], the constitutive law used in this work is formulated in rate form employing the objective Green-Naghdi stress rate to account for finite deformation. Considering the application of the current work, it is of significance to account for temperature variation, strain rate, and isotropic hardening of the material. For that, the phenomenological model of Johnson and Cook [32] is incorporated in the hypoelastic-plastic model used. This is further discussed in the chapters 2, 3, 4, and 5 of the thesis.

1.5.2. DIFFERENT PHASES OF THE FRACTURE MODELLING APPROACH EMPLOYED IN THE CURRENT WORK

To elaborate on the approach employed in this study, an overview of the different phases a material point undergoes during failure is provided in the following. There are three phases that are considered in the current modelling framework, elastic deformation, elasto-plastic with non-localised deformation, and localised deformation, cf. Figure 1.2. During the first phase, i.e. elastic deformation, the material remains elastic and the deformation induced is reversible. Loading the material beyond the yield point, plastic deformation starts which is irreversible. Obviously, to represent the response of a structure during this phase employing a reliable shell formulation as well as an accurate constitutive material model is a necessity. Accounting for the significant plastic deformation and large deformation incurred during this phase is of high importance for such a material model. The transition to the third phase is preceeded by the onset of strain localisation, which refers to the point

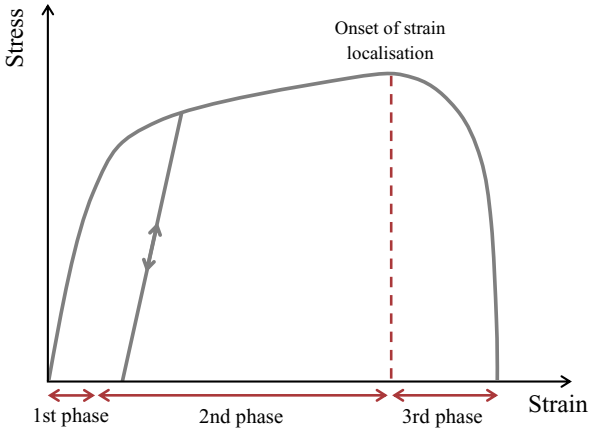

Figure 1.2: Different phases of failure process of a material point

at which the material starts to lose its load carrying capacity. Upon occurrence of this, the deformation starts to localise in a narrow band which forms the failure zone and eventually the material loses its integrity. Finding the onset of strain localisation is a necessity in the model to capture a reliable result. For that there are numerous criteria [33–36] such as loss of ellipticity, maximum energy release rate, maximum tensile principal strain, Johnson and Cook failure criterion, and maximum principal stress. The criteria employed in the current study are the maximum principal stress criterion, for predicting onset and orientation of the cohesive zone, and the Johnson and Cook fracture criterion, to predict onset of damage initiation.

The third phase, i.e. localised deformation and softening/damage, concerns the early degradation of the material until it reaches complete degradation in the failure zone. Undergoing this phase corresponds to total loss of material integrity and load carrying capacity in the material. To represent the excessive deformation that occurs during this phase special consideration is required. In the current study, describing the material behaviour during this phase is carried out using continuum damage modelling and discrete modelling schemes. The continuum damage model utilised herein is extensively explained in chapter 5. For the discrete modelling method, the XFEM and phantom node methods are utilised to represent the strong discontinuity in the displacement field. In line with that, in order to capture the behaviour of the material across the discontinuity at the process zone, and to describe the resisting forces of the material, the Cohesive zone method is used. To elaborate on these methods, in the following a brief description of the XFEM, phantom node method, and the Cohesive zone method are presented.

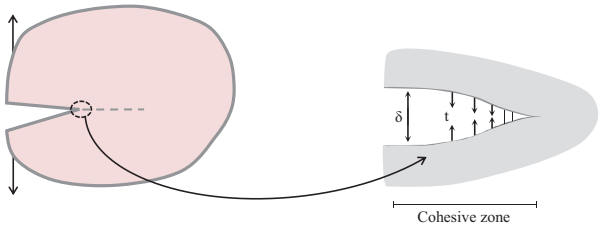

Figure 1.3: Failure process zone

INTERFACE CONSTITUTIVE MODEL

Following the pioneering work of Dugdale [20] cohesive zone models have been widely used in failure process modelling. Unlike the linear elastic fracture mechanics which regards the failure process zone to be confined to the crack tip, in cohesive zone theory a process zone is assumed to be present at the vicinity of the crack tip. In cohesive zone theory, various degradation processes such as the initiation, nucleation of voids and coalescence of these voids to form micro-cracks, which eventually leads to macro-cracks is accounted for along the cohesive zone, cf. Figure 1.3.

In order to represent the cohesive zone, various constitutive models in terms of a traction-separation law have been proposed. In these models, tractions represent the resisting force across the crack prior to the fracture as a function of the crack opening. Depending on the application, there are different parameters, e.g. fracture energy and tensile strength, and also various traction-separation laws, e.g. linear, bilinear, exponential, etc. as in Figure 1.4, that can employed, cf. [23, 37–39].

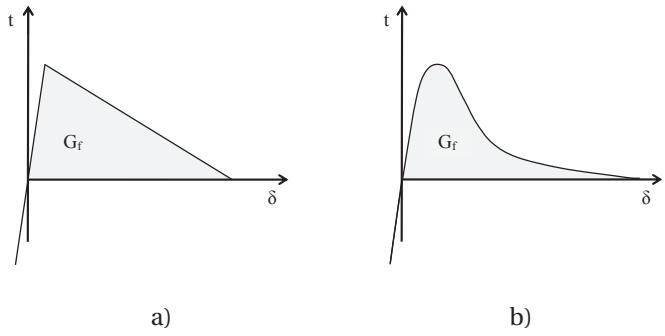

Figure 1.4: Examples of cohesive zone models a) bilinear cohesive zone and b) exponential cohesive zone.

Given the application of the current work, failure of thin-walled structure un-

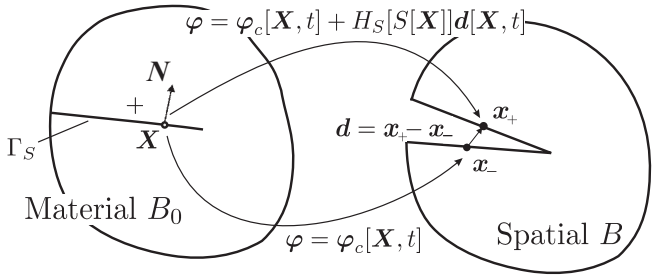

Figure 1.5: Kinematical representation of the discontinuity

der impact loading, the influence of high strain-rates during the failure process may not be neglected, as observed by Ravi-Chandar and Knauss [40]. Therefore, a rate-dependent cohesive zone model in line with the development by Fagerström and Larsson [41, 42] where a damage viscoplastic model represents the traction across the crack is employed.

A BRIEF SUMMARY ON THE EXTENDED FINITE ELEMENT METHOD (XFEM) AND THE PHANTOM NODE APPROACH

In the finite element application to failure modelling, one way to kinematically represent cracks is to directly introduce discontinuities in the displacement field. To maintain accuracy and mesh independence of the discontinuous approximation, two special formulations are considered in the thesis.

The first approach to address this problem is the extended finite element method, where additional enrichments are used together with the standard shape functions to treat the non-smooth character present in the solution field. These additional enrichments are realised by emplying the partition of unity concept [43] such that the approximations for the discontinuous part of the domain can be improved. As a result of that, the approximation of a function $\boldsymbol{\varphi}[\mathbf{X}]$ is enhanced as:

$$\boldsymbol{\varphi} = \boldsymbol{\varphi}_c[\mathbf{X}, t] + H_S[S[\mathbf{X}]]\,\boldsymbol{d}[\mathbf{X}, t] \tag{1.1}$$

$$\boldsymbol{\varphi}^h = \sum_{I \in N_{\text{tot}}} N^I \boldsymbol{\varphi}_c^I + \sum_{J \in N_{\text{enr}}} N^J H_S \boldsymbol{d}^J \tag{1.2}$$

where the shape functions N^I and N^J are employed to approximate the continuous, $\boldsymbol{\varphi}_c$, and discontinuous, $\boldsymbol{d}$, part of the approximation field. To define the enrichment function which is typically a step-function, H_S is described as a function of level set, S, to represent the discontinuity, cf. Figure 1.5.

The second approach that is considered to treat the discontinuity in the solution field is the phantom node method [26, 27]. In this approach, overlapping elements are employed where the connectivity of the elements is updated to capture the discontinuity in the solution field. Once a discontinuity is predicted from the failure

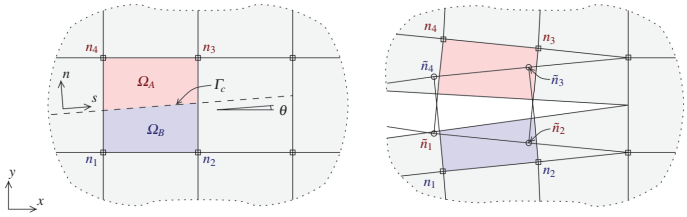

Figure 1.6: Representation of the strong discontinuity using the phantom node method. The cracked element domain is considered as an overlapping of two elements with Ω_A and Ω_B referring to the active part of each element. Image reproduced from [29]. Printed with permission

criterion, the element domain is divided into two parts and the nodes associated with each part of the element are doubled. Therefore, there are two overlapping elements on top of each other, where for each element there exists an active domain and a phantom domain, as shown in Figure 1.6.

In order to introduce the discontinuity in the cracked element domain, finite element nodal force integration is performed only on the active part of the domain of each element. It is shown that the phantom node method provides the same kinematical representation as the XFEM does, cf. [27]; however, the phantom node method is easier to implement [28]. An additional advantage of the use of the phantom node method for dynamics simulations is the possibility to employ the standard row sum procedure to obtain the proper lumped mass matrix.

REFERENCES

[1] W. Garrison Jr and N. Moody, *Ductile fracture,* Journal of Physics and Chemistry of Solids **48**, 1035 (1987).

[2] N. F. Mott, *Brittle fracture in mild steel plates,* Engineering **165** (1948).

[3] S. Razanica, *Ductile damage modeling of the machining process*, Ph.D. thesis, Chalmers University of Technology (2019), iSBN 978-91-7597-884-0.

[4] C. Sansour and F. G. Kollmann, *Families of 4-node and 9-node finite elements for a finite deformation shell theory. an assesment of hybrid stress, hybrid strain and enhanced strain elements,* Computational Mechanics **24**, 435 (2000).

[5] R. Larsson, *A discontinuous shell-interface element for delamination analysis of laminated composite structures,* Computer methods in applied mechanics and engineering **193**, 3173 (2004).

[6] P. Betsch and E. Stein, *A nonlinear extensible 4-node shell element based on continuum theory and assumed strain interpolations,* Journal of Nonlinear Science **6**, 169 (1996).

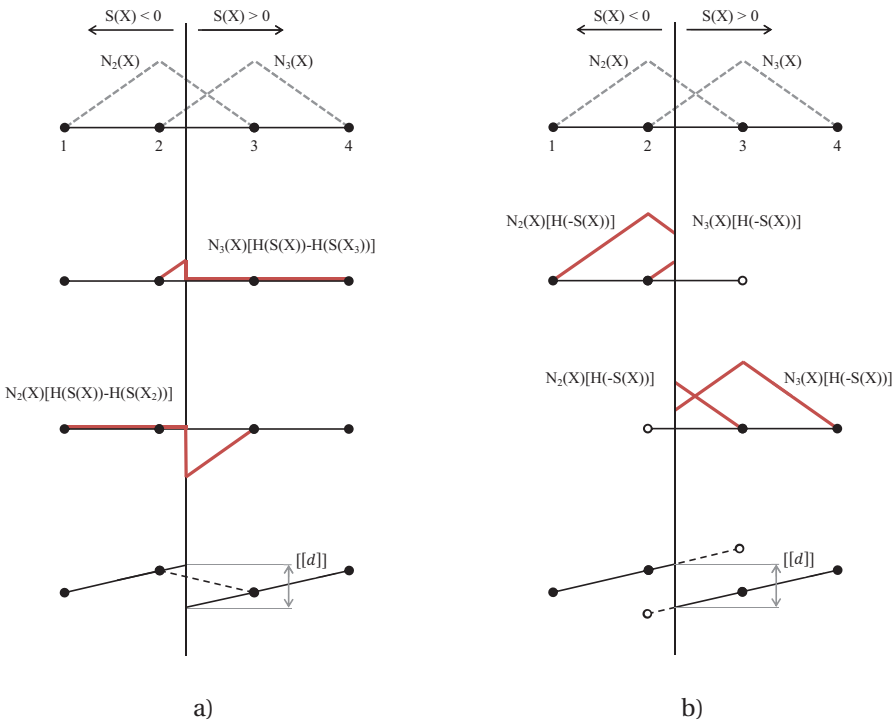

Figure 1.7: Illustration of one dimensional shape functions for both the XFEM and phantom node method a) kinematic representation for the XFEM and b) kinematic representation for the phantom node method.

[7] J.-C. Simo and F. Armero, *Geometrically non-linear enhanced strain mixed methods and the method of incompatible modes,* International Journal for Numerical Methods in Engineering **33**, 1413 (1992).

[8] R. Larsson, J. Mediavilla, and M. Fagerström, *Dynamic fracture modeling in shell structures based on XFEM,* International Journal for Numerical Methods in Engineering **86**, 499 (2010).

[9] M. Bischoff and E. Ramm, *On the physical significance of higher order kinematic and static variables in a three-dimensional shell formulation,* International Journal of Solids and Structures **37**, 6933 (2000).

[10] L. Kachanov, *On the time to failure under creep conditions (in russian),* Izvestiya Akademii Nauk SSSR. Otdelenie Tekhnicheskikh Tauk **8**, 26 (1958).

[11] J. Lemaitre, *A Course on Damage Mechanics* (Springer-Verlag, Berlin, 1992).

[12] A. Gurson, *Continuum theory of ductile rupture by void nucleation and growth: Part I Yield criteria and flow rules for porous ductile media,* Journal of Engineering Materials and Technology **99**, 2 (1977).

[13] V. Tvergaard and A. Needleman, *Analysis of cupcone fracture in a round tensile bar,* Acta Metallurgica **32**, 157 (1984).

[14] B. Patzak and M. Jirasek, *Process zone resolution by extended finite elements,* Engineering Fracture Mechanics **70**, 957 (2003).

[15] B. Patzak and M. Jirasek, *Adaptive resolution of localized damage in quasi-brittle materials,* Journal of Engineering Mechanics **130**, 720 (2004).

[16] Z. Bazant and G. Pijaudier-Cabot, *Nonlocal continuum damage, localization instability and convergence,* Journal of Applied Mechanics **55**, 287 (1988).

[17] R. Peerlings, R. De Borst, W. Brekelmans, and M. Geers, *Gradient-enhanced damage modelling of concrete fracture,* Mechanics of Cohesive-frictional Materials **3**, 323 (1998).

[18] J. Besson, *Continuum models of ductile fracture: a review,* International Journal of Damage Mechanics **19**, 3 (2010).

[19] S. Razanica, R. Larsson, and B. L. Josefson, *A ductile fracture model based on continuum thermodynamics and damage,* Mechanics of Materials , DOI: 10.1016/j.mechmat.2019.103197 (2019).

[20] D. Dugdale, *Yielding of steel sheets containing slits,* Journal of the Mechanics and Physics of Solids **8**, 100 (1960).

[21] G. Barenblatt, *Mathematical theory of equilibrium cracks in brittle fracture,* Advances in Applied Mechanics **7**, 55 (1962).

[22] X. Xu and A. Needleman, *Numerical simulations of fast crack growth in brittle solids,* Journal of the Mechanics and Physics of Solids **42**, 1397 (1994).

[23] G. Camacho and M. Ortiz, *Computational modelling of impact damage in brittle materials,* International Journal of Solids and Structures **33**, 2899 (1996).

[24] T. Belytschko and T. Black, *Elastic crack growth in finite elements with minimal remeshing,* International Journal for Numerical Methods in Engineering **45**, 601 (1999).

[25] N. Moës, J. Dolbow, and T. Belytschko, *A finite element method for crack growth without remeshing,* International Journal for Numerical Methods in Engineering **46**, 131 (1999).

[26] A. Hansbo and P. Hansbo, *A finite element method for the simulation of strong and weak discontinuities in elasticity,* Computer Methods in Applied Mechanics and Engineering **193**, 3523 (2004).

[27] J. Song, P. Areias, and T. Belytschko, *A method for dynamic crack and shear band propagation with phantom nodes,* International Journal for Numerical Methods in Engineering **67**, 868 (2006).

[28] T. Rabczuk, G. Zi, A. Gerstenberger, and W. Wall, *A new crack tip element for the phantom-node method with arbitrary cohesive cracks,* International journal for numerical methods in engineering **75**, 577 (2008).

[29] F. Van der Meer and L. Sluys, *A phantom node formulation with mixed mode cohesive law for splitting in laminates,* International journal of fracture **158**, 107 (2009).

[30] T. Belytschko, W. Liu, and B. Moran, *Nonlinear finite elements for continua and structures*, Vol. 1 (Wiley New York, 2000).

[31] G. Ljustina, M. Fagerström, and R. Larsson, *Hypo-and hyper-inelasticity applied to modeling of compacted graphite iron machining simulations,* European Journal of Mechanics-A/Solids **37**, 57 (2013).

[32] G. Johnson and W. Cook, *Fracture characteristics of three metals subjected to various strains, strain rates, temperatures and pressures,* Engineering Fracture Mechanics **21**, 31 (1985).

[33] G. Sih, *Strain energy-density factor applied to mixed-mode crack problems,* International Journal of Fracture **10**, 305 (1974).

[34] R. Nuismer, *An energy release rate criterion for mixed mode fracture,* International Journal of Fracture **11**, 245 (1975).

[35] F. Erdogan and G. Sih, *On the crack extension in plates under plane loading and transverse shear,* Journal of Basic Engineering **85**, 519 (1963).

[36] G. Johnson and W. Cook, *Fracture characteristics of three metals subjected to various strains, strain rates, temperatures and pressures,* Engineering Fracture Mechanics **21**, 31 (1985).

[37] A. Hillerborg, M.Modéer, and P. Petersson, *Analysis of crack formation and crack growth in concrete by means of fracture mechanics and finite elements,* Cement and Concrete Research **6**, 773 (1976).

[38] A. Needleman, *An analysis of decohesion along an imperfect interface,* International Journal of Fracture **42**, 21 (1990).

[39] J. Mergheim, *Computational Modeling of Strong and Weak Discontinuities*, phdthesis, University of Kaiserslautern (2006), phD thesis.

[40] K. Ravi-Chandar and W. G. Knauss, *An experimental investigation into dynamic fracture: I. Crack initiation and arrest,* International Journal of Fracture **25**, 247 (1984).

[41] M. Fagerström and R. Larsson, *Theory and numerics for finite deformation fracture modelling using strong discontinuities,* International Journal for Numerical Methods in Engineering **66**, 911 (2006).

[42] M. Fagerström and R. Larsson, *Approaches to dynamic fracture modelling at finite deformations,* Journal of the Mechanics and Physics of Solids **56**, 613 (2008).

[43] I. Babuška and J. Melenk, *The partition of unity finite element method: Basic theory and applications,* Computer Methods in Applied Mechanics and Engineering **139**, 289 (1996).

2

DYNAMIC CRACK PROPAGATION IN ELASTOPLASTIC THIN-WALLED STRUCTURES: MODELLING AND VALIDATION

In this chapter, a method to analyse and predict crack propagation in thin-walled structures subjected to large plastic deformations when loaded at high strain rates – such as impact and/or blast – has been proposed. To represent the crack propagation independently of the finite element discretisation, an eXtended Finite Element Method (XFEM) based shell formulation has been employed. More precisely, an underlying 7-parameter shell model formulation with extensible directors has been extended by locally introducing an additional displacement field, representing the displacement discontinuity independently of the mesh. Of special concern in this contribution has been to find a proper balance between, level of detail and accuracy when representing the physics of the problem and, on the other hand, computational efficiency and robustness. To promote computational efficiency, an explicit time step scheme has been employed, which however has been discovered to generate unphysical oscillations in the response upon crack propagation. Therefore, special focus has been placed to investigate these oscillations as well as to find proper remedies. The chapter is concluded with three numerical examples to verify and validate the proposed model.

This chapter was integrally extracted from [1].

2.1. INTRODUCTION

The aim of this contribution is to build a foundation for a more detailed analysis of ductile fracture of thin-walled steel structures loaded at high strain rates. Of particular interest are applications to large scale structures, such as ship panels, off-shore structures etc., for which an adequate modelling and an efficient numerical procedure to handle ductile localised failure are essential ingredients to obtain results at reasonable computational effort.

So far there have been a large number of researches conducted on the modelling of dynamic crack propagation to improve the computational efficiency of the standard finite element method, requiring advanced remeshing and projection procedures of the state variables due to crack growth. As a first step, localised failure was analysed through inter–element techniques in which cohesive zone elements were placed along the edges of the continuum elements. In their pioneering work, Xu and Needleman [2] proposed a method where all continuum elements are separated from the beginning, their coupling being governed simply by cohesive zone elements placed along the element edges. This rendered a very flexible approach in terms of representing arbitrary crack growth, which however unfortunately introduces spurious compliance to the resulting finite element model. To alleviate this problem, Camacho and Oritz [3] improved the method by employing successive introduction of the cohesive zone elements only between continuum elements where a certain fracture criterion is met. Still, the orientation of the crack propagation in both approaches is susceptible to inaccuracy due to its mesh dependency. To address the aforementioned difficulties, the eXtended Finite Element Method (XFEM) was developed by Belytschko and Black [4] and Moës *et al.* [5] based on the partition of unity method by Melenk and Babuška [6] which allows for arbitrary crack growth without remeshing by including an additional approximation field to represent the displacement discontinuity. In order to extend the application of XFEM to quasi-brittle materials, Wells and Sluys [7] utilised cohesive crack models in the XFEM method considering crack propagation to be element-wise. Representation of crack tip location was then improved by Moës and Belytschko [8] and Zi and Belytschko [9] to include crack tip inside the element. To promote computational efficiency in dynamic crack propagation, Menouillard *et al.* [10, 11] suggested simple mass lumping schemes for explicit time integration of the governing equations which increase the stable time step. Furthermore, they also investigated instability issues arising during crack propagation which will be discussed in the current chapter as well. In the current chapter however, we will resort to the consistent mass matrix in the implementation, since lumped mass schemes in combination with XFEM discontinuity enrichments have previously proven to render unrealistic behaviour under certain circumstances, cf. *e.g.* the work by Remmers et al. [12] in which it was shown that unphysical tractions may be transmitted across traction free XFEM discontinuity surfaces if a lumped mass scheme is employed for the temporal integration.

An alternative method to XFEM, capable of representing mesh-independent crack propagation, has also been proposed by Hansbo and Hansbo [13] in which, instead of enriching the approximation space with additional discontinuous degrees of free-

dom, it replaces the cracked element with two overlapping elements by employing so called Phantom nodes. The kinematical representation has later on been proved to be identical to XFEM by Song *et al.* [14], yet computationally easier to implement as it has also been noted by Rabczuk *et al.* [15].

In the particular case of thin-walled structures, different methods of crack representation including through the thickness fracture have been investigated in various studies. Areias and Belytschko [16] utilised a shell element based on Mindlin-Reissner theory, where they made use of an enhanced assumed strain formulation to deal with the locking occurring for thin shells. A Kirchhoff-Love based shell element is also employed by Areias *et al.* [17]. However, a drawback of the Kirchhoff-Love theory is its incapability in representing the shear deformation. Recently, a geometrically nonlinear continuum based shell element has been exploited by Ahmed *et al.* [18] which is based on the solid-like shell theory developed by Parisch [19]. An advantage of this model is its capability to avoid the Poisson locking effect when applied in thin shells. In this contribution, the shell formulation adopted is in line with the developments by Larsson *et al.* [20] based on the shell formulation proposed by Bischoff and Ramm [21], wherein a second order expansion in the director field is utilised. This results for the underlying continuous shell in a 7-parameter displacement formulation that circumvents Poisson locking effect induced by incompatible representation of thickness strains due to bending. In order to represent through-the-thickness fracture with an arbitrary crack path, the shifted version of the XFEM, cf. *e.g.* Reference [9] has been employed, combined with the cohesive zone concept [22, 23] to model the material degradation of the fracture process zone.

A quite common approach described in the literature to address the modelling of dynamic ductile fracture is by means of non-local damage elastoplastic continuum models – either purely phenomenological models in the spirit of *e.g.* Kachanov [24] and Lemaitre [25] or based on assumptions of the micromechanical response of the material following *e.g.* Gurson [26] and Tvergaard and Needleman [27]. In this way, the entire stress-strain relation can be modelled in a unified framework, including the progressive damage evolution until final fracture. The drawback of this approach is that results from continuum damage models are predictive only if the mesh is sufficiently refined having several elements across the damage zone [28]. This requires adaptive mesh refinement to avoid a heavily dense mesh in the entire domain, cf. *e.g.* Patzak and Jirasek [29]. In addition, in its original form, a continuum damage based approach does not allow for a discrete representation of a crack, which, on the one hand, may cause numerical difficulties related to excessive element distortion (before reaching the fully damaged state) and, on the other hand, it precludes the modelling of *e.g.* crack closure. Remedies for the latter, by means of combining the damage modelling with an explicit representation of a crack which is introduced at a 'critical' damaged state (defined differently in the different contributions), have been proposed in the literature - either by employing XFEM kinematics, cf. *e.g.* Wells *et al.* [30] and Seabra *et al.* [31], or by remeshing, cf. *e.g.* Mediavilla *et al.* [32]. However, the requirement of a locally refined mesh in the vicinity of the localisation zone remains. To promote computational efficiency, methods have been proposed

by *e.g.* Areias and Belytschko [33] and Cazes *et al.* [34] in which continuum based damage modelling is combined with surface based 'damage modelling. In both of these contributions, a local damage elastoplastic model to describe the diffuse material degradation before localisation is combined with a cohesive zone model to represent the localised deformation response up until final rupture. In both approaches, the switch from continuum damage modelling to cohesive modelling is made based on the criterion of loss of material stability. Furthermore, the cohesive zone model is adapted to accurately represent the remaining energy dissipation, thus avoiding any pathological mesh dependency but still allowing for a reasonably coarse spatial discretisation. Even though the aforementioned papers include promising results, it should be remarked that the application is in both papers limited to mode I fracture. Furthermore, as observed by Ravi-Chandar and Knauss [35], nucleation, growth and coalescence of microcracks requires sufficient time to create a macrocrack in front of the crack tip. Consequently, the interaction between the microstructural response and the formation of macro–cracks is related to the time interval over which the fracture process takes place. This is accounted for herein by employing a damage–viscoplastic cohesive zone model based on the developments in [36, 37] by Fagerström and Larsson in which rate-dependency has been included to model this interaction. As the material model of the continuously deforming part of the domain, a hypoelastic-inelastic framework is utilised in which the phenomenological model proposed by Johnson and Cook [38] is employed.

The chapter is organised as follows. In Section 2.2, the kinematics of the shell formulation as well as the representation of the discontinuity using XFEM is described. In Section 2.3, the weak form of the momentum balance is presented, where emphasis is placed on stress resultants of the internal work. In Section 2.4, we discuss the material model for the continuously deforming part of the domain as well as the onset criterion for localisation followed by description of the cohesive zone model. In Section 2.5, methods to alleviate numerical instabilities are summarised. In Section 2.6, numerical results and their comparison with experiments are provided. Finally, the chapter is concluded with closing discussion.

2.2. DISCONTINUOUS SHELL KINEMATICS

In this chapter, we extend the developments presented in [20] to account for plastic deformations prior to fracture. In the previous paper, the underlying shell formulation – based on a classical Heaviside enrichment of the displacement field, *e.g.* in the spirit of [39], to account for strong displacement discontinuities – was described in detail. Herein, a slight modification of the kinematical representation is made in the sense that the 'shifted version' of the Heaviside function is utilised to introduce the strong discontinuity, with the benefit of avoiding so-called blending elements. Therefore, to introduce the adopted kinematics and to clarify the differences from Reference [20], a short overview of the kinematical representation is given in the subsections below.

2.2.1. INITIAL SHELL GEOMETRY AND CONVECTED COORDINATES

As a staring point, the initial configuration B_0 of the shell is considered parameterised in terms of convected coordinates (ξ_1, ξ_2, ξ) as

$$\begin{aligned} \mathrm{B}_0 = \big\{ \mathbf{X} := \mathbf{\Phi}_0[\xi_1,\xi_2,\xi] = \bar{\mathbf{\Phi}}[\xi_1,\xi_2] + \xi \mathbf{M}[\xi_1,\xi_2] \\ \text{with } [\xi_1,\xi_2] \in A \text{ and } \xi \in \tfrac{h_0}{2}[-1,1] \big\} \end{aligned} \tag{2.1}$$

where the mapping $\mathbf{\Phi}_0[\xi_1,\xi_2,\xi]$ maps the inertial Cartesian frame into the reference configuration, cf. Figure 2.1. In Eq (2.1), the mapping $\mathbf{\Phi}_0$ is defined by the midsurface placement $\bar{\mathbf{\Phi}}[\xi_1,\xi_2]$ and the outward unit normal vector field $\mathbf{M}$ (with $|\mathbf{M}| = 1$). The coordinate ξ is associated with this direction and h_0 is the initial thickness of the shell.

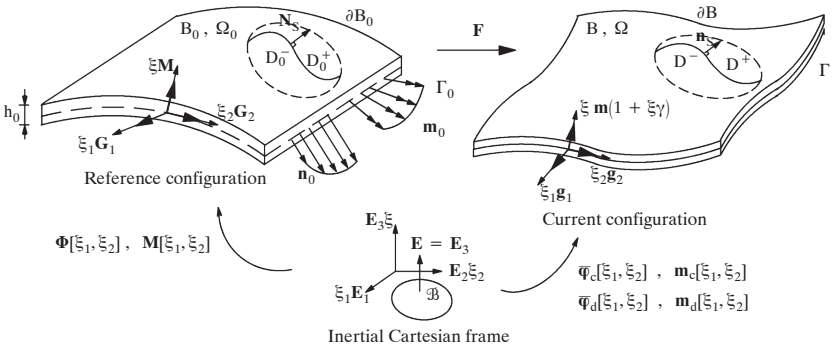

Figure 2.1: Mappings of shell model defining undeformed and deformed shell configurations relative to inertial Cartesian frame

It is remarked that

$$\begin{aligned} \mathrm{d}\mathbf{X} &= \left(\mathbf{G}_\alpha \otimes \mathbf{G}^\alpha\right) \cdot \mathrm{d}\mathbf{X} + \mathbf{M} \otimes \mathbf{M} \cdot \mathrm{d}\mathbf{X} = \\ &= \mathbf{G}_\alpha[\xi_1,\xi_2,\xi]\mathrm{d}\xi_\alpha + \mathbf{M}[\xi_1,\xi_2]\mathrm{d}\xi \end{aligned} \tag{2.2}$$

whereby the co-variant basis vectors are defined by

$$\mathbf{G}_\alpha = \mathbf{\Phi}_{,\alpha} + \xi \mathbf{M}_{,\alpha},\ \alpha = 1,2 \text{ and } \mathbf{G}_3 = \mathbf{G}^3 = \mathbf{M} \tag{2.3}$$

where $\bullet_{,\alpha}$ denotes the derivative with respect to ξ_α. In addition, in Eq. (2.2) it was used that the contra-variant basis vectors $\mathbf{G}^i$ are associated with the co-variant vectors $\mathbf{G}_i$ in the normal way, *i.e.* $\mathbf{G}_i \otimes \mathbf{G}^i = \mathbf{1}$, leading to

$$\mathbf{G}_j = G_{\mathrm{ij}}\mathbf{G}^i\ ,\ \mathbf{G}^j = G^{\mathrm{ij}}\mathbf{G}_i \text{ with } G_{\mathrm{ij}} = \mathbf{G}_i \cdot \mathbf{G}_j \text{ and } G^{\mathrm{ij}} = \left(G_{\mathrm{ij}}\right)^{-1} \tag{2.4}$$

Finally, the infinitesimal volume element $\mathrm{d}B_0$ of the reference configuration is formulated in the convected coordinates as

$$\mathrm{d}B_0 = b_0 \mathrm{d}\xi_1 \mathrm{d}\xi_2 \mathrm{d}\xi \text{ with } b_0 = (\mathbf{G}_1 \times \mathbf{G}_2) \cdot \mathbf{G}^3 \tag{2.5}$$

2.2.2. CURRENT SHELL GEOMETRY BASED ON DISCONTINUOUS KINEMATICS

The current (deformed) geometry is in the current formulation described by the deformation map $\boldsymbol{\varphi}[\mathbf{X}] \in B$, additively composed of the continuous placement field $\boldsymbol{\varphi}_c \in B$ and the (local) discontinuous displacement field $\boldsymbol{\varphi}_d \in D$, parameterised in the convective coordinates (ξ_1, ξ_2, ξ) as

$$\mathbf{x} := \boldsymbol{\varphi}_c[\mathbf{X}[\xi_1,\xi_2,\xi],t] + \boldsymbol{\varphi}_d[\mathbf{X}[\xi_1,\xi_2,\xi],t] \text{ where } \boldsymbol{\varphi}_d \equiv \mathbf{0}\ \forall \mathbf{X} \in B_0 \setminus D_0 \tag{2.6}$$

where, in accordance with standard XFEM methodology, $\boldsymbol{\varphi}_d$ is defined locally in the vicinity of a crack, *i.e.* for $\mathbf{X} \in D_0$ as shown in Figure 2.1. Furthermore, following Reference [20], the through-the-thickness fracture representation is invoked in the shell formulation in terms of strong discontinuities in both the midsurface placements and the director fields using XFEM-kinematics. In particular, the specification of the current configuration corresponds to expansions along the director fields as defined by

$$\begin{cases} \boldsymbol{\varphi}_c[\xi_1,\xi_2,\xi] = \bar{\boldsymbol{\varphi}}_c[\xi_1,\xi_2] + \xi \mathbf{m}_c[\xi_1,\xi_2] + \frac{1}{2}\xi^2 \mathbf{m}_c \gamma[\xi_1,\xi_2] \\ \boldsymbol{\varphi}_d[\xi_1,\xi_2,\xi] = \bar{\boldsymbol{\varphi}}_d[\xi_1,\xi_2] + \xi \mathbf{m}_d[\xi_1,\xi_2] \end{cases} \tag{2.7}$$

where it should be remarked that the continuous placement $\boldsymbol{\varphi}_c$ corresponds to a second order Taylor series expansion in the director $\mathbf{m}_c$, thereby describing inhomogeneous thickness deformation effects of the shell. In particular, the pathological Poisson locking effect is avoided in this fashion. In contrast, for simplicity and efficiency, only a first order expansion is used for the discontinuous part $\boldsymbol{\varphi}_d$.

For the finite element approximation, the continuous part of the mapping is approximated by standard C^0 (quadratic) shape functions $N^I[\xi_1,\xi_2]$ as

$$\boldsymbol{\varphi}_c = \sum_{I \in N_{\text{tot}}} N^I[\xi_1,\xi_2] \left(\bar{\boldsymbol{\varphi}}^I + \xi \mathbf{m}_c^I \left(1 + \frac{1}{2}\xi \sum_{J \in N_{\text{tot}}} N^J[\xi_1,\xi_2] \gamma^J \right) \right) \tag{2.8}$$

where N_{tot} is the total set of nodes in B_0 and $\bar{\boldsymbol{\varphi}}^I$, $\mathbf{m}_c^I$ and γ^J are the corresponding degrees of freedom.

For the local discontinuous enrichment, the 'shifted' form of the Heaviside function is utilised to realise the strong discontinuity. Hence, if we in analogy with *e.g.* Zi and Belytschko [9] let N_{enr} denote the set of enriched nodes, associated only with the particular elements intersected by a segment of the crack, the discontinuous part of the mapping can be written as

$$\boldsymbol{\varphi}_d = \sum_{I \in N_{\text{enr}}} N^I[\xi_1,\xi_2] \psi^I[\xi_1,\xi_2] \left(\bar{\boldsymbol{\varphi}}_d^I + \xi \mathbf{m}_d^I \right) \tag{2.9}$$

where ψ^I are the shifted enrichment functions (associated with each node I) defined as

$$\psi^I[\xi_1,\xi_2] = H[S[\xi_1,\xi_2]] - H[\xi_1^I,\xi_2^I] \tag{2.10}$$

and where $\bar{\boldsymbol{\varphi}}_d^I$ and $\mathbf{m}_d^I$ are the degrees of freedom representing the discontinuous parts of the midsurface displacement and director field respectively. As to the argument of the Heaviside function, the level-set function $S[\xi_1,\xi_2]$ defined on D_0 (in which $\boldsymbol{\varphi}_d \neq \mathbf{0}$) is considered monotonic such that

$$\begin{cases} S[\xi_1,\xi_2] & < 0 \text{ if } \boldsymbol{\Phi}[\xi_1,\xi_2] \in D_0^- \\ S[\xi_1,\xi_2] & = 0 \text{ if } \boldsymbol{\Phi}[\xi_1,\xi_2] \in \Gamma_S \\ S[\xi_1,\xi_2] & > 0 \text{ if } \boldsymbol{\Phi}[\xi_1,\xi_2] \in D_0^+ \end{cases} \tag{2.11}$$

with the additional requirement

$$\frac{\partial S}{\partial \mathbf{X}} = \mathbf{N}_S \tag{2.12}$$

where D_0 is considered subdivided into a minus side D_0^- and a plus side D_0^+ by the discontinuity line Γ_S with the corresponding normal vector $\mathbf{N}_S$, as shown in Figure 2.1. Please note that the level-set function S has the convected midsurface coordinates as arguments, thereby restricting the current formulation to through-the-thickness shell fracture. Furthermore, it is remarked that the enriched reference volume D_0 is here defined only by the finite elements intersected by a crack (or a cohesive segment) since the enrichment functions in Eq. (2.10) are defined such that the discontinuous enrichment vanishes at the (corner) nodes, which is an improvement of the formulation in [20] in the sense that blending elements – elements partially enriched but without any internal displacement jump – are avoided. For completeness, we also note that the displacement jump $\tilde{\mathbf{d}}$ over Γ_S is, with due consideration to the shifted enrichment function in the current formulation, defined along the discontinuity line as

$$\begin{aligned} \tilde{\mathbf{d}} &= \boldsymbol{\varphi}^+ - \boldsymbol{\varphi}^- = \boldsymbol{\varphi}_c^+ + \sum_{I\in D_0^-} N^I\left(\bar{\boldsymbol{\varphi}}_d^I + \xi \mathbf{m}_d^I\right) - \left(\boldsymbol{\varphi}_c^- + \sum_{J\in D_0^+} -N^J\left(\bar{\boldsymbol{\varphi}}_d^J + \xi \mathbf{m}_d^J\right)\right) \\ &= \left\{\boldsymbol{\varphi}_c^+ = \boldsymbol{\varphi}_c^-\right\} = \sum_{K\in D_0} N^K\left(\bar{\boldsymbol{\varphi}}_d^K + \xi \mathbf{m}_d^K\right) = \boldsymbol{\varphi}_d = \bar{\boldsymbol{\varphi}}_d + \xi \mathbf{m}_d. \end{aligned} \tag{2.13}$$

To identify the deformation gradient, a relative motion $\mathrm{d}\mathbf{x}$ of the non-linear placement $\boldsymbol{\varphi}$ is considered as

$$\begin{aligned} \mathrm{d}\mathbf{x} = &\left(\bar{\boldsymbol{\varphi}}_{c,\alpha} + \mathbf{m}_{c,\alpha}\left(\xi + \frac{1}{2}\gamma\xi^2\right) + \frac{1}{2}\gamma_{,\alpha}\xi^2\mathbf{m}_c + (\bar{\boldsymbol{\varphi}}_{d,\alpha} + \mathbf{m}_{d,\alpha}\xi)\right)\mathrm{d}\xi_\alpha + \\ &+ \left(\mathbf{m}_c(1+\gamma\xi) + \mathbf{m}_d\right)\mathrm{d}\xi + \delta_S(\bar{\boldsymbol{\varphi}}_d + \xi\mathbf{m}_d)s_\alpha \mathrm{d}\xi_\alpha \end{aligned} \tag{2.14}$$

whereby the deformation gradient is defined as consisting of one bulk part $\mathbf{F}$ and one interface part $\mathbf{F}_d$ as

$$\mathrm{d}\mathbf{x} = (\mathbf{F} + \delta_S\mathbf{F}_d)\cdot\mathrm{d}\mathbf{X} \text{ with } \mathbf{F} = \mathbf{g}_{\mathrm{ci}}\otimes\mathbf{G}^i,\ i=1,2,3 \text{ and } \mathbf{F}_d = \mathbf{g}_{\mathrm{d}\alpha}\otimes\mathbf{G}^\alpha,\ \alpha = 1,2 \tag{2.15}$$

where a Dirac-delta discontinuity $\delta_S\mathbf{F}_d$ occurs along the discontinuity line Γ_S. This is defined as

$$\int_{B_0} \delta_S \bullet \mathrm{d}B_0 = \int_{\Gamma_S}\int_{-h_0/2}^{h_0/2} \bullet \,\mathrm{d}\xi\,\mathrm{d}\Gamma_0 \tag{2.16}$$

for any quantity $\bullet$. In Eq. (2.15), the spatial co-variant basis vectors are identified from Eq. (2.14) as

$$\mathbf{g}_{\mathrm{ci}} = \begin{cases} \bar{\boldsymbol{\varphi}}_{c,i} + \mathbf{m}_{c,i}\left(\xi + \gamma\frac{1}{2}(\xi)^2\right) + \mathbf{m}_c\gamma_{,i}\frac{1}{2}(\xi)^2 + (\bar{\boldsymbol{\varphi}}_{d,i} + \boldsymbol{m}_{d,i}\xi), i = 1,2 \\ \boldsymbol{m}_c\left(1+\gamma\xi\right) + \mathbf{m}_d\ , \ i = 3 \end{cases} \tag{2.17}$$

$$\mathbf{g}_{\mathrm{d}\alpha} = \left(\bar{\boldsymbol{\varphi}}_d + \xi\mathbf{m}_d\right)s_\alpha\ , \ \alpha = 1,2 \tag{2.18}$$

where $s_\alpha = (\partial S/\partial\xi_\alpha) = \mathbf{N}_S \cdot \mathbf{G}_\alpha$. It should be remarked that the terms $(\bar{\boldsymbol{\varphi}}_{d,i} + \boldsymbol{m}_{d,i}\xi)$ (for $i = 1,2$) and $\mathbf{m}_d$ (for $i = 3$) only give non-zero contributions to $\mathbf{g}_{\mathrm{ci}}$ inside the subdomain D_0.

2.3. BALANCE EQUATIONS

In this section, we establish the momentum balance of the shell considering the weak continuum representation of the shell applied to the shell kinematics introduced above. We thereby highlight the – in relation to Reference [20] – modified formulation in stress resultants emanating from the shell kinematics and the internal work, formulated in the symmetric second Piola Kirchhoff stress tensor $\mathbf{S}$.

To arrive at the current stress resultant formulation, we start from the basic weak form of the momentum balance in terms of contributions from inertia G^{ine}, internal work G^{int} and external work G^{ext} as

Find: $[\bar{\boldsymbol{\varphi}}_c, \mathbf{m}_c, \gamma, \bar{\boldsymbol{\varphi}}_d, \mathbf{m}_d]$

$$\begin{aligned} &G^{\mathrm{ine}}[\ddot{\bar{\boldsymbol{\varphi}}}_c, \ddot{\mathbf{m}}_c, \ddot{\gamma}, \ddot{\bar{\boldsymbol{\varphi}}}_d, \ddot{\mathbf{m}}_d; \delta\bar{\boldsymbol{\varphi}}_c, \delta\mathbf{m}_c, \delta\gamma, \delta\bar{\boldsymbol{\varphi}}_d, \delta\mathbf{m}_d] + \\ &G^{\mathrm{int}}[\bar{\boldsymbol{\varphi}}_c, \mathbf{m}_c, \gamma, \bar{\boldsymbol{\varphi}}_d, \mathbf{m}_d; \delta\bar{\boldsymbol{\varphi}}_c, \delta\mathbf{m}_c, \delta\gamma, \delta\bar{\boldsymbol{\varphi}}_d, \delta\mathbf{m}_d] - \\ &\qquad G^{\mathrm{ext}}[\delta\bar{\boldsymbol{\varphi}}_c, \delta\mathbf{m}_c, \delta\gamma, \delta\bar{\boldsymbol{\varphi}}_d, \delta\boldsymbol{m}_d] = 0 \ \forall\ \delta\bar{\boldsymbol{\varphi}}_c, \delta\mathbf{m}_c, \delta\gamma, \delta\bar{\boldsymbol{\varphi}}_d, \delta\mathbf{m}_d \end{aligned} \tag{2.19}$$

where the inertia and the internal and external virtual work contributions are written as

$$G^{\mathrm{ine}} = \int_{B_0} \rho_0\left(\delta\boldsymbol{\varphi}_c + \delta\boldsymbol{\varphi}_d\right)\cdot\left(\ddot{\boldsymbol{\varphi}}_c + \ddot{\boldsymbol{\varphi}}_d\right)\mathrm{d}B_0, \tag{2.20}$$

$$G^{\mathrm{int}} = \int_{B_0}\left(\delta\mathbf{F}^t\cdot\mathbf{F}\right):\mathbf{S}\mathrm{d}B_0 + \int_{\Gamma_S}\int_{-h_0/2}^{h_0/2}\left(\delta\bar{\boldsymbol{\varphi}}_d + \xi\delta\mathbf{m}_d\right)\cdot\mathbf{t}_1\ \mathrm{d}\xi\ \mathrm{d}\Gamma_0 \tag{2.21}$$

$$G^{\mathrm{ext}} = \int_{B_0}\rho_0\left(\delta\boldsymbol{\varphi}_c + \delta\boldsymbol{\varphi}_d\right)\cdot\mathbf{b}\,\mathrm{d}B_0 + \int_{\partial B_0}\left(\delta\boldsymbol{\varphi}_c + \delta\boldsymbol{\varphi}_d\right)\cdot\bar{\mathbf{t}}_1\mathrm{d}S_0 \tag{2.22}$$

and where $\mathbf{b}$ is the body force per unit volume, $\bar{\mathbf{t}}_1 = \mathbf{P}^t\cdot\mathbf{N}$ is the prescribed nominal traction vector on the outer boundary ∂B_0, $\mathbf{t}_1$ is the nominal traction vector of the cohesive zone defined by $\mathbf{t}_1 = \mathbf{P}^t\cdot\mathbf{N}_S$ and $\mathbf{P}^t = \mathbf{F}\cdot\mathbf{S}$ is the first Piola Kirchhoff stress tensor, cf. also Figure 2.1.

To obtain the explicit form of each term in Eq. (2.19), we introduce the displacement vector $\hat{\mathbf{n}}^t = [\bar{\boldsymbol{\varphi}}_c, \mathbf{m}_c, \gamma, \bar{\boldsymbol{\varphi}}_d, \mathbf{m}_d]$ and start by concluding that the inertia part is

given by

$$G^{\text{ine}} = \int_{B_0} \rho_0 \left(\delta\boldsymbol{\varphi}_c + \delta\boldsymbol{\varphi}_d\right) \cdot \left(\ddot{\boldsymbol{\varphi}}_c + \ddot{\boldsymbol{\varphi}}_d\right) \mathrm{d}B_0 = \int_{\Omega_0} \rho_0\, \delta\hat{\mathbf{n}}^t (\hat{\mathbf{M}}\ddot{\hat{\mathbf{n}}} + \hat{\mathbf{M}}_{\text{con}})\, \omega_0\, \mathrm{d}\xi_1 \mathrm{d}\xi_2 \quad (2.23)$$

where the consistent mass matrix $\hat{\mathbf{M}}$ and the convective mass force $\hat{\mathbf{M}}_{\text{con}}$ per unit area were derived in [20], cf. Appendix A.2 for details with respect to the modified discontinuity enrichment. In order to arrive at Eq. (2.23), a change of the integration domain from B_0 (3D) to Ω_0 (2D) was made via the ratio $j_0[\xi] = b_0/\omega_0$ defining the relation between area and volumetric measures of the shell defined as

$$\mathrm{d}B_0 = j_0 \mathrm{d}\xi \mathrm{d}\Omega_0 \text{ with } \mathrm{d}\Omega_0 = \omega_0 \mathrm{d}\xi_1 \mathrm{d}\xi_2 \text{ and } \omega_0 = |\boldsymbol{\Phi}_{,1} \times \boldsymbol{\Phi}_{,2}| \quad (2.24)$$

Furthermore, when limiting the perpendicular forces to external pressure – in view of the Cauchy traction $\mathbf{t} = -p\mathbf{n}$ on the deformed surface Ω – the external work G^{ext} can be written as

$$\begin{aligned} G^{\text{ext}} = &\int_{\Gamma_0} \left(\delta\bar{\boldsymbol{\varphi}}_c \cdot \mathbf{n}_0 + \delta\mathbf{m}_c \cdot \tilde{\mathbf{m}}_0 + \delta\gamma m_s\right) \mathrm{d}\Gamma_0 + \int_{\Gamma_0 \cap \partial D_0} (\delta\bar{\boldsymbol{\varphi}}_d \cdot \mathbf{n}_0 + \delta\mathbf{m}_d \cdot \mathbf{m}_0) \mathrm{d}\Gamma_0 \\ &- \int_{\Omega} p \left(\delta\bar{\boldsymbol{\varphi}}_c + \delta\bar{\boldsymbol{\varphi}}_d\right) \cdot \mathbf{g}_{\text{c1}} \times \mathbf{g}_{\text{c2}} \mathrm{d}\xi_1 \mathrm{d}\xi_2 \end{aligned} \quad (2.25)$$

where $p = p(t, \xi_1, \xi_2)$ is the external pressure, $\mathbf{n}$ is the spatial normal of the deformed midsurface Ω and $\mathbf{n}_0$, $\tilde{\mathbf{m}}_0$, m_s and $\mathbf{m}_0$ are stress resultants with respect to the prescribed traction acting on the outer boundary, cf. Appendix A.1.

Finally, we note that the 'internal work' can be written as

$$G^{\text{int}} = \int_{\Omega_0} \delta\hat{\mathbf{n}}_c^t \hat{\mathbf{N}}_c \omega_0 \mathrm{d}\xi_1 \mathrm{d}\xi_2 + \int_{\Omega_0} \delta\hat{\mathbf{n}}_d^t \hat{\mathbf{N}}_d \omega_0 \mathrm{d}\xi_1 \mathrm{d}\xi_2 + \int_{\Gamma_S} \delta\hat{\mathbf{n}}_{\text{coh}}^t \hat{\mathbf{N}}_{\text{coh}} \mathrm{d}\Gamma_0 \quad (2.26)$$

where the shell deformation and stress resultant vectors have been introduced as

$$\begin{aligned} &\delta\hat{\mathbf{n}}_c^t = \left[\delta\bar{\boldsymbol{\varphi}}_{c,\alpha}, \delta\mathbf{m}_{c,\alpha}, \delta\mathbf{m}_c, \delta\gamma_{,\alpha}, \delta\gamma\right] \,,\, \delta\hat{\mathbf{n}}_d^t = \left[\delta\bar{\boldsymbol{\varphi}}_{d,\alpha}, \delta\mathbf{m}_{d,\alpha}, \delta\mathbf{m}_d\right] \,,\, \delta\hat{\mathbf{n}}_{\text{coh}}^t = \left[\delta\bar{\boldsymbol{\varphi}}_d, \delta\mathbf{m}_d\right] \\ &\hat{\mathbf{N}}_c^t = \left[\mathbf{N}^\alpha, \mathbf{M}^\alpha, \mathbf{T}, M_s^\alpha, T_s\right] \,,\, \hat{\mathbf{N}}_d^t = \left[\mathbf{N}_d^\alpha, \mathbf{M}_d^\alpha, \mathbf{T}_d\right] \,,\, \hat{\mathbf{N}}_{\text{coh}}^t = [\mathbf{n}_S, \boldsymbol{m}_S] \end{aligned}$$

involving the membrane, bending, shear/thickness stretch stress resultants $\mathbf{N}^\alpha$, $\mathbf{M}^\alpha$, $\mathbf{T}$, $\mathbf{N}_d^\alpha$, $\mathbf{M}_d^\alpha$, $\mathbf{T}_d$ (the three latter being conjugated with the discontinuous displacement variables), higher order stress resultants M_s^α, T_s as well as cohesive stress resultants $\mathbf{n}_S$ and $\mathbf{m}_S$, cf. Appendix A.1 for the explicit expressions. Finally, by substituting the displacement field into the weak form we are given the equation of motion as

$$\boldsymbol{M}\boldsymbol{a} = \boldsymbol{f}^{\text{ext}} - \boldsymbol{M}^{\text{con}} - \boldsymbol{b}^{\text{int}} - \boldsymbol{b}^{\text{coh}} \quad (2.27)$$

where $\boldsymbol{b}^{\text{int}}$, $\boldsymbol{b}^{\text{coh}}$ and $\boldsymbol{f}^{\text{ext}}$ denote internal, cohesive and external forces respectively. Finally, $\boldsymbol{M}^{\text{con}}$ is the convective mass force involving contributions of the first order time derivatives of the displacement field in the inertia term of the virtual work as in Reference [20].

2.4. MATERIAL MODELLING

As stated in the introduction, the current modelling framework is intended for the analysis of large thin-walled structures experiencing localised failure at high strain rates. Consequently, a crucial issue is to balance modelling detail against computational cost. As described above, this issue is partially approached by developing/adopting an XFEM based discontinuous shell formulation for our thin-walled structure. This is in contrast to the corresponding much more computationally expensive 3D solid modelling combined with remeshing. In addition, given the current areas of application of the ductile fracturing processes, the following set of key requirements on the constitutive modelling are considered:

- The occurrence of significant plastic deformations prior to localisation and failure must be considered. Consequently, a model for the non-localised deformation response must include inelastic deformations and be valid at large continuous deformations.

- Given the area of application in terms of impact and blast loading, a wide range of applications in terms of strain rate and temperature must be handled. Thus, viscoplastic and thermal softening effects must be included in the pre-localised stage of the modelling. Furthermore, as will be shown in the final example, in order to obtain realistic results in terms of crack speed, rate-dependence is also of importance in the modelling of the localised failure.

- Possible failure modes pertinent to the progressive localised failure must be handled in a consistent manner in the context of shell analysis to avoid pathological mesh dependence of the energy dissipated. This means to properly enhance the shell modelling with discontinuous modes involving *e.g.* discontinuous mid-surface and director fields. In relation to this, the proper cohesive zone model must be adopted.

In the current chapter, all the material degradation is assumed to be concentrated in the localised zone. Consequently, the modelling of the material degradation and the associated energy dissipation is confined to a damage-plasticity cohesive zone model, whereby any diffuse damage evolution is disregarded. The energy dissipation due to localised deformation is thus treated separately from the dissipation due to regular (non-localised) plastic deformation. In this way, no energy coupling procedure is required between the continuum model and the cohesive zone model, meaning that, in general, no restrictions exist on the mode of deformation, provided that a mixed-mode cohesive zone model is utilised. As a result, a simplified but computationally efficient approach is obtained (no mesh refinement is necessary) consisting of three idealised stages:

- pre-localised (continuous) deformation represented by an elastoplastic material continuum model without damage.

- onset of localisation (criterion)

- post-localised deformation represented by a cohesive zone model

The adopted modelling is described in the separate subsections below. A final remark is that, as can be seen below, thermal softening is included in the modelling of the continuously deforming material. However, this is in the current stage only of theoretical interest since the thermal field itself is disregarded.

2.4.1. MODELLING OF PRE-LOCALISED DEFORMATION RESPONSE

For computational efficiency reasons, a hypoelastic-inelastic framework based on the Green-Naghdi stress rate is employed to provide a framework for finite deformation analysis. Hence, following *e.g.* Ljustina *et al.* [40], the constitutive relation is formulated on rate form in terms of a relation between the Green-Naghdi rate of the Kirchhoff stress tensor

$$\hat{\boldsymbol{\tau}} = \dot{\boldsymbol{\tau}} - \boldsymbol{\omega}\cdot\boldsymbol{\tau} + \boldsymbol{\tau}\cdot\boldsymbol{\omega},\ \boldsymbol{\omega} = \dot{\mathbf{R}}\mathbf{R}^t \tag{2.28}$$

and the elastic part of the spatial velocity gradient $\bar{\mathbf{l}}$ as

$$\hat{\boldsymbol{\tau}} = \mathbb{E} : \bar{\mathbf{l}},\ \bar{\mathbf{l}} = \mathbf{l} - \mathbf{l}_p - \mathbf{l}_{th} \tag{2.29}$$

where $\mathbb{E}$ is the elastic fourth order tensor, $\mathbf{l} = \dot{\boldsymbol{\varphi}} \otimes \nabla_x$ is the total spatial velocity gradient, and where $\mathbf{l}_p$ and $\mathbf{l}_{th} = \alpha\dot{\theta}\mathbf{1}$ are the plastic and thermal contributions respectively. Due to the restriction to elastic and plastic isotropy in this chapter, it is sufficient to assume that the plastic spin is zero. Thereby, we can consider the inelastic portion of the spatial velocity gradient $\mathbf{l}_p$ in the framework of Perzyna visco-plasticity as

$$\mathbf{l}_p \overset{\text{def.}}{=} \lambda\mathbf{f} \text{ with } \mathbf{f} = \frac{3}{2}\frac{\boldsymbol{\tau}_{\text{dev}}}{\tau_e} \tag{2.30}$$

where $\boldsymbol{\tau}_{\text{dev}}$ is the deviatoric part of the Kirchhoff stress tensor, τ_e is the effective von Mises stress thereof and $\lambda \geq 0$ is the plastic multiplier, determined based on the overstress function $\eta[\Phi]$ in the quasi static yield function $\Phi[\boldsymbol{\tau}, k_i ...]$ (where k_i are internal hardening variables), cf. below.

Furthermore, the elastic material operator in Eq. (2.29) is taken as the constant isotropic spatial material tensor so that

$$\mathbb{E} = 2G\mathbf{I}^{dev} + K\mathbf{1}\otimes\mathbf{1} \text{ with } \mathbf{I}^{dev} = \mathbf{I}^{sym} - \frac{1}{3}\mathbf{1}\otimes\mathbf{1} \tag{2.31}$$

where $\mathbf{I}^{sym}$ is the fourth order unit symmetric projection tensor with the property that $\mathbf{d} = \mathbf{l}^{sym} = \mathbf{I}^{sym} : \mathbf{l}$, where $\mathbf{d}$ is the rate of deformation tensor. Moreover, G and K are the elastic constants pertinent to shear and volumetric response, respectively.

To represent the elastoplastic response of the bulk material at full integrity, the phenomenological model proposed by Johnson and Cook [38] is utilised. This model is most commonly presented in terms of a "rate dependent yield function" F, invoking also effects of isotropic non-linear hardening and thermal softening, as

$$F = \tau_e - \left(A + B\left(\varepsilon_e^p\right)^n\right)\left(1 + C < \ln\left[\frac{\dot{\varepsilon}_e^p}{\dot{\varepsilon}_0}\right] >\right)\left(1 - \hat{\theta}^m\right) \tag{2.32}$$

where ε_e^p is the equivalent accumulated plastic strain characterising the rate-independent strain hardening part, $\dot{\varepsilon}_e^p = \lambda$ is the effective plastic strain rate, and $\hat{\theta}$ is the so-called homologous temperature defined as

$$\hat{\theta} = \begin{cases} 0 & \theta < \theta_{trans} \\ \dfrac{\theta - \theta_{trans}}{\theta_{melt} - \theta_{trans}} & \theta_{trans} < \theta < \theta_{melt} \\ 1 & \theta > \theta_{melt} \end{cases} \tag{2.33}$$

where θ_{trans} is the transition temperature for the temperature dependence and θ_{melt} is the melting temperature of the material.

Clearly, the material parameters A, B and n represents the rate-independent strain hardening, whereas C and $\dot{\varepsilon}_0$ defines the strain-rate dependence and θ_{trans} and m the dependency of temperature on the plastic evolution. As to the parameter $\dot{\varepsilon}_0$, we note that it evidently has a strong influence on the rate sensitivity – it behaves like a relaxation time parameter. Also, in order to avoid an unphysical response, the original model has been adapted by application of the Macaulay bracket $< \bullet >$, to experience a cut–off in the rate dependency. Hence, for $\dot{\varepsilon}_e^p < \dot{\varepsilon}_0$ the model response becomes completely rate independent. In fact, without the proposed "cut–off" the model exhibits numerical instabilities under certain conditions, cf. Ljustina *et al.* [40].

Given the current framework, in accordance to the flow rule for the inelastic portion of the spatial velocity gradient $\mathbf{l}_p$ in Eq. (2.30), we conclude that the Johnson-Cook model can be reformulated as

$$\begin{cases} \lambda = \dot{\epsilon}_0 \exp\left[\dfrac{<\Phi>}{C(1-\hat{\theta}^m)(A+Bk^n)}\right] & \rightsquigarrow \ \lambda > 0 \text{ if } \frac{\lambda}{\dot{\epsilon}_0} \geq 1 \\ \Phi \leq 0,\ \lambda \geq 0,\ \lambda\Phi = 0 & \rightsquigarrow \ \lambda > 0 \text{ if } \frac{\lambda}{\dot{\epsilon}_0} < 1 \end{cases} \tag{2.34}$$

where it is noted that, for the current model, the single isotropic hardening parameter k corresponds to ε_e^p leading to the following form of the quasi-static yield function Φ

$$\Phi = \tau_e - \left(A + Bk^n\right)\left(1 - \hat{\theta}^m\right) \tag{2.35}$$

TRANSFORMATION OF STRESS COMPONENTS

As can be seen in Appendix A.1, the stress resultants involve contra-variant components of the second Piola Kirchhoff stress tensor, denoted S^{ij} in contrast to Cartesian components S_{ij}. In [20], this was treated by formulating the hyperelastic constitutive equations directly in the co-variant frame, which however is not trivial in the case of finite elastoplasticity. Instead, the procedure in this chapter is to handle the integration of the constitutive equations in the Cartesian frame, followed by a transformation of the Cartesian stress tensor components into contra-variant components, with due consideration of the standard relation between the Kirchhoff stress tensor $\boldsymbol{\tau}$ and the second Piola Kirchhoff stress tensor

$$\mathbf{S} = \mathbf{F}^{-1} \cdot \boldsymbol{\tau} \cdot \mathbf{F}^{-t}. \tag{2.36}$$

To be explicit, the coordinate transformation is given by

$$S^{kl} = \left(\mathbf{G}^k \cdot \mathbf{E}_i\right) S_{ij} \left(\mathbf{E}_j \cdot \mathbf{G}^l\right) \tag{2.37}$$

where $\mathbf{E}_i$ are the Cartesian basis vectors and $\mathbf{G}^k$ the contra-variant basis vectors given by Eq (2.4).

2.4.2. ONSET OF LOCALISATION

To determine the onset of localisation, *i.e.* activation of the cohesive zone, we limit ourselves in this chapter to mode I applications whereby the onset and direction of propagation is determined by the maximum principal stress criterion evaluated for the most critical integration layer through the thickness. Currently, four integration points are used through the thickness of the shell, whereby the principal stress criterion is evaluated for the averaged stress state of each of these 'layers', and propagation is predicted whenever a critical state (principal stress exceeds cohesive failure stress) is reached in any of these. It should be remarked that this localisation criterion is simple and purely phenomenological, yet sufficient for the mode I applications considered in the current chapter. However, to obtain a more general approach, the parts describing the pre-localised stage of deformation (including the detection of transition into localised deformation) needs to be further developed.

2.4.3. MODELLING OF POST-LOCALISED FAILURE RESPONSE - COHESIVE ZONE MODEL

From Appendix A.1, it is clear that the cohesive stress resultants are formulated directly in the Cartesian frame. Thus, no transformation of the nominal traction components is necessary. Consequently, any standard formulation can be utilised in which the nominal traction $\mathbf{t}_1$ is directly related to the spatial discontinuity $\tilde{\mathbf{d}}$. To account for rate-dependency also in the localised response, a rate-dependent cohesive zone model developed by Fagerström and Larsson [37] is employed in the current work. In this model, the degradation of the stress traction across the fracture interface is described by a damage - (visco)plasticity model in terms of an effective traction vector $\hat{\mathbf{t}}_1$ and a damage variable $0 \leq \alpha \leq 1$ as

$$\mathbf{t}_1 = (1-\alpha)\,\hat{\mathbf{t}}_1 \tag{2.38}$$

Furthermore, to ensure material frame indifference, the effective nominal traction $\hat{\mathbf{t}}_1$ is related to the effective Mandel stress traction $\hat{\mathbf{Q}} = (1-\alpha)\mathbf{T}\cdot\mathbf{N}_S$ (on the minus side of the crack) as

$$\hat{\mathbf{t}}_1 = \mathbf{F}_{(-)}^{-t} \cdot \hat{\mathbf{Q}} \tag{2.39}$$

based on the general relation between the first Piola Kirchhoff stress tensor and the Mandel stress tensor $\mathbf{T}$

$$\mathbf{T} = \mathbf{F}^{\mathrm{t}} \cdot \mathbf{P}^{t}. \tag{2.40}$$

Based on the definition of a material jump $\mathbf{J}$, associated with the spatial discontinuity, as

$$\mathbf{J} = \mathbf{F}_{(-)}^{-1} \cdot \tilde{\mathbf{d}} \tag{2.41}$$

the traction - displacement relation can be formulated as

$$\hat{\mathbf{Q}} = \mathbf{K} \cdot (\mathbf{J} - \mathbf{J}^p) = \mathbf{K} \cdot \mathbf{J}^e. \tag{2.42}$$

Furthermore, whenever a cohesive segment is introduced, the loading/unloading condition for the considered segment is determined based on the (quasi-static) loading function F_{qs}

$$F_{qs} = \sigma_f \left(\frac{\langle \hat{Q}_n \rangle}{\sigma_f} \right)^2 + \sigma_f \left(\frac{\hat{Q}_t}{\hat{\gamma} \sigma_f} \right)^2 - \sigma_f \tag{2.43}$$

where $\hat{Q}_n = \hat{\mathbf{Q}} \cdot \mathbf{N}_S$ and $\hat{Q}_t = \left| (\mathbf{1} - \mathbf{N}_S \otimes \mathbf{N}_S) \cdot \hat{\mathbf{Q}} \right|$ are the normal and tangential components of $\hat{\mathbf{Q}}$ respectively, σ_f is the failure stress in simple tension and $\hat{\gamma}$ is the ratio between the failure stress in simple shear and simple tension. It is emphasised that the shear component is the magnitude of the tangential part of the traction along the discontinuity surface, thereby including both mode II and mode III shear deformations.

The discontinuity evolution is expressed in the inelastic portion $\dot{\mathbf{J}}^p$, where the loading function defines the flow rule as

$$\dot{\mathbf{J}}^p = \frac{\lambda_d}{1 - \alpha} \mathbf{H} \tag{2.44}$$

where

$$\mathbf{H} = \frac{\partial F_{qs}}{\partial \hat{\mathbf{Q}}} = 2 \frac{\langle \hat{Q}_n \rangle}{\sigma_f} \mathbf{e}_n + 2 \frac{\hat{Q}_t}{\hat{\gamma}^2 \sigma_f} \mathbf{e}_t \tag{2.45}$$

In Eq. (2.44), a 'plastic' multiplier λ_d is introduced, which in the *rate-independent* case is controlled by the Karush-Kuhn-Tucker conditions

$$F_{qs} \leq 0, \ \lambda_d > 0, \ \lambda_d F_{qs} = 0. \tag{2.46}$$

To invoke the rate dependence, these conditions are relaxed and the plastic evolution is formulated in an 'over-stress' manner, in analogy to *e.g* Perzyna. [41], as

$$\lambda_d = \frac{1}{c^*} \left(\frac{\langle F_{qs} \rangle}{\sigma_f} \right)^{1/m} \frac{1}{|\mathbf{H}|} \tag{2.47}$$

where c^* and m are two material constants determining the viscous fracture behaviour. Hence, the evolution of the plastic jump is given by

$$\dot{\mathbf{J}}^p = \frac{1}{c^*} \left(\frac{\langle F_{qs} \rangle}{\sigma_f} \right)^{1/m} \frac{\mathbf{H}}{|\mathbf{H}|} \tag{2.48}$$

which in the simplest case of a relation between the plastic multiplier λ_d and the rate of damage $\dot{\alpha}$ according to

$$\dot{\alpha} = \frac{1}{s(1-\alpha)}\lambda_d \tag{2.49}$$

is linearly related to the amount of damage evolution as

$$\dot{\mathbf{J}}^p = s\dot{\alpha}\mathbf{H} \tag{2.50}$$

where s is a damage parameter which may be used for calibrating the model. As shown in *e.g.* [37], in the case of mode I fracture, s takes the form

$$s = \frac{G_f^I}{\sigma_f} \tag{2.51}$$

where G_f^I is the corresponding mode I fracture energy.

2.5. Implementation Aspects

This section is intended to address the issue arising from kinematical inconsistency amid activation of a new cohesive zone due to nonconforming stress state during initiation of localisation. It also explores the presence and remedy for unwanted (non-physical) stress wave induced by a sudden discontinuity in the internal forces upon introduction of a new crack segment, which may lead to instability in the solution during the crack propagation. To tackle these issues two approaches are investigated herein which are of computational significance.

2.5.1. Shifted Cohesive Zone

To obtain a consistent transition from a continuous to a discontinuous state in explicit time integration, the crack interface should be exposed to the same stress state as before the initiation of localisation. However, upon onset of localisation (enrichment) the interface opening is still zero. Consequently, in order to provide a smooth and consistent transition from a continuous to a discontinuous element, the traction value at the integration points along the crack path should be computed such that the initial traction in the cohesive zone corresponds to the stress state prior to the discontinuous enrichment. To overcome the aforementioned difficulty, the idea proposed by Hille *et al.* [42] is resorted to, whereby a shift is added to the crack interface opening.

To clarify, the algorithm for this method is to compute the shift based on the initial stiffness of the cohesive interface $\mathbf{K}$, normal vector to the crack segment $\mathbf{N}_S$, and the Mandel stress $\mathbf{T}$ at the integration point along the crack interface once the cohesive crack segment is to be inserted

$$\mathbf{J}^0 = \frac{1}{K}\mathbf{T}\cdot\mathbf{N}_S. \tag{2.52}$$

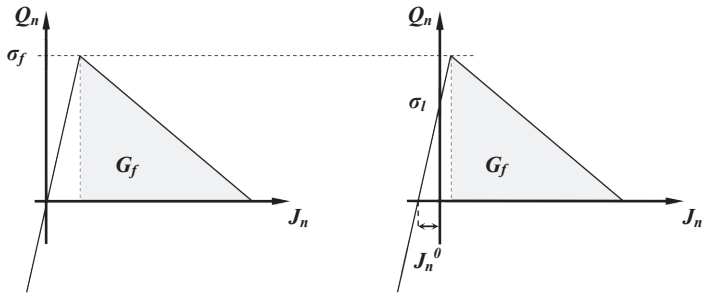

Figure 2.2: Sketch to visualise the effect of adding a shift to the cohesive zone opening

Having the shift computed at the onset of the localisation, it is added to the material jump $\bar{\mathbf{J}}(\mathbf{t})$, wherein the material jump has been determined by XFEM kinematics as a result of additional degrees of freedom to represent the discontinuity. This summation is then to be utilised as the argument for the cohesive zone model as

$$\mathbf{J}(t) = \bar{\mathbf{J}}(t) + \mathbf{J}^0. \tag{2.53}$$

Furthermore, to ensure that the stress state in the bulk material in the vicinity of the crack does not exceed the maximum traction in the cohesive zone, such that the crack insertion will be acceptably smooth, the failure stress in the localisation criterion, σ_l, is assigned to be 90% of the ultimate tensile stress, σ_f. Thereby, provided that the time step employed is sufficiently small, implying that stress variation during the crack insertion is limited, the stress will never exceed the maximum loading point of the cohesive zone model. Consequently, the bulk stress state across the crack will be maintained.

Another feature of the shifted cohesive zone is that it offsets the discrepancy in dissipated energy. As it is depicted in Figure 2.2, the area below the traction-separation law is not completely accounted for by fracture energy, G_f, and it is just the area below the descending part which represents the dissipation. Despite the fact that the initial stiffness is comparatively very high such that the area below the ascending part is more or less insignificant, this still will introduce a discrepancy in the dissipated energy. Clearly, adding the shift to the cohesive opening, more consistent energy balance will be experienced and the aforementioned issue will be settled.

2.5.2. CORRECTION FORCE

Insertion of any new crack segment is accompanied by addition of new degrees of freedom to the solution field with initially zero values. It should be remarked that, by adopting the current temporal discretisation and integration technique, whenever a new crack segment is inserted in the discretisation of the domain, the continuity in time of this space discretisation is not ensured. Physically, the crack propagates with a finite velocity, whereas in the numerical simulation, the crack propagation speed

will be implicitly governed by the time step size because the crack is propagated segment by segment whenever a propagation criterion is satisfied. Consequently, because of the influence of preexisting internal, external and cohesive forces, the current procedure induces an abrupt change in the internal forces corresponding to the newly enriched degrees of freedom as the crack propagates.This discontinuity in the internal forces of newly enriched degrees of freedom and their associated accelerations will lead to an unphysical stress wave and should be avoided.

To circumvent this issue herein, the method proposed by Menouillard and Belytschko [43] is exploited, whereby a correction force is added to the balance equation in order to smoothen any abrupt change in the newly enriched degrees of freedom during the transition from the continuous element to the discontinuous cracked element. Consequently, the pre-existing forces are invoked gradually within a short time interval. To clarify, the procedure is to compute the influence of the internal force $\boldsymbol{b}^{\text{int}}_{t_{act}}$, cohesive force $\boldsymbol{b}^{\text{coh}}_{t_{act}}$, external force $\boldsymbol{f}^{\text{ext}}_{t_{act}}$, and convective mass force $\boldsymbol{M}^{\text{con}}_{t_{act}}$, for the new degrees of freedom to be enriched once the localisation criterion is met at t_{act}. Thereafter, the correction force may be defined as

$$\boldsymbol{f}^{corr} = \boldsymbol{M}^{\text{con}}_{t_{act}} + \boldsymbol{b}^{\text{int}}_{t_{act}} + \boldsymbol{b}^{\text{coh}}_{t_{act}} - \boldsymbol{f}^{\text{ext}}_{t_{act}} \tag{2.54}$$

where the definition of all terms used above and also details of the explicit time integration scheme in terms of the central difference method employed in this development are provided in [20].
This correction force is to be added to the balance equation with opposite sign right after activation of newly enriched degrees of freedom, such that it follows a decaying pattern within a short time interval

$$\boldsymbol{a}_n = -\boldsymbol{M}^{-1}(\boldsymbol{M}^{\text{con}}_n + \boldsymbol{b}^{\text{int}}_n + \boldsymbol{b}^{\text{coh}}_n - \boldsymbol{f}^{\text{ext}}_n - \boldsymbol{f}^{corr} \cdot C^{decay}_n) \tag{2.55}$$

where C^{decay}_n may have any pattern, *e.g.* linear or nonlinear, provided that it decreases from one to zero so that the effect of the corresponding correction force vanish by the end of its activation interval, $\triangle\, t_{corr}$.

In the implementation herein, the decaying pattern is provided using a nonlinear function, cf. Figure 2.3, that smoothen the abrupt change in the newly enriched degrees of freedom for limited yet sufficient number of time steps

$$C^{decay}_n = \begin{cases} 0 & t_n > t_{act} + \triangle\, t_{corr} \\ \frac{1}{2}(\cos(\frac{t_n - t_{act}}{\triangle\, t_{corr}})\pi + 1) & t_{act} < t_n < t_{act} + \triangle\, t_{corr} \end{cases} \tag{2.56}$$

Utilising the aforementioned method, the abrupt change in the acceleration field, $\boldsymbol{a}_n$, will be mitigated and the response enjoys reasonable smoothness. A practical application of this method is shown in the second numerical example in the current chapter.

2.6. NUMERICAL EXAMPLES

In this section, three different examples are presented in order to verify the accuracy and robustness of the model as well as its implementation. In the first example, im-

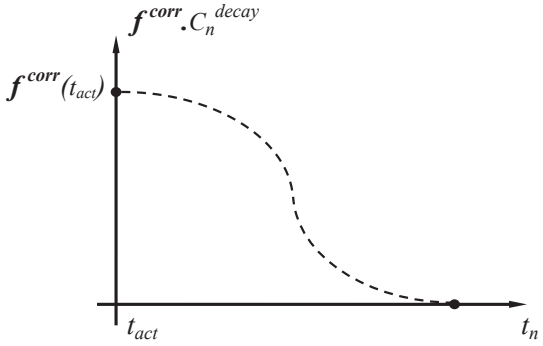

Figure 2.3: Time variation of the correction force

pact loading of a rectangular plate, the accuracy of the shell formulation is validated. The second example, tearing of a plate by out-of-plane loading, is to investigate the implementation of the crack propagation scheme and stability of the responses. Finally, the third example concerns blast loading of a cylindrical barrel and its purpose is to examine the speed of the crack propagation and the influence of rate dependencies involved in the bulk material model as well as in the cohesive zone model. The simulations are performed using a 6-node triangular element mesh, with 6 integration points per element in-plane, and 4 integration points through the thickness. The in-plane integration scheme is as utilised in the 2D plane strain case cf. [37], including sub-triangulation and integration over each sub-triangle of the elements cut by a crack, where 6 integration points are necessary to integrate the mass matrix in each sub-triangle exactly.

2.6.1. IMPACT LOADING OF RECTANGULAR PLATE

To verify and validate the continuum response of the shell formulation presented in this chapter, an impact loading test on a simply supported square plate cf. Figure 2.4, is analysed which has already been studied by Belytschko *et al.* [44] and later by Tabiei and Tanov [45].

The $10 \times 10\,\text{in}^2$ plate with thickness 0.5 in is loaded by a constant pressure of 300 psi applied instantly at the beginning of the analysis. In order to investigate both hypo-elastic inelastic and elastic responses, two material models are implemented, and the following material parameters are used in analyses of both models: the Young's modulus and the Poisson's ratio are $E = 10^7$ psi and $\nu = 0.3$ respectively, and the density is $\rho_0 = 2.588 \cdot 10^{-4}$ lbf·s^2/in^4. To make the hypo-elastoplastic model in accordance with the elastic-perfectly plastic model used by Tabiei and Tanov, the influence of the rate dependency and material hardening are omitted.

Exploiting the symmetry of the problem, only a quarter of the plate is modelled. To investigate the sensitivity of the results with respect to spatial discretisation, both a coarse and a fine mesh consisting of 50 and 200 elements are examined. To make the comparison with previously reported results complete, we note that the results

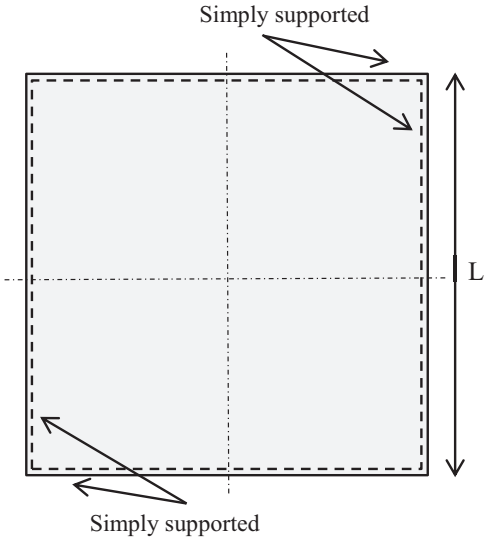

Figure 2.4: The geometry and boundary conditions for impact loading of a square plate.

presented by Tabiei and Tomov [45] and Belytschko *et al.* [44] are obtained using a spatial discretisation in terms of quadrilateral elements of size 1.25×1.25 in.^{2}.

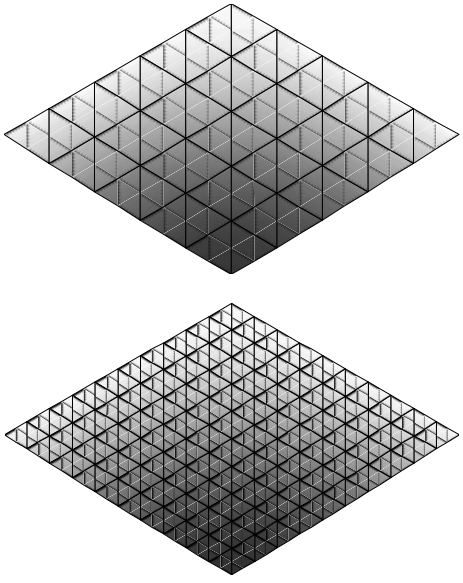

Figure 2.5: Discretisations used in the analysis of the simply supported square plate - a quarter of the domain with coarse and fine mesh

Since no crack is involved, only continuous degrees of freedom are activated. The time step Δt used for hyper-elastic material in the computations is 10^{-7} s. The same time step is also used for hypo-elastoplastic material considering the fact that unloading may occur at any moment *e.g.* amid numerical noise and instability cf. [46]. Note that Tabiei's equation predicts increase in the critical time step with the shell thickness. This effect was also observed in our simulations. The total number of time steps is 12000, for a 1.2 ms long dynamic simulation. Fig. 2.5-2.6 show the structured mesh used in the simulations and the midpoint displacement history. The obtained result matches the one by Tabiei and Tanov [45] quite satisfactory, in terms of both amplitude and vibration period.

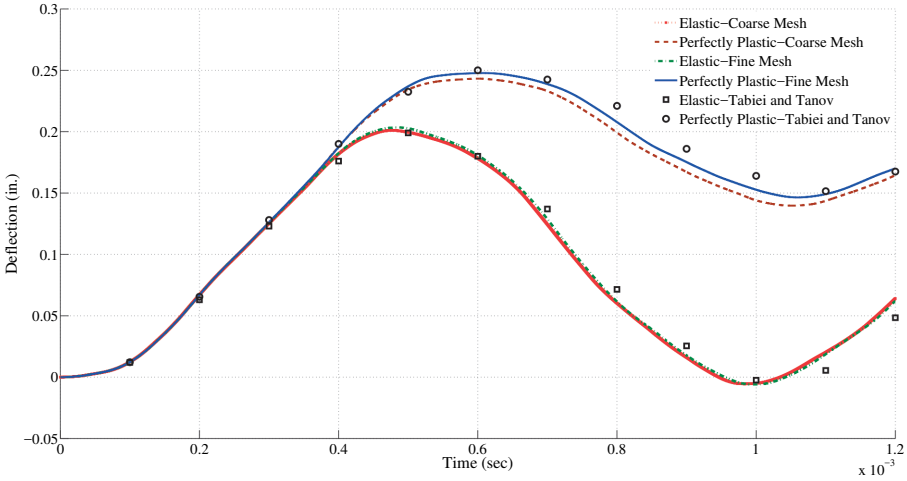

Figure 2.6: Midpoint displacement history for the square plate where the coloured solid and dashed-lines represent the current simulated response and the square and circular markers denote the results reported by Tabiei and Tanov [45] .

2.6.2. TEARING OF A PLATE BY OUT-OF-PLANE LOADING

This numerical example is based on the experiments by Muscat-Fenech *et al.* [47], and deals with a pre-notched elastic-inelastic plate of dimension $203 \times 203\,\text{mm}^2$ and thickness of 0.8 mm where, in the present case, the length of the initial crack is $a_0 = 40\,\text{mm}$. This experiment has previously also been analysed numerically by Areias and Belytschko [16] with good accuracy, hence it is considered as a good benchmark for the current model. The material parameters are $E = 210\,\text{GPa}$, $\nu = 0.3$, $G_f = 250\,\text{kJ/m}^2$, and the same value as ultimate tensile stress 306 MPa is used for maximum cohesive traction σ_f. The plate is acted on by a quasi-static transverse loading at the tip of the notch located on the free edge, cf. Figure 2.7. To be consistent with the experiment,

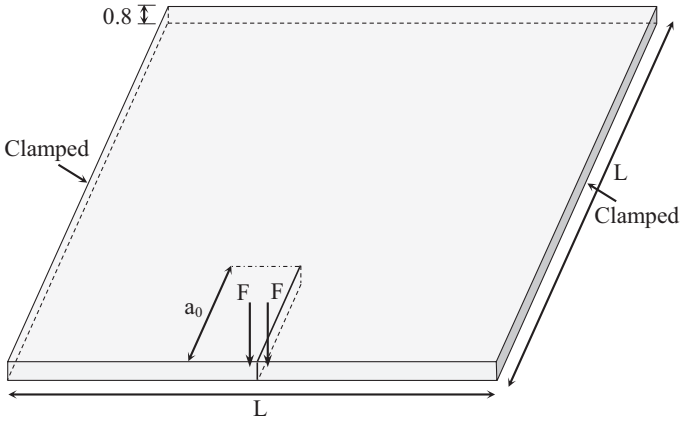

Figure 2.7: The geometry and boundary condition of the plate acted on by out-of-plane loading.

the rate independent part of the Eq. (2.32) is utilised and the hardening parameters are calibrated against the model in [16]

$$F = \tau_e - \left(A + B\left(\varepsilon_e^p\right)^n\right) \tag{2.57}$$

where $A = 175\,\text{MPa}$, $B = 767\,\text{MPa}$, and $n = 0.6722$.

Owing to the fact that the effect of inertia is accounted for herein, the applied transverse load is replaced by a constant velocity of $20\,\text{m/s}$ such that it resembles the experiment. This test is intended to investigate the implementation of the crack propagation for both predefined and non-predefined crack path, where, in the former case, cohesive segments are activated along the entire crack path prior to the application of the load. In order to avoid any unphysical instability and guarantee smoothness of the response, the stabilising techniques, *i.e.* adding correction force to the new discontinuous degrees of freedom as well as shift to the crack interface opening, discussed in the previous section are utilised. The domain is meshed with 502 six-node triangular elements with a densification of the mesh along the crack path to promote a smoother propagation. This is similar to the discretisation procedure utilised in [16] where, however, quadrilateral elements were utilised in the discretisation.

To compare the result obtained with the experiment, force versus displacement at the mid-point of the cracked edge of the plate is stored and plotted in Figure 2.9. As it is seen in Figure 2.9a, despite the oscillatory response obtained in the current dynamic analysis – caused by reflecting stress wave – good agreement between the simulated and experimentally observed force-deflection curve is obtained, provided that the stabilisation features are activated. In Figure 2.9b, the response where no stabilising technique has been employed is shown. For the case where new segments are inserted sequentially whenever the propagation criterion is met, one may note that noise amplitude reaches $62\,\text{N}$ which is not negligible, even though computationally reasonable refinement is furnished. It should be remarked that employing a

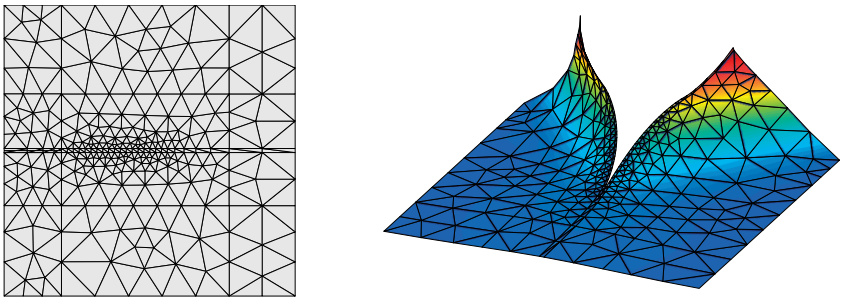

Figure 2.8: Undeformed (left) and deformed mesh (right) for out-of-plane loading of plate - different colours represent different displacements

more coarse mesh in the vicinity of the crack would lead to an extreme increase in the observed noise. Applying the aforementioned stabilising techniques the response in Figure 2.9d is obtained, and clearly, the noise amplitude is reduced by 90% which is a significant improvement compared to the non-stabilised response in Figure 2.9c. To conclude, the result corresponds to the experiment, as well as the result achieved in the case of predefined crack path. It should be emphasised that these oscillations has not been as pronounced in the case of in-plane loading of the plate. It is also observed that, by adding the stabilisation measures, the current approach is also applicable where extreme refinement of the mesh is not feasible, *i.e.* analyses of large structures, which proves its significance.

2.6.3. BLAST LOADING OF A CYLINDRICAL BARREL

To investigate the accuracy of the proposed method in the case of dynamic ductile crack propagation, a dynamic fracture test on a pressurised barrel is chosen for comparison. The aim is primarily to highlight the influence of the rate dependencies included in the bulk material model and cohesive zone model. This example is also intended to emphasise the importance of involving plasticity in the bulk material where plastic deformation is dominant, *e.g.* impact analysis, to achieve more reasonable results. It is advocated by the experiments reported by Ravi-Chandar and Knauss [35] that as crack propagates, microcracks located in front of the crack tip interact and create macrocracks. This process of nucleation and coalescence between microcracks and the time period over which this occurs is accounted for herein by including rate dependency in the cohesive zone model, cf. above. In Reference [20] this example has already been discussed in detail, therefore only the most significant details are repeated herein.

EXPERIMENT DESCRIPTION

In this example, the dynamic crack propagation behaviour incurred by an internal blast explosion in a barrel is to be investigated. The barrel is made of 1 mm thick aluminum 2024-T3, with dimensions 1.2 m by 1 m (diameter x height). To trigger crack propagation, a 56 mm long pre-notch was cut in the middle of the barrel, along the vertical direction. The notch is taped off, in order to pressurise the barrel without any outflow. Once the desired pressure level was reached, 2 bar, the explosive was detonated. Figure 2.10 shows a sketch of the barrel. Sketches of a simplified pressure-time history and the measured pressure-time history at the bottom of the barrel are shown in Figure 2.11.

SIMULATION

Because of symmetry, only one half of the barrel has been modelled.To allow for a comparison with the results previously reported in Reference [20], the same spatial discretisation has been employed in this example. Consequently, the finite element mesh consists of 310 six-node triangular elements with total number of 8476 degrees of freedom, cf. Figure 2.12. It should be remarked that, for a full validation of the proposed approach, a mesh convergence study would be valuable. However, since the main intention of the current example is to perform a relative comparison with results obtained without accounting for plasticity in the bulk material, such mesh convergence study is left for future developments.

The simulation was done in two stages, *pressurisation* and *explosive detonation*. The first stage, pressurisation, is done using an implicit static analysis as in [20] assuming that plastic strains during this stage are negligible and thereby, only elastic deformations need to be considered in this stage of the analysis. The pressure load is applied on the entire inner surface of the barrel statically by means of a ramp function, cf. Figure 2.11. The second stage, explosive detonation, is performed employing an explicit dynamic analysis with time step of $\Delta t = 10^{-8}$ s.

The mechanical properties of Al2024-T3 used in the analyses are, Young's modulus $E = 73$ GPa, Poisson's ratio $\nu = 0.3$, and density $\rho_0 = 2780\,\mathrm{Kg/m^3}$. The JC-model parameters are $A = 369$ MPa, B =684 MPa, $C = 8.3 \cdot 10^{-3}$, $m = 1$, $n = .73$ and $\dot{\varepsilon}_0 = 1$ which are obtained from Reference [48]. Values for the static fracture toughness $G_f = 67 \cdot 10^3$ N/m, and the static cohesive strength $\sigma_f = 775$ MPa are both taken from Reference [49]. The visco-plastic material parameters c^* and m have been varied, cf. Figure 2.13, in order to match the crack speed observed in the experiments. As it is observed in Figure 2.13, in which the crack speed vs. crack length is illustrated for all analysed combinations of viscous parameters, it is clearly possible to significantly control the crack speed in the simulations by choosing the right viscous parameters in order to match the experiments. Thereby, the validity of the method exploited herein is proven to be acceptable, and, in comparison to the previous paper [20], we are now able to obtain more realistic results by including plasticity in the bulk material model.

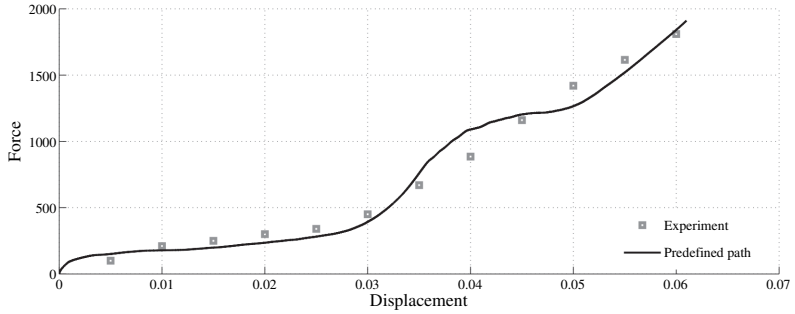

a)

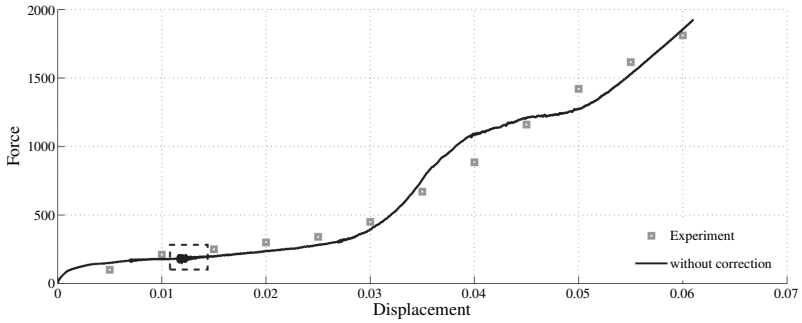

b)

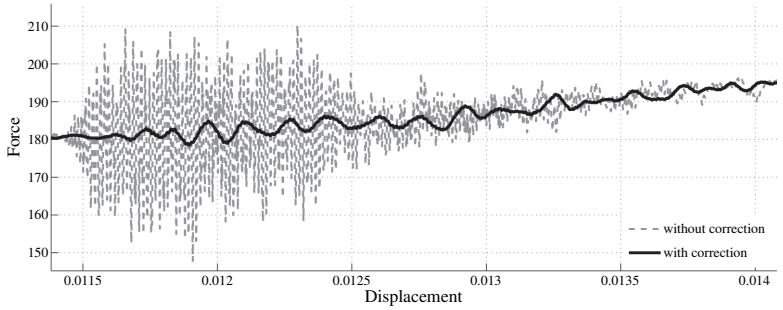

c)

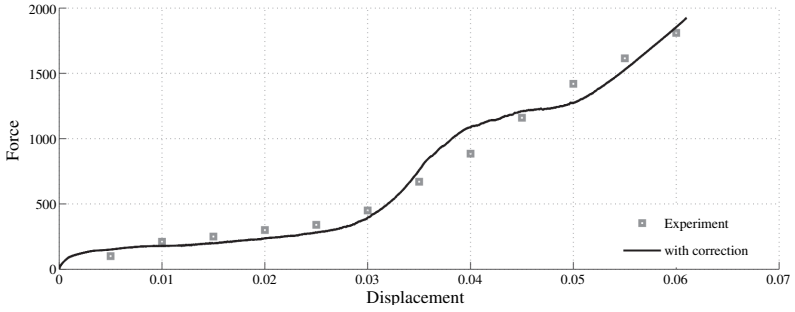

d)

Figure 2.9: Tearing of the plate: a) load-deflection curve for predefined path, b) response with no correction force and shift in the cohesive zone, c) comparison of the results with and without the correction force and shift in the cohesive zone and d) response with correction force.

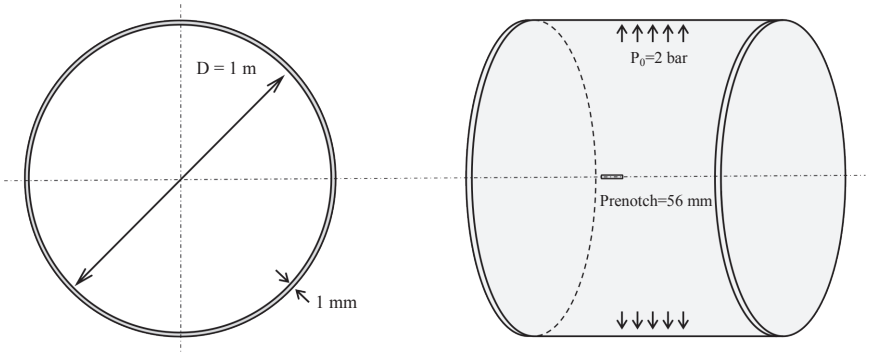

Figure 2.10: Geometry and boundary conditions for the barrel.

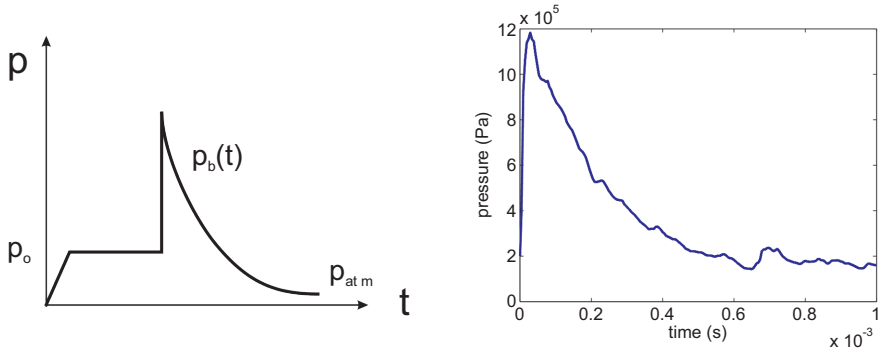

Figure 2.11: Simplified pressure history (left) and measured pressure history at the bottom of the barrel (right).

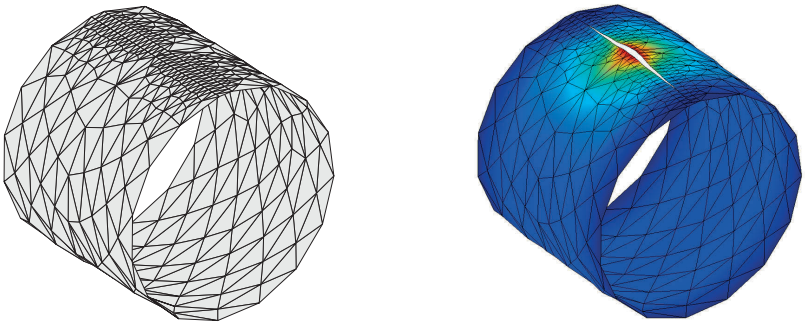

a) b)

Figure 2.12: a) Initial undeformed mesh of analysed pressurised barrel and b) deformed contour plots of blast loaded barrel after approximately 7 ms.

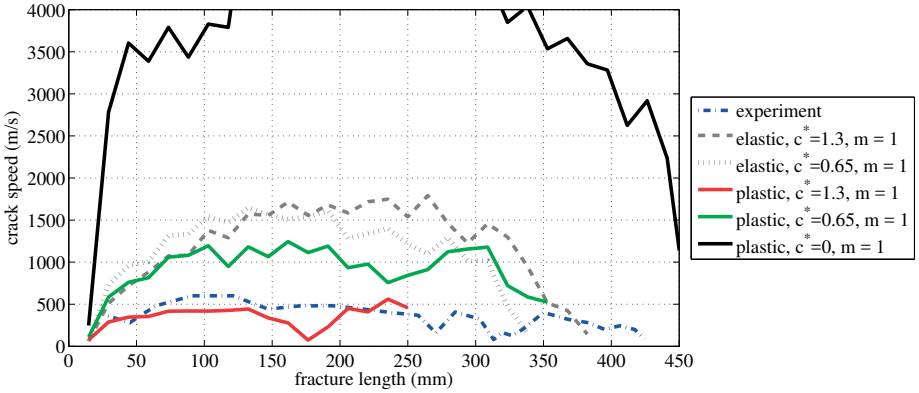

Figure 2.13: Crack speed vs. propagated crack distance for all sets of analysed viscous cohesive parameters.

2.7. CONCLUDING REMARKS

In order to capture the response of thin-walled structures when exposed to impact loading inducing large plastic strains, a hypoelastic-inelastic material model was employed. We also incorporated the Johnson and Cook phenomenological model to account for temperature and plastic strain rate dependencies which has been proved to be essential in dynamic high rate loadings, *e.g.* explosive load.

To represent the shell kinematics, a shell formulation with extensible directors and second order inhomogeneous thickness deformation has been employed. The advantage of this formulation over traditional shell models such as Kirchhoff-Love and Mindlin-Reissner is its capability of describing thickness stretch as well as shear deformations, eliminating the transverse shear locking effect. The configuration of the shell is described by 7 parameters representing the continuous deformation field while for discontinuous field it was 6 parameters describing it to avoid any further complexity. To include the through-the-thickness discontinuity in the solution field, a shifted version of XFEM was utilised, in which the resisting force of the process zone is governed by a damage-viscoplastic cohesive zone model.

Different examples were performed to validate the shell model, and verify the influence of the rate dependencies included in the bulk material model as well as in the cohesive zone model. All simulations were carried out using 6-node triangle elements with quadratic interpolation in order to mitigate the in-plane shear locking. In the first example, impact loading of plate, our shell formulation was validated against both the elastic and perfect plastic materials, and the results were in complete agreement with the benchmark. For the out-of-plane loading of plate, there were instabilities incurred by initialisation of the newly enriched degrees of freedom in XFEM. To cope with that, two methods were investigated which were proved essential to avoid instabilities occurring in conjunction with explicit temporal integration of the dynamic response. It was also noted that, although both methods improved the results, the influence of adding correction force was determined to be much more pronounced than adding shift to the cohesive zone argument. It is also worth mentioning that the extent of the aforementioned instabilities was observed to be influenced by the loading condition. This is due to the fact that the instabilities were negligible in the in-plane loading case. In the final example, it was observed that the crack propagation speed can be limited by the rate dependency involved in the cohesive zone model as it was expected.

REFERENCES

[1] S. Mostofizadeh, M. Fagerström, and R. Larsson, *Dynamic crack propagation in elastoplastic thin-walled structures: Modelling and validation,* International Journal for Numerical Methods in Engineering **96**, 63 (2013).

[2] X. Xu and A. Needleman, *Numerical simulations of fast crack growth in brittle solids,* Journal of the Mechanics and Physics of Solids **42**, 1397 (1994).

[3] G. Camacho and M. Ortiz, *Computational modelling of impact damage in brittle materials,* International Journal of Solids and Structures **33**, 2899 (1996).

[4] T. Belytschko and T. Black, *Elastic crack growth in finite elements with minimal remeshing,* International Journal for Numerical Methods in Engineering **45**, 601 (1999).

[5] N. Moës, J. Dolbow, and T. Belytschko, *A finite element method for crack growth without remeshing,* International Journal for Numerical Methods in Engineering **46**, 131 (1999).

[6] I. Babuška and J. Melenk, *The partition of unity finite element method: Basic theory and applications,* Computer Methods in Applied Mechanics and Engineering **139**, 289 (1996).

[7] G. Wells and L. Sluys, *A new method for modelling cohesive cracks using finite elements,* International Journal for Numerical Methods in Engineering **50**, 2667 (2001).

[8] N. Moës and T. Belytschko, *Extended finite element method for cohesive crack growth,* Engineering Fracture Mechanics **69**, 813 (2002).

[9] G. Zi and T. Belytschko, *New crack-tip elements for XFEM and applications to cohesive cracks,* International Journal for Numerical Methods in Engineering **57**, 2221 (2003).

[10] T. Menouillard, J. Réthoré, A. Combescure, and H. Bung, *Efficient explicit time stepping for the extended finite element method (x-fem),* International Journal for Numerical Methods in Engineering **68**, 911 (2006).

[11] T. Menouillard, J. Réthoré, N. Moës, A. Combescure, and H. Bung, *Mass lumping strategies for x-fem explicit dynamics: Application to crack propagation,* International Journal for Numerical Methods in Engineering **74**, 447 (2008).

[12] J. Remmers, R. de Borst, and A. Needleman, *The simulation of dynamic crack propagation using the cohesive segments method,* Journal of the Mechanics and Physics of Solids **56**, 70 (2008).

[13] A. Hansbo and P. Hansbo, *A finite element method for the simulation of strong and weak discontinuities in elasticity,* Computer Methods in Applied Mechanics and Engineering **193**, 3523 (2004).

[14] J. Song, P. Areias, and T. Belytschko, *A method for dynamic crack and shear band propagation with phantom nodes,* International Journal for Numerical Methods in Engineering **67**, 868 (2006).

[15] T. Rabczuk, G. Zi, A. Gerstenberger, and W. Wall, *A new crack tip element for the phantom-node method with arbitrary cohesive cracks,* International journal for numerical methods in engineering **75**, 577 (2008).

[16] P. Areias and T. Belytschko, *Non-linear analysis of shells with arbitrary evolving cracks using xfem,* International Journal for Numerical Methods in Engineering **62**, 384 (2005).

[17] P. Areias, J. Song, and T. Belytschko, *Analysis of fracture in thin shells by overlapping paired elements,* Computer methods in applied mechanics and engineering **195**, 5343 (2006).

[18] A. Ahmed, F. van der Meer, and L. Sluys, *A geometrically nonlinear discontinuous solid-like shell element (dsls) for thin shell structures,* Computer Methods in Applied Mechanics and Engineering (2011).

[19] H. Parisch, *A continuum-based shell theory for non-linear applications,* International Journal for Numerical Methods in Engineering **38**, 1855 (1995).

[20] R. Larsson, J. Mediavilla, and M. Fagerström, *Dynamic fracture modeling in shell structures based on XFEM,* International Journal for Numerical Methods in Engineering **86**, 499 (2010).

[21] M. Bischoff and E. Ramm, *On the physical significance of higher order kinematic and static variables in a three-dimensional shell formulation,* International Journal of Solids and Structures **37**, 6933 (2000).

[22] D. Dugdale, *Yielding of steel sheets containing slits,* Journal of the Mechanics and Physics of Solids **8**, 100 (1960).

[23] G. Barenblatt, *Mathematical theory of equilibrium cracks in brittle fracture,* Advances in Applied Mechanics **7**, 55 (1962).

[24] L. Kachanov, *On the time to failure under creep conditions (in russian),* Izvestiya Akademii Nauk SSSR. Otdelenie Tekhnicheskikh Tauk **8**, 26 (1958).

[25] J. Lemaitre, *A Course on Damage Mechanics* (Springer-Verlag, Berlin, 1992).

[26] A. Gurson, *Continuum theory of ductile rupture by void nucleation and growth: Part I Yield criteria and flow rules for porous ductile media,* Journal of Engineering Materials and Technology **99**, 2 (1977).

[27] V. Tvergaard and A. Needleman, *Analysis of cupcone fracture in a round tensile bar,* Acta Metallurgica **32**, 157 (1984).

[28] B. Patzak and M. Jirasek, *Process zone resolution by extended finite elements,* Engineering Fracture Mechanics **70**, 957 (2003).

[29] B. Patzak and M. Jirasek, *Adaptive resolution of localized damage in quasi-brittle materials,* Journal of Engineering Mechanics **130**, 720 (2004).

[30] G. Wells, L. Sluys, and R. de Borst, *Simulating the propagation of displacement discontinuities in a regularized strain-softening medium,* International Journal for Numerical Methods in Engineering **53**, 1235 (2002).

[31] M. Seabra, J. de Sa, F. Andrade, and F. Pires, *Continuous-discontinouos formulation of ductile fracture,* International Journal of Material Forming **4**, 271 (2011).

[32] J. Mediavilla, R. Peerlings, and M. Geers, *An integrated continuous-discontinuous approach towards damage engineering in sheet metal forming processes,* Eng. Fract. Mech. **73**, 895 (2006).

[33] P. Areais and T. Belytschko, *Analysis of three-dimensional crack initiation and propagation using the extended finite element method,* International Journal for Numerical Methods in Engineering **63**, 760 (2005).

[34] F. Cazes, M. Coret, A. Combescure, and A. Gravouil, *A thermodynamic method for the construction of a cohesive law from a nonlocal damage model,* International Journal of Solids and Structures **46**, 1476 (2009).

[35] K. Ravi-Chandar and W. G. Knauss, *An experimental investigation into dynamic fracture: I. Crack initiation and arrest,* International Journal of Fracture **25**, 247 (1984).

[36] M. Fagerström and R. Larsson, *Theory and numerics for finite deformation fracture modelling using strong discontinuities,* International Journal for Numerical Methods in Engineering **66**, 911 (2006).

[37] M. Fagerström and R. Larsson, *Approaches to dynamic fracture modelling at finite deformations,* Journal of the Mechanics and Physics of Solids **56**, 613 (2008).

[38] G. Johnson and W. Cook, *Fracture characteristics of three metals subjected to various strains, strain rates, temperatures and pressures,* Engineering Fracture Mechanics **21**, 31 (1985).

[39] G. Wells, R. de Borst, and L. Sluys, *A consistent geometrically non-linear approach for delamination,* International Journal for Numerical Methods in Engineering **54**, 1333 (2002).

[40] G. Ljustina, M. Fagerström, and R. Larsson, *Hypo-and hyper-inelasticity applied to modeling of compacted graphite iron machining simulations,* European Journal of Mechanics-A/Solids **37**, 57 (2013).

[41] P. Perzyna, *Fundamental problems in viscoplasticity,* Advances in Applied Mechanics **9**, 243 (1966).

[42] T. Hille, A. Suiker, and S. Turteltaub, *Microcrack nucleation in thermal barrier coating systems,* Engineering Fracture Mechanics **76**, 813 (2009).

[43] T. Menouillard and T. Belytschko, *Smoothed nodal forces for improved dynamic crack propagation modeling in xfem,* International Journal for Numerical Methods in Engineering **84**, 47 (2010).

[44] T. Belytschko, J. Lin, and C. Tsay, *Explicit algorithms for the nonlinear dynamics of shells,* Computer methods in applied mechanics and engineering **42**, 225 (1984).

[45] A. Tabiei and R. Tanov, *A nonlinear higher order shear deformation shell element for dynamic explicit analysis: Part ii. performance validation through standard tests,* Finite elements in analysis and design **36**, 39 (2000).

[46] T. Belytschko, W. Liu, and B. Moran, *Nonlinear finite elements for continua and structures*, Vol. 1 (Wiley New York, 2000).

[47] C. Muscat-Fenech and A. Atkins, *Out-of-plane stretching and tearing fracture in ductile sheet materials,* International journal of fracture **84**, 297 (1997).

[48] T. de Varis, *Blunt and sharp notch behaviour of Glare laminates*, Ph.D. thesis, Delft University of Technology (2001).

[49] T. de Vries and C. Vermeeren, *R-curve test data 2024-t3, 7075-t6, glare-2 and glare-3,* Memorandum M-705, University of Delft (1995).

3

XFEM BASED ELEMENT SUBSCALE REFINEMENT FOR DETAILED REPRESENTATION OF CRACK PROPAGATION IN LARGE SCALE ANALYSES

In the present contribution, we address the delicate balance between computational efficiency and level of detailing at the modelling of ductile fracture in thin-walled structures. To represent the fine scale nature of the ductile process, we propose a new XFEM based enrichment of the displacement field to allow for cracks tips that end or kink within an element. The idea is to refine the crack tip element locally in a way such that the macroscale node connectivity is unaltered. This allows for a better representation of the discontinuous kinematics without affecting the macroscale solution procedure, which would be a direct consequence of a regular mesh refinement. The method is first presented in a general 3D setting and thereafter it is specialised to shell theory for the modelling of crack propagation in thin-walled structures. This chapter is concluded by a number of representative examples showing the accuracy of the method. We conclude that the ideas proposed in this chapter enhance the current methodology for the analysis of ductile fracture of thin-walled large scale structures under high strain rates.

This chapter was integrally extracted from [1].

3.1. INTRODUCTION

When performing finite element analyses of large scale structures under impact and/or blast loading, *e.g.* aircraft fuselage or off-shore structures, consideration of the proper balance between the level of detailing in the model and the computational cost for the dynamic ductile fracture analysis has to be taken. A natural choice is thereby to model these structures by using shell theory. Still, when dealing with really large structures, the possibility to furnish sufficient refinement in the mesh, so that an accurate analysis of the dynamic ductile fracture process can be guaranteed, is an issue. Even when adopting a shell modelling approach based on the eXtended Finite Element Method (XFEM), cf. *e.g.* References [2–4], it may be too expensive to accommodate the required degree of refinement in the mesh due to the non-linearity involved. Given this perspective, we have identified a need to develop a method capable of representing the crack propagation sufficiently accurate and smooth, without requiring heavily refined meshes.

A method to describe crack tips inside elements within an XFEM framework was proposed already by Zi and Belytschko [5] in 2003, although they did not explain how to conserve a potential element-internal kink of the element upon further crack propagation. A more recent approach, similar to what is proposed herein, is the VNXFEM recently published by Kumar *et al.* [6]. Their method, just as the one we propose, is based on an element-local mesh refinement in order to describe tips and kinks by inserting what they denote as virtual nodes. These locally refined (tip and kink) elements are then connected to the surrounding mesh by specially designed transition elements. The VNXFEM is an interesting approach but it requires some modifications of the common XFEM procedures by requiring these specially designed transition elements.

In this chapter, we propose a method which fits in a regular 'macroscopic' XFEM framework, such that any detailing of the crack representation (including crack tips or kinks inside the macroscopic elements) is encapsulated in these elements of the original computational domain. Thereby, we can avoid remeshing, as suggested by Fries *et al.* [7], or non-local enrichments of the approximation as when introducing crack tip branch functions, cf. e.g. Belytschko and Black [8]. Thus, the method is free from any modifications on the macroscale. To be specific, we propose a new refinement for a tip element in XFEM that is capable of representing a crack kink or a tip inside elements of different order of approximation, without introducing modifications on the macroscale.

The current work is thus focusing on the enhancement of the XFEM method to handle the fracture progression in a flexible way, where the crack tip advancement is allowed to occur not only segment wise from one element edge to the next one, *e.g.* Wells and Sluys [9]. The method is quite general and can in principle handle several kinks inside a macroscopic element, provided that conformity with the surrounding macroscopic mesh is preserved. However, in the examples shown in this chapter we restrict to one kink inside a macroscopic element in order to simplify the implementation.

In addition to the representation of crack kinks inside the element, the method

we propose also allows for a smoother crack propagation scheme since in general shorter crack segments may be inserted – on the refined subscale – compared to the typical element-wise propagation. As discussed by Menouilliard *et al.* [10], the insertion of finite crack tip segments of significant length may lead to significant oscillations in the dynamic fracture response depending on the loading case. For that purpose, and to mimic more of a continuous crack growth, they proposed to use a force-correction method to stabilise the response, which was also adopted with success in one of our previous papers [11]. Interestingly though, it has been found that the oscillatory behaviour is reduced upon mesh refinement [12]. Thus, we argue that the proposed method will be more in accordance with the physics of crack propagation, thereby also yielding a more stable simulation response, without requiring a high degree of mesh refinement. We finally note that a variant of the proposed method can in principle also be employed for the so-called Phantom node method initially proposed by Hansbo and Hansbo [13], which is an alternative method to XFEM, capable of representing mesh-independent crack propagation.

The outline of this chapter is as follows: In Section 3.2, the kinematics of the standard 3D continuum including the macroscopic discontinuity representation using XFEM is described. Here, also the basic concepts of the subscale element crack tip refinement are outlined. The resulting FE–equations are derived and the consequent explicit time integration solution procedure is described involving the typical out–condensing of element internal degrees of freedom. In Section 3.3, the discussion made in Section 3.2 is specialised to a seven parameter shell element formulation as described in References [4, 11]; the shell formulation is in line with the developments by Larsson *et al.* [4] and Bischoff and Ramm [14]. In particular, the weak form of the momentum balance is presented, where emphasis is placed on stress resultants of the internal work. We also present the consequent FE–equations and some further remarks on the solution procedure due to the shell context are made. In Section 3.4, a couple of numerical results and their behaviour as compared to the standard XFEM formulation are discussed, where it is shown that the concept yields an accurate kinematical representation of kinks and crack tips within an element. Finally, this chapter is concluded with some closing remarks where we stress that the proposed subscale refined XFEM based shell element allows for an increased detailing of the crack path, without having to resort to mesh refinement on the structural scale.

3.2. SUBSCALE REFINEMENT OF DISCONTINUITY FIELD - 3D FORMULATION

In this section, we outline the crack tip element subscale approximation, where, in addition to the macroscopic FE approximations of the continuous and discontinuous displacement fields, a subscale local refinement is introduced 'macro-element-wise' to allow for a better representation of the discontinuous kinematics. For generality and to simplify the developments of this chapter, the proposed approach is presented in the current section for the general 3D case. Thereafter, it is specialised to the application of interest in terms of thin-walled shell structures in Section 3.3.

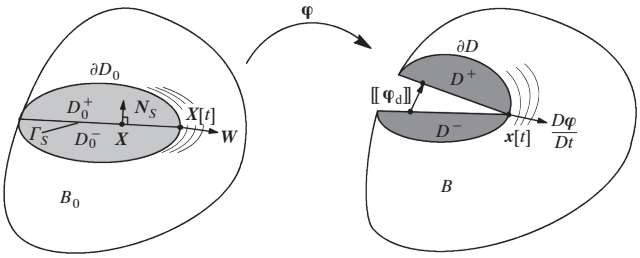

Figure 3.1: Continuous progression of crack tip with the speed $\boldsymbol{W}$ evolving in B_0.

3.2.1. CONTINUUM REPRESENTATION OF DISPLACEMENT DISCONTINUITY

To set the stage, we first start by stating the continuum (non-discretised) framework for large deformations including displacement discontinuities according to XFEM, presented earlier in several papers, cf. the early work by Wells *et al.* [15]. Consequently, the total deformation map $\boldsymbol{\varphi}$ is considered to be partitioned into a continuous and a discontinuous field as

$$\boldsymbol{\varphi} = \boldsymbol{\varphi}_c + \boldsymbol{\varphi}_d \,. \tag{3.1}$$

As usual, $\boldsymbol{\varphi}_d$ is a displacement field defined only locally within a region D_0 in the vicinity of the crack, where D_0 is decomposed into D_0^- and D_0^+ by the internal discontinuity surface Γ_S with corresponding surface normal $\mathbf{N}_S$, cf. Figure 3.1. We note that D_0 is evolving with time in the material due to the crack propagation. Furthermore, $\boldsymbol{\varphi}_d$ is discontinuous across the discontinuity surface Γ_S so that

$$\boldsymbol{\varphi}_d = \boldsymbol{\varphi}_d^- + H_S[\mathbf{S}[\mathbf{X}]] \left(\boldsymbol{\varphi}_d^+ - \boldsymbol{\varphi}_d^-\right) \tag{3.2}$$

where we introduced the level set function $S[\mathbf{X}]$ defining the positioning of the discontinuity surface by $S[\mathbf{X}] = 0$ and where H_S is the discontinuity enrichment function in terms of the classical Heaviside function.

As a consequence of the construction of the discontinuity field $\boldsymbol{\varphi}_d$, the gradient thereof has the properties

$$\boldsymbol{\varphi}_d \otimes \nabla_X \quad = \quad \begin{cases} \boldsymbol{\varphi}_d^- \otimes \nabla_X & \forall \mathbf{X} \in D_0^- \setminus \Gamma_S \\ \boldsymbol{\varphi}_d^+ \otimes \nabla_X & \forall \mathbf{X} \in D_0^+ \setminus \Gamma_S \\ \delta_S \left(\boldsymbol{\varphi}_d^+ - \boldsymbol{\varphi}_d^-\right) \otimes \mathbf{N}_S & \forall \mathbf{X} \in \Gamma_S \end{cases} \tag{3.3}$$

where δ_S is the Dirac-delta function, defined for any quantity $\bullet$ as

$$\int_{B_0} \delta_s \bullet \mathrm{d}V = \int_{\Gamma_S} \bullet \, \mathrm{d}A. \tag{3.4}$$

Consequently, the deformation gradient takes the form

$$\mathbf{F} = \mathbf{F}_b + \delta_S \mathbf{F}_d \tag{3.5}$$

where $\mathbf{F}_b$ and $\mathbf{F}_d$ are the bulk part and the interface part respectively, defined as:

$$\mathbf{F}_b = \begin{cases} \boldsymbol{\varphi}_c \otimes \nabla_X & \forall \mathbf{X} \in B_0 \setminus D_0 \\ \boldsymbol{\varphi}_c \otimes \nabla_X + \boldsymbol{\varphi}_d^- \otimes \nabla_X & \forall \mathbf{X} \in D_0^- \setminus \Gamma_S \\ \boldsymbol{\varphi}_c \otimes \nabla_X + \boldsymbol{\varphi}_d^+ \otimes \nabla_X & \forall \mathbf{X} \in D_0^+ \setminus \Gamma_S \end{cases} \tag{3.6}$$

$$\mathbf{F}_d = \left(\boldsymbol{\varphi}_d^+ - \boldsymbol{\varphi}_d^-\right) \otimes \mathbf{N}_S = [\![\boldsymbol{\varphi}_d]\!] \otimes \mathbf{N}_S \;\; \forall \mathbf{X} \in \Gamma_S \tag{3.7}$$

where we also introduced the jump in the discontinuous field $[\![\boldsymbol{\varphi}_d]\!]$.

Given the kinematical representation of the displacement discontinuity, the weak form of the momentum balance (assuming zero body forces) now becomes, cf. *e.g.* Reference [16]

Find: $[\boldsymbol{\varphi}_c, \boldsymbol{\varphi}_d]$

$$\begin{aligned} &\int_{B_0} \rho_0 \left(\delta\boldsymbol{\varphi}_c + \delta\boldsymbol{\varphi}_d\right) \cdot \left(\ddot{\boldsymbol{\varphi}}_c + \ddot{\boldsymbol{\varphi}}_d\right) \mathrm{dV} = \\ &\qquad \int_{\partial B_0} \left(\delta\boldsymbol{\varphi}_c + \delta\boldsymbol{\varphi}_d\right) \cdot \bar{\mathbf{t}}_1 \,\mathrm{dA} - \int_{B_0} \delta {\mathbf{F}_b}^t : \mathbf{P}^t \mathrm{dV} + \int_{\Gamma_S} \underbrace{\delta\mathbf{F}_d : \mathbf{P}^t}_{[\![\delta\boldsymbol{\varphi}_d]\!] \cdot \mathbf{t}_1} \mathrm{dA}, \quad \forall\, \delta\boldsymbol{\varphi}_c, \delta\boldsymbol{\varphi}_d \end{aligned} \tag{3.8}$$

where $\mathbf{P}^t$ is the first Piola Kirchhoff stress tensor and where $\bar{\mathbf{t}}_1 = \mathbf{P}^t \cdot \mathbf{N}$ and $\mathbf{t}_1 = \mathbf{P}^t \cdot \mathbf{N}_S$ are the prescribed nominal traction vector on the boundary ∂B_0 and the resulting (continuous) traction along the discontinuity surface Γ_S respectively.

3.2.2. SPATIAL DISCRETISATION INCLUDING SUBSCALE REFINEMENT

To obtain a method that does not influence the spatial discretisation of the domain of interest on the macroscopic (structural) scale, we propose a subscale local refinement of the continuous and discontinuous fields. In order to avoid introduction of new nodes in the macroscale mesh, still having the possibility to represent kinks and crack tips within one (or several) macroscopic element, a local model reduction technique is employed. Furthermore, despite the fact that internal crack tips were treated already in the pioneering work by Belytschko and Black [8], we require the method to be free of any non-local enrichments in order to avoid unnecessary complexities in the modelling and implementation.

Hence, we consider the crack tip (or kink) element as refined in terms of 'sub-elements', for a more detailed representation of the crack kinematics. In the simplest case where one kink is present within the macro element, cf. Figure 3.2, it is partitioned into the three sub-elements associated with shape functions ψ^i with local support within a subdomain of the macroscopic crack tip element. These shape functions are utilised for the interpolation of the continuous and discontinuous fields

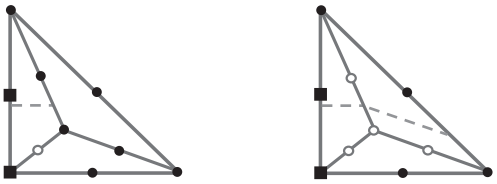

Figure 3.2: 6-noded element with quadratic interpolation for the continuous $\boldsymbol{\varphi}_c$ and discontinuous field $\boldsymbol{\varphi}_d$ enhanced with internal degrees of freedom for $\boldsymbol{\varphi}_c^S$ and $\boldsymbol{\varphi}_d^S$. The element allows for the successive advancement of the crack tip by the successive activation of boundary nodes (black squares) and internal nodes (white circles).

associated with the subscale nodes. In this context, the continuous and discontinuous contribution associated with the internal nodes can be interpreted as a subscale domain on which a local refinement is carried out to achieve a more accurate representation for the discontinuity.

In this subsection, we will discuss the spatial discretisation of the most general case for which all approximations are active. Consequently, we start by introducing the shifted enrichment function, cf. *e.g.* Reference [5],

$$\tilde{H}_S[\mathbf{X},\mathbf{X}^j] = H_S[\mathbf{X}] - H_S[\mathbf{X}^j] \tag{3.9}$$

where $\mathbf{X}^j$ denotes the reference coordinates of node j, in order to obtain the finite element approximation of the deformation map on the element level as

$$\boldsymbol{\varphi}^{h,e} = \underbrace{\sum_{i\in I} \psi^i \hat{\boldsymbol{\varphi}}_c^{M,i} + \sum_{j\in J} \psi^j \hat{\boldsymbol{\varphi}}_c^{s,j}}_{\boldsymbol{\varphi}_c^{h,e}} + \underbrace{\sum_{k\in K} \tilde{H}_S[\mathbf{X},\mathbf{X}^k]\psi^k \hat{\boldsymbol{\varphi}}_d^{M,k} + \sum_{l\in L} \tilde{H}_S[\mathbf{X},\mathbf{X}^l]\psi^l \hat{\boldsymbol{\varphi}}_d^{s,l}}_{\boldsymbol{\varphi}_d^{h,e}} . \tag{3.10}$$

In Eq. (3.10), referring to Figure 3.2, I is the set of boundary or macroscopic, M, nodes of the crack tip element, $K \subset I$ is the set of boundary nodes enriched with discontinuous degrees of freedom (black squares), J is the set of internal or subscale, s, nodes and $L \subset J$ is the set of internal nodes enriched with discontinuous degrees of freedom (white circles). In fact, the current FE-approximation results in a hidden local mesh refinement, where additional internal degrees of freedom are utilised for the interpolation. In this way, both a crack tip and crack kink within an element can be represented. Based on the current approximation in Eq. (3.10), we also note that the FE approximation of the bulk and interface parts of the deformation gradient can be written as

$$\mathbf{F}_b^{h,e} = \sum_{i\in I} \hat{\boldsymbol{\varphi}}_c^{M,i} \otimes \nabla_X \psi^i + \sum_{j\in J} \hat{\boldsymbol{\varphi}}_c^{s,j} \otimes \nabla_X \psi^j + \sum_{k\in K} \tilde{H}_S[\mathbf{X}] \hat{\boldsymbol{\varphi}}_d^{M,k} \otimes \nabla_X \psi^k + \sum_{l\in L} \tilde{H}_S[\mathbf{X}] \hat{\boldsymbol{\varphi}}_d^{s,l} \otimes \nabla_X \psi^l \tag{3.11}$$

$$\delta_S \mathbf{F}_d^{h,e} = \delta_S [\![\boldsymbol{\varphi}_d^{h,e}]\!] \otimes \mathbf{N}_S = \delta_S \left(\sum_{k\in K} \psi^k \hat{\boldsymbol{\varphi}}_d^{M,k} + \sum_{l\in L} \psi^l \hat{\boldsymbol{\varphi}}_d^{s,l} \right) \otimes \mathbf{N}_S \,. \tag{3.12}$$

Adopting Voight matrix notation ($\hat{\bullet}$), we now introduce the matrix representation of Eqs. (3.10)-(3.12) so that

$$\boldsymbol{\varphi}^{h,e} = \hat{\boldsymbol{\psi}} \hat{\boldsymbol{\varphi}}_c^{M,e} + \hat{\boldsymbol{\psi}} \hat{\boldsymbol{\varphi}}_c^{s,e} + \hat{\boldsymbol{\psi}}_{\tilde{H}_S} \hat{\boldsymbol{\varphi}}_d^{M,e} + \hat{\boldsymbol{\psi}}_{\tilde{H}_S} \hat{\boldsymbol{\varphi}}_d^{s,e} \tag{3.13}$$

$$\hat{\mathbf{F}}_b^{h,e} = \hat{\mathbf{B}} \hat{\boldsymbol{\varphi}}_c^{M,e} + \hat{\mathbf{B}} \hat{\boldsymbol{\varphi}}_c^{s,e} + \hat{\mathbf{B}}_{\tilde{H}_S} \hat{\boldsymbol{\varphi}}_d^{M,e} + \hat{\mathbf{B}}_{\tilde{H}_S} \hat{\boldsymbol{\varphi}}_d^{s,e} \tag{3.14}$$

$$[\![\boldsymbol{\varphi}_d^{h,e}]\!] = \hat{\boldsymbol{\psi}}_{\tilde{H}_S} \hat{\boldsymbol{\varphi}}_d^{M,e} + \hat{\boldsymbol{\psi}}_{\tilde{H}_S} \hat{\boldsymbol{\varphi}}_d^{s,e} . \tag{3.15}$$

In Eq. (3.13), we introduced $\hat{\boldsymbol{\psi}}$ and $\hat{\boldsymbol{\psi}}_{\tilde{H}_S}$ as the standard non-enriched and enriched shape function matrices ($H_S[\mathbf{X},\mathbf{X}^j]\psi^j$) respectively. Furthermore, in Eq. (3.14), $\hat{\mathbf{B}}$ and $\hat{\mathbf{B}}_{\tilde{H}_S}$ was introduced as the standard shape function derivative matrix associated with the non-enriched and enriched nodes. Subscript $\tilde{H}_S$ implies multiplication of the derivatives with the enrichment function $\tilde{H}_S$. Consequently, using Galerkin's method, we obtain the corresponding virtual displacement fields according to

$$\delta\boldsymbol{\varphi}^{h,e} = \hat{\boldsymbol{\psi}} \delta\hat{\boldsymbol{\varphi}}_c^{M,e} + \hat{\boldsymbol{\psi}} \delta\hat{\boldsymbol{\varphi}}_c^{s,e} + \hat{\boldsymbol{\psi}}_{\tilde{H}_S} \delta\hat{\boldsymbol{\varphi}}_d^{M,e} + \hat{\boldsymbol{\psi}}_{\tilde{H}_S} \delta\hat{\boldsymbol{\varphi}}_d^{s,e} \tag{3.16}$$

$$\delta\hat{\mathbf{F}}_b^{h,e} = \hat{\mathbf{B}} \delta\hat{\boldsymbol{\varphi}}_c^{M,e} + \hat{\mathbf{B}} \delta\hat{\boldsymbol{\varphi}}_c^{s,e} + \hat{\mathbf{B}}_{\tilde{H}_S} \delta\hat{\boldsymbol{\varphi}}_d^{M,e} + \hat{\mathbf{B}}_{\tilde{H}_S} \delta\hat{\boldsymbol{\varphi}}_d^{s,e} \tag{3.17}$$

$$[\![\delta\boldsymbol{\varphi}_d^{h,e}]\!] = \hat{\boldsymbol{\psi}}_{\tilde{H}_S} \delta\hat{\boldsymbol{\varphi}}_d^{M,e} + \hat{\boldsymbol{\psi}}_{\tilde{H}_S} \delta\hat{\boldsymbol{\varphi}}_d^{s,e} . \tag{3.18}$$

By inserting the FE approximation above into Eq. (3.8), we arrive at the discretised weak form of the momentum balance

$$\begin{bmatrix} \mathbf{M}_{cc}^e & \mathbf{M}_{cd}^e & \mathbf{M}_{cc_s}^e & \mathbf{M}_{cd_s}^e \\ \mathbf{M}_{dc}^e & \mathbf{M}_{dd}^e & \mathbf{M}_{dc_s}^e & \mathbf{M}_{dd_s}^e \\ \mathbf{M}_{c_sc}^e & \mathbf{M}_{c_sd}^e & \mathbf{M}_{c_sc_s}^e & \mathbf{M}_{c_sd_s}^e \\ \mathbf{M}_{d_sc}^e & \mathbf{M}_{d_sd}^e & \mathbf{M}_{d_sc_s}^e & \mathbf{M}_{d_sd_s}^e \end{bmatrix} \begin{bmatrix} \hat{\boldsymbol{a}}_c^{M,e} \\ \hat{\boldsymbol{a}}_d^{M,e} \\ \hat{\boldsymbol{a}}_c^{s,e} \\ \hat{\boldsymbol{a}}_d^{s,e} \end{bmatrix} = \begin{bmatrix} \mathbf{f}_c^{e,ext} - \mathbf{f}_c^{e,int} \\ \mathbf{f}_d^{e,ext} - \mathbf{f}_d^{e,int} + \mathbf{f}_d^{e,coh} \\ -\mathbf{f}_{c_s}^{e,int} \\ -\mathbf{f}_{d_s}^{e,int} + \mathbf{f}_{d_s}^{e,coh} \end{bmatrix} \tag{3.19}$$

where

$$\hat{\boldsymbol{a}}_c^{M,e} = \frac{\partial^2 \hat{\boldsymbol{\varphi}}_c^{M,e}}{\partial t^2}, \; \hat{\boldsymbol{a}}_d^{M,e} = \frac{\partial^2 \hat{\boldsymbol{\varphi}}_d^{M,e}}{\partial t^2}, \; \hat{\boldsymbol{a}}_c^{s,e} = \frac{\partial^2 \hat{\boldsymbol{\varphi}}_c^{s,e}}{\partial t^2}, \; \hat{\boldsymbol{a}}_d^{s,e} = \frac{\partial^2 \hat{\boldsymbol{\varphi}}_d^{s,e}}{\partial t^2} \tag{3.20}$$

Please refer to Appendix B.1 for details of individual terms in Eq. (3.19).

Since the support for the subscale node vanishes along the macroscopic crack tip element edges – leading to $\mathbf{f}_{d_s}^{e,ext} = \mathbf{0}$ and $\mathbf{f}_{c_s}^{e,ext} = \mathbf{0}$ – the subscale degrees of freedom can be implicitly solved for in terms of the macroscopic ones. By that, unnecessary introduction of additional degrees of freedom is avoided on the structural scale. As

a first step, if we let M denote the macroscopic degrees of freedom and s denote the subscale degrees of freedom, Eq. (3.19) can be re-written as

$$\begin{bmatrix} \mathbf{M}^e_{MM} & \mathbf{M}^e_{Ms} \\ \mathbf{M}^e_{sM} & \mathbf{M}^e_{ss} \end{bmatrix} \begin{bmatrix} \hat{\boldsymbol{a}}^e_M \\ \hat{\boldsymbol{a}}^e_s \end{bmatrix} = \begin{bmatrix} \mathbf{f}^{e,ext}_M - \mathbf{f}^{e,int}_M + \mathbf{f}^{e,coh}_M \\ -\mathbf{f}^{e,int}_s + \mathbf{f}^{e,coh}_s \end{bmatrix} \tag{3.21}$$

with

$$\mathbf{M}^e_{MM} = \begin{bmatrix} \mathbf{M}^e_{cc} & \mathbf{M}^e_{cd} \\ \mathbf{M}^e_{dc} & \mathbf{M}^e_{dd} \end{bmatrix} \tag{3.22}$$

$$\mathbf{M}^e_{Ms} = \left(\mathbf{M}^e_{sM}\right)^t = \begin{bmatrix} \mathbf{M}^e_{cc_s} & \mathbf{M}^e_{cd_s} \\ \mathbf{M}^e_{dc_s} & \mathbf{M}^e_{dd_s} \end{bmatrix} \tag{3.23}$$

$$\mathbf{M}^e_{ss} = \begin{bmatrix} \mathbf{M}^e_{c_sc_s} & \mathbf{M}^e_{c_sd_s} \\ \mathbf{M}^e_{d_sc_s} & \mathbf{M}^e_{d_sd_s} \end{bmatrix} \tag{3.24}$$

$$\hat{\boldsymbol{a}}^e_M = \begin{bmatrix} \hat{\boldsymbol{a}}^e_c \\ \hat{\boldsymbol{a}}^e_d \end{bmatrix} \tag{3.25}$$

$$\hat{\boldsymbol{a}}^e_s = \begin{bmatrix} \hat{\boldsymbol{a}}^e_{c_s} \\ \hat{\boldsymbol{a}}^e_{d_s} \end{bmatrix} \tag{3.26}$$

$$\mathbf{f}^{e,ext}_M = \begin{bmatrix} \mathbf{f}^{e,ext}_c \\ \mathbf{f}^{e,ext}_d \end{bmatrix} \tag{3.27}$$

$$\mathbf{f}^{e,int}_M = \begin{bmatrix} \mathbf{f}^{e,int}_c \\ \mathbf{f}^{e,int}_d \end{bmatrix} \tag{3.28}$$

$$\mathbf{f}^{e,coh}_M = \begin{bmatrix} \mathbf{0} \\ \mathbf{f}^{e,coh}_d \end{bmatrix} \tag{3.29}$$

$$\mathbf{f}^{e,int}_s = \begin{bmatrix} \mathbf{f}^{e,int}_{c_s} \\ \mathbf{f}^{e,int}_{d_s} \end{bmatrix} \tag{3.30}$$

$$\mathbf{f}^{e,coh}_s = \begin{bmatrix} \mathbf{0} \\ \mathbf{f}^{e,coh}_{d_s} \end{bmatrix}. \tag{3.31}$$

3.2.3. TEMPORAL DISCRETISATION AND MODEL REDUCTION

With the application of our methodology in mind (blast or impact loaded thin-walled structures), we employ an explicit time integration scheme in terms of the central difference method with variable time step size. Thus, for time step $n+1$ at $t = {}^{n+1}t$, the accelerations (with respect to both the continuous and discontinuous macroscopic degrees of freedom) are obtained from

$${}^{n+1}\mathbf{M}\,{}^{n+1}\hat{\boldsymbol{a}} = {}^{n+1}\mathbf{f} \tag{3.32}$$

where the mass matrix and the unbalance force vector, obtained by assembling the element contributions

$$\mathbf{M} = \mathop{\mathscr{A}}_{e=1}^{\text{NEL}} \mathbf{M}_M^e \tag{3.33}$$

$$\mathbf{f} = \mathop{\mathscr{A}}_{e=1}^{\text{NEL}} \left(\mathbf{f}_M^{e,ext} - \bar{\mathbf{f}}_M^{e,int} \right), \tag{3.34}$$

in the general case are functions of the velocities at time $t = {}^{n+1/2}t$ and the displacements and the reference (crack) geometry at time $t = {}^{n+1}t$. We would like to emphasise that we refrain from using a lumped mass matrix scheme in this contribution, although this generally provides a faster solution algorithm. The reason is that previous work by Remmers *et al.* [17] has shown that a lumped mass matrix time integration scheme together with XFEM may lead to transfer of stress wave across traction-free discontinuities. Thereby to avoid the aforementioned problem, in Eq. (3.33), $\mathbf{M}_M^e$ was introduced as the condensed consistent element mass matrix. Furthermore, in Eq. (3.34), $\bar{\mathbf{f}}_M^{e,int}$ was introduced as the condensed internal force vector. These two are the result from a dynamical condensation of the discretised momentum balance of the crack tip element, cf. Eq. (3.21), according to

$$\mathbf{M}_M^e \hat{\boldsymbol{a}}_M^e = \mathbf{f}_M^{e,ext} - \bar{\mathbf{f}}_M^{e,int} \tag{3.35}$$

with

$$\mathbf{M}_M^e = \mathbf{M}_{MM}^e - \mathbf{M}_{Ms}^e \mathbf{M}_{ss}^{e\ -1} \mathbf{M}_{sM}^e \tag{3.36}$$

$$\bar{\mathbf{f}}_M^{e,int} = \mathbf{f}_M^{e,int} - \mathbf{f}_M^{e,coh} - \mathbf{M}_{Ms}^e \mathbf{M}_{ss}^{e\ -1} \left(\mathbf{f}_s^{e,int} - \mathbf{f}_s^{e,coh} \right) \tag{3.37}$$

which has been obtained by eliminating the subscale degrees of freedom through

$$\hat{\boldsymbol{a}}_s^e = \mathbf{M}_{ss}^{e\ -1} \left(-\mathbf{M}_{sM}^e \hat{\boldsymbol{a}}_M^e - \mathbf{f}_s^{e,int} + \mathbf{f}_s^{e,coh} \right). \tag{3.38}$$

As stated above, this elimination is possible due to the fact that the support for the subscale degrees of freedom vanishes along the edges of the crack tip element. Consequently, only macroscopic degrees of freedom of the enriched 6 noded element in Figure 3.2 are solved for on the macroscopic level, where, in this case, the cohesive (or process zone forces) are embedded into the modified internal forces, cf. Eq. (3.37). From Eq. (3.32) we directly obtain the updated continuous and discontinuous macroscopic accelerations, whereby also the associated velocities and displacements can be updated.

As for the subscale degrees of freedom, these can be interpreted as internal variables of the crack tip element and consequently be updated on the element level. Naturally, in time step ${}^{n+1}t$, the velocity degrees of freedom ${}^{n+1/2}\mathbf{v}_s$ (at $t = {}^{n+1/2}t = \frac{{}^{n+1}t + {}^{n}t}{2}$) and the displacement degrees of freedom ${}^{n+1}\mathbf{u}_s$ associated with the internal subscale nodes are needed to compute the updated mass and unbalance force contributions. These can be directly obtained (on the element level) from the corresponding accelerations

$${}^{n}\hat{\boldsymbol{a}}_s^e = {}^{n}\mathbf{M}_{ss}^{e\ -1} \left(-{}^{n}\mathbf{M}_{sM}^e\ {}^{n}\hat{\boldsymbol{a}}_M^e - {}^{n}\mathbf{f}_s^{e,int} + {}^{n}\mathbf{f}_s^{e,coh} \right) \tag{3.39}$$

as

$$^{n+1/2}\mathbf{v}_s^e = {}^{n-1/2}\mathbf{v}_s^e + \left(^{n+1/2}t - ^{n-1/2}t\right)\ {}^n\hat{\boldsymbol{a}}_s^e \tag{3.40}$$

$$^{n+1}\mathbf{u}_s^e = {}^n\mathbf{u}_s^e + \left(^{n+1}t - ^{n}t\right)^{n+1/2}\mathbf{v}_s^e \tag{3.41}$$

where ${}^n\mathbf{M}_{ss}^{e\ -1}$, ${}^n\mathbf{M}_{sM}^e$, ${}^n\mathbf{f}_s^{e,int}$ and ${}^n\mathbf{f}_s^{e,coh}$ are taken from the previous time step.

It should be remarked that, by adopting the current temporal discretisation and integration technique, whenever a new crack segment is inserted in the discretisation of the domain, the continuity in time of this space discretisation is not ensured. Physically, the crack propagates with a finite velocity, whereas in the numerical simulation the crack propagation speed will be implicitly governed by the time step size since the crack is propagated segment by segment whenever a propagation criterion is satisfied. Consequently, when a new segment is inserted, the new degrees of freedom are injected with a zero initialisation leading to the release of a stress wave emanating from the crack tip. In [11], this was discovered to have a significant effect on the structural response. As a remedy, a force-correction method, initially proposed by Menouilliard *et al.* [10] was employed therein with good results. In the method we propose here, a correction force is introduced in a similar fashion which takes into account the fraction ratio of the crack tip element which is cut by the crack, making the new degrees of freedom continuous in time.

3.3. SUBSCALE ENRICHMENT OF DISCONTINUITY FIELD - SHELL FORMULATION

As mentioned in the introduction, the current method is intended to be applied to ductile crack propagation in thin-walled (shell) structures loaded at high strain rates, extending the developments in [11] to allow for not only crack segments through the entire shell elements (edge to edge). Consequently, the specialisation of the proposed method to a seven parameter shell element formulation is presented in this section.

3.3.1. INITIAL SHELL GEOMETRY AND CONVECTED COORDINATES

For completeness, let us first repeat the basics of the discontinuous shell element concept, as it was introduced in [4] and later modified in [11]. Referring to Figure 3.3, the initial configuration B_0 of the shell is considered parameterised in terms of convected coordinates (ξ_1, ξ_2, ξ) as

$$\begin{aligned} \mathrm{B}_0 = \big\{ \mathbf{X} := \boldsymbol{\Phi}_0[\xi_1,\xi_2,\xi] = \bar{\boldsymbol{\Phi}}[\xi_1,\xi_2] + \xi \mathbf{M}_\Phi[\xi_1,\xi_2] \\ \text{with } [\xi_1,\xi_2] \in A \text{ and } \xi \in \tfrac{h_0}{2}[-1,1] \big\} \end{aligned} \tag{3.42}$$

where the mapping $\Phi_0[\xi_1,\xi_2,\xi]$ maps the inertial Cartesian frame into the current configuration and where the mapping $\boldsymbol{\Phi}_0$ is defined by the midsurface placement $\bar{\boldsymbol{\Phi}}[\xi_1,\xi_2]$ and the outward unit normal vector field $\mathbf{M}_\Phi$ (with $|\mathbf{M}_\Phi| = 1$), as shown in

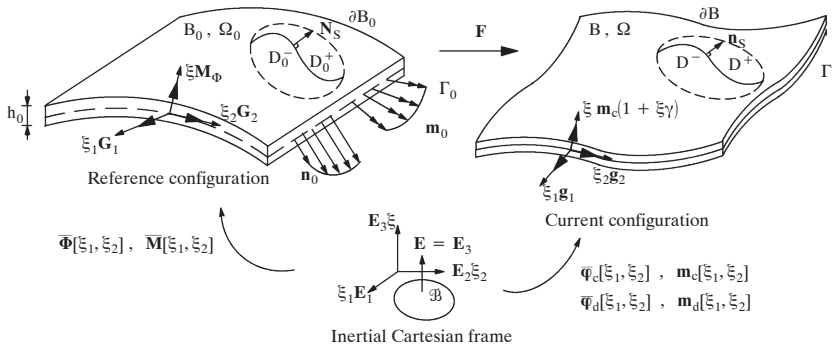

Figure 3.3: Mappings of 7-parameter shell model defining undeformed and deformed shell configurations relative to the inertial Cartesian frame.

Figure 3.3. The coordinate ξ is associated with the direction of $\mathbf{M}_\Phi$ and h_0 is the initial thickness of the shell. The pertinent co-variant basis vectors are defined by

$$\mathbf{G}_\alpha = \mathbf{\Phi}_{,\alpha} + \xi \mathbf{M}_{\Phi,\alpha},\ \alpha = 1,2 \text{ and } \mathbf{G}_3 = \mathbf{G}^3 = \mathbf{M}_\Phi. \tag{3.43}$$

where $\bullet_{,\alpha}$ denotes the derivative with respect to ξ_α. Furthermore, we note that the co-variant vectors $\mathbf{G}_i$ are associated with the contra-variant basis vectors $\mathbf{G}^i$ in the normal way, *i.e.* $\mathbf{G}_i \otimes \mathbf{G}^i = \mathbf{1}$, leading to

$$\mathbf{G}_j = G_{\mathrm{ij}}\mathbf{G}^i\ ,\ \mathbf{G}^j = G^{\mathrm{ij}}\mathbf{G}_i \text{ with } G_{\mathrm{ij}} = \mathbf{G}_i \cdot \mathbf{G}_j \text{ and } G^{\mathrm{ij}} = \left(G_{\mathrm{ij}}\right)^{-1}. \tag{3.44}$$

Finally, the infinitesimal volume element $\mathrm{d}B_0$ of the reference configuration is formulated in the convected coordinates as

$$\mathrm{d}B_0 = b_0 \mathrm{d}\xi_1 \mathrm{d}\xi_2 \mathrm{d}\xi \text{ with } b_0 = (\mathbf{G}_1 \times \mathbf{G}_2) \cdot \mathbf{G}^3. \tag{3.45}$$

3.3.2. CURRENT SHELL GEOMETRY BASED ON DISCONTINUOUS KINEMATICS

In analogy with the 3D representation presented in Section 3.2, the current (deformed) geometry is described by the deformation map $\boldsymbol{\varphi}[\mathbf{X}] \in B$, additively composed of the continuous displacement field $\boldsymbol{\varphi}_c \in B$ and the (local) discontinuous displacement field $\boldsymbol{\varphi}_d \in D$, parameterised in the convective coordinates (ξ_1, ξ_2, ξ) as:

$$\mathbf{x} := \boldsymbol{\varphi}_c[\mathbf{X}[\xi_1,\xi_2,\xi], t] + \boldsymbol{\varphi}_d[\mathbf{X}[\xi_1,\xi_2,\xi], t] \text{ where } \boldsymbol{\varphi}_d \equiv \mathbf{0}\ \ \forall\, \mathbf{X} \in B_0 \setminus D_0 \tag{3.46}$$

where (again) $\boldsymbol{\varphi}_d$ exhibits the general structure

$$\boldsymbol{\varphi}_d = \boldsymbol{\varphi}_d^- + H_S[S[\mathbf{X}]]\left(\boldsymbol{\varphi}_d^+ - \boldsymbol{\varphi}_d^-\right). \tag{3.47}$$

Furthermore, following the development in Reference [4], we allow for a through-the-thickness fracture by assuming $S[\mathbf{X}] \to S[\xi_1, \xi_2]$. As to the shell kinematics, the

representation of the current configuration is made in terms of strong discontinuities in both the midsurface placements and the director fields using XFEM-kinematics formulated as

$$\begin{cases} \boldsymbol{\varphi}_c[\xi_1,\xi_2,\xi] = \bar{\boldsymbol{\varphi}}_c[\xi_1,\xi_2] + \xi \mathbf{m}_c[\xi_1,\xi_2] + \frac{1}{2}\xi^2 \mathbf{m}_c \gamma[\xi_1,\xi_2] \\ \boldsymbol{\varphi}_d[\xi_1,\xi_2,\xi] = \bar{\boldsymbol{\varphi}}_d[\xi_1,\xi_2] + \xi \mathbf{m}_d[\xi_1,\xi_2] \end{cases} \tag{3.48}$$

where it should be remarked that the continuous placement $\boldsymbol{\varphi}_c$ corresponds to a second order Taylor series expansion in the director $\mathbf{m}_c$, thereby describing inhomogeneous thickness deformation effects of the shell, cf. Figure 3.3. In particular, the pathological Poisson locking effect is avoided in this fashion. In contrast, for computational efficiency only a first order expansion is used for the discontinuous part $\boldsymbol{\varphi}_d$, thereby assuming that the discontinuity in the second order inhomogeneity strain is negligible. Furthermore, in [11], it was shown that the deformation gradient takes on the form

$$\mathbf{F} = \mathbf{F}_b + \delta_S \mathbf{F}_d \text{ with } \mathbf{F}_b = \mathbf{g}_{\mathrm{b}m} \otimes \mathbf{G}^m \text{ and } \mathbf{F}_d = \mathbf{g}_{\mathrm{d}\alpha} \otimes \mathbf{G}^\alpha \tag{3.49}$$

in terms of the spatial co-variant basis vectors

$$\mathbf{g}_m = \boldsymbol{\varphi} \otimes \nabla_{\xi_m} = \mathbf{g}_{b_m} + \delta_S \mathbf{g}_{d_\alpha}. \tag{3.50}$$

3.3.3. WEAK FORM OF MOMENTUM BALANCE

In this section we establish the weak form of the momentum balance of the shell. To simplify the discussion, we will not distinguish between the regions in which the enrichments are active or not. Instead, we will focus on the case where all approximation fields are active.

To arrive at a stress resultant formulation, we start from the basic weak form of the momentum balance in Eq. (3.8) applied to the current shell kinematics introduced in Eq. (3.48) which yields

$$\begin{aligned} &\textit{Find: } [\bar{\boldsymbol{\varphi}}_c, \mathbf{m}_c, \gamma, \bar{\boldsymbol{\varphi}}_d, \mathbf{m}_d] \\ &G^{\mathrm{ine}}[\ddot{\bar{\boldsymbol{\varphi}}}_c, \ddot{\mathbf{m}}_c, \ddot{\gamma}, \ddot{\bar{\boldsymbol{\varphi}}}_d, \ddot{\mathbf{m}}_d; \delta\bar{\boldsymbol{\varphi}}_c, \delta\mathbf{m}_c, \delta\gamma, \delta\bar{\boldsymbol{\varphi}}_d, \delta\mathbf{m}_d] + \\ &G^{\mathrm{int}}[\bar{\boldsymbol{\varphi}}_c, \mathbf{m}_c, \gamma, \bar{\boldsymbol{\varphi}}_d, \mathbf{m}_d; \delta\bar{\boldsymbol{\varphi}}_c, \delta\mathbf{m}_c, \delta\gamma, \delta\bar{\boldsymbol{\varphi}}_d, \delta\mathbf{m}_d] - \\ &\qquad G^{\mathrm{ext}}[\delta\bar{\boldsymbol{\varphi}}_c, \delta\mathbf{m}_c, \delta\gamma, \delta\bar{\boldsymbol{\varphi}}_d, \delta\boldsymbol{m}_d] = 0 \;\forall\; \delta\bar{\boldsymbol{\varphi}}_c, \delta\mathbf{m}_c, \delta\gamma, \delta\bar{\boldsymbol{\varphi}}_d, \delta\mathbf{m}_d \end{aligned} \tag{3.51}$$

Following Larsson *et al.* [4] and introducing the displacement vector $\hat{\mathbf{n}}^t = [\bar{\boldsymbol{\varphi}}_c, \mathbf{m}_c, \gamma, \bar{\boldsymbol{\varphi}}_d, \mathbf{m}_d]$ and the shell deformation and stress resultant vectors (cf. Appendix B.2 for definitions of all stress resultants)

$$\begin{aligned} \delta\hat{\mathbf{n}}_c^t &= \left[\delta\bar{\boldsymbol{\varphi}}_{c,\alpha}, \delta\mathbf{m}_{c,\alpha}, \delta\mathbf{m}_c, \delta\gamma_{,\alpha}, \delta\gamma\right], \delta\hat{\mathbf{n}}_d^t = \left[\delta\bar{\boldsymbol{\varphi}}_{d,\alpha}, \delta\mathbf{m}_{d,\alpha}, \delta\mathbf{m}_d\right], \\ \delta\hat{\mathbf{n}}_{\mathrm{coh}}^t &= \left[\delta[\![\bar{\boldsymbol{\varphi}}_d]\!], \delta[\![\mathbf{m}_d]\!]\right] \end{aligned} \tag{3.52}$$

$$\begin{aligned} \hat{\mathbf{N}}_c^t &= \left[\mathbf{N}^\alpha, \mathbf{M}^\alpha, \mathbf{T}, M_h^\alpha, T_h\right], \hat{\mathbf{N}}_d^t = \left[\mathbf{N}_d^\alpha, \mathbf{M}_d^\alpha, \mathbf{T}_d\right], \hat{\mathbf{N}}_{\mathrm{coh}}^t = [\mathbf{n}_S, \mathbf{m}_S], \end{aligned} \tag{3.53}$$

the inertia and the internal and external virtual work contributions can be written as

$$G^{\text{ine}} = \int_{\Omega_0} \rho_0\, \delta\hat{\mathbf{n}}^t (\hat{\mathbf{M}}\ddot{\hat{\mathbf{n}}} + \hat{\mathbf{M}}_{\text{con}})\, \omega_0\, \mathrm{d}\xi_1 \mathrm{d}\xi_2 \tag{3.54}$$

$$G^{\text{int}} = \int_{\Omega_0} \delta\hat{\mathbf{n}}_c^t \hat{\mathbf{N}}_c \omega_0\, \mathrm{d}\xi_1 \mathrm{d}\xi_2 + \int_{\Omega_0} \delta\hat{\mathbf{n}}_d^t \hat{\mathbf{N}}_d \omega_0\, \mathrm{d}\xi_1 \mathrm{d}\xi_2 + \oint_{\mathscr{L}_{\Gamma_S}} \delta\hat{\mathbf{n}}_{\text{coh}}^t \hat{\mathbf{N}}_{\text{coh}}\, \mathrm{d}\mathscr{L} \tag{3.55}$$

$$\begin{aligned} G^{\text{ext}} = {} & \oint_{\mathscr{L}_{\partial\Omega_0}} \left(\delta\bar{\boldsymbol{\varphi}}_c \cdot \mathbf{n}_0 + \delta\mathbf{m}_c \cdot \bar{\mathbf{m}}_0 + \delta\gamma m_s\right) \mathrm{d}\mathscr{L} + \oint_{\mathscr{L}_{\partial\Omega_0} \cap \mathscr{L}_{\partial D_0}} (\delta\bar{\boldsymbol{\varphi}}_d \cdot \mathbf{n}_0 + \delta\mathbf{m}_d \cdot \mathbf{m}_0)\, \mathrm{d}\mathscr{L} \\ & - \int_{\Omega} p \left(\delta\bar{\boldsymbol{\varphi}}_c + \delta\bar{\boldsymbol{\varphi}}_d\right) \cdot \mathbf{g}_{b_1} \times \mathbf{g}_{b_2}\, \mathrm{d}\Omega. \end{aligned} \tag{3.56}$$

In Eq. (3.56), the perpendicular forces have been limited to external pressure in view of the Cauchy traction $\mathbf{t} = -p\mathbf{n}$ on the deformed surface Ω. Furthermore, the consistent mass matrix $\hat{\mathbf{M}}$ and the convective mass force $\hat{\mathbf{M}}_{\text{con}}$ per unit area were derived in [4], cf. Appendix B.3 for details. To be specific, the convective mass (force) $\hat{\mathbf{M}}^{\text{con}}$ involves contributions from the first order time derivative of the continuous director field and the inhomogeneity strain field.

In order to arrive at Eqs. (3.54)-(3.56), a change of the integration domain from B_0 (3D) to Ω_0 (2D) was made via the ratio $j_0[\xi] = b_0/\omega_0$, defining the relation between area and volumetric measures of the shell as

$$\mathrm{d}B_0 = j_0 \mathrm{d}\xi \mathrm{d}\Omega_0 \text{ with } \mathrm{d}\Omega_0 = \omega_0 \mathrm{d}\xi_1 \mathrm{d}\xi_2 \text{ and } \omega_0 = |\boldsymbol{\Phi}_{,1} \times \boldsymbol{\Phi}_{,2}| \tag{3.57}$$

Furthermore, $\mathscr{L}_\Gamma$ was introduced to denote the line defined as the intersection between the corresponding boundary surface and the shell midsurface.

3.3.4. SPATIAL DISCRETISATION INCLUDING SUBSCALE REFINEMENT

The approximation of the different fields involved in the shell formulation will follow the general structure as defined for the 3D case. As a starting point, the finite element approximation of the continuous part of the mapping is approximated by standard shape functions $\hat{\boldsymbol{\psi}}[\xi_1, \xi_2]$ associated with boundary nodes and subscale nodes as

$$\begin{aligned} \boldsymbol{\varphi}_c^h &= \sum_{i \in I} \psi^i[\xi_1,\xi_2] \left(\hat{\bar{\boldsymbol{\varphi}}}_c^{M,i} + \xi \hat{\mathbf{m}}_c^{M,i} \left(1 + \frac{1}{2}\xi \sum_{n \in I \cup J} \psi^n[\xi_1,\xi_2] \hat{\gamma}^n \right) \right) \\ &\quad + \sum_{j \in J} \psi^j[\xi_1,\xi_2] \left(\hat{\bar{\boldsymbol{\varphi}}}_c^{s,j} + \xi \hat{\mathbf{m}}_c^{s,j} \left(1 + \frac{1}{2}\xi \sum_{p \in I \cup J} \psi^p[\xi_1,\xi_2] \hat{\gamma}^p \right) \right) \\ &= \hat{\boldsymbol{\psi}}^M \left(\hat{\bar{\boldsymbol{\varphi}}}_c^M + \xi \hat{\mathbf{m}}_c^M \left(1 + \frac{1}{2}\xi \hat{\boldsymbol{\psi}}_\gamma \hat{\boldsymbol{\gamma}} \right) \right) + \hat{\boldsymbol{\psi}}^s \left(\hat{\bar{\boldsymbol{\varphi}}}_c^s + \xi \hat{\mathbf{m}}_c^s \left(1 + \frac{1}{2}\xi \hat{\boldsymbol{\psi}}_\gamma \hat{\boldsymbol{\gamma}} \right) \right) \end{aligned} \tag{3.58}$$

where I and J are the total sets of macroscale nodes and subscale nodes in B_0 and $\hat{\bar{\boldsymbol{\varphi}}}_c^{M,i}$, $\hat{\mathbf{m}}_c^{M,i}$, $\hat{\gamma}^n$, $\hat{\bar{\boldsymbol{\varphi}}}_c^{s,j}$, $\hat{\mathbf{m}}_c^{s,j}$ and $\hat{\gamma}^p$ are the corresponding degrees of freedom associated with both sets of nodes. In Eq. (3.58), we also introduced $\hat{\boldsymbol{\psi}}_\gamma$ as being the shape function matrix (row vector) associated with the scalar field γ, and $\hat{\boldsymbol{\psi}}^M$ and $\hat{\boldsymbol{\psi}}^s$ as shape functions associated with the macroscale and subscale nodes cf. the discussion in Subsection 3.2.2.

As in the 3D case, for the local discontinuous enrichment, the 'shifted' form of the Heaviside function is utilised to realise the strong discontinuity, which results in the following FE

approximation of the discontinuous field:

$$\begin{aligned}\boldsymbol{\varphi}_d^h &= \sum_{k\in K}\tilde{H}_S[\mathbf{X},\mathbf{X}^k]\psi^k\left(\hat{\bar{\boldsymbol{\varphi}}}_d^{M,k}+\xi\hat{\mathbf{m}}_d^{M,k}\right)+\sum_{l\in L}\tilde{H}_S[\mathbf{X},\mathbf{X}^l]\psi^l\left(\hat{\bar{\boldsymbol{\varphi}}}_d^{s,l}+\xi\hat{\mathbf{m}}_d^{s,l}\right)\\ &= \hat{\boldsymbol{\psi}}_{H_S}^M\left(\hat{\bar{\boldsymbol{\varphi}}}_d^M+\xi\hat{\mathbf{m}}_d^M\right)+\hat{\boldsymbol{\psi}}_{H_S}^s\left(\hat{\bar{\boldsymbol{\varphi}}}_d^s+\xi\hat{\mathbf{m}}_d^s\right)\end{aligned} \tag{3.59}$$

where, in analogy to Subsection 3.2.2, $K\subset I$ is the set of macroscale enriched with discontinuous degrees of freedom and $L\subset J$ is the set of subscale nodes enriched with subscale (discontinuous) degrees of freedom. At this point, we also note that

$$[\![\boldsymbol{\varphi}_d^h]\!] = \hat{\boldsymbol{\psi}}_{H_S}^M\left(\hat{\bar{\boldsymbol{\varphi}}}_d^M+\xi\hat{\mathbf{m}}_d^M\right)+\hat{\boldsymbol{\psi}}_{H_S}^s\left(\hat{\bar{\boldsymbol{\varphi}}}_d^s+\xi\hat{\mathbf{m}}_d^s\right). \tag{3.60}$$

Given the FE approximation of the different fields involved, we can also establish the approximation of the corresponding spatial co-variant basis vectors as

$$\mathbf{g}_{b_m}^h = \begin{cases} \displaystyle\sum_{i\in I}\left(\left(\hat{\bar{\boldsymbol{\varphi}}}_c^{M,i}+\xi\hat{\mathbf{m}}_c^{M,i}\left(1+\frac{1}{2}\xi\sum_{n\in I\cup J}\psi^n\hat{\gamma}^n\right)\right)\frac{\partial\psi^i}{\partial\xi_m}+\frac{1}{2}\xi^2\psi^i\hat{\mathbf{m}}_c^{M,i}\left(\sum_{n\in I\cup J}\frac{\partial\psi^n}{\partial\xi_m}\hat{\gamma}^n\right)\right)+ \\ \displaystyle\sum_{j\in J}\left(\left(\hat{\bar{\boldsymbol{\varphi}}}_c^{s,j}+\xi\hat{\mathbf{m}}_c^{s,j}\left(1+\frac{1}{2}\xi\sum_{p\in I\cup J}\psi^p\hat{\gamma}^p\right)\right)\frac{\partial\psi^j}{\partial\xi_m}+\frac{1}{2}\xi^2\psi^j\hat{\mathbf{m}}_c^{s,j}\left(\sum_{p\in I\cup J}\frac{\partial\psi^p}{\partial\xi_m}\hat{\gamma}^p\right)\right)+ \\ \displaystyle\sum_{k\in K}\tilde{H}_S[\mathbf{X},\mathbf{X}^k]\left(\hat{\bar{\boldsymbol{\varphi}}}_d^{M,k}+\xi\hat{\mathbf{m}}_d^{M,k}\right)\frac{\partial\psi^k}{\partial\xi_m}+\sum_{l\in L}\tilde{H}_S[\mathbf{X},\mathbf{X}^l]\left(\hat{\bar{\boldsymbol{\varphi}}}_d^{s,l}+\xi\hat{\mathbf{m}}_d^{s,l}\right)\frac{\partial\psi^l}{\partial\xi_m} \end{cases} \quad m=1,2 \tag{3.61}$$

$$\mathbf{g}_{b_m}^h = \begin{cases} \displaystyle\sum_{i\in I}\psi^i\hat{\mathbf{m}}_c^{M,i}\left(1+\xi\sum_{n\in I\cup J}\psi^n\hat{\gamma}^n\right)+\sum_{j\in J}\psi^j\hat{\mathbf{m}}_c^{s,j}\left(1+\xi\sum_{p\in I\cup J}\psi^p\hat{\gamma}^p\right)+ \\ \displaystyle\sum_{k\in K}\tilde{H}_S[\mathbf{X},\mathbf{X}^k]\psi^k\hat{\mathbf{m}}_d^{M,k}+\sum_{l\in L}\tilde{H}_S[\mathbf{X},\mathbf{X}^l]\psi^l\hat{\mathbf{m}}_d^{s,l} \end{cases} \quad m=3$$

$$\mathbf{g}_{d_\alpha}^h = [\![\boldsymbol{\varphi}_d^h]\!]s_\alpha = \sum_{k\in K}\psi^k\left(\hat{\bar{\boldsymbol{\varphi}}}_d^{M,k}+\xi\hat{\mathbf{m}}_d^{M,k}\right)s_\alpha+\sum_{l\in L}\psi^l\left(\hat{\bar{\boldsymbol{\varphi}}}_d^{s,l}+\xi\hat{\mathbf{m}}_d^{s,l}\right)s_\alpha \quad \alpha=1,2 \tag{3.62}$$

where $s_\alpha = (\partial S/\partial\xi_\alpha) = \mathbf{N}_S\cdot\mathbf{G}_\alpha$. To obtain the discretised set of equations, let us first formulate the shell displacement and deformation vectors in terms of the approximated fields. Given the FE approximation of the displacement, director and inhomogeneity fields, the corresponding virtual fields and their respective derivatives, we note that, on the element level, these vectors can be written on Voight form as

$$\hat{\mathbf{n}}_c^h = \begin{bmatrix} \bar{\boldsymbol{\varphi}}_{c,\alpha}^{h,e} \\ \mathbf{m}_{c,\alpha}^{h,e} \\ \mathbf{m}_c^{h,e} \\ \gamma_{,\alpha}^{h,e} \\ \gamma^e \end{bmatrix} = \underbrace{\begin{bmatrix} \hat{\mathbf{B}}^M & \mathbf{0} & \mathbf{0} & \hat{\mathbf{B}}^s & \mathbf{0} & \mathbf{0} \\ \mathbf{0} & \hat{\mathbf{B}}^M & \mathbf{0} & \mathbf{0} & \hat{\mathbf{B}}^s & \mathbf{0} \\ \mathbf{0} & \hat{\boldsymbol{\psi}}^M & \mathbf{0} & \mathbf{0} & \hat{\boldsymbol{\psi}}^s & \mathbf{0} \\ \mathbf{0} & \mathbf{0} & \hat{\mathbf{B}}_\gamma^M & \mathbf{0} & \mathbf{0} & \hat{\mathbf{B}}_\gamma^s \\ \mathbf{0} & \mathbf{0} & \hat{\boldsymbol{\psi}}_\gamma^M & \mathbf{0} & \mathbf{0} & \hat{\boldsymbol{\psi}}_\gamma^s \end{bmatrix}}_{\left[\mathbf{B}_1^{FE}\,\mathbf{B}_2^{FE}\right]} \underbrace{\begin{bmatrix} \hat{\bar{\boldsymbol{\varphi}}}_c^{M,e} \\ \hat{\mathbf{m}}_c^{M,e} \\ \hat{\boldsymbol{\gamma}}^{M,e} \\ \hat{\bar{\boldsymbol{\varphi}}}_c^{s,e} \\ \hat{\mathbf{m}}_c^{s,e} \\ \hat{\boldsymbol{\gamma}}^{s,e} \end{bmatrix}}_{\begin{bmatrix} \hat{\boldsymbol{\varphi}}_c^{M,e} \\ \hat{\boldsymbol{\varphi}}_c^{s,e} \end{bmatrix}} \Rightarrow \delta\hat{\mathbf{n}}_c^h = \mathbf{B}_1^{FE}\delta\hat{\boldsymbol{\varphi}}_c^{M,e}+\mathbf{B}_2^{FE}\delta\hat{\boldsymbol{\varphi}}_c^{s,e} \tag{3.63}$$

$$\hat{\mathbf{n}}_d^h = \begin{bmatrix} \bar{\boldsymbol{\varphi}}_{d,\alpha}^{h,e} \\ \mathbf{m}_{d,\alpha}^{h,e} \\ \mathbf{m}_d^{h,e} \end{bmatrix} = \underbrace{\begin{bmatrix} \hat{\mathbf{B}}_{H_S}^M & \mathbf{0} & \hat{\mathbf{B}}_{H_S}^s & \mathbf{0} \\ \mathbf{0} & \hat{\mathbf{B}}_{H_S}^M & \mathbf{0} & \hat{\mathbf{B}}_{H_S}^s \\ \mathbf{0} & \hat{\boldsymbol{\psi}}_{H_S}^M & \mathbf{0} & \hat{\boldsymbol{\psi}}_{H_S}^s \end{bmatrix}}_{\left[\mathbf{B}_3^{FE}\,\mathbf{B}_4^{FE}\right]} \underbrace{\begin{bmatrix} \hat{\bar{\boldsymbol{\varphi}}}_d^{M,e} \\ \hat{\mathbf{m}}_d^{M,e} \\ \hat{\bar{\boldsymbol{\varphi}}}_d^{s,e} \\ \hat{\mathbf{m}}_d^{s,e} \end{bmatrix}}_{\begin{bmatrix} \hat{\boldsymbol{\varphi}}_d^{M,e} \\ \hat{\boldsymbol{\varphi}}_d^{s,e} \end{bmatrix}} \tag{3.64}$$

$$\Rightarrow \delta\hat{\mathbf{n}}_d^h = \mathbf{B}_3^{FE}\delta\hat{\boldsymbol{\varphi}}_d^{M,e} + \mathbf{B}_4^{FE}\delta\hat{\boldsymbol{\varphi}}_d^{s,e}$$

$$\hat{\mathbf{n}}^{h,e} = \begin{bmatrix} \bar{\boldsymbol{\varphi}}_c^{h,e} \\ \mathbf{m}_c^{h,e} \\ \gamma^{h,e} \\ \bar{\boldsymbol{\varphi}}_d^{h,e} \\ \mathbf{m}_d^{h,e} \end{bmatrix} = \underbrace{\begin{bmatrix} \hat{\boldsymbol{\psi}}^M & \mathbf{0} & \mathbf{0} & \hat{\boldsymbol{\psi}}^s & \mathbf{0} & \mathbf{0} & \mathbf{0} & \mathbf{0} & \mathbf{0} & \mathbf{0} \\ \mathbf{0} & \hat{\boldsymbol{\psi}}^M & \mathbf{0} & \mathbf{0} & \hat{\boldsymbol{\psi}}^s & \mathbf{0} & \mathbf{0} & \mathbf{0} & \mathbf{0} & \mathbf{0} \\ \mathbf{0} & \mathbf{0} & \hat{\boldsymbol{\psi}}_\gamma^M & \mathbf{0} & \mathbf{0} & \hat{\boldsymbol{\psi}}_\gamma^s & \mathbf{0} & \mathbf{0} & \mathbf{0} & \mathbf{0} \\ \mathbf{0} & \mathbf{0} & \mathbf{0} & \mathbf{0} & \mathbf{0} & \mathbf{0} & \hat{\boldsymbol{\psi}}_{H_S}^M & \mathbf{0} & \hat{\boldsymbol{\psi}}_{H_S}^s & \mathbf{0} \\ \mathbf{0} & \mathbf{0} & \mathbf{0} & \mathbf{0} & \mathbf{0} & \mathbf{0} & \mathbf{0} & \hat{\boldsymbol{\psi}}_{H_S}^M & \mathbf{0} & \hat{\boldsymbol{\psi}}_{H_S}^s \end{bmatrix}}_{[\boldsymbol{\psi}_1^{FE}\,\boldsymbol{\psi}_2^{FE}\,\boldsymbol{\psi}_3^{FE}\,\boldsymbol{\psi}_4^{FE}]} \begin{bmatrix} \hat{\bar{\boldsymbol{\varphi}}}_c^{M,e} \\ \hat{\mathbf{m}}_c^{M,e} \\ \hat{\boldsymbol{\gamma}}^{M,e} \\ \hat{\bar{\boldsymbol{\varphi}}}_c^{s,e} \\ \hat{\mathbf{m}}_c^{s,e} \\ \hat{\boldsymbol{\gamma}}^{s,e} \\ \hat{\bar{\boldsymbol{\varphi}}}_d^{M,e} \\ \hat{\mathbf{m}}_d^{M,e} \\ \hat{\bar{\boldsymbol{\varphi}}}_d^{s,e} \\ \hat{\mathbf{m}}_d^{s,e} \end{bmatrix}$$

$$\Rightarrow \delta\hat{\mathbf{n}}^h = \boldsymbol{\psi}_1^{FE}\delta\hat{\boldsymbol{\varphi}}_c^{M,e} + \boldsymbol{\psi}_2^{FE}\delta\hat{\boldsymbol{\varphi}}_c^{s,e} + \boldsymbol{\psi}_3^{FE}\delta\hat{\boldsymbol{\varphi}}_d^{M,e} + \boldsymbol{\psi}_4^{FE}\delta\hat{\boldsymbol{\varphi}}_d^{s,e} \tag{3.65}$$

and

$$\hat{\mathbf{n}}_{\text{coh}}^{h,e} = \begin{bmatrix} [\![\bar{\boldsymbol{\varphi}}_d^{h,e}]\!] \\ [\![\mathbf{m}_d^{h,e}]\!] \end{bmatrix} = \underbrace{\begin{bmatrix} \hat{\boldsymbol{\psi}}_{H_S}^M & \mathbf{0} & \hat{\boldsymbol{\psi}}_{H_S}^s & \mathbf{0} \\ \mathbf{0} & \hat{\boldsymbol{\psi}}_{H_S}^M & \mathbf{0} & \hat{\boldsymbol{\psi}}_{H_S}^s \end{bmatrix}}_{[\boldsymbol{\psi}_5^{FE}\,\boldsymbol{\psi}_6^{FE}]} \begin{bmatrix} \hat{\bar{\boldsymbol{\varphi}}}_d^{M,e} \\ \hat{\mathbf{m}}_d^{M,e} \\ \hat{\bar{\boldsymbol{\varphi}}}_d^{s,e} \\ \hat{\mathbf{m}}_d^{s,e} \end{bmatrix} \tag{3.66}$$

$$\Rightarrow \delta\hat{\mathbf{n}}_{\text{coh}}^h = \boldsymbol{\psi}_5^{FE}\delta\hat{\boldsymbol{\varphi}}_d^{M,e} + \boldsymbol{\psi}_6^{FE}\delta\hat{\boldsymbol{\varphi}}_d^{s,e}$$

By inserting the FE approximation in the weak form of the momentum balance, and neglecting edge tractions, one finally arrives at

$$\underbrace{\begin{bmatrix} \mathbf{M}_{cc}^e & \mathbf{M}_{cd}^e & \mathbf{M}_{cc_s}^e & \mathbf{M}_{cd_s}^e \\ \mathbf{M}_{dc}^e & \mathbf{M}_{dd}^e & \mathbf{M}_{dc_s}^e & \mathbf{M}_{dd_s}^e \\ \mathbf{M}_{c_sc}^e & \mathbf{M}_{c_sd}^e & \mathbf{M}_{c_sc_s}^e & \mathbf{M}_{c_sd_s}^e \\ \mathbf{M}_{d_sc}^e & \mathbf{M}_{d_sd}^e & \mathbf{M}_{d_sc_s}^e & \mathbf{M}_{d_sd_s}^e \end{bmatrix}}_{\mathbf{M}^e} \begin{bmatrix} \hat{\boldsymbol{a}}_c^{M,e} \\ \hat{\boldsymbol{a}}_d^{M,e} \\ \hat{\boldsymbol{a}}_c^{s,e} \\ \hat{\boldsymbol{a}}_d^{s,e} \end{bmatrix} = \begin{bmatrix} \mathbf{f}_c^{e,ext} - \mathbf{f}_c^{e,int} \\ \mathbf{f}_d^{e,ext} - \mathbf{f}_d^{e,int} + \mathbf{f}_d^{e,coh} \\ -\mathbf{f}_{c_s}^{e,int} \\ -\mathbf{f}_{d_s}^{e,int} + \mathbf{f}_{d_s}^{e,coh} \end{bmatrix} \tag{3.67}$$

where

$$\hat{\boldsymbol{a}}_c^{M,e} = \frac{\partial^2}{\partial t^2}\left(\begin{bmatrix} \hat{\tilde{\boldsymbol{\varphi}}}_c^M \\ \hat{\mathbf{m}}_c^M \\ \hat{\boldsymbol{\gamma}}^M \end{bmatrix}\right),\ \hat{\boldsymbol{a}}_d^{M,e} = \frac{\partial^2}{\partial t^2}\left(\begin{bmatrix} \hat{\tilde{\boldsymbol{\varphi}}}_d^M \\ \hat{\mathbf{m}}_d^M \end{bmatrix}\right),\ \hat{\boldsymbol{a}}_c^{s,e} = \frac{\partial^2}{\partial t^2}\left(\begin{bmatrix} \hat{\tilde{\boldsymbol{\varphi}}}_c^s \\ \hat{\mathbf{m}}_c^s \\ \hat{\boldsymbol{\gamma}}^s \end{bmatrix}\right),\ \hat{\boldsymbol{a}}_d^{s,e} = \frac{\partial^2}{\partial t^2}\left(\begin{bmatrix} \hat{\tilde{\boldsymbol{\varphi}}}_d^s \\ \hat{\mathbf{m}}_d^s \end{bmatrix}\right) \tag{3.68}$$

and where explicit expressions for the terms in Eq. (3.67) can be found in Appendix B.1.

It may be noted that Eqs. (3.67)-(3.68) are idential in structure to Eqs. (3.19)-(3.20), whereby the same condensation approach is proposed also for the shell. Thereby, if the central difference scheme with variable time step is utilised for the temporal discretisation of the shell problem, it can be solved by the solution methodology proposed for the 3D case (including local model reduction), cf. Eqs. (3.21)-(3.41), in exactly the same fashion.

3.4. NUMERICAL EXAMPLES

In order to verify the theory and implementation of the proposed methodology in the previous sections, we present four numerical examples in this section. In the first example we verify that the kinematics represented by the subscale element refinement yields the same (or similar) response as the corresponding formulation using the conventional XFEM formulation. This example also examines the capability of the new scheme to represent crack tips as well as kinks inside the elements. The second example explores the application of the subscale crack tip refinement in conjunction with cohesive zone models. In the third example, we are investigating the significance of describing kinks inside the cracked elements. Finally, in the fourth example we show the capability of the proposed subscale method in a more refined case involving an out-of-plane loaded plate.

For all simulations, 6-node triangular elements are employed. For the spatial integration, 6 integration points in-plane and 4 integration points through the thickness are utilised per element. The in-plane integration scheme is carried out as in the 2D plane strain case in Reference [16], including the sub–triangulation of the elements cut by a crack. As to the integration of the mass matrix, it appears that (at least) 6 integration points are necessary in each subtriangle to obtain a stable time stepping procedure. All simulations in the first three examples are carried out using the explicit central difference scheme with a time step of $\Delta t = 10^{-7}$ s. In the fourth example a time step of $\Delta t = 2.5 \times 10^{-8}$ s is used.

The response of the bulk material is represented according to the isotropic hypoelastic-inelastic framework, cf. Reference [18], to properly account for finite deformations. In this context, the Green-Naghdi stress rate of the Kirchhoff stress is used. The material elastic parameters are taken as $E = 210\,\text{GPa}$, $\nu = 0.3$. Furthermore, the elastoplastic response is accounted for utilising the Johnson and Cook [19] (JC) phenomenological model, where e.g. an isotropic non-linear hardening effect is invoked. We thus disregard the influence of rate-dependency and temperature and thereby consider only the quasi-static isothermal yield function of the JC–model written as

$$F = \tau_e - \left(A + B\left(\varepsilon_e^p\right)^n\right) \tag{3.69}$$

where the parameters are taken as $A = 175\,\text{MPa}$, $B = 767\,\text{MPa}$, and $n = 0.67$.

As to the constitutive model governing the traction-separation of the interface, the cohesive zone model developed by Fagerström and Larsson [20] is employed, where the degradation of the traction across the interface is described by a damage-viscoplasticity model. For the sake of simplicity, rate-dependence of the interface material model is also disregarded.

3.4.1. EXAMPLE 1: MEMBRANE LOADED PLATE WITH NO INTERFACE TRACTION

This example is intended to explore the accuracy of the crack kinematics applying the proposed method. It concerns a pre-notched elastic-inelastic plate of dimension $1.5 \times 1\,\mathrm{m}^2$ with a thickness of 8 mm. In a first case the plate is discretised with a refined mesh and analysed using conventional XFEM enrichment in terms of the shifted enrichment function, cf. Figure 3.4a. In the second case the plate is analysed using the proposed subscale refinement method, and it is discretised with a coarser mesh whose subscale mesh mimics the discretisation of the first case, cf. Figure 3.4b. In order to ensure that the new method is capable of representing a crack kink and/or a tip inside the element, the crack path is predefined to inside the first cracked element and to end inside the second one. For both cases, the bottom side of the plate is constrained and fixed and the top side is prescribed by a constant velocity of 20 m/s, as shown in Figure 3.4.

Given that the boundary conditions in both cases are the same, and that the discretisation in the case of the conventional XFEM enrichment corresponds to the discretisation in the case analysed with the proposed subscale crack refinement, the results are expected to be the same. By comparing the deformed geometries in Figure 3.5 and resulting force-displacement curves in Figure 3.6, obtained from the both cases, it is obvious that the results agree well which verifies the potential of the proposed methodology in capturing the accurate kinematics of crack opening once the crack kinks and/or ends inside an element.

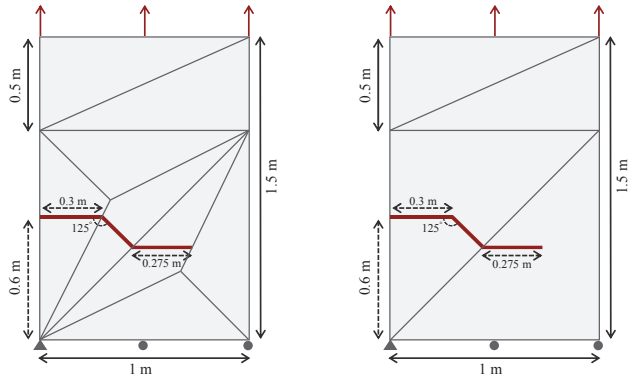

Figure 3.4: Boundary conditions for a) a refined mesh with conventional XFEM enrichment and b) a coarse mesh with the proposed subscale refinement.

3.4.2. EXAMPLE 2: MEMBRANE LOADED PLATE WITH INTERFACE TRACTION

In this example, the aim is to ensure that the new methodology can be extended to include dynamic ductile fracture, where the crack propagates progressively and a cohesive zone is

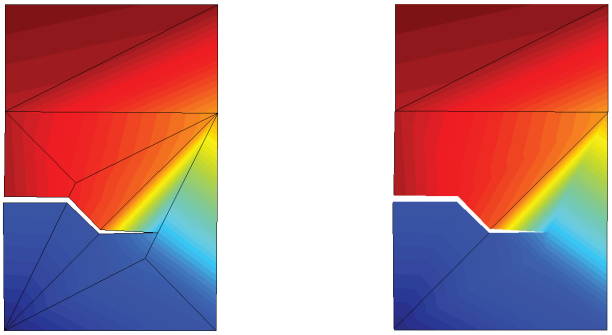

a) b)

Figure 3.5: Example 1: Deformed geometry for a) the refined mesh with conventional enrichment and b) the coarse mesh with subscale refinement analysed in the first numerical example.

present in the vicinity of the crack tip. In order to demonstrate the influence of including cohesive tractions along the crack interface together with the subscale refinement, we consider again the plate in the previous example, but now including cohesive tractions acting along the same crack path. The same bulk material model and associated parameters are utilised and the boundary conditions are unchanged. The parameters used in cohesive zone model are a fracture energy of $G_f = 250\,\mathrm{kJ/m^2}$, and a tensile strength of 306 MPa.

As can be observed in Figure 3.7, the difference between the forces obtained by the conventional XFEM and the proposed method is less than one percent which proves that the proposed method is able to treat the case where cohesive tractions are active on the crack segments.

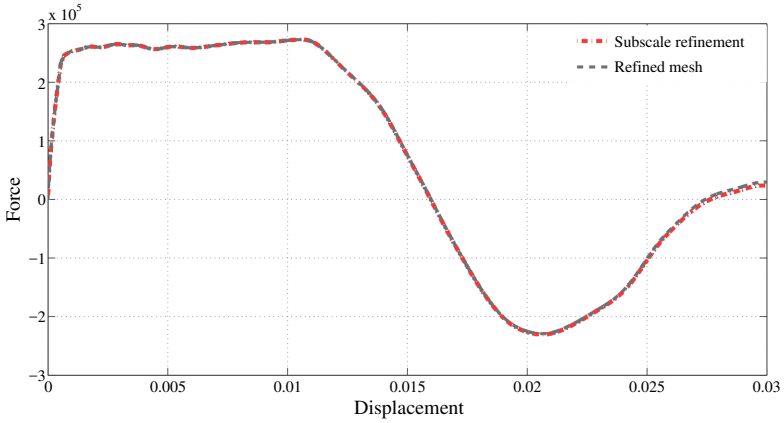

Figure 3.6: Example 1: Force versus displacement diagram measured at upper left corner point where no cohesive traction is involved, both for XFEM with conventional enrichment and subscale refinement.

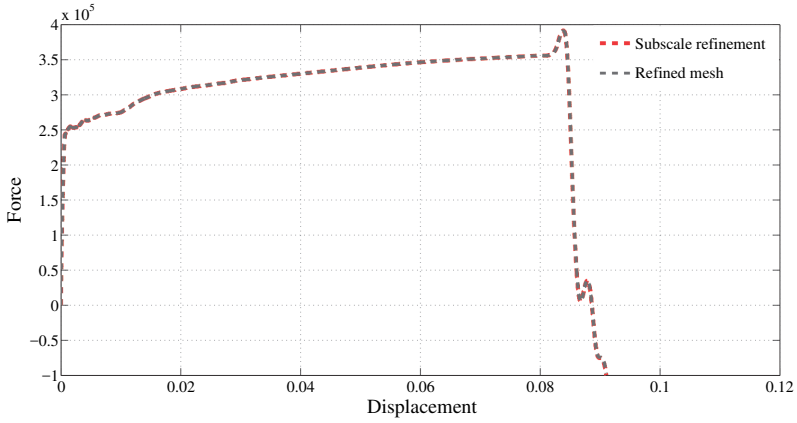

Figure 3.7: Example 2: Force versus displacement diagram measured at upper left corner point in the case of cohesive traction acting on the crack surfaces, both for XFEM with conventional enrichment and subscale refinement.

3.4.3. EXAMPLE 3: MEMBRANE LOADED PLATE WITH AND WITHOUT KINK

In the third example, we want to emphasise the importance of describing cracks that kink inside the element when predicted to do so. For this purpose, the two cases depicted in Figure 3.8 are considered.

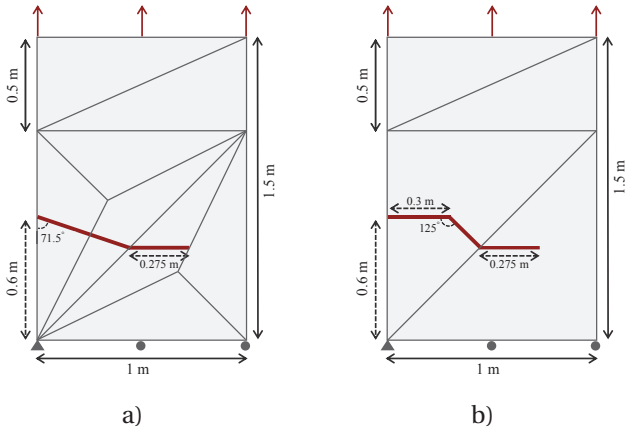

Figure 3.8: Example 3: Boundary conditions for a) the refined mesh with standard enrichment with no kink inside and b) the coarse mesh enriched based on subscale refinement technique including a kink inside the first cracked element

As can be observed in Figure 3.8b, in the case enriched with the subscale refinement, the crack kink is represented inside the cracked element. In contrast, in order to prove the importance of representing the kink inside the element, this subscale refined case is compared to a refined case with standard XFEM enrichment not including the kink, cf. Figure 3.8a. Therefore, in the latter case, the crack path for the first two crack segments is defined between the corresponding entry and exit points of the first and second macroscopic element of the standard enrichment case.

As demonstrated from the results shown in Figure 3.9, the resulting force-displacement curves do not match one another. This is explained by a difference in mass distribution but also (mainly) by the difference in the effect from the cohesive traction due to a different length and orientation of the crack.

3.4.4. EXAMPLE 4: PRE-NOTCHED PLATE UNDER OUT-OF-PLANE LOADING

This example concerns a plate with the dimension of 203 × 203 mm and thickness of 0.8 mm, where it is clamped on two sides. It is pre-notched and loaded in out-of-plane direction so that the initial crack with length of 40 mm starts to propagate, cf. Reference. [21].

Here we aim at investigating the accuracy of the proposed subscale refinement approach in comparison with the conventional XFEM in a case involving thin-shells. For that, two different mesh discretisations, i.e. a fine mesh and a coarse mesh, are employed where the domain is meshed using 502 elements for the fine case and 380 elements for the coarse case. In both

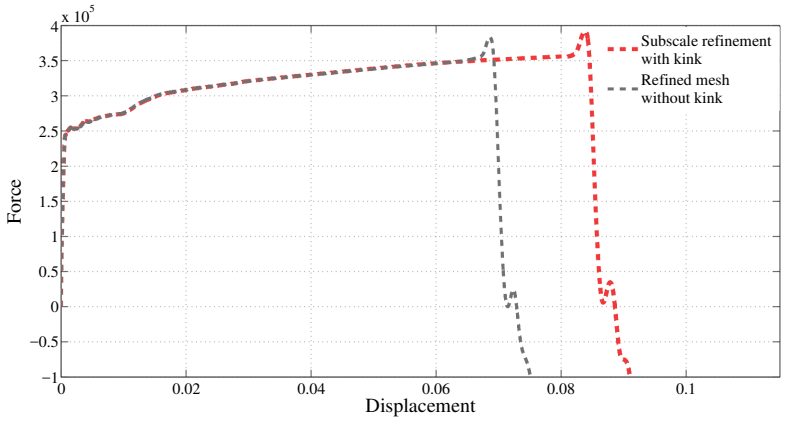

Figure 3.9: Example 3: Force versus displacement diagram measured at upper left corner point both for XFEM with conventional enrichment including no kink and subscale refinement including kink.

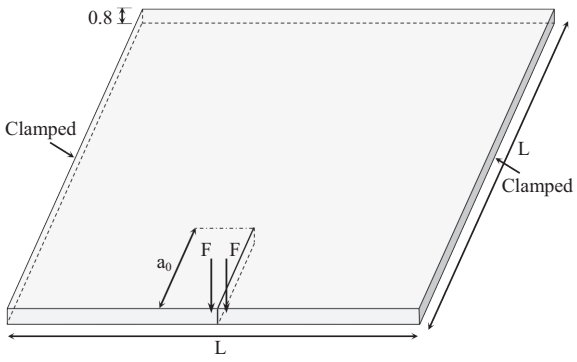

Figure 3.10: Example 4: Geometry and boundary condition of the plate

cases the mesh is unstructured and the type of the elements used is 6-noded triangle, cf. Figure 3.11.

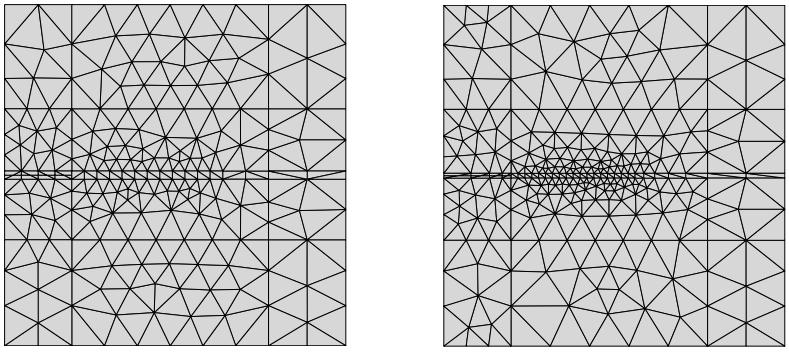

a) b)

Figure 3.11: Boundary conditions for a) a coarse mesh to be used for the simulation by the proposed subscale refinement approach and b) a fine mesh to be used for the simulation by the conventional XFEM.

As in Reference. [11], the values assigned for the fracture energy, and the maximum traction in the cohesive zone are 250 kJ/m^2, and 306 MPa respectively. All other parameters are set as in the introduction of Section 3.4. Employing explicit time integration scheme it is decided to apply a constant velocity of 20 m/s at the tip of the notch rather than the force in the actual experiment which is carried out in a quasi-static manner. In the case of the fine mesh where more elements are furnished along the crack path it is the conventional XFEM used while for the coarse mesh it is the subscale refinement approach employed.

As it is seen in Figure 3.13, due to employing dynamic analysis the force captured at the tip of the notch shows an oscillatory pattern which is caused by the reflection of the stress wave at the boundaries of the domain. However, there is still a good agreement between the numerical results and the experimental result.

It is observed in Reference [11] that edge-to-edge representation of the crack propagation may induce artificial oscillations. In this example a relatively coarse mesh is used for the simulation carried out by the subscale refinement approach. However, the amplitude of the oscillations seen in both fine mesh and coarse mesh is about the same. It shows the potential of the proposed method to obtain an accurate and smooth propagation in a computationally less expensive way.

3.5. CONCLUSIONS

The main message of the present chapter concerns the development of a special type of discontinuity representation for the ductile fracture processes in thin-walled large scale structures subjected to dynamic impact loading. The method does not influence the macroscopic base FE-mesh of the domain and it avoids the introduction of new nodes in the same mesh. This is achieved via a subscale refinement of the continuous and the discontinuous fields com-

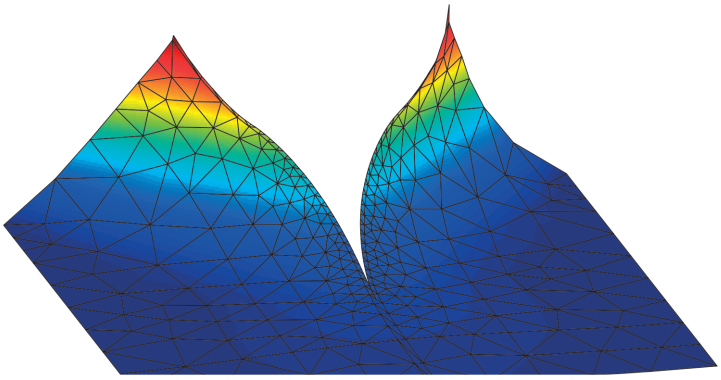

Figure 3.12: Deformed mesh after the crack propagation

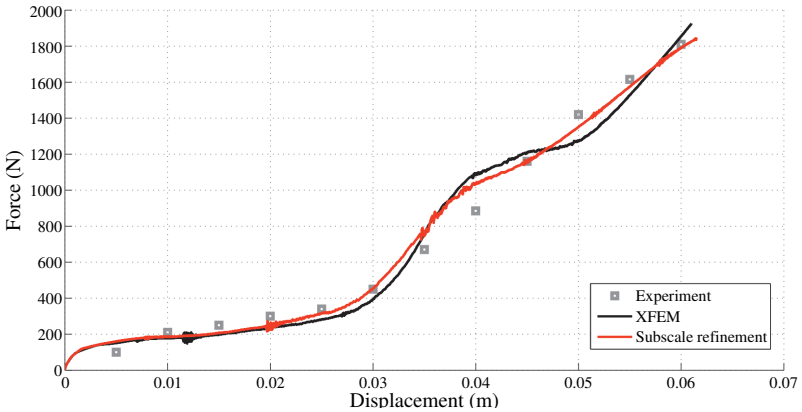

Figure 3.13: Load-deflection curve for the subscale refinement approach and conventional XFEM compared with the experimental result in case of the out-of-plane loaded plate

bined with dynamic condensation of the additional continuous and discontinuous degrees of freedom. In this way, the crack tip is generally not apparent on the structural scale, whereby the crack tip element can be interpreted as a "fracture process zone element" that becomes fully cracked first in the case of being fully penetrated.

The subscale refinement idea has been exemplified through four numerical examples, where it is shown that the concept yields an accurate kinematical representation of kinks and crack tips within an element. The investigations were done for both open (traction free) as well as cohesive zone cracks, describing ductile failure along the crack segments. From the comparison with and without element crack kinks, we showed the relevance of actually resolving the internal crack kink. A significant difference in the load-displacement relation was then obtained due to differences in crack length, crack orientation and mass distribution between the different sides of the crack.

We also note that the subscale treatment of the crack tip ensures the introduction of shorter crack segments (as compared to without the subscale treatment) whenever the propagation criterion is met. This behaviour relates to the observed artificial oscillatory structural response, cf. Reference [11], due to the (inevitable) "segment by segment"-wise imposed crack propagation. Since these oscillations decrease upon mesh refinement, we believe that the subscale refinement method will (in addition to various stabilisation procedures) contribute to reduce such oscillations. To support this, it is shown in the fourth example that using the subscale refinement method one can capture a smooth crack propagation compared to the conventional XFEM even though the mesh used is coarser. This offers an approach to deal with simulation of big structures where usage of coarse mesh is preferable, however accuracy and smoothness of representation of the crack propagation is of high importance.

As an extension of the proposed methodology, it would be possible to include more than one element in the model reduction domain so that the entire process zone, as defined by the cracked elements in which the cohesive zone is still active. There are however computational efficiency aspects of this that need to be considered since the model reduction technique introduces (non-local) couplings between the nodes on the boundary of the considered domain.

To conclude, the steps taken in this chapter are directed towards a balanced computational efficiency and level of detailing in the modelling of larger structures. On the one hand, we want to model and account for the entire thin-walled structure using shell theory. On the other hand, we need to realistically describe the fine scaled nature of the ductile failure process using the proposed elementwise subscale refinement. Clearly, the subscale refined XFEM based shell element increase the detailing of the crack path without having to resort to additional mesh refinement on the structural scale.

REFERENCES

[1] S. Mostofizadeh, M. Fagerström, and R. Larsson, *Xfem-based element subscale refinement for detailed representation of crack propagation in large-scale analyses,* International Journal for Numerical Methods in Engineering **110**, 549 (2017).

[2] P. Areias and T. Belytschko, *Non-linear analysis of shells with arbitrary evolving cracks using xfem,* International Journal for Numerical Methods in Engineering **62**, 384 (2005).

[3] J. Song, P. Areias, and T. Belytschko, *A method for dynamic crack and shear band propagation with phantom nodes,* International Journal for Numerical Methods in Engineering **67**, 868 (2006).

[4] R. Larsson, J. Mediavilla, and M. Fagerström, *Dynamic fracture modeling in shell structures based on XFEM,* International Journal for Numerical Methods in Engineering **86**, 499 (2010).

[5] G. Zi and T. Belytschko, *New crack-tip elements for XFEM and applications to cohesive cracks,* International Journal for Numerical Methods in Engineering **57**, 2221 (2003).

[6] S. Kumar, I. Singh, B. Mishra, and T. Rabczuk, *Modeling and simulation of kinked cracks by virtual node {XFEM},* Computer Methods in Applied Mechanics and Engineering **283**, 1425 (2015).

[7] T.-P. Fries, A. Byfut, A. Alizada, K. W. Cheng, and A. Schröder, *Hanging nodes and xfem,* International Journal for Numerical Methods in Engineering **86**, 404 (2011).

[8] T. Belytschko and T. Black, *Elastic crack growth in finite elements with minimal remeshing,* International Journal for Numerical Methods in Engineering **45**, 601 (1999).

[9] G. Wells and L. Sluys, *A new method for modelling cohesive cracks using finite elements,* International Journal for Numerical Methods in Engineering **50**, 2667 (2001).

[10] T. Menouillard and T. Belytschko, *Smoothed nodal forces for improved dynamic crack propagation modeling in xfem,* International Journal for Numerical Methods in Engineering **84**, 47 (2010).

[11] S. Mostofizadeh, M. Fagerström, and R. Larsson, *Dynamic crack propagation in elasto-plastic thin-walled structures: Modelling and validation,* International Journal for Numerical Methods in Engineering **96**, 63 (2013).

[12] S. Mostofizadeh, M. Fagerström, and R. Larsson, *Dynamic ductile fracture in shells.* 6th European Congress on Computational Methods in Applied Sciences and Engineering (ECCOMAS 2012) , (2012).

[13] A. Hansbo and P. Hansbo, *An unfitted finite element method, based on Nitsche's method, for elliptic interface problems,* Computer Methods in Applied Mechanics and Engineering **191**, 5537 (2002).

[14] M. Bischoff and E. Ramm, *On the physical significance of higher order kinematic and static variables in a three-dimensional shell formulation,* International Journal of Solids and Structures **37**, 6933 (2000).

[15] G. Wells, R. de Borst, and L. Sluys, *A consistent geometrically non-linear approach for delamination,* International Journal for Numerical Methods in Engineering **54**, 1333 (2002).

[16] M. Fagerström and R. Larsson, *Approaches to dynamic fracture modelling at finite deformations,* Journal of the Mechanics and Physics of Solids **56**, 613 (2008).

[17] J. J. Remmers, R. de Borst, and A. Needleman, *The simulation of dynamic crack propagation using the cohesive segments method,* Journal of the Mechanics and Physics of Solids **56**, 70 (2008).

[18] G. Ljustina, M. Fagerström, and R. Larsson, *Hypo-and hyper-inelasticity applied to modeling of compacted graphite iron machining simulations,* European Journal of Mechanics-A/Solids **37**, 57 (2013).

[19] G. Johnson and W. Cook, *Fracture characteristics of three metals subjected to various strains, strain rates, temperatures and pressures,* Engineering Fracture Mechanics **21**, 31 (1985).

[20] M. Fagerström and R. Larsson, *Theory and numerics for finite deformation fracture modelling using strong discontinuities,* International Journal for Numerical Methods in Engineering **66**, 911 (2006).

[21] C. Muscat-Fenech and A. Atkins, *Out-of-plane stretching and tearing fracture in ductile sheet materials,* International journal of fracture **84**, 297 (1997).

4

AN ELEMENT SUBSCALE REFINEMENT FOR REPRESENTATION OF THE PROGRESSIVE FRACTURE BASED ON THE PHANTOM NODE APPROACH

A new approach for the analysis of the ductile fracture of thin-walled large scale structures is developed. The method proposes a subscale refinement of the elements containing the crack. It allows for smooth progression of the crack without furnishing required level of the mesh refinement, and a more detailed representation of the crack tip and crack kink within the cracked elements. This approach is based on the phantom node method and is intended to be applicable for different types of elements including both low and high order elements. Numerical examples for dynamic crack propagation are presented and compared to conventional solutions to prove the accuracy and effectiveness of the proposed approach.

This chapter was integrally extracted from [1].

4.1. INTRODUCTION

Thin-walled structures are widely used for different applications, such as maritime structures, off-shore structures, and aircraft fuselages. These various engineering applications call for a reliable methodology to predict their failure under different loading conditions. One of the main challenges of such a problem is to find a methodology to analyse the ductile failure of large-structures using shell theory. In this respect a complexity addressed in the current chapter is accounting for the fine scale of ductile failure.

Analysing large-scale thin-walled structures requires sufficient level of mesh refinement to maintain a high degree of accuracy in the results. However, mesh refinement inherently adds to the cost of the computation. Therefore, there is a need for a methodology that simplifies such analyses, and yet includes the required level of detail in the model. In line with developments by Rabczuk *et al.*[2] and Mostofizadeh *et al.*[3], we propose herein a method to ensure smoothness and accuracy of the crack propagation without requiring a high degree of mesh refinement. A new crack tip element based on the phantom node method [4] is presented which brings in the possibility to represent the growth of a crack through a single element in multiple steps using a subscale refinement. The current approach bears similarity to the developments by Zi and Belytschko [5], Chau-Dinh *et al.*[6] and Xiao and Karihaloo [7]. However, in the current method the treatment of the crack kinks internal to the element can also be represented which is an addition to the previous developments. The method is applicable to different type of elements with both low and high order approximations and it does not require any change in the spatial discretisation of the neighbouring elements which leads to less degree of mesh refinement.

The chapter is outlined as follows. In Section 4.2, the subscale refinement of a crack tip element based on the phantom node method is described. In Section 4.3, the formulation is extended to shell theory. In Section 4.4, the continuum material model and interface material model are summarised. In Section 4.5, numerical results are verified and compared with the results obtained from the conventional phantom node method. Finally, the chapter is concluded in Section 4.6, where conclusions are discussed.

4.2. SUBSCALE REFINEMENT OF DISPLACEMENT FIELD

In this section, the subscale refinement of the crack tip element based on the phantom node method will be presented. The underlying concept of this method is to enhance the representation of the kinematics of the discontinuity with a subscale refinement. That is, additional degrees of freedom are added on the subscale level of the cracked element. The conformity of this additional field is imposed with Dirichlet boundary condition on the boundary nodes of the subscale problem.

Below, a review of the phantom node method will be given, followed by the details of the subscale refinement of the crack tip element. It should be emphasised that we herein consider standard Phantom node kinematical relations for a 2D continuum with cracks, although presented in a somewhat non-standard format to provide a basis for the subsequent application to shell problems in Section 4.3.

4.2.1. A REVIEW ON THE PHANTOM NODE METHOD

To set the stage, we introduce three configurations: the reference (or inertial) cartesian configuration $\mathscr{B}$, the undeformed (material) configuration B_0 and the deformed (spatial) configuration B as indicated in Figure 4.1. In this framework, any material point (in 2D) $\mathbf{X} = (X_1, X_2)$

in the undeformed configuration is related to a point in the intertial configuration $\boldsymbol{\xi} = (\xi_1, \xi_2)$ via the mapping

$$\mathbf{X} = \boldsymbol{\Phi}[\boldsymbol{\xi}]. \tag{4.1}$$

Similarly, any point $\mathbf{x} = (x_1, x_2)$ in the deformed configuration relates to the point $\boldsymbol{\xi}$ in the inertial configuration via the (time-dependent) mapping from the inertial to the deformed configuration, herein denoted as the placement, as

$$\mathbf{x} = \boldsymbol{\varphi}[\boldsymbol{\xi}, t]. \tag{4.2}$$

Analysing problems that concern strong and weak discontinuities, such as cracks, and shear bands, poses a modelling challenge. In the conventional finite element method, accuracy of the approximation field is maintained provided that the field of approximation is sufficiently smooth and continuous. In case of presence of a crack within an element, the displacement field is continuous on each side of the crack, while it is discontinuous across it. Exploiting the partition of unity concept, cf. Melenk and Babuška [8], this has been treated in the eXtended Finite Element Method (XFEM), pioneered by Belytschko and Black [9] and Moës *et al.* [10], by enriching the approximation function with additional bases allowing for the representation of discontinuities. However, depending on the enrichment function employed, neighbouring elements may require changes to be made.

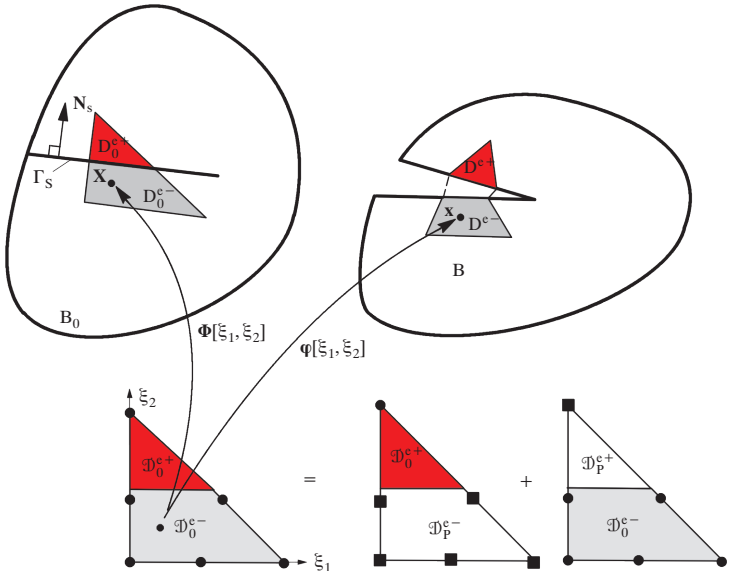

Figure 4.1: A domain containing a crack in which the displacement jump is described by the phantom node method - the solid circles represent real nodes and the solid squares represent phantom nodes.

An alternative approach, the phantom node method, has been proposed by Hansbo and Hansbo [4]. In terms of the represented kinematics, the phantom node method is identical to XFEM [11], but it enjoys an easier implementation. In the current approach, rather than adding additional degrees of freedom as in XFEM, a jump in the displacement field is realised

with overlapping elements as indicated in the bottom of Figure 4.1. Each of these elements, whose support is partially active, represents the displacement field on one side of the crack. It requires the integrations to be carried out only partially, on the active support of the overlapping elements.

Now, consider a discretised cracked body as in Figure 4.1, and particularly a subdomain (equal to an element) cut by the crack. In the material configuration, this subdomain (element), denoted D_0^e, is decomposed into a plus side, D_0^{e+}, and a minus side, D_0^{e-}, on either side of the discontinuity surface, Γ_S with normal $\mathbf{N}_S$. As for the mapping $\boldsymbol{\Phi}$, it can then be approximated in a standard isoparametric[1] fashion, irrespectively if it is cut by a crack or not, as

$$\boldsymbol{\Phi}^{h,e} = \sum_{i \in I} N^i[\xi_1, \xi_2] \hat{\mathbf{X}}^i \tag{4.3}$$

where N^i are shape functions associated with the set of nodes I belonging to the plus side[2] element and $\hat{\mathbf{X}}^i$ are their coordinates.

As for the mapping from the inertial to the current configuration, it is approximated as

$$\boldsymbol{\varphi}^{h,e} = \sum_{i \in I} N^i[\xi_1, \xi_2] \hat{\boldsymbol{\varphi}}^i H_S[S[\mathbf{X}]] + \sum_{j \in J} N^j[\xi_1, \xi_2] \hat{\boldsymbol{\varphi}}^j H_S[-S[\mathbf{X}]] \tag{4.4}$$

where in addition to N^i we have introduced N^j as the shape functions associated with the set of nodes J belonging to the minus side element, and $\hat{\boldsymbol{\varphi}}^i$ and $\hat{\boldsymbol{\varphi}}^j$ are placement fields associated with the plus and minus side element. Therein $S[\mathbf{X}]$ is the level set function defining the position of the discontinuity line where $S[\mathbf{X}] = 0$. H_S, is the classical Heaviside function, which returns one for positive values and zero for negative values.

The jump in the placement field at a point $\mathbf{x} \in \Gamma_S$ is given as

$$[\![\boldsymbol{\varphi}^{h,e}]\!] = \sum_{i \in I} N^i \hat{\boldsymbol{\varphi}}^i - \sum_{j \in J} N^j \hat{\boldsymbol{\varphi}}^j \tag{4.5}$$

Given that the continuous placement field is at hand, the deformation gradient pertinent to the bulk material, $\mathbf{F}_b$, is defined as follows

$$\mathbf{F}_b = \boldsymbol{\varphi} \otimes \nabla_{\mathbf{X}} = \quad \forall \mathbf{X} \in B_0 \setminus \Gamma_S \tag{4.6}$$

Neglecting the body force and utilising the displacement field as already stated, the weak form of the momentum balance becomes

$$\int_{B_0} \rho_0 \delta\boldsymbol{\varphi} \cdot \ddot{\boldsymbol{\varphi}} \mathrm{dV} = \int_{\partial B_0} \delta\boldsymbol{\varphi} \cdot \bar{\mathbf{t}}_1 \mathrm{dA} - \int_{B_0} \delta {\mathbf{F}_b}^t : \mathbf{P}^t \mathrm{dV} + \int_{\Gamma_S} [\![\delta\boldsymbol{\varphi}]\!] \cdot \mathbf{t}_1 \mathrm{dA}, \quad \forall\, \delta\boldsymbol{\varphi} \tag{4.7}$$

in which $\mathbf{P}^t$ is the first Piola Kirchhoff stress tensor. Therein, the prescribed nominal traction vector along the boundary (with normal $\mathbf{N}$) and the cohesive traction along the crack surface are respectively $\bar{\mathbf{t}}_1 = \mathbf{P}^t \cdot \mathbf{N}$ and $\mathbf{t}_1 = \mathbf{P}^t \cdot \mathbf{N}_S$.

[1] To make it clear: even though we in the continuous case consider three different configurations and a unique one-to-one mapping between a point $\boldsymbol{\xi}$ in the inertial configuration and a point $\mathbf{X}$ in the undeformed configuration, we consider for simpler implementation of the discretised case a single parent element (with local coordinates) in the inertial configuration.

[2] One can just as well consider the minus side element since, for both these elements, the nodal coordinates in B_0 will be the same.

4.2.2. SPATIAL DISCRETISATION BASED ON THE SUBSCALE REFINEMENT OF THE PHANTOM NODE METHOD

In order to allow for a more detailed representation of the discontinuity in cracked elements, a method is proposed wherein refinement of the discontinuity is realised via additional nodes and degrees of freedom within the domain of interest. This accommodates the possibility to represent kinks and crack tips within several subscale elements inside the macroscale element. To avoid introduction of new nodes on the macroscale level, this refinement is carried out in conjunction with a model reduction technique, *i.e.* dynamic condensation. There are other

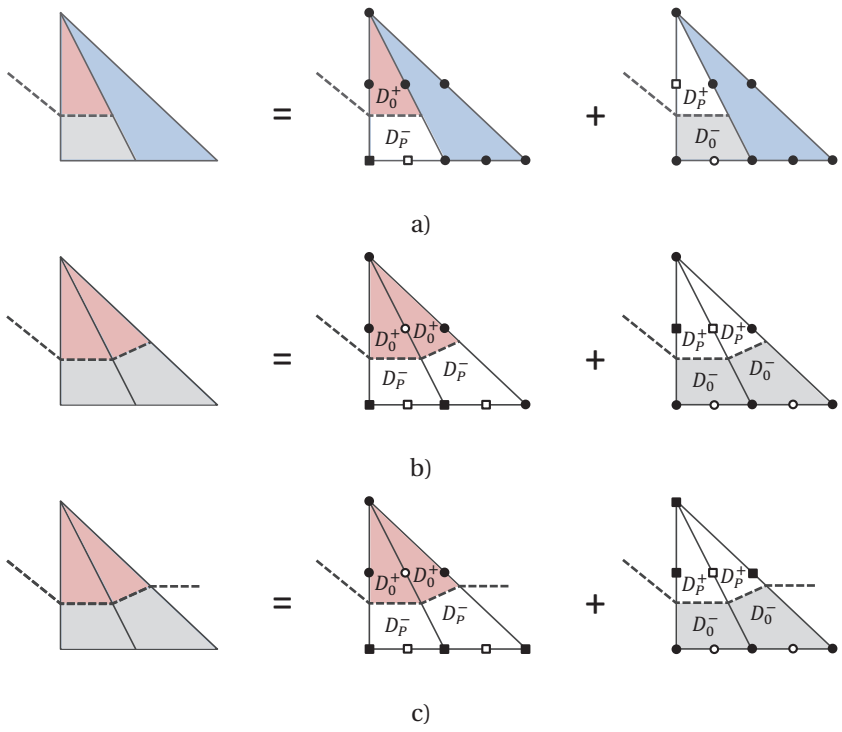

Figure 4.2: Progression of crack within an element based on the subscale refined phantom node method: Crack ends inside the element (a), Crack ends at the element edge (b), Crack crosses the element edge (c) - Solid and empty circles represent macro-scale and subscale nodes on the original support and solid and empty squares represent macro-scale and subscale nodes on the phantom support respectively.

methods, cf. Rabczuk *et al.*[2], to treat cracks which end inside the element, however, these methods are only applicable to linear elements. We propose an alternative method applicable to any type of element, however for sake of briefness only triangular elements are discussed in this chapter.

The current approach considers the cracked element as a subscale problem, wherein the domain of the macroscale element is divided into sub-domains according to the progression of the crack within the element. In the subscale problem, each of these sub-domains is re-

garded as an element whose nodes consist of the macroscale nodes on the boundary of the macroscale element and additional subscale nodes introduced to the subscale problem, cf. Figure 4.2. Once the crack propagates into the element, the subscale element whose support is cracked will be doubled as in the conventional phantom node method. In order to enforce continuity at the crack tip, nodes along the edge of the subscale element, where the crack tip is located on, will not be doubled.

Considering the Figure 4.2, based on the failure criterion and length and direction of progression of the crack, the subscale domain is partitioned into a number of subscale elements - in this case two elements - to represent the discontinuity path. Shape functions utilised for interpolations, N^i, are limited in terms of their support to the domain of each subscale elements. Thereby, on the element level, the approximation of the deformation map becomes

$$\boldsymbol{\varphi}^{h,e} = \sum_{i\in I} N^i \hat{\boldsymbol{\varphi}}^i H_S[S[\mathbf{X}]] + \sum_{j\in J} N^j \hat{\boldsymbol{\varphi}}^j H_S[S[\mathbf{X}]] + \sum_{k\in K} N^k \hat{\boldsymbol{\varphi}}^k H_S[-S[\mathbf{X}]] + \sum_{l\in L} N^l \hat{\boldsymbol{\varphi}}^l H_S[-S[\mathbf{X}]] \tag{4.8}$$

where N^i and N^j are shape functions of the plus side elements associated with macroscale, I, and subscale, J, sets of nodes respectively, and N^k and N^l are also shape functions of the minus side elements associated with macroscale, K, and subscale, L, sets of nodes respectively. It may also be described as

$$\boldsymbol{\varphi}^{h,e} = \hat{\mathbf{N}}^m_{H^p_S}\,\hat{\boldsymbol{\varphi}}^{m,e}_p + \hat{\mathbf{N}}^f_{H^p_S}\,\hat{\boldsymbol{\varphi}}^{f,e}_p + \hat{\mathbf{N}}^m_{H^m_S}\,\hat{\boldsymbol{\varphi}}^{m,e}_m + \hat{\mathbf{N}}^f_{H^m_S}\,\hat{\boldsymbol{\varphi}}^{f,e}_m = \hat{\mathbf{N}}^m\,\hat{\boldsymbol{\varphi}}^{m,e} + \hat{\mathbf{N}}^f\,\hat{\boldsymbol{\varphi}}^{f,e} \tag{4.9}$$

where $\hat{\mathbf{N}}^m_{H^p_S}$ and $\hat{\mathbf{N}}^f_{H^p_S}$, are shape functions associated with macro-scale nodes and subscale nodes located on the plus side, while $\hat{\mathbf{N}}^m_{H^m_S}$ and $\hat{\mathbf{N}}^f_{H^m_S}$ are the corresponding vectors evaluated on the minus side of the crack. Thereafter, for sake of simplicity the following substitutions are made

$$\hat{\mathbf{N}}^m = [\hat{\mathbf{N}}^m_{H^p_S}, \hat{\mathbf{N}}^m_{H^m_S}],\ \hat{\mathbf{N}}^f = [\hat{\mathbf{N}}^f_{H^p_S}, \hat{\mathbf{N}}^f_{H^m_S}],\ \hat{\boldsymbol{\varphi}}^{m,e} = \begin{bmatrix} \hat{\boldsymbol{\varphi}}^{m,e}_p \\ \hat{\boldsymbol{\varphi}}^{m,e}_m \end{bmatrix},\ \hat{\boldsymbol{\varphi}}^{f,e} = \begin{bmatrix} \hat{\boldsymbol{\varphi}}^{f,e}_p \\ \hat{\boldsymbol{\varphi}}^{f,e}_m \end{bmatrix} \tag{4.10}$$

Accordingly the approximations of the deformation gradient in terms of the bulk material is defined as

$$\begin{aligned} \mathbf{F}^{h,e}_b = &\sum_{i\in I} H_S[S[\mathbf{X}]]\,\hat{\boldsymbol{\varphi}}^i \left(\frac{\partial N^i}{\partial \mathbf{X}}\right)^t + \sum_{j\in J} H_S[S[\mathbf{X}]]\,\hat{\boldsymbol{\varphi}}^j \left(\frac{\partial N^j}{\partial \mathbf{X}}\right)^t + \\ &\sum_{k\in K} H_S[-S[\mathbf{X}]]\,\hat{\boldsymbol{\varphi}}^k \left(\frac{\partial N^k}{\partial \mathbf{X}}\right)^t + \sum_{l\in L} H_S[-S[\mathbf{X}]]\,\hat{\boldsymbol{\varphi}}^l \left(\frac{\partial N^l}{\partial \mathbf{X}}\right)^t \end{aligned} \tag{4.11}$$

Employing Voigt notation and Galerkin's method, virtual displacement fields become

$$\delta\boldsymbol{\varphi}^{h,e} = \hat{\mathbf{N}}^m_{H^p_S}\,\delta\hat{\boldsymbol{\varphi}}^{m,e}_p + \hat{\mathbf{N}}^f_{H^p_S}\,\delta\hat{\boldsymbol{\varphi}}^{f,e}_p + \hat{\mathbf{N}}^m_{H^m_S}\,\delta\hat{\boldsymbol{\varphi}}^{m,e}_m + \hat{\mathbf{N}}^f_{H^m_S}\,\delta\hat{\boldsymbol{\varphi}}^{f,e}_m = \hat{\mathbf{N}}^m\,\delta\hat{\boldsymbol{\varphi}}^{m,e} + \hat{\mathbf{N}}^f\,\delta\hat{\boldsymbol{\varphi}}^{f,e} \tag{4.12}$$

$$[\![\delta\boldsymbol{\varphi}^{h,e}]\!] = \hat{\mathbf{N}}^m_{H^p_S}\,\delta\hat{\boldsymbol{\varphi}}^{m,e}_p + \hat{\mathbf{N}}^f_{H^p_S}\,\delta\hat{\boldsymbol{\varphi}}^{f,e}_p - \hat{\mathbf{N}}^m_{H^m_S}\,\delta\hat{\boldsymbol{\varphi}}^{m,e}_m - \hat{\mathbf{N}}^f_{H^m_S}\,\delta\hat{\boldsymbol{\varphi}}^{f,e}_m = \hat{\mathbf{N}}^m_d\,\delta\hat{\boldsymbol{\varphi}}^{m,e} + \hat{\mathbf{N}}^f_d\,\delta\hat{\boldsymbol{\varphi}}^{f,e} \tag{4.13}$$

$$\delta\hat{\mathbf{F}}^{h,e}_b = \hat{\mathbf{B}}^m_{H^p_S}\,\delta\hat{\boldsymbol{\varphi}}^{m,e}_p + \hat{\mathbf{B}}^f_{H^p_S}\,\delta\hat{\boldsymbol{\varphi}}^{f,e}_p + \hat{\mathbf{B}}^m_{H^m_S}\,\delta\hat{\boldsymbol{\varphi}}^{m,e}_m + \hat{\mathbf{B}}^f_{H^m_S}\,\delta\hat{\boldsymbol{\varphi}}^{f,e}_m = \hat{\mathbf{B}}^m\,\delta\hat{\boldsymbol{\varphi}}^{m,e} + \hat{\mathbf{B}}^f\,\delta\hat{\boldsymbol{\varphi}}^{f,e} \tag{4.14}$$

Therein $\hat{\mathbf{B}}^m_{H^p_S}$ and $\hat{\mathbf{B}}^f_{H^p_S}$, are introduced as derivatives of shape functions associated with macroscale nodes and subscale nodes of the element that is active on the plus side, and $\hat{\mathbf{B}}^m_{H^m_S}$ and $\hat{\mathbf{B}}^f_{H^m_S}$, are similar quantities, associated with nodes of the element active on the minus side. There the following substitutions are also made

$$\hat{\mathbf{N}}^m_d = [\hat{\mathbf{N}}^m_{H^p_S}, -\hat{\mathbf{N}}^m_{H^m_S}],\ \hat{\mathbf{N}}^f_d = [\hat{\mathbf{N}}^f_{H^p_S}, -\hat{\mathbf{N}}^f_{H^m_S}],\ \hat{\mathbf{B}}^m = [\hat{\mathbf{B}}^m_{H^p_S}, \hat{\mathbf{B}}^m_{H^m_S}],\ \hat{\mathbf{B}}^f = [\hat{\mathbf{B}}^f_{H^p_S}, \hat{\mathbf{B}}^f_{H^m_S}] \tag{4.15}$$

Employing the aforementioned variational field into Eq. (4.7), the contribution of the cracked elements to the discretised form of the momentum balance becomes

$$\begin{bmatrix} \mathbf{M}^e_{mm} & \mathbf{M}^e_{mf} \\ \mathbf{M}^e_{fm} & \mathbf{M}^e_{ff} \end{bmatrix} \begin{bmatrix} \hat{\boldsymbol{a}}^e_m \\ \hat{\boldsymbol{a}}^e_f \end{bmatrix} = \begin{bmatrix} \mathbf{f}^{e,ext}_m - \mathbf{f}^{e,int}_m + \mathbf{f}^{e,coh}_m \\ -\mathbf{f}^{e,int}_f + \mathbf{f}^{e,coh}_f \end{bmatrix} \tag{4.16}$$

where

$$\hat{\boldsymbol{a}}^e_m = \frac{\partial^2 \hat{\boldsymbol{\varphi}}^{m,e}}{\partial t^2},\ \hat{\boldsymbol{a}}^e_f = \frac{\partial^2 \hat{\boldsymbol{\varphi}}^{f,e}}{\partial t^2} \tag{4.17}$$

Therein, the contributions from mass, external force, internal force, and cohesive force are

$$\mathbf{M}^e_{mm} = \int_{D^{e^+}_0} \rho_0 (\hat{\mathbf{N}}^m_{H^p_S})^t \hat{\mathbf{N}}^m_{H^p_S}\, \mathrm{dV} + \int_{D^{e^-}_0} \rho_0 (\hat{\mathbf{N}}^m_{H^m_S})^t \hat{\mathbf{N}}^m_{H^m_S}\, \mathrm{dV} \tag{4.18}$$

$$\mathbf{M}^e_{mf} = \left(\mathbf{M}^e_{fm}\right)^t = \int_{D^{e^+}_0} \rho_0 (\hat{\mathbf{N}}^m_{H^p_S})^t \hat{\mathbf{N}}^f_{H^p_S}\, \mathrm{dV} + \int_{D^{e^-}_0} \rho_0 (\hat{\mathbf{N}}^m_{H^m_S})^t \hat{\mathbf{N}}^f_{H^m_S}\, \mathrm{dV} \tag{4.19}$$

$$\mathbf{M}^e_{ff} = \int_{D^{e^+}_0} \rho_0 (\hat{\mathbf{N}}^f_{H^p_S})^t \hat{\mathbf{N}}^f_{H^p_S}\, \mathrm{dV} + \int_{D^{e^-}_0} \rho_0 (\hat{\mathbf{N}}^f_{H^m_S})^t \hat{\mathbf{N}}^f_{H^m_S}\, \mathrm{dV} \tag{4.20}$$

$$\mathbf{f}^{e,ext}_m = \int_{\partial D^{e^+}_0} (\hat{\mathbf{N}}^m_{H^p_S})^t \bar{\mathbf{t}}_1\, \mathrm{dA} + \int_{\partial D^{e^-}_0} (\hat{\mathbf{N}}^m_{H^m_S})^t \bar{\mathbf{t}}_1\, \mathrm{dA} \tag{4.21}$$

$$\mathbf{f}^{e,int}_m = \int_{D^{e^+}_0} (\hat{\mathbf{B}}^m_{H^p_S})^t \hat{\mathbf{P}}^t\, \mathrm{dV} + \int_{D^{e^-}_0} (\hat{\mathbf{B}}^m_{H^m_S})^t \hat{\mathbf{P}}^t\, \mathrm{dV} \tag{4.22}$$

$$\mathbf{f}^{e,int}_f = \int_{D^{e^+}_0} (\hat{\mathbf{B}}^f_{H^p_S})^t \hat{\mathbf{P}}^t\, \mathrm{dV} + \int_{D^{e^-}_0} (\hat{\mathbf{B}}^f_{H^m_S})^t \hat{\mathbf{P}}^t\, \mathrm{dV} \tag{4.23}$$

$$\mathbf{f}^{e,coh}_m = \int_{\Gamma^e_S} (\hat{\mathbf{N}}^m_{H^p_S})^t \mathbf{t}_1\, \mathrm{dA} - \int_{\Gamma^e_S} (\hat{\mathbf{N}}^m_{H^m_S})^t \mathbf{t}_1\, \mathrm{dA} \tag{4.24}$$

$$\mathbf{f}^{e,coh}_f = \int_{\Gamma^e_S} (\hat{\mathbf{N}}^f_{H^p_S})^t \mathbf{t}_1\, \mathrm{dA} - \int_{\Gamma^e_S} (\hat{\mathbf{N}}^f_{H^m_S})^t \mathbf{t}_1\, \mathrm{dA} \tag{4.25}$$

where subscript $\mathbf{M}$ and $\mathbf{f}$, in force and mass contributions, denote macroscale and subscale degrees of freedom respectively, and also $D^{e^+}_0$ and $D^{e^-}_0$ denote parts of the plus and minus side elements that belong to the original domain adjacent to the crack.

4.2.3. SCALE COUPLING USING DYNAMIC CONDENSATION

For the time integration, a central difference time integration method is employed. Thereby, in every time step the current configuration is updated using the accelerations, $\hat{\boldsymbol{a}}$, found in

$$\mathbf{M}\,\hat{\boldsymbol{a}} = \mathbf{f} \tag{4.26}$$

where **M** and **f** are mass matrix and unbalance force vectors.

In the current proposed approach for the sub-scale refinement of the crack tip element, there are two scales each of which has a separate time integration schemes and spatial discretisation. The coupling between the two scales is realised by applying the boundary condition from the macro-scale problem to the sub-scale one. In order to separate sub-scale from macro-scale, it is opted to employ dynamic condensation technique, by which, the subscale degrees of freedom may be solved.

COUPLING AND KINEMATIC CONSTRAINTS

To ensure conformity of the boundaries between two scales, it is required to constrain the additional subscale nodes positioned on the sub-scale boundary using a kinematic constraint. For this, the constraint may be established utilising constraint matrix, **P**, which relates the full set of degrees of freedom in the sub-scale elements $\hat{\boldsymbol{a}}^e$ to the reduced set of degrees of freedom present on the macro-scale element $\hat{\hat{\boldsymbol{a}}}^e$ as

$$\hat{\boldsymbol{a}}^e = \mathbf{P}\,\hat{\hat{\boldsymbol{a}}}^e \tag{4.27}$$

where **P** consist of all basis functions of the macro-scale element including linear relation of the ones required to interpolate for the subscale nodes on the boundary, $\hat{\boldsymbol{a}}^e = [\hat{\boldsymbol{a}}^e_m, \hat{\boldsymbol{a}}^e_c, \hat{\boldsymbol{a}}^e_f]^T$ and $\hat{\hat{\boldsymbol{a}}}^e = [\hat{\boldsymbol{a}}^e_m, \hat{\boldsymbol{a}}^e_f]^T$. Therefore Eq. (4.26) can be rewritten with three types of degrees of freedom now as

$$\begin{bmatrix} \mathbf{M}^e_{mm} & \mathbf{M}^e_{mc} & \mathbf{M}^e_{mf} \\ \mathbf{M}^e_{cm} & \mathbf{M}^e_{cc} & \mathbf{M}^e_{cf} \\ \mathbf{M}^e_{fm} & \mathbf{M}^e_{fc} & \mathbf{M}^e_{ff} \end{bmatrix} \begin{bmatrix} \hat{\boldsymbol{a}}^e_m \\ \hat{\boldsymbol{a}}^e_c \\ \hat{\boldsymbol{a}}^e_f \end{bmatrix} = \begin{bmatrix} \mathbf{f}^e_m \\ \mathbf{f}^e_c \\ \mathbf{f}^e_f \end{bmatrix} \tag{4.28}$$

where subscripts m, c, and f denote macro-scale dofs, constrained subscale dofs, and free subscale dofs respectively as illustrated in the Figure 4.3.

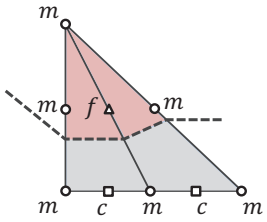

Figure 4.3: Illustration of different types of nodes namely macro-scale node (m), constrained subscale node (c) and free subscale node (f).

Employing the constraint matrix, **P**, with the same constraints enforced also on the corresponding virtual displacement field, Eq. (4.28) can be reformulated as

$$\mathbf{P}^T \begin{bmatrix} \mathbf{M}^e_{mm} & \mathbf{M}^e_{mc} & \mathbf{M}^e_{mf} \\ \mathbf{M}^e_{cm} & \mathbf{M}^e_{cc} & \mathbf{M}^e_{cf} \\ \mathbf{M}^e_{fm} & \mathbf{M}^e_{fc} & \mathbf{M}^e_{ff} \end{bmatrix} \mathbf{P} \begin{bmatrix} \hat{\boldsymbol{a}}^e_m \\ \hat{\boldsymbol{a}}^e_f \end{bmatrix} = \mathbf{P}^T \begin{bmatrix} \mathbf{f}^e_m \\ \mathbf{f}^e_c \\ \mathbf{f}^e_f \end{bmatrix} \tag{4.29}$$

which results in the reduced form of Eq. (4.29) as

$$\begin{bmatrix} \tilde{\mathbf{M}}^e_{mm} & \tilde{\mathbf{M}}^e_{mf} \\ \tilde{\mathbf{M}}^e_{fm} & \tilde{\mathbf{M}}^e_{ff} \end{bmatrix} \begin{bmatrix} \hat{\boldsymbol{a}}^e_m \\ \hat{\boldsymbol{a}}^e_f \end{bmatrix} = \begin{bmatrix} \tilde{\mathbf{f}}^e_m \\ \tilde{\mathbf{f}}^e_f \end{bmatrix} \tag{4.30}$$

DYNAMIC CONDENSATION

In order to obtain the element mass and force contribution to Eq. (4.26) considering only macroscopic degrees of freedom, the discretised momentum balance in Eq. (4.30) needs to be condensed into

$$\mathbf{M}^e_m \hat{\boldsymbol{a}}^e_m = \mathbf{f}^{e,ext}_m - \tilde{\mathbf{f}}^{e,int}_m \tag{4.31}$$

utilising

$$\mathbf{M}^e_m = \tilde{\mathbf{M}}^e_{mm} - \tilde{\mathbf{M}}^e_{mf} {\tilde{\mathbf{M}}^e_{ff}}^{-1} \tilde{\mathbf{M}}^e_{fm} \tag{4.32}$$

$$\tilde{\mathbf{f}}^{e,int}_m = \tilde{\mathbf{f}}^{e,int}_m - \tilde{\mathbf{f}}^{e,coh}_m - \tilde{\mathbf{M}}^e_{mf} {\tilde{\mathbf{M}}^e_{ff}}^{-1} \left(\tilde{\mathbf{f}}^{e,int}_f - \tilde{\mathbf{f}}^{e,coh}_f \right) \tag{4.33}$$

which are given via solving for acceleration of subscale dofs employing the central difference method for the sub-scale problem as

$$\hat{\boldsymbol{a}}^e_f = {\tilde{\mathbf{M}}^e_{ff}}^{-1} \left(-\tilde{\mathbf{M}}^e_{fm} \hat{\boldsymbol{a}}^e_m - \tilde{\mathbf{f}}^{e,int}_f + \tilde{\mathbf{f}}^{e,coh}_f \right). \tag{4.34}$$

4.3. APPLICATION OF SUBSCALE REFINEMENT TO SHELLS

With respect to the main application of this development which is dynamic ductile fracture of the thin-walled structures, the 7-parameter shell formulation employed in [12] is extended based on the phantom node method. Therein the current approach for the representation of the discontinuity within the crack tip element is addressed accordingly. The element formulation will be described in this section. For this, we start off on the initial and current shell geometry, which will be then followed by the spatial discretisation of the subscale refinement. For sake of briefness the weak form of the momentum balance is covered in the Appendix C.1.

4.3.1. INITIAL SHELL GEOMETRY IN TERMS OF CONVECTED COORDINATES

As described in [13] and [12], and demonstrated in Figure 4.4, the initial configuration B_0 of the shell is introduced in terms of the convected coordinates (ξ_1, ξ_2, ξ) as

$$\begin{aligned} \mathrm{B}_0 = \big\{ \mathbf{X} = \boldsymbol{\Phi}_0[\xi_1,\xi_2,\xi] = \bar{\boldsymbol{\Phi}}[\xi_1,\xi_2] + \xi \mathbf{M}_\Phi[\xi_1,\xi_2] \\ \text{with } [\xi_1,\xi_2] \in A \text{ and } \xi \in \tfrac{h_0}{2}[-1,1] \big\} \end{aligned} \tag{4.35}$$

where $\Phi_0[\xi_1,\xi_2,\xi]$ defines the mapping from the inertial Cartesian frame to the reference configuration and is specified in terms of the midsurface placement $\bar{\boldsymbol{\Phi}}[\xi_1,\xi_2]$, the outward unit normal vector field $\mathbf{M}_\Phi$ (with $|\mathbf{M}_\Phi| = 1$) and coordinate ξ, as in Figure 4.4. The coordinate ξ is defined in the direction of $\mathbf{M}_\Phi$ using h_0 as the initial thickness of the shell. The co-variant basis vectors are defined as

$$\mathbf{G}_\alpha = \boldsymbol{\Phi}_{,\alpha} + \xi \mathbf{M}_{\Phi,\alpha},\ \alpha = 1,2 \text{ and } \mathbf{G}_3 = \mathbf{G}^3 = \mathbf{M}_\Phi. \tag{4.36}$$

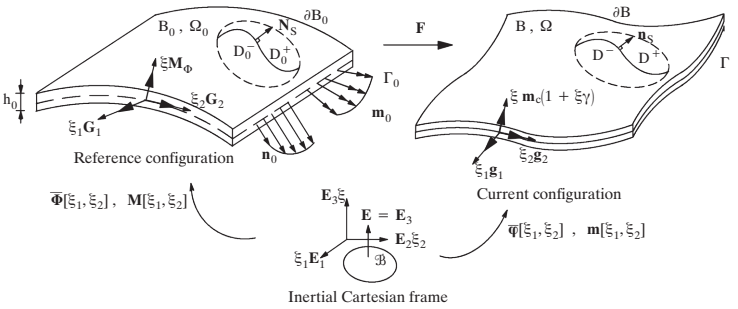

Figure 4.4: Mappings of 7-parameter shell model defining undeformed and deformed shell configurations relative to the inertial Cartesian frame.

where $\bullet_{,\alpha}$ denotes the derivative with respect to ξ_α. The co-variant vectors $\mathbf{G}_i$ and the contra-variant basis vectors $\mathbf{G}^i$ are correlated via $\mathbf{G}_i \otimes \mathbf{G}^i = \mathbf{1}$, which results in

$$\mathbf{G}_j = G_{\mathrm{ij}}\mathbf{G}^i \,,\, \mathbf{G}^j = G^{\mathrm{ij}}\mathbf{G}_i \text{ with } G_{\mathrm{ij}} = \mathbf{G}_i \cdot \mathbf{G}_j \text{ and } G^{\mathrm{ij}} = \left(G_{\mathrm{ij}}\right)^{-1} \tag{4.37}$$

The infinitesimal volume element $\mathrm{d}B_0$ in the reference configuration can also be defined in the convected coordinates as

$$\mathrm{d}B_0 = b_0 \mathrm{d}\xi_1 \mathrm{d}\xi_2 \mathrm{d}\xi \text{ with } b_0 = (\mathbf{G}_1 \times \mathbf{G}_2) \cdot \mathbf{G}^3 \tag{4.38}$$

4.3.2. DISCONTINUOUS CURRENT SHELL GEOMETRY

The continuous deformation map for the current geometry is formulated in terms of the convected coordinates (ξ_1, ξ_2, ξ) as

$$\mathbf{x} = \boldsymbol{\varphi}[\mathbf{X}[\xi_1, \xi_2, \xi], t] \;\; \forall \mathbf{X} \in B_0 \setminus \Gamma_S \tag{4.39}$$

where considering $\boldsymbol{\varphi}^+$ and $\boldsymbol{\varphi}^-$ to be the placement on the plus and minus side of the discontinuity, the jump of the mapping can be expressed as

$$[\![\boldsymbol{\varphi}]\!] = \boldsymbol{\varphi}^+ - \boldsymbol{\varphi}^- \tag{4.40}$$

In line with the developments in Reference [13], the through-the-thickness fracture is represented in terms of subtraction of the continuous placement of both sides of the crack using the phantom node method. Thereby the mapping $\boldsymbol{\varphi}$ and its discontinuity over Γ_S are defined as

$$\begin{cases} \boldsymbol{\varphi}[\xi_1, \xi_2, \xi] = \bar{\boldsymbol{\varphi}}[\xi_1, \xi_2] + \xi \mathbf{m}[\xi_1, \xi_2] + \frac{1}{2}\xi^2 \mathbf{m}\gamma[\xi_1, \xi_2] & \forall \mathbf{X} \in B_0 \setminus \Gamma_S \\ [\![\boldsymbol{\varphi}[\xi_1, \xi_2, \xi]]\!] = \boldsymbol{\varphi}^+[\xi_1, \xi_2, \xi] - \boldsymbol{\varphi}^-[\xi_1, \xi_2, \xi] & \forall \mathbf{X} \in \Gamma_S \end{cases} \tag{4.41}$$

where in order to avoid Possion locking effect, the continuous placement $\boldsymbol{\varphi}$ is specified in terms of a second order Taylor series expansion in the director $\mathbf{m}$, which leads to representation of inhomogeneous thickness deformation effects of the shell, γ, cf. Figure 4.4. It is also shown in [12] that the deformation gradient can be formulated as

$$\mathrm{d}\mathbf{x} = \mathbf{F}_b \cdot \mathrm{d}\mathbf{X} \text{ with } \mathbf{F}_b = \mathbf{g}_{\mathrm{b}\,m} \otimes \mathbf{G}^m \tag{4.42}$$

in terms of the spatial co-variant basis vectors

$$\mathbf{g}_{b_m} = \boldsymbol{\varphi} \otimes \nabla_{\xi\, m}. \tag{4.43}$$

4.3.3. FINITE ELEMENT APPROXIMATION OF THE CURRENT SHELL GEOMETRY BASED ON THE PHANTOM NODE METHOD

We continue to extend the spatial discretisation presented in section 4.2 based on the shell formulation employed. Thereby, on the element level, the continuous part of mapping is approximated as

$$\begin{aligned}\boldsymbol{\varphi}^{h,e} &= \sum_{i\in I\cup J} N^i[\xi_1,\xi_2]\, H_S^p \left(\hat{\boldsymbol{\varphi}}^i + \xi\hat{\mathbf{m}}^i\left(1+\frac{1}{2}\xi\sum_{j\in I\cup J} N^j[\xi_1,\xi_2]\hat{\gamma}^j\right)\right)\\ &+ \sum_{k\in K\cup L} N^k[\xi_1,\xi_2]\, H_S^m \left(\hat{\boldsymbol{\varphi}}^k + \xi\hat{\mathbf{m}}^k\left(1+\frac{1}{2}\xi\sum_{l\in K\cup L} N^l[\xi_1,\xi_2]\hat{\gamma}^l\right)\right)\\ &= \hat{\mathbf{N}}^m\left(\hat{\boldsymbol{\varphi}}^m + \xi\hat{\mathbf{m}}^m\left(1+\frac{1}{2}\xi\hat{\mathbf{N}}_\gamma\hat{\boldsymbol{\gamma}}\right)\right) + \hat{\mathbf{N}}^f\left(\hat{\boldsymbol{\varphi}}^f + \xi\hat{\mathbf{m}}^f\left(1+\frac{1}{2}\xi\hat{\mathbf{N}}_\gamma\hat{\boldsymbol{\gamma}}\right)\right)\end{aligned} \tag{4.44}$$

where I and J are the macroscale and subscale sets of nodes belong to D_0^+ and K and L are the macroscale and subscale sets of nodes belong to D_0^-. There we also introduced $\hat{\mathbf{N}}_\gamma$ as the shape function matrix associated with the thickness inhomogeneous field. As it is noted and already discussed in subsection 4.2.2, in addition to the approximation functions related to the marco-scale nodes, approximations related to the subscale nodes is also added to improve the kinematic representation of the discontinuous field. Consequently, discontinuity across the crack can be approximated as

$$\begin{aligned}[\![\boldsymbol{\varphi}^{h,e}]\!] &= \sum_{i\in I} N^i[\xi_1,\xi_2]\, H_S^p \left(\hat{\boldsymbol{\varphi}}^i + \xi\hat{\mathbf{m}}^i\left(1+\frac{1}{2}\xi\sum_{j\in I} N^j[\xi_1,\xi_2]\hat{\gamma}^j\right)\right)\\ &- \sum_{k\in K} N^k[\xi_1,\xi_2]\, H_S^m \left(\hat{\boldsymbol{\varphi}}^k + \xi\hat{\mathbf{m}}^k\left(1+\frac{1}{2}\xi\sum_{l\in K} N^l[\xi_1,\xi_2]\hat{\gamma}^l\right)\right)\\ &= \hat{\mathbf{N}}_d^m\left(\hat{\boldsymbol{\varphi}} + \xi\hat{\mathbf{m}}\left(1+\frac{1}{2}\xi\hat{\mathbf{N}}_\gamma\hat{\boldsymbol{\gamma}}\right)\right) + \hat{\mathbf{N}}_d^f\left(\hat{\boldsymbol{\varphi}} + \xi\hat{\mathbf{m}}\left(1+\frac{1}{2}\xi\hat{\mathbf{N}}_\gamma\hat{\boldsymbol{\gamma}}\right)\right)\end{aligned} \tag{4.45}$$

Considering the approximation of the continuous field, the special co-variant basis vectors can be written as

$$\mathbf{g}_{b_m}^{h,e} = \begin{cases} \displaystyle\sum_{i\in I} H_S^p\left(\left(\hat{\boldsymbol{\varphi}}^i + \xi\hat{\mathbf{m}}^i\left(1+\frac{1}{2}\xi\sum_{j\in I} N^j\hat{\gamma}^j\right)\right)\frac{\partial N^i}{\partial\xi_m} + \frac{1}{2}\xi^2 N^i\hat{\mathbf{m}}^i\left(\sum_{j\in I}\frac{\partial N^j}{\partial\xi_m}\hat{\gamma}^j\right)\right) & \\ \displaystyle+\sum_{k\in K} H_S^m\left(\left(\hat{\boldsymbol{\varphi}}^k + \xi\hat{\mathbf{m}}^k\left(1+\frac{1}{2}\xi\sum_{l\in K} N^l\hat{\gamma}^l\right)\right)\frac{\partial N^k}{\partial\xi_m} + \frac{1}{2}\xi^2 N^k\hat{\mathbf{m}}^k\left(\sum_{l\in K}\frac{\partial N^l}{\partial\xi_m}\hat{\gamma}^l\right)\right) & m=1,2\\ \displaystyle\sum_{i\in I} H_S^p\, N^i\hat{\mathbf{m}}^i\left(1+\xi\sum_{j\in I} N^j\hat{\gamma}^j\right) + \sum_{k\in K} H_S^m\, N^k\hat{\mathbf{m}}_c^k\left(1+\xi\sum_{l\in K} N^l\hat{\gamma}^l\right) & m=3\end{cases} \tag{4.46}$$

4.4. BULK AND INTERFACE MATERIAL MODEL

Capturing the accurate response of a structure under impact loading requires employing a reliable material model for the continuum and interface material where failure occurs. To model occurrence of the plastic deformation in the bulk material prior to the localisation, in line with the developments in [14] and [12], a hypoelastic-inelastic framework is used in which to represent the yield function the Johnson and Cook model [15] is incorporated. Thereby the

isotropic non-linear hardening behaviour, rate-dependency, and thermal softening effect are included as

$$F = \tau_e - \left(A + B\left(\varepsilon_e^p\right)^n\right)\left(1 + C < \ln\left[\frac{\dot{\varepsilon}_e^p}{\dot{\varepsilon}_0}\right] >\right)\left(1 - \hat{\theta}^m\right) \tag{4.47}$$

where ε_e^p is the equivalent accumulated plastic strain, $\dot{\varepsilon}_e^p$ is the effective plastic strain rate, and $\hat{\theta}$ is the so-called homologous temperature. Therein also A, B and C represent the initial yield, strain hardening, and rate sensitivity parameters, whereas n and $\dot{\varepsilon}_0$ defines the hardening exponent and the cut-off strain-rate. In case a quasi-static loading case is under investigation, by disregarding the strain rate and temperature dependencies the yield function may be simplified as

$$F = \tau_e - \left(A + B\left(\varepsilon_e^p\right)^n\right) \tag{4.48}$$

Modelling ductile fracture requires accurate modelling of the material at the localisation process zone. For this, in line with the developments in [12] and [13] a damage-viscoplastic cohesive zone model where traction across the interface is described in terms of an effective traction ($\hat{\mathbf{t}}_1$) and a damage parameter (α) as

$$\mathbf{t}_1 = (1 - \alpha)\,\hat{\mathbf{t}}_1 \tag{4.49}$$

The effective traction may be transferred to effective Mandel stress traction by

$$\hat{\mathbf{t}}_1 = \mathbf{F}^{-t} \cdot \hat{\mathbf{Q}} \tag{4.50}$$

whereby, considering the stiffness of the cohesive zone $\mathbf{K}$, the total material jump $\mathbf{J}$, the elastic material jump $\mathbf{J}^e$, and the plastic material jump $\mathbf{J}^p$, the bilinear traction-separation law is formulated as

$$\hat{\mathbf{Q}} = \mathbf{K} \cdot (\mathbf{J} - \mathbf{J}^p) = \mathbf{K} \cdot \mathbf{J}^e. \tag{4.51}$$

In the above, the plastic part of the material jump and the damage parameter are obtained via evolution laws as in [16], which for sake of briefness are not detailed here. The response of the bilinear traction-separation law for pure mode I and mode II is depicted in the Figure 4.5. Therein σ_{fn} and σ_{fs} are maximum normal and shear stress, Q_n and Q_n are normal and shear components of the traction, and J_n and J_s are normal and tangential parts of the crack opening.

4.5. NUMERICAL EXAMPLES

In the numerical section, we intend to prove that the subscale in fact works as expected; that i) it provides the same results as a more refined model with the same crack path and ii) that it indeed captures the effect of a tortuous crack path in the case when the subscale enrichment is utilised. For this, in this section three numerical examples are investigated to verify the theory of the proposed method as well as the accuracy it provides. The first example is intended to investigate a loaded membrane with a predefined crack path which kinks and ends inside the element. This example examines the potential of the subscale refinement of the phantom node approach compared to the conventional phantom node method. The second example explores the influence of the subscale refinement of the cracked element on the cohesive zone present at the interface and with dissipative material bulk behaviour. The third example concerns the advantage the new approach provides dealing with a complex crack path.

In all examples, the quadratic triangle element is used for which the spatial integration is carried out employing six integration points in-plane and four integration points through the

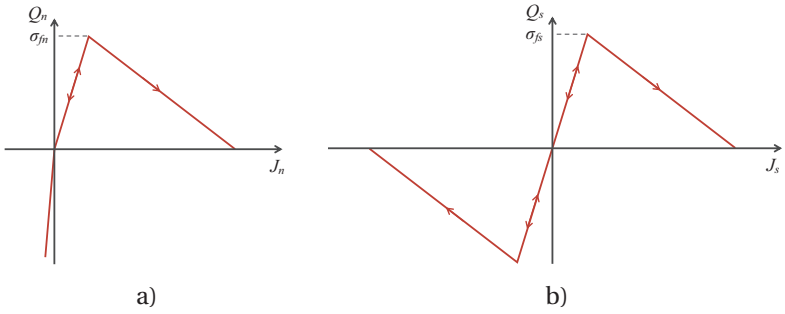

Figure 4.5: Illustration of a) the pure mode I and b) pure mode II response of the bilinear traction-separation law.

thickness. For integration of the cracked elements, sub-triangulation is performed as in [16], where six integration points are required for every subtriangle in-plane integration of the mass matrix. The time integration for all simulations is done using an explicit central difference scheme.

4.5.1. MEMBRANE LOADED PLATE WITH TRACTION-FREE FACES ALONG THE PREDEFINED CRACK

In first example the accuracy of the kinematics represented by the proposed approach is investigated and compared to the result obtained by the conventional phantom node approach. It is also intended to show how the crack kink and tip can be represented employing the current approach without furnishing required spatial discretisation of the cracked region of the domain. As depicted in the Figure 4.6, the plate is of dimension $1 \times 1\,\mathrm{m}^2$ and is discretised with both a coarse and a refined mesh. The number of elements in the refined mesh is double that of the coarse mesh case. The path of the predefined crack is the same for both cases and is defined such that it kinks and ends inside the cracked elements. The bottom edge of the plate is clamped and all nodes of the top edge is prescribed with a constant velocity of 20 m/s. The response of the bulk material is captured using an isotropic hypoelastic material model where Young's modulus and Poisson's ratio are $E = 210\,\mathrm{GPa}$, $\nu = 0.3$.

To examine the accuracy and efficiency of the proposed method, the coarse mesh is analysed using subscale refinement of the phantom node method and the fine mesh is analysed using the conventional phantom node method. Comparing the results of force versus displacement measured on all nodes of the top edge in both cases, as it is seen in Figure 4.8, although the number of elements used for simulation of the coarse mesh is half of the fine mesh, the results are in perfect agreement which verifies the accuracy of the kinematics captured by the proposed approach.

4.5.2. MEMBRANE LOADED PLATE WITH ACTIVE COHESIVE ZONE ALONG THE PREDEFINED CRACK

The second example explores how accurate the new approach captures the plastic deformation of the bulk and the traction across the interface of the crack. For this, the same test case

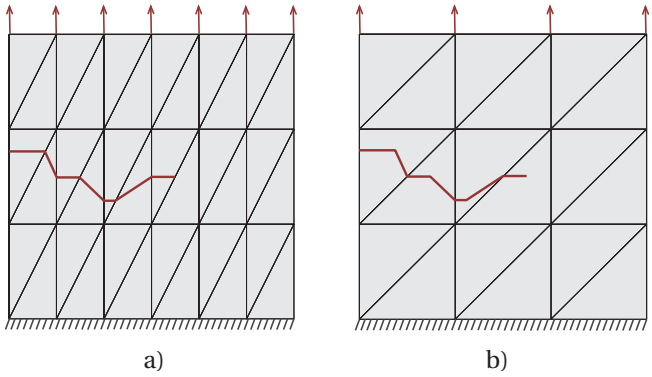

Figure 4.6: Example 1: Boundary conditions for a) a refined mesh simulated using the conventional phantom node method and b) a coarse mesh simulated using the proposed subscale refinement.

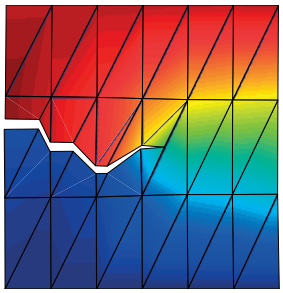

Figure 4.7: Example 1: Deformed geometry for the refined mesh with conventional refinement - different colours represent different displacements.

as in the previous example is considered but with a straight crack as seen in the Figure 4.9. As in the first test case, the plate is of dimension $1 \times 1\,\mathrm{m}^2$ and is discretised in the same way as in the previous example. The bottom edge of the plate is clamped and all nodes of the top edge is prescribed with a constant velocity of 20 m/s.

The crack path is predefined such that it ends inside the element for the coarse case and along its path the cohesive zone, discussed in Section 4.4, is active. The case with fine discretisation is simulated using the conventional phantom node while for the case with the coarse mesh the new approach is utilised.

To capture the accurate behaviour of the bulk material, the hypoelasto-plastic material frame work as in Section 4.4 with the yield function as mentioned in Eq. (4.48) is employed where Young's modulus and Poisson's ratio are $E = 210\,\mathrm{GPa}$, $\nu = 0.3$. The parameters assigned for the yield function are as $A = 175$ MPa, $B = 767$ MPa, and $n = 0.67$.

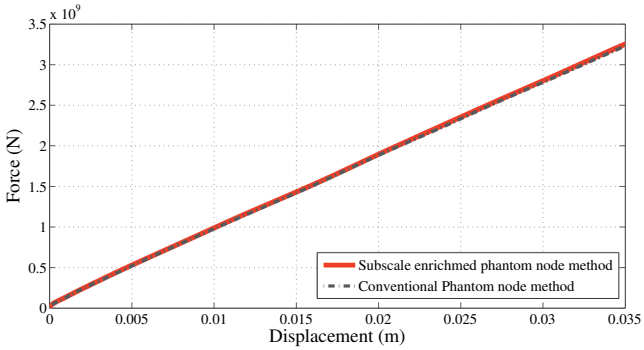

Figure 4.8: Example 1: Force versus displacement diagram measured at all nodes of the top edge for the conventional phantom node method and subscale refinement of the phantom node method.

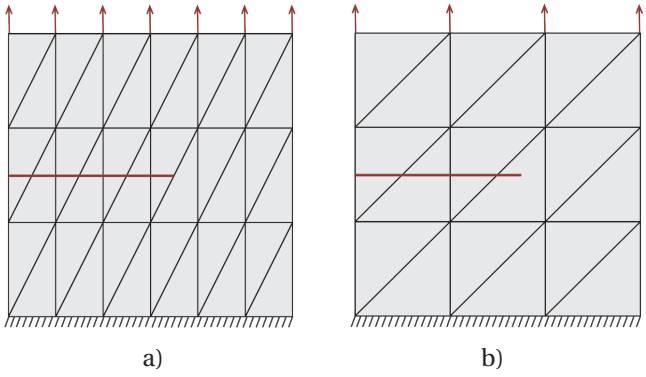

Figure 4.9: Example 2: Boundary conditions for a) a refined mesh simulated using the conventional phantom node method and b) a coarse mesh simulated using the proposed subscale refinement.

As can be seen in the Figure 4.11, the force versus displacement curves captured on all nodes of the top edge of the domain for both cases perfectly match one another. Initially that the material deforms elastically and in the following starts hardening there is no deviation between the results observed, while once the cohesive zone degrades completely then the curves don't match perfectly. Considering the fact that the number of degrees of freedom utilised in both cases is different, perfect correlation between the oscillations may not be expected. However, once oscillations are damped out a perfect match between them is again obtained.

4.5.3. MEMBRANE LOADED PLATE WITH A COMPLEX COHESIVE CRACK

The third example aims at investigating the advantage of the current approach once a cohesive crack propagates in a complex pattern. Representing progression of such a cohesive crack requires a higher degree of refinement around the failure zone to capture the accurate energy

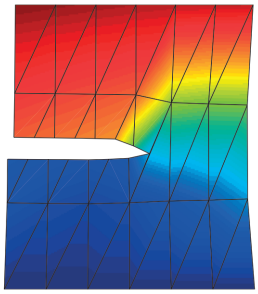

Figure 4.10: Example 2: Deformed geometry for the refined mesh with conventional refinement - different colours represent different displacements.

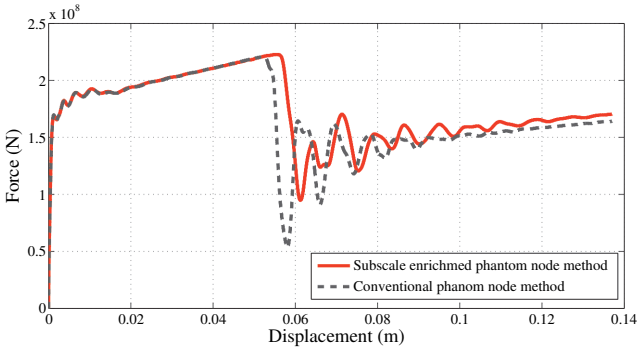

Figure 4.11: Example 2: Force versus displacement diagram measured at all nodes of the top edge for the conventional phantom node method and subscale refinement of the phantom node method.

being dissipated due to degradation of the cohesive zone. For this, the same coarse mesh as in the previous examples is utilised but with two different crack patterns, one straight and one zigzag shaped, cf. Figure 4.12. Once again, the plate is of dimension $1 \times 1\,\mathrm{m}^2$ and it is clamped at the bottom edge while constant velocity of $20\,m/s$ is prescribed on all nodes of the top edge. To capture the plastic deformation of the bulk material and cohesive force across the crack the same material and cohesive zone model as previous example is employed. In order to explore advantage of the proposed method, the plate with straight predefined cohesive crack is simulated using the conventional phantom node method while the plate with predefined zigzag cohesive crack is simulated using the proposed method which offers the possibility to represent kinking inside the element. As it can be observed in the Figure 4.13, during the initial elastic response and the following plastic hardening phase no deviation takes place. However the deviation appears during the degradation of cohesive zone along the crack path. As it is expected and may also be seen due to longer crack path present in case of the zigzag cohesive

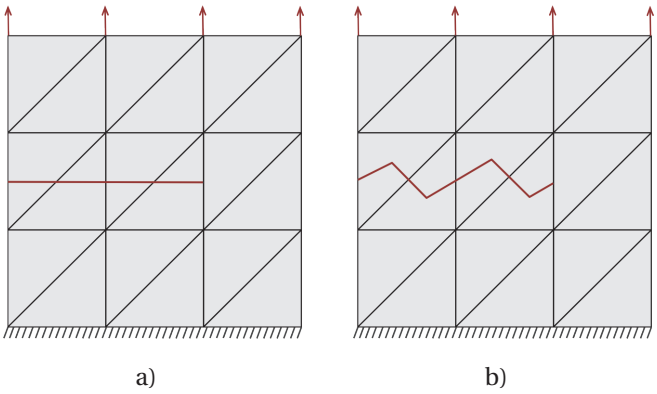

Figure 4.12: Example 3: Boundary conditions for a) a straight crack simulated using the conventional phantom node method and b) a zigzag crack using the proposed subscale refinement.

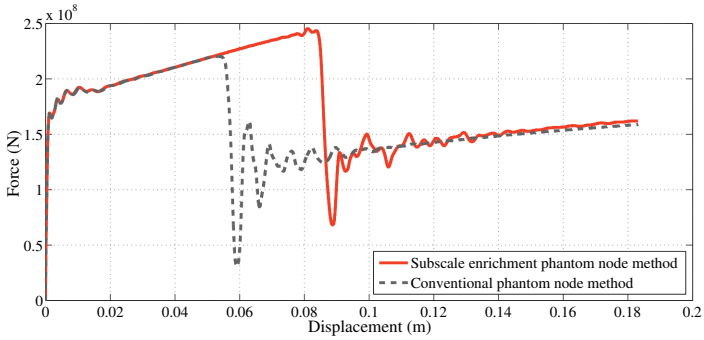

Figure 4.13: Example 3: Force versus displacement diagram measured at all nodes of the top edge for the conventional phantom node method and subscale refinement of the phantom node method.

zone it takes more energy to be dissipated up until the cohesive zone is fully degraded. By the time the resisting forces of the cohesive cracks are completely degraded the forces measured at all nodes of the top edges of both cases match each other once again which is due the same bulk material remaining in front of the crack tip to sustain the loading. Thereby one may conclude that the proposed method suggests a more detailed approach towards representing the failure zone without need to refine the neighbouring elements.

4.6. CONCLUSIONS

A new approach to represent crack tips and kinks within the elements, based on the phantom node method has been developed. This is in line with Mostofizadeh *et al.*[3] where a similar method based on the XFEM is presented. However, due to less complexities in the implemen-

tation of the Phantom node approach, compared to the XFEM, the current approach can be regarded as an advantageous alternative. The method introduces a sub-scale problem for each cracked element using additional subscale nodes. In order to do that without influencing the macro-scale domain a dynamic condensation technique is utilised, which results in a more efficient computation. Therefore, in contrary to the conventional approach, high level of refinement needed for the spatial discretisation around the crack tip is avoided. Although the method has been implemented and presented for a shell formulation using 6-node triangle elements, it has the potential to be applied to any type of element.

To evaluate the accuracy of the proposed approach, several examples have been investigated. It is shown that for both hypo-elastic and hypo-plastic cases it captures the accurate kinematics as expected. It has also represented the cohesive traction along the crack with proper accuracy.

One step towards making this approach even more efficient is to solve for the cracked elements only in the macro-scale level once the crack tip progressed to the next element and the cohesive zone degradation has been captured with sufficient accuracy the method provides. Therefore history variables of the sub-scale domain can be mapped back to the macro-scale domain and the rest of the simulation for that part of the domain may be carried out only on the macro-scale level.

It would also be an interesting step forward to develop a mass lumping method to lower the computational cost even further. However, in the current development the emphasis was given to address subscale refinement alone.

REFERENCES

[1] S. Mostofizadeh, F. van der Meer, M. Fagerström, R. Larsson, and B. Sluys, *An element subscale refinement for representation of the progressive fracture based on the phantom node approach,* Computers and Structures **196**, 134 (2018).

[2] T. Rabczuk, G. Zi, A. Gerstenberger, and W. Wall, *A new crack tip element for the phantom-node method with arbitrary cohesive cracks,* International journal for numerical methods in engineering **75**, 577 (2008).

[3] S. Mostofizadeh, M. Fagerström, and R. Larsson, *Xfem-based element subscale refinement for detailed representation of crack propagation in large-scale analyses,* International Journal for Numerical Methods in Engineering **110**, 549 (2017).

[4] A. Hansbo and P. Hansbo, *An unfitted finite element method, based on Nitsche's method, for elliptic interface problems,* Computer Methods in Applied Mechanics and Engineering **191**, 5537 (2002).

[5] G. Zi and T. Belytschko, *New crack-tip elements for XFEM and applications to cohesive cracks,* International Journal for Numerical Methods in Engineering **57**, 2221 (2003).

[6] T. Chau-Dinh, G. Zi, P.-S. Lee, T. Rabczuk, and J.-H. Song, *Phantom-node method for shell models with arbitrary cracks,* Computers & Structures **92**, 242 (2012).

[7] Q. Xiao and B. L. Karihaloo, *Enrichment schemes and accuracy of the xfem for modelling traction-free and cohesive cracks,* (2006).

[8] I. Babuška and J. Melenk, *The partition of unity finite element method: Basic theory and applications,* Computer Methods in Applied Mechanics and Engineering **139**, 289 (1996).

[9] T. Belytschko and T. Black, *Elastic crack growth in finite elements with minimal remeshing,* International Journal for Numerical Methods in Engineering **45**, 601 (1999).

[10] N. Moës, J. Dolbow, and T. Belytschko, *A finite element method for crack growth without remeshing,* International Journal for Numerical Methods in Engineering **46**, 131 (1999).

[11] J. Song, P. Areias, and T. Belytschko, *A method for dynamic crack and shear band propagation with phantom nodes,* International Journal for Numerical Methods in Engineering **67**, 868 (2006).

[12] S. Mostofizadeh, M. Fagerström, and R. Larsson, *Dynamic crack propagation in elasto-plastic thin-walled structures: Modelling and validation,* International Journal for Numerical Methods in Engineering **96**, 63 (2013).

[13] R. Larsson, J. Mediavilla, and M. Fagerström, *Dynamic fracture modeling in shell structures based on XFEM,* International Journal for Numerical Methods in Engineering **86**, 499 (2010).

[14] G. Ljustina, M. Fagerström, and R. Larsson, *Hypo-and hyper-inelasticity applied to modeling of compacted graphite iron machining simulations,* European Journal of Mechanics-A/Solids **37**, 57 (2013).

[15] G. Johnson and W. Cook, *Fracture characteristics of three metals subjected to various strains, strain rates, temperatures and pressures,* Engineering Fracture Mechanics **21**, 31 (1985).

[16] M. Fagerström and R. Larsson, *Approaches to dynamic fracture modelling at finite deformations,* Journal of the Mechanics and Physics of Solids **56**, 613 (2008).

5

A CONTINUUM DAMAGE FAILURE MODEL FOR THIN-WALLED STRUCTURES

A new approach is developed to the analysis of failure in thin-walled structures based on ductile failure described by continuum damage. A continuum damage coupled to visco-plasticity formulation is proposed, where the total response is obtained from a damage enhanced effective visco-plastic material model. The fracture area production is based on a rate dependent damage evolution law, where the damage–visco-plasticity coupling is modeled via the inelastic damage driving dissipation. A local damage enhanced model is obtained for the ductile failure analysis, which contributes to computational efficiency. The Johnson-Cook visco-plasticity and failure initiation models are used as main prototypes in the implementation. In the numerical examples, the accuracy of the model is investigated and an experimental case is validated. From the examples, the resulting model yields mesh convergence for a finite damage propagation parameter.

5.1. INTRODUCTION

For large scale structures, *e.g.* impact and/or blast loading of aircraft fuselage and off-shore structures, we are particularly concerned with the level of detailing in the structural and material models balanced against the computational cost of the ductile fracture analysis. To tackle the problem, we have previously (among others) considered shell modelling combined with "Cohesive Zone" (CZ) modelling of the fracture, cf. Larsson *et al.* [1], Mostofizadeh *et al.* [2–4]. Typically, in the CZ approach, XFEM is a main ingredient to resolve the fracture zones to obtain the proper balance between "sufficient" fracture resolution and FE resolution of the remainder of the large scale structure, cf. Melenk and Babuška [5], Belytschko and Black [6] and Moës *et al.* [7], Wells and Sluys [8]. From these developments there is still a need to consider alternative methodology capable of representing the crack propagation efficiently and in a sufficiently accurate manner. The final model should not need to require too heavily refined meshes to yield reasonable results. For this, we propose a continuum damage mechanics approach combined with shell theory for the analysis of ductile fracture of thin-walled structures subjected to high rates of loading. As to ductile damage it is often attributed to the growth of micro voids, as described in Gurson [9]. Typically, the (local) plasticity models of Gurson type are coupled to void volume growth, that is assumed to coalesce into fracture surfaces in the FE-application. Various formulations of void growth, including extensions from the local Gurson model, have been considered, e.g. Needleman and Tvergaard [10], Pardoen and Hutchinson [11], Reusch et al. [12].

Another approach to fracture modelling is to consider a damage enhanced effective material of "Lemaitre" type combined with phase field models. This concept has been extensively investigated for brittle fracture processes, e.g. cf. [13], [14], [15], [16], [17]. The generalisation to ductile fracture modelling has been considered by e.g. [18], [19], [20]. Along these lines, we present in this paper a damage enhanced effective material based on the visco-plastic JC-model [21]. Special focus is placed on the resulting energy dissipation, involving elastic and inelastic contributions in terms of a damage threshold, cf. also [22], based on the JC-fracture model [23]. As to damage evolution, the developments in Larsson *et al.* [24] are reconsidered for ductile fracture, where the fracture area production is formulated in terms of a propagation velocity and a length-scale parameter without any non-local gradient term. The resulting damage evolution model is completely local, which contributes to computational efficiency of the final model. For the handling of the thin-walled nature of the problem considered, different methods of crack representation, including through the thickness fracture have been investigated. By making use of an enhanced assumed strain formulation to deal with the locking occurring for thin shells, Areias and Belytschko [25] developed a shell element based on Mindlin-Reissner theory was developed, A Kirchhoff-Love shell model was employed by Areias *et al.* [26]. However, a possible drawback of the Kirchhoff-Love theory is that it is not capable to represent out-of-plane shear deformation. As to continuum damage with the involved damage field representation a special shell model has been proposed by Kiendl *et al.* [27]. In order to properly handle thin-walled structures including general (3D) non-linear ductile failure analyses, we adopt in this paper the 7-parameter shell model (without discontinuous XFEM enhancement) used in e.g. refs. [1, 2]. The formulation avoids the "Poisson locking" effect occurring in the thin shell limit and allows for the representation of thickness strains due to bending, cf. Betsch *et al.* [28], Parisch [29] and Bischoff and Ramm [30].

The paper is organised as follows: In Section 5.2, the kinematics of the 7-parameter shell element formulation is reviewed, followed the momentum balance formulation. In Section 5.3, the visco-elasto-plasticity coupled to damage formulation is specified. In the damage–

visco-plasticity coupling, a special damage driving energy (including a threshold for damage initiation) is used in the damage evolution law based on the developments in [20]. In Section 5.4, two examples are presented in which the modelling approach to represent the ductile failure process and its accuracy is verified and compared to an experiment. Finally, in Section 5.5, the paper is concluded with closing remarks and discussion.

5.2. SHELL KINEMATICS

In this section, the shell model for thin-walled structures subjected to dynamic ductile fracture processes is outlined. In this development, the kinematics of the 7-parameter shell formulation used in [4] is considered. We start by describing the reference and current configurations of the shell and continue with weak form of the momentum balance.

5.2.1. REFERENCE AND CURRENT CONFIGURATIONS IN CONVECTED COORDINATES

The reference configuration B_0 of the shell is defined in terms of the convected coordinates (ξ_1, ξ_2, ξ) as

$$\mathrm{B}_0 = \left\{ \mathbf{X} = \mathbf{\Phi}_0[\xi_1,\xi_2,\xi] = \bar{\mathbf{\Phi}}[\xi_1,\xi_2] + \xi \mathbf{M}_\Phi[\xi_1,\xi_2] \text{ and } \xi \in \frac{h_0}{2}[-1,1] \right\} \tag{5.1}$$

where, as shown in Figure 5.1, $\Phi_0[\xi_1,\xi_2,\xi]$ defines the mapping from a point in the inertial Cartesian domain to the corresponding one in the reference domain. Therein, $\bar{\mathbf{\Phi}}$ defines the placement of the points on the mid-surface of the shell, $\mathbf{M}_\Phi$ defines outward unit normal vector to the mid-surface of the shell, and ξ_1, ξ_2 are the in-plane convected coordinates of the shell. In order to further specify the placement of a point through-the-thickness of the shell, the coordinate ξ is defined along the unit normal vector $\mathbf{M}_\Phi$ using the initial thickness of the shell h_0.

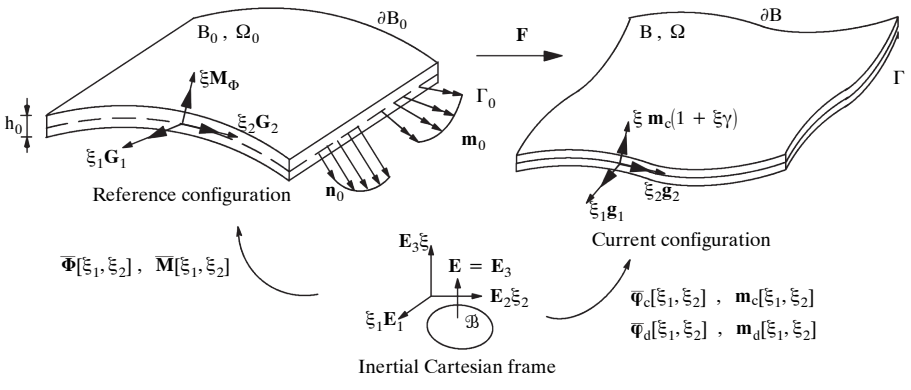

Figure 5.1: Mappings of the reference and current shell configurations with respect to the inertial Cartesian frame. Here, B_0 defines the 3D region of the shell, whereas Ω_0 defines the mid-surface. Moreover, ∂B_0 denotes the external boundary of the 3D domain and Γ_0 refers to the (line) boundary of the mid-surface.

The co-variant base vectors in the reference configuration are expressed as

$$\mathbf{G}_\alpha = \mathbf{\Phi}_{0,\alpha} = \bar{\mathbf{\Phi}}_{,\alpha} + \xi \mathbf{M}_{\Phi,\alpha},\ \alpha = 1,2 \text{ and } \mathbf{G}_3 = \mathbf{G}^3 = \mathbf{M}_\Phi. \tag{5.2}$$

where $\bullet_{,\alpha}$ refers to the derivative with respect to ξ_α. The co-variant base vectors $\mathbf{G}_i$ and the contra-variant base vectors $\mathbf{G}^i$ are related by $\mathbf{G}_i \otimes \mathbf{G}^i = \mathbf{1}$. Using the metric tensors G_{ij} and G^{ij} we arrive at

$$\mathbf{G}_j = G_{\mathrm{ij}}\mathbf{G}^i\ ,\ \mathbf{G}^j = G^{\mathrm{ij}}\mathbf{G}_i \text{ where } G_{\mathrm{ij}} = \mathbf{G}_i \cdot \mathbf{G}_j \text{ and } G^{\mathrm{ij}} = \left(G_{\mathrm{ij}}\right)^{-1} \tag{5.3}$$

Moreover, the infinitesimal volume element $\mathrm{d}B_0$ in the reference configuration can be defined using the convected coordinates as

$$\mathrm{d}B_0 = b_0 \mathrm{d}\xi_1 \mathrm{d}\xi_2 \mathrm{d}\xi \text{ with } b_0 = (\mathbf{G}_1 \times \mathbf{G}_2) \cdot \mathbf{G}^3 \tag{5.4}$$

In a similar fashion as before, the current configuration of the shell, B, can be specified in terms of convected coordinates as

$$\mathrm{B} = \left\{ \mathbf{x} = \boldsymbol{\varphi}[\xi_1, \xi_2, \xi] = \bar{\boldsymbol{\varphi}}[\xi_1, \xi_2] + \xi \mathbf{m}[\xi_1, \xi_2] + \tfrac{1}{2}\xi^2 \mathbf{m}\gamma[\xi_1, \xi_2] \right\} \tag{5.5}$$

where $\bar{\boldsymbol{\varphi}}$ is the mid-surface placement, $\mathbf{m}$ is the extensible director vector, and γ is the thickness inhomogeneous field in the current configuration. In fact, the current mapping, $\boldsymbol{\varphi}$, corresponds to the second order Taylor expansion along the director, and the latter additional field is intended to avoid Possion locking effect in shells, cf. ref. [28]. Furthermore, by defining the spatial co-variant base vectors as

$$\mathbf{g}_\alpha = \boldsymbol{\varphi} \otimes \nabla_{\xi_i}\ ,\ i = 1,2,3. \tag{5.6}$$

the deformation gradient can be expressed as

$$\mathrm{d}\mathbf{x} = \mathbf{F} \cdot \mathrm{d}\mathbf{X} \text{ with } \mathbf{F} = \mathbf{g}_i \otimes \mathbf{G}^i \tag{5.7}$$

and given Eq. (5.6), the spatial co-variant base vectors can be elaborated as

$$\mathbf{g}_\mathrm{i} = \begin{cases} \bar{\boldsymbol{\varphi}}_{,i} + \mathbf{m}_{,i}\left(\xi + \gamma\tfrac{1}{2}(\xi)^2\right) + \mathbf{m}\gamma_{,i}\tfrac{1}{2}(\xi)^2 & i = 1,2 \\ \boldsymbol{m}\left(1 + \gamma\xi\right) & i = 3 \end{cases} \tag{5.8}$$

5.2.2. MOMENTUM BALANCE

In line with refs [2–4], the weak form of the momentum balance is formulated in terms of contributions from inertia G^{ine}, internal- G^{int} and external virtual work G^{ext} as *Find:* $[\bar{\boldsymbol{\varphi}}, \mathbf{m}, \gamma]$ so that

$$\begin{aligned} &G^{\mathrm{ine}}[\ddot{\bar{\boldsymbol{\varphi}}}, \ddot{\mathbf{m}}, \ddot{\gamma}; \delta\bar{\boldsymbol{\varphi}}, \delta\mathbf{m}, \delta\gamma] + \\ &G^{\mathrm{int}}[\bar{\boldsymbol{\varphi}}, \mathbf{m}, \gamma; \delta\bar{\boldsymbol{\varphi}}, \delta\mathbf{m}, \delta\gamma] - \\ &\qquad G^{\mathrm{ext}}[\delta\bar{\boldsymbol{\varphi}}, \delta\mathbf{m}, \delta\gamma] = 0\ \forall\ \delta\bar{\boldsymbol{\varphi}}, \delta\mathbf{m}, \delta\gamma \end{aligned} \tag{5.9}$$

where each contribution is further described as

$$G^{\mathrm{ine}} = \int_{B_0} \rho_0 \delta\boldsymbol{\varphi} \cdot \ddot{\boldsymbol{\varphi}}\, \mathrm{dB}_0, \tag{5.10}$$

$$G^{\mathrm{int}} = \int_{B_0} \left(\delta\mathbf{F}^t \cdot \mathbf{F}\right) : \mathbf{S}\, \mathrm{dB}_0, \tag{5.11}$$

$$G^{\mathrm{ext}} = \int_{B_0} \rho_0 \delta\boldsymbol{\varphi} \cdot \mathbf{b}\, \mathrm{dB}_0 + \int_{\partial B_0} \delta\boldsymbol{\varphi} \cdot \bar{\mathbf{t}}_1\, \mathrm{dS}_0 \tag{5.12}$$

Here, $\mathbf{b}$ is the body force per unit volume, $\mathbf{S}$ is second Piola Kirchhoff stress tensor, and $\bar{\mathbf{t}}_1 = \mathbf{P}^t \cdot \mathbf{N}$ ($\mathbf{P}^t$ is the first Piola-Kirchhoff stress) is the prescribed nominal traction vector on the outer boundary ∂B_0 as in Figure 5.1. Upon defining the displacement vector as $\hat{\mathbf{n}}^t = [\bar{\boldsymbol{\varphi}}, \mathbf{m}, \gamma]$, each contribution to the momentum balance can be reformulated as

$$G^{\text{ine}} = \int_{\Omega_0} \rho_0 \, \delta\hat{\mathbf{n}}^t (\hat{\mathbf{M}}\ddot{\hat{\mathbf{n}}} + \hat{\mathbf{M}}_{\text{con}}) \, \omega_0 \, \mathrm{d}\xi_1 \mathrm{d}\xi_2 \tag{5.13}$$

$$G^{\text{int}} = \int_{\Omega_0} \delta\hat{\mathbf{n}}_c^t \hat{\mathbf{N}}_c \omega_0 \, \mathrm{d}\xi_1 \mathrm{d}\xi_2 \tag{5.14}$$

$$G^{\text{ext}} = \int_{\Gamma_0} \left(\delta\bar{\boldsymbol{\varphi}} \cdot \mathbf{n}_0 + \delta\mathbf{m} \cdot \tilde{\mathbf{m}}_0 + \delta\gamma \, m_s \right) \mathrm{d}\Gamma_0 - \int_{\Omega} p \, \delta\bar{\boldsymbol{\varphi}} \cdot \mathbf{g}_{b_1} \times \mathbf{g}_{b_2} \, \mathrm{d}\Omega \tag{5.15}$$

where in Eq. (5.14), $\delta\hat{\mathbf{n}}_c^t$ and $\hat{\mathbf{N}}_c^t$ are introduced as

$$\delta\hat{\mathbf{n}}_c^t = \left[\delta\bar{\boldsymbol{\varphi}}_{,\alpha}, \delta\mathbf{m}_{,\alpha}, \delta\mathbf{m}, \delta\gamma_{,\alpha}, \delta\gamma \right] \tag{5.16}$$

$$\hat{\mathbf{N}}_c^t = \left[\mathbf{N}^\alpha, \mathbf{M}^\alpha, \mathbf{T}, M_s^\alpha, T_s \right] \tag{5.17}$$

Here, $\mathbf{N}^\alpha$, $\mathbf{M}^\alpha$, $\mathbf{T}$ are the membrane, bending and shear/thickness stretch stress resultants, respectively, whereas M_s^α and T_s are higher order stress resultants, cf. D.1 for the detailed expressions. In Eq. (5.13), $\hat{\mathbf{M}}$ and $\hat{\mathbf{M}}_{\text{con}}$ are respectively consistent mass matrix and convective mass force per unit area, where convective mass involves contributions from the thickness inhomogeneous strain fields and the first order time derivative of the director vector (cf. D.2 and [1, 2]). Therein, to perform the integration a change in the domain from B_0 (3D) to Ω_0 (2D) via $j_0[\xi] = b_0/\omega_0$ is carried out as

$$\mathrm{dB}_0 = j_0 \mathrm{d}\xi \mathrm{d}\Omega_0 \text{ with } \mathrm{d}\Omega_0 = \omega_0 \mathrm{d}\xi_1 \mathrm{d}\xi_2 \text{ and } \omega_0 = |\boldsymbol{\Phi}_{,1} \times \boldsymbol{\Phi}_{,2}| \tag{5.18}$$

Furthermore, in Eq. (5.15), p denotes pressure and $\mathbf{n}_0$, $\tilde{\mathbf{m}}_0$, m_s, $\mathbf{m}_0$ are the stress resultants due to the traction applied on the outer boundary, cf. D.1.

5.3. CONTINUUM DAMAGE MODELLING FRAMEWORK

In this section, we outline a thermodynamically motivated visco-elasto-plasticity formulation, combined with a continuum damage model. Details may be found in [20]. Here, the deformation gradient $\mathbf{F}$ is considered subdivided into an elastic component $\bar{\mathbf{F}}$ and the inelastic part $\mathbf{F}_p$, forming the total deformation gradient multiplicatively as $\mathbf{F} = \bar{\mathbf{F}} \cdot \mathbf{F}_p$. We also introduce the spatial velocity gradient $\mathbf{l} = \dot{\mathbf{F}} \cdot \mathbf{F}^{-1}$, which in view of the multiplicative split induces an additive decomposition of $\mathbf{l}$ in elastic and inelastic portions $\bar{\mathbf{l}}$ and $\mathbf{l}_p$ as

$$\mathbf{l} = \bar{\mathbf{l}} + \mathbf{l}_p \text{ with } \bar{\mathbf{l}} = \dot{\bar{\mathbf{F}}} \cdot \bar{\mathbf{F}}^{-1} \text{ and } \mathbf{l}_p = \bar{\mathbf{F}} \cdot \mathbf{L}_p \cdot \bar{\mathbf{F}}^{-1} \tag{5.19}$$

where $\mathbf{L}_p =: \dot{\mathbf{F}}_p \cdot \mathbf{F}_p^{-1}$ is the plastic velocity gradient. Related to the non-symmetric spatial velocity gradient $\mathbf{l}$, let us also introduce the symmetric total and plastic rate of deformation tensors as

$$\mathbf{d} = \mathbf{l}^{\text{sym}} \,, \mathbf{d}_p = \mathbf{l}_p^{\text{sym}} = -\mathscr{L}_v \left[\bar{\mathbf{b}} \right] \cdot \bar{\mathbf{b}}^{-1} \text{ with } \mathscr{L}_v \left[\bar{\mathbf{b}} \right] = \mathbf{F} \cdot \dot{\overline{\mathbf{F}^{-1} \cdot \bar{\mathbf{b}} \cdot \mathbf{F}^{-t}}} \cdot \mathbf{F}^t \tag{5.20}$$

where the $\bullet^{\text{sym}}$ denotes the symmetric portion of the second order tensor $\bullet$ and $\mathscr{L}_v \left[\bar{\mathbf{b}} \right]$ is the Lie derivative of the reversible Finger tensor $\bar{\mathbf{b}} = \bar{\mathbf{F}} \cdot \bar{\mathbf{F}}$.

In order to represent the stress response, we introduce the stored free energy function $\psi = \psi\left[\overline{\mathbf{b}}, k, \alpha\right]$ in the micro hardening k and the isotropic damage variable $0 \leq \alpha \leq 1$. Direct application of the dissipation rate $\mathscr{D} \geq 0$ together with Colemans equations at isothermal conditions yields the reduced disspation rate

$$\mathscr{D} = \tau : \mathbf{l} - \dot{\psi} = \tau : \mathbf{d}_p + \kappa \dot{k} + \mathscr{A}\dot{\alpha} \geqslant 0 \tag{5.21}$$

corresponding to the Kirchhoff stress τ, the micro hardening stress κ and the *elastic* damage driving force $\mathscr{A}$ obtained as

$$\tau = 2\overline{\mathbf{b}} \cdot \frac{\partial \psi}{\partial \overline{\mathbf{b}}} \ , \ \kappa = -\frac{\partial \psi}{\partial k} \ , \ \mathscr{A} = -\frac{\partial \psi}{\partial \alpha} \tag{5.22}$$

5.3.1. A VISCO-PLASTIC MODEL COUPLED TO CONTINUUM DAMAGE

In the present framework, we consider a scalar damage enhanced effective material model where the damage evolution is induced by inelastic damage driving dissipation related to the effective material, whose quantities are denoted by a hat, i.e. $\hat{\bullet}$. This is achieved by considering the isochoric part of the effective (=undamaged) material degraded with the damage degradation function $f[\alpha] = (1-\alpha)^2$ (where $0 \leq \alpha \leq 1$ is the isotropic damage variable) written as

$$\psi = f[\alpha]\left(\hat{\psi}^{\text{iso}}\left[\overline{\mathbf{b}}\right] + \hat{\psi}^{\text{mic}}[k]\right) + \hat{\psi}^{\text{vol}}[J] \tag{5.23}$$

where $\hat{\psi}^{\text{iso}}$ is the isochoric part of the effective free energy, $\hat{\psi}^{\text{mic}}$ represents stored energy due to internal (isotropic) hardening processes in the material and $\hat{\psi}^{\text{vol}}$ is the stored free energy due to volumetric deformation. Moreover, $J = \det[\mathbf{F}]$ denotes the (reversible) volumetric deformation.

In line with the Johnson-Cook (JC) model [21] for the *effective material response*, the stored energy contributions are defined as

$$\hat{\psi}^{\text{iso}} = \frac{1}{2}G\left(\mathbf{1} : \overline{\mathbf{b}}^{\text{iso}} - 3\right) \ , \ \hat{\psi}^{\text{vol}} = \frac{1}{2}K\log[J]^2 \ , \ \hat{\psi}^{\text{mic}} = \frac{B}{1+n}(-k)^{1+n} \tag{5.24}$$

where $\overline{\mathbf{b}}^{\text{iso}} = J^{-\frac{2}{3}}\overline{\mathbf{b}}$ is the isochoric portion of $\overline{\mathbf{b}}$, G is the shear modulus, K is the bulk modulus, and according to the JC-model, B is the isotropic hardening parameter and n is the hardening exponent.

In view of (5.22), (5.23) and (5.24), we now obtain the continuum stress, internal hardening and elastic damage driving force as

$$\tau = f[\alpha]\hat{\tau}^{\text{iso}} - Jp\mathbf{1} \ , \ \kappa = f[\alpha]\hat{\kappa} \ , \ \mathscr{A} = -f'[\alpha]\left(\hat{\psi}^{\text{iso}} + \hat{\psi}^{\text{mic}}\right) \tag{5.25}$$

where $\hat{\tau}^{\text{iso}}$ is the effective isochoric Kirchhoff stress tensor, $\hat{\kappa}$ is the effective micro hardening stress and p is the pressure. Note that the pressure is undamaged during the entire damage process, i.e. $p = \hat{p}$. The explicit expressions of the effective stress response (=response of the virgin undamaged material) for our prototype model become

$$\hat{\tau}^{\text{iso}} = 2\frac{\partial \hat{\psi}^{\text{iso}}}{\partial \overline{\mathbf{b}}} \cdot \overline{\mathbf{b}} = G\overline{\mathbf{b}}^{\text{iso}} \ , \ p = -\frac{\partial \hat{\psi}^{\text{vol}}}{\partial \bar{J}} = -KJ^{-1}\log[J] \ , \ \hat{\kappa} = -\frac{\partial \hat{\psi}^{\text{mic}}}{\partial k} = Bk^n \tag{5.26}$$

where $\hat{\kappa}$ is the isotropic hardening stress and p is the pressure in the material. This corresponds to the dissiation rate (5.21) formulated in the effective and damage driving contributions, cf. ref [22], as

$$\mathscr{D} = f[\alpha]\hat{\mathscr{D}} + \mathscr{A}\dot{\alpha} \geq 0 \text{ with } \hat{\mathscr{D}} = \hat{\tau} : \mathbf{d}_p + \hat{\kappa}\dot{k} \tag{5.27}$$

According to the Perzyna visco-plasticity format, the (deviatoric) rate of deformation is postulated as

$$\mathbf{d}_p = \lambda \frac{3}{2} \frac{\hat{\tau}^{\text{iso}}}{\hat{\tau}_e} \ , \ \dot{k} = -\lambda \text{ with } \lambda = \dot{\epsilon}_0 \exp\left[\frac{< \phi_s >}{C\,(A + \hat{\kappa})} \right] \geq \dot{\epsilon}_0 > 0 \tag{5.28}$$

where the plastic multiplier $\lambda \geq 0$ is determined by the positive part $< \phi_s >$. Here, ϕ_s is the static "yield" function defined as

$$\phi_s = \hat{\tau}_e - (A + \hat{\kappa}) \ , \ \hat{\kappa} = B(-k)^n \tag{5.29}$$

where $\hat{\tau}_e$ is the von Mises stress. Moreover, in line with the JC-model, A is the initial yield stress, B is the isotropic hardening parameter, n is the hardening exponent, C is a viscosity parameter and $\dot{\epsilon}_0$ is the reference strain rate parameter. In view of the visco-plastic flow rule (5.28), the effective dissipation rate $\hat{\mathscr{D}}$ in (5.27) for visco-plastic loading $\phi_s \geq 0$ is obtained as $\hat{\mathscr{D}} = \lambda \left(A + < \phi_s > \right)$.

5.3.2. DAMAGE DRIVING DISSIPATION RATE AND DAMAGE EVOLUTION MODEL

To motivate the damage driving dissipation rate, let us reconsider the dissipation rate (5.27) in terms of the total dissipation $\hat{\mathscr{D}}_T$ of the effective material defined as

$$\mathscr{D}[t] = f[\alpha]\hat{\mathscr{D}} + \mathscr{A}\,\dot{\alpha} = \dot{\overline{f\hat{\mathscr{D}}_T}} + (\mathscr{B} + \mathscr{A})\,\dot{\alpha} \approx \dot{\overline{f\hat{\mathscr{D}}_T}} + \mathscr{B}\dot{\alpha} \tag{5.30}$$

where the inelastic damage driving force $\mathscr{B}$ and the total effective dissipation are defined as

$$\hat{\mathscr{D}}_T[t] = \int_0^t \hat{\mathscr{D}}\, dt \ , \ \mathscr{B}[t] - f'[\alpha]\hat{\mathscr{D}}_T \tag{5.31}$$

As alluded to in (5.30), it is assumed in this paper that the elastic damage driving energy $\mathscr{A}$ is small enough to be neglected. This approximation is justified from that the elastic deformation is limited by the yield stress A, whereby the damage driving energy is dominated by the inelastic contribution $\mathscr{B}$. In this way the total dissipation is completely described the inelastic damage driving energy, i.e. during a full damage evolution process one obtains

$$\mathscr{D}_T = \int_0^t \mathscr{D}\, dt = f\hat{\mathscr{D}}_T + \int_0^t \mathscr{B}\dot{\alpha}\, dt \rightarrow \int_0^1 \mathscr{B}\, d\alpha \tag{5.32}$$

To increase flexibility of damage driving energy, a damage threshold for onset of damage evolution is introduced. This is done by considering the dissipation rate (5.27) evaluated before and after the onset of damage happening at $t = t_f$, where t_f is the threshold time dictated by e.g. the JC–fracture initiation criterion [23]. To this end, it appears, cf. also [22], that the total dissipation rate (5.27) can be formulated in the total shifted effective dissipation $\hat{\mathscr{D}}^f_T$, evaluated for $t \geq t_f$. This is written as

$$\mathscr{D}[t] = \begin{cases} f[\alpha]\hat{\mathscr{D}} + \mathscr{A}\,\dot{\alpha} \approx f[\alpha]\hat{\mathscr{D}} & 0 \leq t \leq t_f \\ \dot{\overline{f\hat{\mathscr{D}}^f_T}} + \left(\mathscr{B}^f + \mathscr{A} \right)\dot{\alpha} \approx \dot{\overline{f\hat{\mathscr{D}}^f_T}} + \mathscr{B}^f\,\dot{\alpha} & t \geq t_f \end{cases} \tag{5.33}$$

Hence, onset of damage evolution occurs when $t = t_f$ is apporached and $\mathscr{B}^f$ is the shifted inelastic damage driving energy defined as

$$\mathscr{B}^f[t] - f'[\alpha]\hat{\mathscr{D}}^f_T \text{ and } \hat{\mathscr{D}}^f_T[t] = \int_{t_f}^t \hat{\mathscr{D}}\, dt \tag{5.34}$$

Evidently, different expressions for the dissipation rate are obtained whether the damage threshold has been arrived at or not. Damage loading/unloading $\dot{\alpha} \geq 0$ may happen only for $t \geq t_f$. For $t \geq t_f$ damage loading $\dot{\alpha} > 0$ is controlled by the damage evolution law of Bingham type, cf. Larsson et. al [24], defined as

$$l_c \dot{\alpha} = v^* < \alpha^s[\alpha] - \alpha > \text{ with } \alpha^s = \frac{l_c}{\mathscr{G}_c} \mathscr{B}^f \tag{5.35}$$

where (again) $< \bullet >$ is the positive part function and α^s represents source of damage energy from elastic-plastic deformation. Here, $\mathscr{G}_c$ is the fracture energy release parameter and l_c is the internal length parameter describing the diffuse character of the fracture area as indicated in Fig 5.2. Please note that the damage evolution law may be interpreted as a local balance for law for the damage production. In the case of damage loading $\alpha^s - \alpha > 0$, the local damage production $l_c \dot{\alpha}$ and the convection $v^* \alpha$ (where v^* is the damage progression velocity) balance input damage production $v^* \alpha^s = v^* \alpha + l_c \dot{\alpha}$. This is depicted in Fig. 5.2. As opposed to the rate independent damage evolution case corresponding $v^* \to \infty$ and $\alpha = \alpha^s[\alpha]$, we find in the FE-application that the damage field corresponding to (5.35) exhibits a damage pattern that generally localise in a consistent way within a fixed shear band width, depending on the internal crack evolution velocity v^* and the internal length parameter l_c.

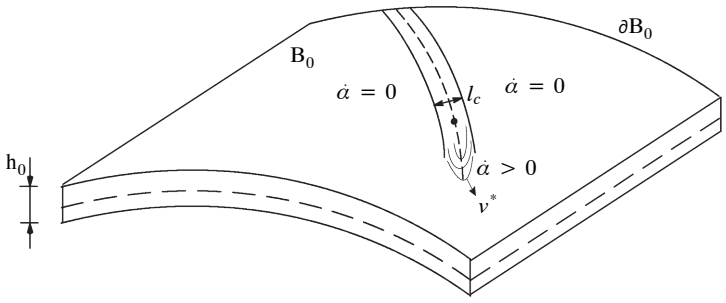

Figure 5.2: Diffuse fracture area progression within localisation zone $\dot{\alpha} > 0$ of width l_c in shell structure.

5.4. NUMERICAL EXAMPLES

In this section, in order to verify and investigate the accuracy of the continuum ductile failure model, two examples are presented. In the first example, a plane strain plate subjected to a uniform tensile loading is considered to study the influence of the mesh refinement and damage zone front propagation velocity. The second example concerns a pre-notched pipe under a four point bending load case, where the accuracy of the proposed continuum ductile damage model together with the shell kinematics is investigated.

In all the simulations a 6-node triangular element mesh with 6 in-plane integration points and 4 through-the-thickness integration points is used. For computational efficiency, we exploit the hypo-inelastic concept based on the Green-Naghdi stress rate for the numerical integration of the visco-plastic flow rule, as proposed in [31] and [2]. To define the damage threshold time t_f in (5.33), we consider the JC-fracture criterion [23] stating that onset of plastic

damage evolution is obtained whenever the equivalent plastic strain k approaches the plastic failure strain ϵ_f^p, where

$$\epsilon_f^p = \left(d_1 + d_2 \exp\left[-d_3 r\right]\right)\left(1 + d_4 \log\left[\frac{\lambda}{\dot{\epsilon}_0}\right]\right) \tag{5.36}$$

and d_1–d_4 and $\dot{\epsilon}_0$ are parameters.

5.4.1. UNIFORM HIGH SPEED TENSION LOADED PLANE STRAIN PLATE WITH AN IMPERFECTION

In this example, a plane strain plate under high speed extension is investigated. Here, the sensitivity of the response to the damage zone front propagation velocity; also the FE–convergence behaviour for reduced mesh sizes is studied.

As depicted in Figure 5.3, the plate is 50 mm by 50 mm with an imperfection with a degraded yield stress and size of 4 mm by 4 mm located in the center of the plate in order to avoid homogeneous stress state and promote a pattern for the failure zone. At the bottom side of the plate all nodes are constrained in the vertical direction while the left corner is fully constrained. To introduce the deformation in the plate a velocity of 2500 mm/s in vertical direction is also applied on all nodes associated with the top edge of the plate. The parameters used for the failure model and Johnson-Cook material model to capture the response of the pearlitic steel assigned to the plate are provided in Table 5.1.

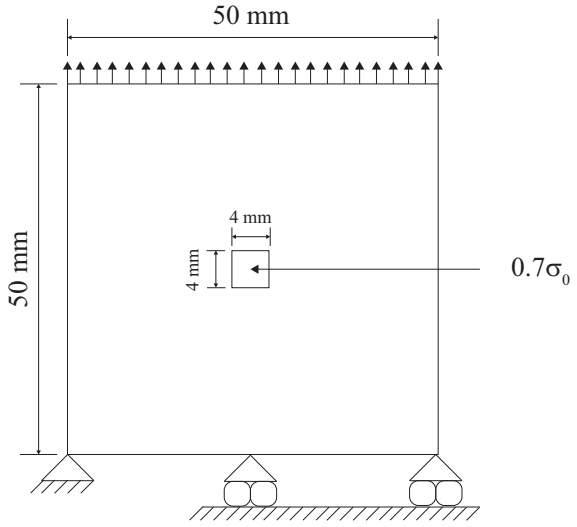

Figure 5.3: Tensile loading of the plane strain plate with an imperfection in the center. The yield limit is assigned to be 70% less than rest of the domain.

Table 5.1: Material parameters used for Johnson-Cook model as well as the failure parameters for the pearlitic plane strain plate from [32].

A [MPa]	B [MPa]	C	n	m	ν	ρ [$\frac{kg}{m^3}$]
550	500	0.0804	0.4	1.68	0.3	7850
d_1	d_2	d_3	d_4	d_5	$\dot{\epsilon}_0[s^{-1}]$	E [GPa]
0.25994	0.61368	2.5569	-0.027652	0.6	0.001	190

SENSITIVITY STUDY OF THE PROPAGATION VELOCITY v^*

In order to investigate the sensitivity of the response to the damage zone front propagation velocity, four different cases with velocities ranging from 10000 mm/s to 1000000 mm/s are considered for which the element size is l_e=1mm.

As shown in Figure 5.5, a lower propagation velocity results in a more ductile response of the plate. It is due to the fact that lower propagation velocity provides more time for the damage zone to develop. It is also observed that the convergence in the response for the pearlitic steel is obtained for $v^* = 250000$ mm/s.

SENSITIVITY STUDY OF INTERNAL LENGTH PARAMETER AND ELEMENT SIZE

In order to investigate the influence of the internal length parameter l_c on the response of the plate, a range of different internal length values between 0.1 mm to 10 mm is studied while keeping the FE-element size l_e =1 mm fixed. As it may be seen in Figure 5.6, assigning a lower internal length parameter, response of the plate becomes more ductile. It is also clear that a converged response is reached at internal length of 1mm. Considering the fixed element size, it can be concluded that in order to achieve the converged response, the minimum length assigned to the internal length parameter needs to be the same size as the element size used.

In line with the previous finding, we assign the converged propagation velocity 250000 mm/s, and also the internal length parameter as the mesh size, sensitivity of the response with respect to different discretisations is studied. As it is seen in Figure 5.8, mesh convergence is obtained between the element sizes l_e = 1 mm and l_e = 1.5 mm.

5.4.2. PRE-NOTCHED PIPE UNDER FOUR POINT BENDING LOAD

In order to verify the behaviour of the damage model in conjunction with the current shell kinematics, a four point bending test of a pre-notched carbon-steel pipe is studied. As it is seen in Figure 5.9, the pipe is of length of 4 m, diameter of 219 mm and thickness of 15.1 mm. For the boundary condition, at the right bottom corner of the pipe all translational degrees of freedom are constrained while at the left bottom corner it is free to slide along the longitudinal direction. In order to apply the displacement to the pipe, a velocity of 2 m/s in the vertical direction is prescribed at two points on top of the pipe. To mimic the physical test, the rate-dependent part of the model is eased and for sake of simplicity only the inelastic part, $\mathscr{B}^f$, of the damage driving force is considered. Material parameters used for the Johnson-Cook model are also listed in Table 5.2.

It is found in [33] that the fracture energy, G_c, varies from 2×10^3 and 8×10^3 kJ/m^2 as the crack length increases. However for simplicity it is opted to consider the median value, 5×10^3 kJ/m^2, as the fracture energy. For the internal length parameter, l_c, in line with the findings in the previous example, it is chosen to be the average mesh size around the failure

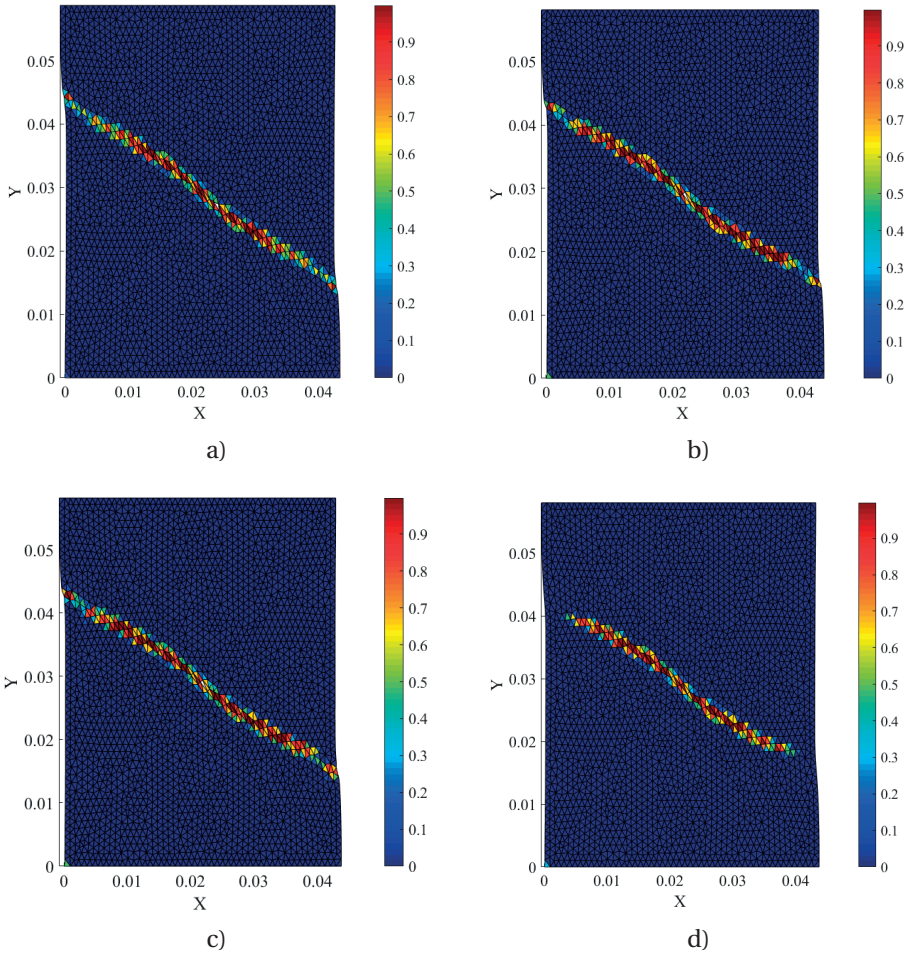

Figure 5.4: Convergence study of damage zone front propagation velocity, a) v^* of 10000 mms^{-1}, b) v^* of 250000 mms^{-1}, c) v^* of 500000 mms^{-1} and , d) v^* of 1000000 mms^{-1}.

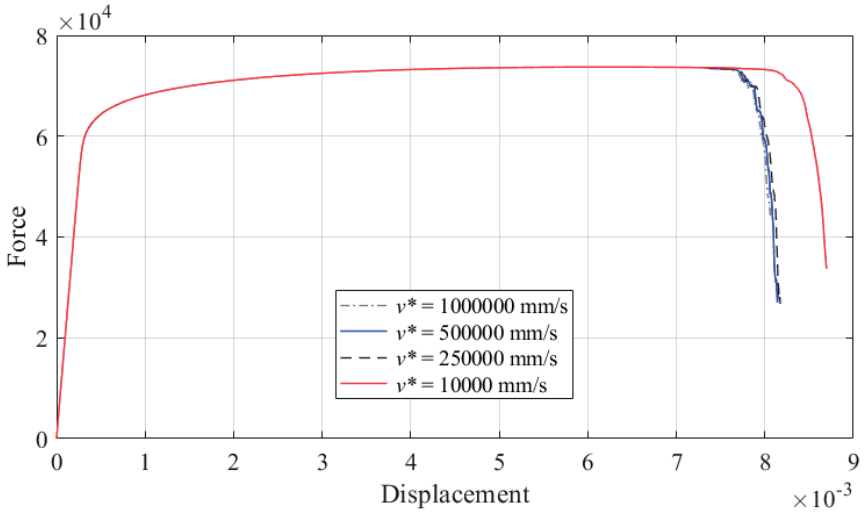

Figure 5.5: Force versus displacement relationships at convergence study with respect to the propagation velocity v^*. The element size is l_e = 1mm.

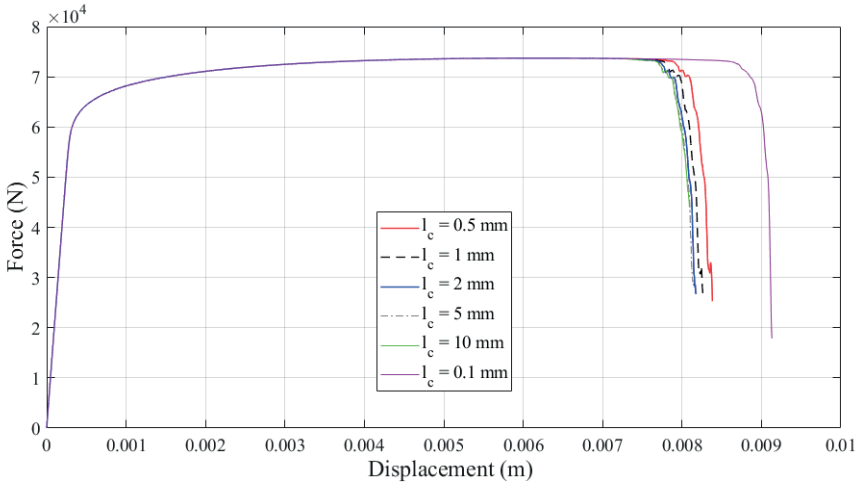

Figure 5.6: Force versus displacement relation for different choices of the internal length parameter.

zone. The fracture criterion utilised herein is von Mises yield stress given the fact there was no data available in terms of Johnson-Cook fracture criterion for carbon-steel $SA333Gr6$.

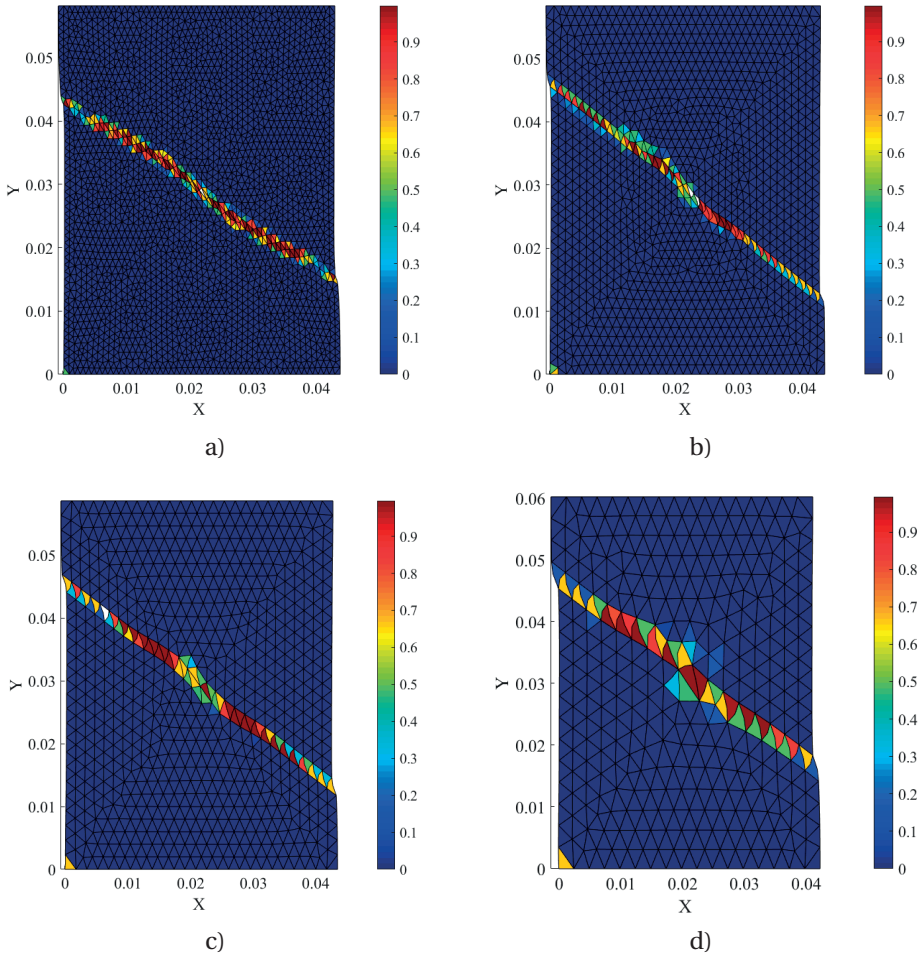

Figure 5.7: Convergence study with respect to mesh size, a) l_e of 1 mm, b) l_e of 1.5 mm, c) l_e of 2 mm, and , d) l_e of 3 mm.

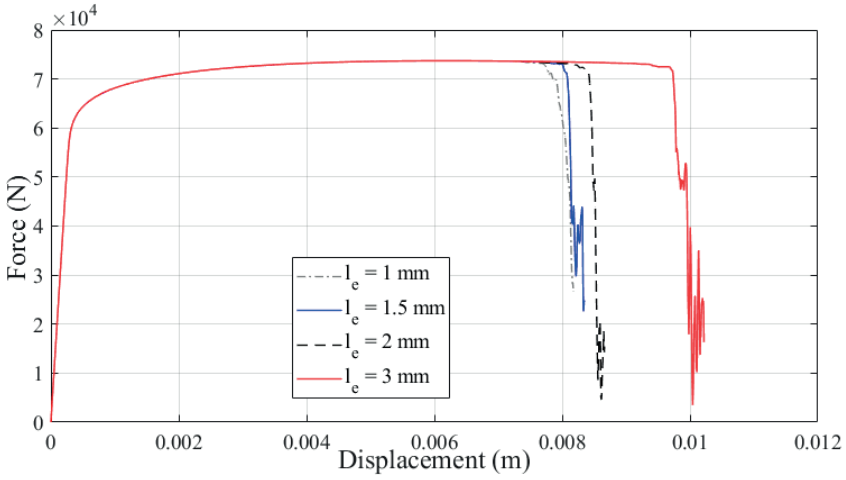

Figure 5.8: Force versus displacement relations for different choices of element size. The internal length is l_c=2mm.

Table 5.2: Material parameters used for Johnson-Cook model for the carbon-steel pipe.

A [MPa]	B [MPa]	n	E [GPa]	ν	ρ [$\frac{kg}{m^3}$]
288	558	0.535	180	0.3	7850

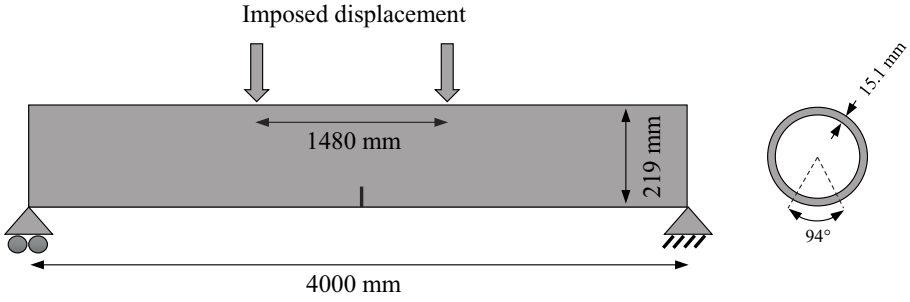

Figure 5.9: Four point bending test of a pre-notched carbon-steel pipe

SENSITIVITY STUDY WITH RESPECT TO PROPAGATION VELOCITY

In this subsection, and in line with the previous example, in order to find the propagation velocity v^* at which convergence in results is achieved, five cases with different propagation ve-

locities are investigated. As seen in Figure 5.10, different velocities studied are between 10 m/s and 500 m/s and convergence in the result is observed at 100 m/s. Given the converged propagation velocity further investigation on sensitivity of the results with respect to mesh size may be carried out.

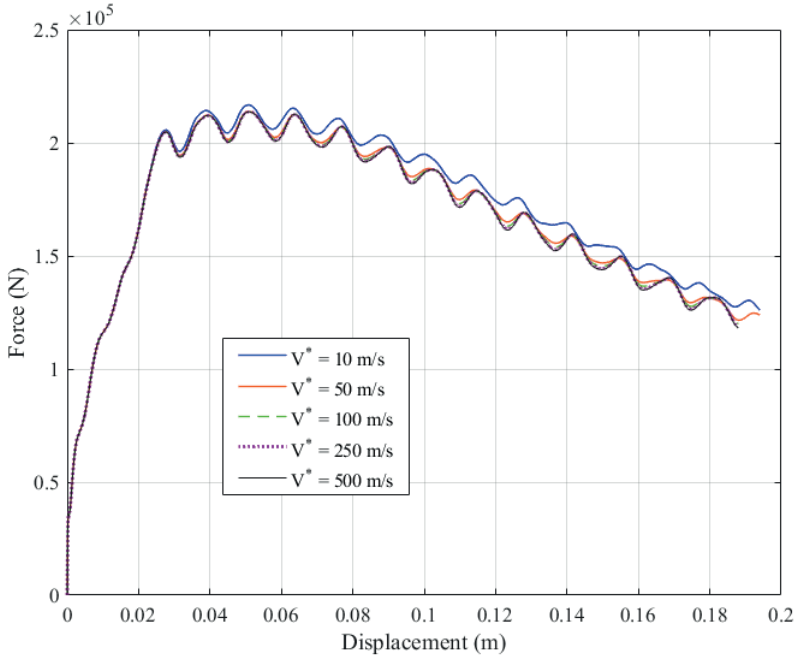

Figure 5.10: Force versus displacement for different propagation velocities

SENSITIVITY STUDY WITH RESPECT TO MESH SIZE

In order to validate the damage model, two different discretisations are utilised where for the coarse and fine cases, size of the mesh around the damage zone is respectively 20 mm and 12 mm. In line with the findings in the previous example, the internal length parameter is assigned the same length as the mesh size around the damage zone. Figure 5.11, 5.12 and 5.13 present respectively the deformed state of the pipe once loaded and the force versus displacement measured at the points where displacement is prescribed for. As it is seen in Figure 5.13, Comparing the results with the experimental result in [33], the response captured using the proposed approach is in perfect agreement with experimental one.

5.5. CONCLUDING REMARKS

In the current contribution, a method to represent the ductile fracture process of thin-walled structures under high strain rate loads is presented. For this, a scalar damage enhanced model

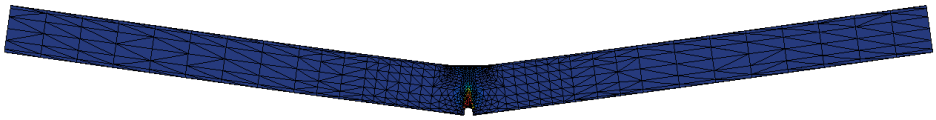

Figure 5.11: Deformed state of the pipe once loaded

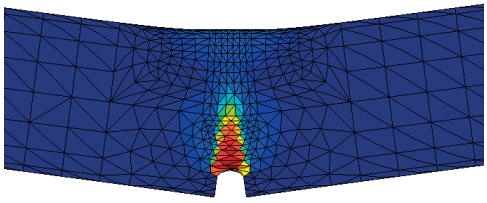

Figure 5.12: Deformed state of the pipe once loaded

where the damage is induced by shear deformation via degradation of the isochoric part of the effective material is developed. To represent the response of the effective material, visco-elaso-plastic model of Johnson-Cook is employed, where evolution of the damage is governed by the balance between the energy dissipation due to damage driving energy and the energy dissipation due to production of new fracture surface area. Progression of the fracture surface is formulated in terms of the fracture area propagation velocity and an internal length parameter specifying the diffuse character of the fracture area. Therein, the inelastic part of the contribution to the damage driving energy is regarded to be dominant whereas onset of the damage evolution occurs once the threshold is reached. Based on the numerical examples presented, it is observed that lowering the propagation velocity leads to a more ductile behaviour which is due to more time available for the damage to develop. Moreover, by increasing the propagation velocity convergence in the response is achieved. Performing the sensitivity studies on the internal length parameter and the element size, it is shown that by assigning a lower internal length the response becomes more ductile. It is also seen that by increasing the internal length convergence in the response is obtained. Another finding is that the internal length should be assigned such that it is the same size as the element size or preferably larger than the element size employed.

As the validation case, a four point bending test of a pre-notched pipe is investigated. In line with the findings of the first examples, the internal length parameter is assigned the same size as the average element size within the neighbourhood of the damage zone. Performing the sensitivity study with respect to the propagation velocity, the velocity at which convergence is obtained is used to compare the response captured by the model against the experiment. Comparing the force versus displacement obtained from the proposed model to the experiment a perfect agreement between the two is seen. It shows the capability of the proposed approach to capture the accurate behaviour of the structure provided that the proper

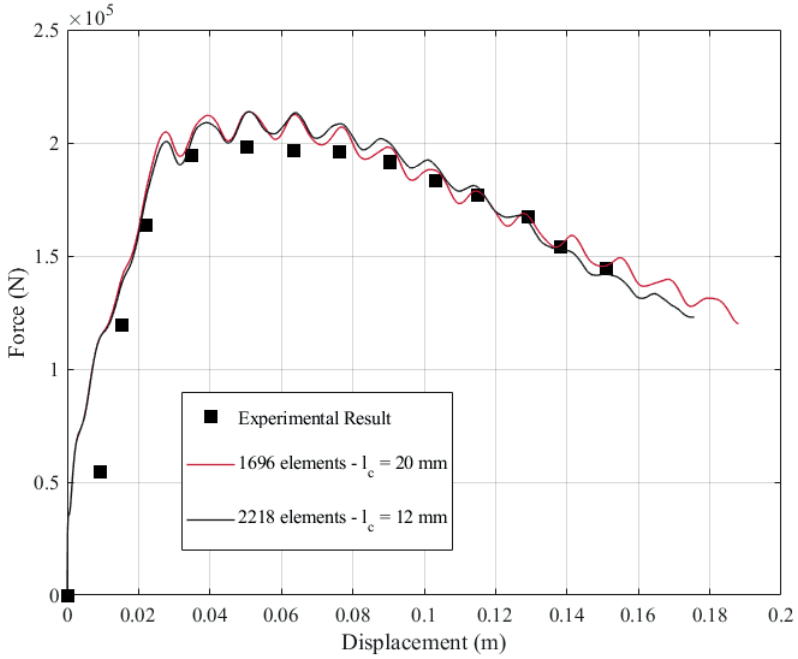

Figure 5.13: Force versus displacement for different mesh sizes

calibration for the parameters in the model is carried out.

REFERENCES

[1] R. Larsson, J. Mediavilla, and M. Fagerström, *Dynamic fracture modeling in shell structures based on XFEM,* International Journal for Numerical Methods in Engineering **86**, 499 (2010).

[2] S. Mostofizadeh, M. Fagerström, and R. Larsson, *Dynamic crack propagation in elasto-plastic thin-walled structures: Modelling and validation,* International Journal for Numerical Methods in Engineering **96**, 63 (2013).

[3] S. Mostofizadeh, M. Fagerström, and R. Larsson, *XFEM based element subscale refinement for detailed representation of crack propagation in large scale analyses,* International Journal for Numerical Methods in Engineering **10**, 549 (2016).

[4] S. Mostofizadeh, F. van der Meer, M. Fagerström, R. Larsson, and B. Sluys, *An element subscale refinement for representation of the progressive fracture based on the phantom node approach,* Computers and Structures **196**, 134 (2018).

[5] I. Babuška and J. Melenk, *The partition of unity finite element method: Basic theory and applications,* Computer Methods in Applied Mechanics and Engineering **139**, 289 (1996).

[6] T. Belytschko and T. Black, *Elastic crack growth in finite elements with minimal remeshing,* International Journal for Numerical Methods in Engineering **45**, 601 (1999).

[7] N. Moës, J. Dolbow, and T. Belytschko, *A finite element method for crack growth without remeshing,* International Journal for Numerical Methods in Engineering **46**, 131 (1999).

[8] G. Wells and L. Sluys, *A new method for modelling cohesive cracks using finite elements,* International Journal for Numerical Methods in Engineering **50**, 2667 (2001).

[9] A. L. Gurson, *Continuum theory of ductile rupture by void nucleation and growth: Part i-yield criteria and flow rules for porous ductile media,* J. Engrg. Mater. Technology **99**, 2– (1977).

[10] A. Needleman and V. Tvergaard, *An analysis of ductile rupture in notched bars,* J. Mech. Phys. Solids **32**, 461– (1984).

[11] T. Pardoen and J. Hutchinson, *An extended model for void growth and coalescence,* Journal of the Mechanics and Physics of Solids **48**, 2467– (2000).

[12] F. Reusch and D. Svendsen, B. amd Klingbeil, *Local and non-local gurson-based ductile damage and failure modelling at large deformation,* European Journal of Mechanics A/Solids **22**, 779– (2003).

[13] O. Abiri and L. Lindgren, *Non-local damage models in manufacturing simulations,* European Journal of Mechanics - A/Solids **49**, 548 (2015).

[14] M. Ambati, T. Gerasimov, and L. De Lorenzis, *A review on phase-field models of brittle fracture and a new fast hybrid formulation,* Computational Mechanics **55**, 383 (2014).

[15] B. Bourdin, G. A. Francfort, and J. J. Marigo, *Numerical experiments in revisited brittle fracture,* Journal of the Mechanics and Physics of Solids **48**, 797 (2000).

[16] C. Miehe, F. Welschinger, and M. Hofacker, *Thermodynamically consistent phase-field models of fracture: Variational principles and multi-field fe implementations,* International Journal for Numerical Methods in Engineering **83**, 1273 (2010).

[17] C. Miehe, L. M. Schanzel, and H. Ulmer, *Phase field modeling of fracture in multi-physics problems. part i. balance of crack surface and failure criterioa for brittle crack propagation in thermo-elastic solids,* Comput Methods Appl Mech Engrg **294**, 449 (2015).

[18] M. Ambati, T. Gerasimov, and L. De Lorenzis, *Phase-field modeling of ductile fracture,* Computational Mechanics **55**, 1017 (2015).

[19] C. Miehe, M. Hofacker, L. Schanzel, and F. Aldakheel, *Phase field modeling of fracture in multi-physics problems. part ii. coupled brittle-to-ductile failure criteria and crack propagation in thermo-elastic–plastic solids,* Comput Methods Appl Mech Engrg **294**, 486 (2015).

[20] S. Razanica, R. Larsson, and B. L. Josefson, *A ductile fracture model based on continuum thermodynamics and damage,* Mechanics of Materials , DOI: 10.1016/j.mechmat.2019.103197 (2019).

[21] G. Johnson and W. Cook, *A constitutive model and data for metals subjected to large strains, high strain rates and high temperatures,* (Hague, Netherlands, April 19–21, 1983).

[22] R. Larsson, S. Razanica, and B. Josefson, *Mesh objective continuum damage models for ductile fracture,* International Journal for Numerical Methods in Engineering **106**, 840 (2015).

[23] G. Johnson and W. Cook, *Fracture characteristics of three metals subjected to various strains, strain rates, temperatures and pressures,* Engineering Fracture Mechanics **21**, 31 (1985).

[24] R. Larsson, R. Gutkin, and M. Rouhi, *Damage growth and strain localization in compressive loaded fiber reinforced composites,* Mechanics of Materialas **127**, 77 (2018).

[25] P. Areias and T. Belytschko, *Non-linear analysis of shells with arbitrary evolving cracks using xfem,* International Journal for Numerical Methods in Engineering **62**, 384 (2005).

[26] P. Areias, J. Song, and T. Belytschko, *Analysis of fracture in thin shells by overlapping paired elements,* Computer methods in applied mechanics and engineering **195**, 5343 (2006).

[27] J. Kiendl, M. Ambati, L. De Lorenzis, H. Gomez, and A. Reali, *Phase-field description of brittle fracture in plates and shells,* Comput. Methods Appl. Mech. Engrg. **312**, 374 (2016).

[28] P. Betsch, F. Gruttmann, and E. Stein, *A 4 node finite shell element for the implementation of general hyperelastic 3D-elasticity at finite strains,* Computer Methods in Applied Mechanics and Engineering **130**, 57– (1995).

[29] H. Parisch, *A continuum-based shell theory for non-linear applications,* International Journal for Numerical Methods in Engineering **38**, 1855 (1995).

[30] M. Bischoff and E. Ramm, *On the physical significance of higher order kinematic and static variables in a three-dimensional shell formulation,* International Journal of Solids and Structures **37**, 6933 (2000).

[31] G. Ljustina, M. Fagerström, and R. Larsson, *Hypo and hyperinelasticity applied to modeling of compact graphite iron machining simulations,* European Journal of Mechanics - A/Solids **37**, 57 (2012).

[32] G. Ljustina, M. Fagerström, and R. Larsson, *Rate sensitive continuum damage models and mesh dependence in finite element analyses,* The Scientific World Journal **2014** (2014).

[33] J. Chattopadhyay, B. Dutta, and H. Kushwaha, *Experimental and analytical study of tpb specimen and throughwall circumferentially cracked straight pipe,* International Journal of Pressure Vessels and Piping **77**, 455 (2000).

6

CONCLUSION

A framework capable of analysing ductile fracture of thin-walled steel structures subjected to high strain rates has been developed. Of particular importance was the application to large scale structures for which an efficient numerical procedure is required.

As the first contribution, a modelling approach for dynamic crack propagation in elasto-plastic thin-walled structures is proposed. For that, a hypoelastic-inelastic framework based on the Johnson and Cook phenomenological model is employed. Therefore, temperature and plastic strain rate dependencies that are of high significance in case of impact load are accounted for. To represent the shell kinematics a 7-parameter shell formulation with extensible directors and second order inhomogeneous thickness deformation is used. To model the through-the-thickness crack, the shifted version of XFEM is utilised. Resisting forces at the failure process zone are represented using a damage-viscoplastic cohesive zone model. To validate the proposed model different numerical examples are presented and the results obtained are shown to correlate well with the experiments. Based on the results, accounting for the large plastic deformation and including the rate dependency in both bulk and cohesive zone models are of high significance. Furthermore, in order to mitigate the oscillations triggered during crack propagation, two methods are investigated which are proven to be of computational importance for explicit temporal integration. Another finding in the current development is that if the crack is made to propagate in a more smooth way by extending it step-wise with shorter segments less oscillations occur. This is due to the fact that a smaller part of the domain is affected by the enrichment to introduce the discontinuity.

Given the intended application of the current developments to large scale structures, furnishing a coarse mesh for spatial discretisation is preferable. It is therefore of importance to represent the crack path with more detail without resorting to the standard remeshing procedures which increases the computational cost. To this end, the second contribution concerns representation of the discontinuity via an XFEM based subscale refinement of the crack tip element where the spatial discretisation of the domain remains intact. For this, a combination of subscale refinement of the continuous and discontinuous fields with dynamic condensation of the additional continuous and discontinuous degrees of freedom is employed. The proposed method is verified using various numerical examples and it is shown that accurate kinematical representation of the kinks and crack tip within an element is captured. Moreover,

it is shown that a more detailed crack path representation may result in a significantly different load-displacement relation. It is caused by a different crack path and orientation captured which also leads to a different mass distribution. It is also noted that the proposed approach allows for the introduction of shorter crack segments during crack propagation which is observed to decrease the artificial oscillations in the structural response.

In line with the previous development, the third contribution involves a new phantom node based method to represent the crack tips and kinks within an element. The main advantage compared to the previous developments lies in the more straightforward implementation of the phantom node method. Similar to XFEM, this approach considers each cracked element as a sub-scale problem for which additional nodes are introduced. To couple the sub-scale problem with the macro-scale domain, a dynamic condensation method is employed which results in a more efficient computation. Using this approach, further refinement around the crack tip needed to capture the accurate response can be avoided. The proposed method is presented using a 6-node triangle element, however it is applicable to any type of finite element. To investigate the accuracy of the proposed method, several examples are presented and it is shown that for both hypo-elastic and hypo-plastic cases the accurate kinematics are captured. Moreover, cohesive traction along the crack is also represented accurately.

As a final contribution, in order to investigate a diffuse failure modelling approach, a scalar damage enhanced model is developed. In this, the damage is governed by shear deformation via degradation of the isochoric part of the effective material. The behaviour of the effective material is captured via a visco-elasto-plastic framework based on the Johnson-Cook model. For damage evolution, an energy balance is specified between the damage driving dissipation and the dissipation due to production of new fracture surface. To specify diffuse fracture and its progression, it is formulated in terms of the fracture area progression velocity, the rate of damage, and the internal length parameter representing the width of the diffuse fracture area. In order to perform sensitivity analyses with respect to the various parameters in the model, different examples are presented. Based on the results, it is shown that lowering the propagation velocity leads to a more ductile behaviour. This is due to the fact that damage has time to develop. As expected, by increasing the propagation velocity, convergence in the force-displacement curve is observed. Investigating the influence of the internal length parameter, it is observed that considering a smaller internal length parameter results in a more ductile behaviour. It is also shown that increasing the internal length parameter, convergence in the force-displacement curve is achieved. Furthermore it is noted that the internal length parameter needs to be assigned properly such that it is not lower than the average element size in the vicinity of the failure process zone. Given all the aforementioned findings regarding different parameters in the model, a four point bending test as a validation case is investigated and the response obtained is found to be in perfect agreement with the experiment. It shows the capability of the proposed model to accurately represent the response of the structure provided that calibration of the internal parameters is carried out properly.

In the current research, main emphasis was on the accurate modelling of the shell kinematics, the representation of the propagating strong discontinuity and the diffuse fracture in the domain under consideration. Capturing the accurate behaviour of the bulk material as well as the interface material were also of importance to propose a framework capable of representing the response of a thin-walled structure under impact load case. However, there are other influential factors and details which can be further explored. Future research may investigate developing a reliable mass scaling scheme to lower the computational cost, yet maintaining the accurate kinematics of the shell formulation required. It is considered to be of high importance to be able to model behaviour of the large scale structures within reasonable time

and cost. In the current research, initial steps towards this goal are taken, however due to lack of validation study it is not included in this manuscript. An addition to the current kinematic representation of the crack to address in future research is a curved crack path within cracked elements. To clarify, in case of elements spanning along a curvature, proper representation of the crack path such that it follows the curvature within the element is of significance. Ignoring such details once modelling shell structures with a coarse mesh may result in large errors in the crack propagation path. In the current research initial developments to tackle this problem are carried out, however due to lack of experimental result and validation test cases, it is not addressed in this manuscript. Considering the main application of the current research, impact loading, accounting for temperature variation in material can result in a more accurate response captured. Addressing this requires a thermo-mechanical coupling model which can be studied in future research.

ACKNOWLEDGEMENTS

This research was carried out in the project M41.2.10378 "Failure of thin-walled structures under blast and impact loading" within the framework of the Research Program of the Materials innovation institute M2i, (www.m2i.nl), at the Department of Applied Mechanics at Chalmers University of Technology and Faculty of Civil Engineering and Geosciences at Delft University of Technology.

First of all, I would like to take the opportunity to thank my excellent supervisors at Chalmers University of Technology, Professor Ragnar Larsson and my co-supervisor Associate professor Martin Fagerström, for their invaluable guidance, involvement, encouragement and especially their endless patience and understanding. I would also like to express my gratitude and appreciation to my supervisors at Delft University of Technology, Professor Bert Sluys and Frans van der Meer, for their support and guidance during this research.

Furthermore, I want to thank my friends and colleagues at the Division of Material and Computational Mechanics at Chalmers and structural mechanics section at Delft for creating a motivating and pleasant working environment. I specially thank Mohammad Rouhi, Amin Karamnejad, Mehdi Musivand Arzanfudi and Senad Razanica for being such a great friend during this journey.

Most importantly, I would like to thank my lovely parents and my sister, for their endless support through these years. Last, but definitely not least, I wish to thank my wonderful wife, Shabnam Ilchikabir, and my lovely baby girl , Elena, for all their love and patience.

Salar Mostofizadeh
Gothenburg, Oct 2019

A

APPENDIX A

A.1. STRESS RESULTANTS

The through-thickness integrated stress resultants referred to in Eq. (2.26) are defined as

$$\mathbf{N}^{\alpha} = \int_{-h_0/2}^{h_0/2} S^{\alpha k}\mathbf{g}_{\mathrm{ck}} j_0 \mathrm{d}\xi \tag{A.1}$$

$$\mathbf{M}^{\alpha} = \int_{-h_0/2}^{h_0/2} \left(1+\frac{1}{2}\gamma\xi\right)\xi S^{\alpha k}\mathbf{g}_{\mathrm{ck}} j_0 \mathrm{d}\xi \tag{A.2}$$

$$\mathbf{T} = \int_{-h_0/2}^{h_0/2} \left(\left(1+\gamma\xi\right)S^{3k}\mathbf{g}_{\mathrm{ck}} + \frac{1}{2}\xi^2 S^{\alpha k}\cdot\mathbf{g}_{\mathrm{ck}}\gamma_{,\alpha}\right)\mathrm{j}_0 \mathrm{d}\xi \tag{A.3}$$

$$M_s^{\alpha} = \int_{-h_0/2}^{h_0/2} \frac{1}{2}\xi^2 S^{\alpha k}\mathbf{m}_c\cdot\mathbf{g}_{\mathrm{ck}} j_0 \mathrm{d}\xi \tag{A.4}$$

$$T_s = \int_{-h_0/2}^{h_0/2} \left(\frac{1}{2}\xi^2 S^{\alpha k}\mathbf{m}_{c,\alpha}\cdot\mathbf{g}_{\mathrm{ck}} + \xi S^{3k}\mathbf{m}_c\cdot\mathbf{g}_{\mathrm{ck}}\right) j_0 \mathrm{d}\xi \tag{A.5}$$

$$\mathbf{N}_d^{\alpha} = \int_{-h_0/2}^{h_0/2} S^{\alpha k}\mathbf{g}_{\mathrm{ck}} j_0 \mathrm{d}\xi \tag{A.6}$$

$$\mathbf{M}_d^{\alpha} = \int_{-h_0/2}^{h_0/2} \xi S^{\alpha k}\mathbf{g}_{\mathrm{ck}} j_0 \mathrm{d}\xi \tag{A.7}$$

$$\mathbf{T}_d = \int_{-h_0/2}^{h_0/2} S^{3k}\mathbf{g}_{\mathrm{ck}} j_0 \mathrm{d}\xi \tag{A.8}$$

$$\mathbf{n}_0 = \int_{-h_0/2}^{h_0/2} \bar{\mathbf{t}}_1 \mathrm{d}\xi \tag{A.9}$$

$$\tilde{\mathbf{m}}_0 = \int_{-h_0/2}^{h_0/2} \xi\left(1+\frac{1}{2}\xi\gamma\right)\bar{\mathbf{t}}_1 \mathrm{d}\xi \tag{A.10}$$

$$m_s = \int_{-h_0/2}^{h_0/2} \frac{1}{2}\xi^2\mathbf{m}_c\cdot\bar{\mathbf{t}}_1 \mathrm{d}\xi \tag{A.11}$$

$$\mathbf{m}_0 = \int_{-h_0/2}^{h_0/2} \xi\bar{\mathbf{t}}_1 \mathrm{d}\xi \tag{A.12}$$

$$\mathbf{n}_S = \int_{-h_0/2}^{h_0/2} \mathbf{t}_1 \mathrm{d}\xi \tag{A.13}$$

$$\mathbf{m}_S = \int_{-h_0/2}^{h_0/2} \xi\mathbf{t}_1 \mathrm{d}\xi \tag{A.14}$$

where $S^{\alpha k}$ are the contra-variant components of the second Piola Kirchhoff stress tensor $\mathbf{S}$, $\mathbf{g}_{\mathrm{ck}}$ the spatial co-variant basis vectors defined in Eq. (2.17), j_0 the relation between area and volumetric measures of the shell defined in Eq. (2.24) and $\mathbf{t}_1$ is the nominal traction vector of the cohesive zone defined by $\mathbf{t}_1 = \mathbf{P}^t\cdot\mathbf{N}_S$. It should be remarked that these stress resultants are very similar to the ones obtained in the formulation by Larsson *et al.* [1]. However, since the discontinuity enrichment is introduced in a different way in the current paper, they are not identically the same.

A.2. MASS MATRIX

The consistent mass matrix $\hat{\mathbf{M}}$ and the convective mass (force) $\hat{\mathbf{M}}^{\text{con}}$ introduced in Eq. (2.23) have, for the current kinematical representation, the explicit forms

$$\hat{\mathbf{M}} = \int_{-\frac{h_0}{2}}^{\frac{h_0}{2}} \frac{\rho_0}{4} \cdot \begin{pmatrix} 4\mathbf{1} & 2\xi\left(2+\gamma\xi\right)\mathbf{1} & 2\mathbf{m}_c\xi^2 & 4\mathbf{1} & 4\xi\mathbf{1} \\ 2\xi\left(2+\gamma\xi\right)\mathbf{1} & \xi^2\left(2+\gamma\xi\right)^2\mathbf{1} & \xi^3\left(2+\gamma\xi\right)\mathbf{m}_c & 2\xi\left(2+\gamma\xi\right)\mathbf{1} & 2\xi^2\left(2+\gamma\xi\right)\mathbf{1} \\ 2\xi^2\mathbf{m}_c & \xi^3\left(2+\gamma\xi\right)\mathbf{m}_c & \xi^4\mathbf{m}_c\cdot\mathbf{m}_c & 2\xi^2\mathbf{m}_c & 2\xi^3\mathbf{m}_c \\ 4\mathbf{1} & 2\xi\left(2+\gamma\xi\right)\mathbf{1} & 2\mathbf{m}_c\xi^2 & 4\mathbf{1} & 4\xi\mathbf{1} \\ 4\xi\mathbf{1} & 2\xi^2\left(2+\gamma\xi\right)\mathbf{1} & 2\mathbf{m}_c\xi^3 & 4\xi\mathbf{1} & 4\xi^2\mathbf{1} \end{pmatrix} \cdot j_0[\xi]\,\mathrm{d}\xi \tag{A.15}$$

and

$$\hat{\mathbf{M}}^{\text{con}} = \int_{-\frac{h}{2}}^{\frac{h}{2}} \rho_0 \begin{pmatrix} \xi^2\mathbf{1} \\ \frac{1}{2}\xi^3\left(2+\gamma\xi\right)\mathbf{1} \\ \frac{1}{2}\xi^4\mathbf{m}_c^t \\ \xi^2\mathbf{1} \\ \xi^3\mathbf{1} \end{pmatrix} \dot{\mathbf{m}}_c\dot{\gamma}\, j_0[\xi]\,\mathrm{d}\xi. \tag{A.16}$$

It turns out that the mass contributions can be integrated explicitly in the thickness direction, whereby in view of Eq. (2.24) it is noted that the volume measure $j_0[\xi]$ (relating to the undeformed configuration) can to be developed in terms of the covariant vectors as

$$j_0 = \frac{b_0}{\omega_0} = a_1\xi^2 + a_2\xi + a_3 \tag{A.17}$$

where

$$a_1 = \frac{|\mathbf{M}_{\Phi,1}\times\mathbf{M}_{\Phi,2}|}{|\mathbf{\Phi}_{,1}\times\mathbf{\Phi}_{,2}|}, a_2 = \frac{\mathbf{M}_\Phi\cdot\left(\mathbf{\Phi}_1\times\mathbf{M}_{\Phi,2}+\mathbf{M}_{\Phi,1}\times\mathbf{\Phi}_2\right)}{|\mathbf{\Phi}_{,1}\times\mathbf{\Phi}_{,2}|}\,,\ a_3 = 1 \tag{A.18}$$

Hence, the explicit integrated result of the consistent mass matrix $\hat{\mathbf{M}}$ in Eq. (A.15) is in view of (A.17) obtained as

$$\hat{\mathbf{M}} = \begin{pmatrix} \mathbf{M}_{11} & \mathbf{M}_{12} & \mathbf{M}_{13} & \mathbf{M}_{14} & \mathbf{M}_{15} \\ \mathbf{M}_{21} & \mathbf{M}_{22} & \mathbf{M}_{23} & \mathbf{M}_{24} & \mathbf{M}_{25} \\ \mathbf{M}_{31} & \mathbf{M}_{32} & \mathbf{M}_{33} & \mathbf{M}_{34} & \mathbf{M}_{35} \\ \mathbf{M}_{41} & \mathbf{M}_{42} & \mathbf{M}_{43} & \mathbf{M}_{44} & \mathbf{M}_{45} \\ \mathbf{M}_{51} & \mathbf{M}_{52} & \mathbf{M}_{53} & \mathbf{M}_{54} & \mathbf{M}_{55} \end{pmatrix} \tag{A.19}$$

where one obtains e.g. the components

$$\begin{pmatrix} \mathbf{M}_{11} & \mathbf{M}_{12} \\ \mathbf{M}_{21} & \mathbf{M}_{22} \end{pmatrix} = \\ = \rho_0 \begin{pmatrix} \left(\frac{1}{12}h^3a_1 + ha_3\right)\mathbf{1} & \frac{1}{480}h^3\left(3h^2\gamma a_1 + 40a_2 + 20\gamma a_3\right)\mathbf{1} \\ \frac{1}{480}h^3\left(3h^2\gamma a_1 + 40a_2 + 20\gamma a_3\right)\mathbf{1} & \frac{h^3\left(3h^2\left(\left(112+5h^2\gamma^2\right)a_1+112\gamma a_2\right)+28\left(80+3h^2\gamma^2\right)a_3\right)}{26880}\mathbf{1} \end{pmatrix} \tag{A.20}$$

We also obtain the integrated result for the convective contribution $\hat{\mathbf{M}}^{\text{con}}$ in Eq. (A.16) as

$$\hat{\mathbf{M}}^{\text{con}} = \rho_0 \begin{pmatrix} \frac{1}{240} h^3 \left(3h^2 a_1 + 20 a_3\right) \\ \frac{h^5 \left(5h^2 \gamma a_1 + 56 a_2 + 28 \gamma a_3\right)}{4480} \\ \frac{h^5 \left(5h^2 a_1 + 28 a_3\right)}{4480} \mathbf{m}_c^t \\ \frac{1}{240} h^3 \left(3h^2 a_1 + 20 a_3\right) \\ \frac{1}{80} h^5 a_2 \end{pmatrix} \dot{\mathbf{m}}_c \dot{\gamma} \tag{A.21}$$

REFERENCES

[1] R. Larsson, J. Mediavilla, and M. Fagerström, *Dynamic fracture modeling in shell structures based on XFEM,* International Journal for Numerical Methods in Engineering **86**, 499 (2010).

B

APPENDIX B

B.1. EXPLICIT TERMS IN THE DISCRETISED FORM OF THE MOMENTUM BALANCE

Individual terms in Eq. (3.19) are defined as:

$$\mathbf{M}^e_{cc} = \int_{B^e_0} \rho_0 \left(\hat{\boldsymbol{\psi}}\right)^t \hat{\boldsymbol{\psi}} \, \mathrm{dV} \tag{B.1}$$

$$\mathbf{M}^e_{cd} = \left(\mathbf{M}^e_{dc}\right)^t = \int_{B^e_0} \rho_0 \left(\hat{\boldsymbol{\psi}}\right)^t \hat{\boldsymbol{\psi}}_{\tilde{H}_S} \, \mathrm{dV} \tag{B.2}$$

$$\mathbf{M}^e_{cc_s} = \left(\mathbf{M}^e_{c_s c}\right)^t = \int_{B^e_0} \rho_0 \left(\hat{\boldsymbol{\psi}}\right)^t \hat{\boldsymbol{\psi}} \tag{B.3}$$

$$\mathbf{M}^e_{cd_s} = \left(\mathbf{M}^e_{d_s c}\right)^t = \int_{B^e_0} \rho_0 \left(\hat{\boldsymbol{\psi}}\right)^t \hat{\boldsymbol{\psi}}_{\tilde{H}_S} \, \mathrm{dV} \tag{B.4}$$

$$\mathbf{M}^e_{dd} = \int_{B^e_0} \rho_0 \left(\hat{\boldsymbol{\psi}}_{\tilde{H}_S}\right)^t \hat{\boldsymbol{\psi}}_{\tilde{H}_S} \, \mathrm{dV} \tag{B.5}$$

$$\mathbf{M}^e_{dc_s} = \left(\mathbf{M}^e_{c_s d}\right)^t = \int_{B^e_0} \rho_0 \left(\hat{\boldsymbol{\psi}}_{\tilde{H}_S}\right)^t \hat{\boldsymbol{\psi}} \, \mathrm{dV} \tag{B.6}$$

$$\mathbf{M}^e_{dd_s} = \left(\mathbf{M}^e_{d_s d}\right)^t = \int_{B^e_0} \rho_0 \left(\hat{\boldsymbol{\psi}}_{\tilde{H}_S}\right)^t \hat{\boldsymbol{\psi}}_{\tilde{H}_S} \, \mathrm{dV} \tag{B.7}$$

$$\mathbf{M}^e_{c_s c_s} = \int_{B^e_0} \rho_0 \left(\hat{\boldsymbol{\psi}}\right)^t \hat{\boldsymbol{\psi}} \, \mathrm{dV} \tag{B.8}$$

$$\mathbf{M}^e_{c_s d_s} = \left(\mathbf{M}^e_{d_s c_s}\right)^t = \int_{B^e_0} \rho_0 \left(\hat{\boldsymbol{\psi}}\right)^t \hat{\boldsymbol{\psi}}_{\tilde{H}_S} \, \mathrm{dV} \tag{B.9}$$

$$\mathbf{M}^e_{d_s d_s} = \int_{B^e_0} \rho_0 \left(\hat{\boldsymbol{\psi}}_{\tilde{H}_S}\right)^t \hat{\boldsymbol{\psi}}_{\tilde{H}_S} \, \mathrm{dV} \tag{B.10}$$

$$\mathbf{f}^{e,ext}_c = \int_{\partial B^e_0} \left(\hat{\boldsymbol{\psi}}\right)^t \bar{\mathbf{t}}_1 \, \mathrm{dA} \tag{B.11}$$

$$\mathbf{f}^{e,int}_c = \int_{B^e_0} \left(\hat{\mathbf{B}}\right)^t \hat{\mathbf{P}}^t \, \mathrm{dV} \tag{B.12}$$

$$\mathbf{f}^{e,ext}_d = \int_{\partial B^e_0} \left(\hat{\boldsymbol{\psi}}_{\tilde{H}_S}\right)^t \bar{\mathbf{t}}_1 \, \mathrm{dA} \tag{B.13}$$

$$\mathbf{f}^{e,int}_d = \int_{B^e_0} \left(\hat{\mathbf{B}}_{\tilde{H}_S}\right)^t \hat{\mathbf{P}}^t \, \mathrm{dV} \tag{B.14}$$

$$\mathbf{f}^{e,coh}_d = \int_{\Gamma^e_S} \left(\hat{\boldsymbol{\psi}}_{\tilde{H}_S}\right)^t \mathbf{t}_1 \, \mathrm{dA} \tag{B.15}$$

$$\mathbf{f}^{e,int}_{c_s} = \int_{B^e_0} \left(\hat{\mathbf{B}}\right)^t \hat{\mathbf{P}}^t \, \mathrm{dV} \tag{B.16}$$

$$\mathbf{f}^{e,int}_{d_s} = \int_{B^e_0} \left(\hat{\mathbf{B}}_{\tilde{H}_S}\right)^t \hat{\mathbf{P}}^t \, \mathrm{dV} \tag{B.17}$$

$$\mathbf{f}^{e,coh}_{d_s} = \int_{\Gamma^e_S} \left(\hat{\boldsymbol{\psi}}_{\tilde{H}_S}\right)^t \mathbf{t}_1 \, \mathrm{dA}. \tag{B.18}$$

Individual terms in Eq. (3.67) are defined as:

$$\mathbf{M}^e_{cc} = \int_{\Omega^e_0} \rho_0 \mathbf{N}_1^{FE\,t} \hat{\mathbf{M}} \mathbf{N}_1^{FE}\, \omega_0 \mathrm{d}\xi_1 \mathrm{d}\xi_2 \tag{B.19}$$

$$\mathbf{M}^e_{cd} = \left(\mathbf{M}^e_{dc}\right)^t = \int_{\Omega^e_0} \rho_0 \mathbf{N}_1^{FE\,t} \hat{\mathbf{M}} \mathbf{N}_2^{FE}\, \omega_0 \mathrm{d}\xi_1 \mathrm{d}\xi_2 \tag{B.20}$$

$$\mathbf{M}^e_{cc_s} = \left(\mathbf{M}^e_{c_s c}\right)^t = \int_{\Omega^e_0} \rho_0 \mathbf{N}_1^{FE\,t} \hat{\mathbf{M}} \mathbf{N}_3^{FE}\, \omega_0 \mathrm{d}\xi_1 \mathrm{d}\xi_2 \tag{B.21}$$

$$\mathbf{M}^e_{cd_s} = \left(\mathbf{M}^e_{d_s c}\right)^t = \int_{\Omega^e_0} \rho_0 \mathbf{N}_1^{FE\,t} \hat{\mathbf{M}} \mathbf{N}_4^{FE}\, \omega_0 \mathrm{d}\xi_1 \mathrm{d}\xi_2 \tag{B.22}$$

$$\mathbf{M}^e_{dd} = \int_{\Omega^e_0} \rho_0 \mathbf{N}_2^{FE\,t} \hat{\mathbf{M}} \mathbf{N}_2^{FE}\, \omega_0 \mathrm{d}\xi_1 \mathrm{d}\xi_2 \tag{B.23}$$

$$\mathbf{M}^e_{dc_s} = \left(\mathbf{M}^e_{c_s d}\right)^t = \int_{\Omega^e_0} \rho_0 \mathbf{N}_2^{FE\,t} \hat{\mathbf{M}} \mathbf{N}_3^{FE}\, \omega_0 \mathrm{d}\xi_1 \mathrm{d}\xi_2 \tag{B.24}$$

$$\mathbf{M}^e_{dd_s} = \left(\mathbf{M}^e_{d_s d}\right)^t = \int_{\Omega^e_0} \rho_0 \mathbf{N}_2^{FE\,t} \hat{\mathbf{M}} \mathbf{N}_4^{FE}\, \omega_0 \mathrm{d}\xi_1 \mathrm{d}\xi_2 \tag{B.25}$$

$$\mathbf{M}^e_{c_s c_s} = \int_{\Omega^e_0} \rho_0 \mathbf{N}_3^{FE\,t} \hat{\mathbf{M}} \mathbf{N}_3^{FE}\, \omega_0 \mathrm{d}\xi_1 \mathrm{d}\xi_2 \tag{B.26}$$

$$\mathbf{M}^e_{c_s d_s} = \left(\mathbf{M}^e_{d_s c_s}\right)^t = \int_{\Omega^e_0} \rho_0 \mathbf{N}_3^{FE\,t} \hat{\mathbf{M}} \mathbf{N}_4^{FE}\, \omega_0 \mathrm{d}\xi_1 \mathrm{d}\xi_2 \tag{B.27}$$

$$\mathbf{M}^e_{d_s d_s} = \int_{\Omega^e_0} \rho_0 \mathbf{N}_4^{FE\,t} \hat{\mathbf{M}} \mathbf{N}_4^{FE}\, \omega_0 \mathrm{d}\xi_1 \mathrm{d}\xi_2 \tag{B.28}$$

$$\mathbf{f}^{e,int}_c = \int_{\Omega^e_0} \mathbf{B}_1^{FE\,t} \hat{\mathbf{N}}_c\, \omega_0 \mathrm{d}\xi_1 \mathrm{d}\xi_2 \tag{B.29}$$

$$\mathbf{f}^{e,int}_d = \int_{\Omega^e_0} \mathbf{B}_3^{FE\,t} \hat{\mathbf{N}}_d\, \omega_0 \mathrm{d}\xi_1 \mathrm{d}\xi_2 \tag{B.30}$$

$$\mathbf{f}^{e,int}_{c_s} = \int_{\Omega^e_0} \mathbf{B}_2^{FE\,t} \hat{\mathbf{N}}_c\, \omega_0 \mathrm{d}\xi_1 \mathrm{d}\xi_2 \tag{B.31}$$

$$\mathbf{f}^{e,int}_{d_s} = \int_{\Omega^e_0} \mathbf{B}_4^{FE\,t} \hat{\mathbf{N}}_d\, \omega_0 \mathrm{d}\xi_1 \mathrm{d}\xi_2 \tag{B.32}$$

$$\mathbf{f}^{e,coh}_d = \oint_{\mathscr{L}_{\Gamma^e_S}} \mathbf{N}_5^{FE\,t} \hat{\mathbf{N}}_{\mathrm{coh}}\, \mathrm{d}\mathscr{L} \tag{B.33}$$

$$\mathbf{f}^{e,coh}_{d_s} = \oint_{\mathscr{L}_{\Gamma^e_S}} \mathbf{N}_6^{FE\,t} \hat{\mathbf{N}}_{\mathrm{coh}}\, \mathrm{d}\mathscr{L} \tag{B.34}$$

$$\tag{B.35}$$

B.2. STRESS RESULTANTS

The through-thickness integrated stress resultants referred to in Eq. (3.55) are defined as:

$$\mathbf{N}^{\alpha} = \int_{-h_0/2}^{h_0/2} S^{\alpha k}\mathbf{g}_{b_k} j_0 \mathrm{d}\xi \tag{B.36}$$

$$\mathbf{M}^{\alpha} = \int_{-h_0/2}^{h_0/2} \left(1+\frac{1}{2}\gamma\xi\right)\xi S^{\alpha k}\mathbf{g}_{c_k} j_0 \mathrm{d}\xi \tag{B.37}$$

$$\mathbf{T} = \int_{-h_0/2}^{h_0/2} \left(\left(1+\gamma\xi\right) S^{3k}\mathbf{g}_{b_k} + \frac{1}{2}\xi^2 S^{\alpha k}\cdot\mathbf{g}_{b_k}\gamma_{,\alpha}\right) \mathrm{j}_0 \mathrm{d}\xi \tag{B.38}$$

$$M_h^{\alpha} = \int_{-h_0/2}^{h_0/2} \frac{1}{2}\xi^2 S^{\alpha k}\mathbf{m}_c\cdot\mathbf{g}_{b_k} j_0 \mathrm{d}\xi \tag{B.39}$$

$$T_h = \int_{-h_0/2}^{h_0/2} \left(\frac{1}{2}\xi^2 S^{\alpha k}\mathbf{m}_{c,\alpha}\cdot\mathbf{g}_{b_k} + \xi S^{3k}\mathbf{m}_c\cdot\mathbf{g}_{b_k}\right) j_0 \mathrm{d}\xi \tag{B.40}$$

$$\mathbf{N}_d^{\alpha} = \int_{-h_0/2}^{h_0/2} S^{\alpha k}\mathbf{g}_{b_k} j_0 \mathrm{d}\xi \tag{B.41}$$

$$\mathbf{M}_d^{\alpha} = \int_{-h_0/2}^{h_0/2} \xi S^{\alpha k}\mathbf{g}_{b_k} j_0 \mathrm{d}\xi \tag{B.42}$$

$$\mathbf{T}_d = \int_{-h_0/2}^{h_0/2} S^{3k}\mathbf{g}_{b_k} j_0 \mathrm{d}\xi \tag{B.43}$$

$$\mathbf{n}_0 = \int_{-h_0/2}^{h_0/2} \bar{\mathbf{t}}_1 \mathrm{d}\xi \tag{B.44}$$

$$\tilde{\mathbf{m}}_0 = \int_{-h_0/2}^{h_0/2} \xi\left(1+\frac{1}{2}\xi\gamma\right)\bar{\mathbf{t}}_1 \mathrm{d}\xi \tag{B.45}$$

$$m_s = \int_{-h_0/2}^{h_0/2} \frac{1}{2}\xi^2\mathbf{m}_c\cdot\bar{\mathbf{t}}_1 \mathrm{d}\xi \tag{B.46}$$

$$\mathbf{m}_0 = \int_{-h_0/2}^{h_0/2} \xi\bar{\mathbf{t}}_1 \mathrm{d}\xi \tag{B.47}$$

$$\mathbf{n}_S = \int_{-h_0/2}^{h_0/2} \mathbf{t}_1 \mathrm{d}\xi \tag{B.48}$$

$$\mathbf{m}_S = \int_{-h_0/2}^{h_0/2} \xi\mathbf{t}_1 \mathrm{d}\xi \tag{B.49}$$

where $S^{\alpha k}$ are the contra-variant components of the second Piola Kirchhoff stress tensor $\mathbf{S}$, $\mathbf{g}_{b_k}$ the spatial co-variant basis vectors defined in Eq. (3.50), j_0 the relation between area and volumetric measures of the shell defined in Eq. (3.57) and $\mathbf{t}_1$ is the nominal traction vector of the cohesive zone defined by $\mathbf{t}_1 = \mathbf{P}^t\cdot\mathbf{N}_S$.

B.3. MASS MATRIX

The consistent mass matrix $\hat{\mathbf{M}}$ and the convective mass (force) $\hat{\mathbf{M}}^{\text{con}}$ introduced in Eq. (3.54) have, for the current kinematical representation, the explicit forms

$$\hat{\mathbf{M}} = \int_{-\frac{h_0}{2}}^{\frac{h_0}{2}} \frac{\rho_0}{4} \cdot \begin{pmatrix} 4\mathbf{1} & 2\xi\left(2+\gamma\xi\right)\mathbf{1} & 2\mathbf{m}_c\xi^2 & 4\mathbf{1} & 4\xi\mathbf{1} \\ 2\xi\left(2+\gamma\xi\right)\mathbf{1} & \xi^2\left(2+\gamma\xi\right)^2\mathbf{1} & \xi^3\left(2+\gamma\xi\right)\mathbf{m}_c & 2\xi\left(2+\gamma\xi\right)\mathbf{1} & 2\xi^2\left(2+\gamma\xi\right)\mathbf{1} \\ 2\xi^2\mathbf{m}_c & \xi^3\left(2+\gamma\xi\right)\mathbf{m}_c & \xi^4\mathbf{m}_c\cdot\mathbf{m}_c & 2\xi^2\mathbf{m}_c & 2\xi^3\mathbf{m}_c \\ 4\mathbf{1} & 2\xi\left(2+\gamma\xi\right)\mathbf{1} & 2\mathbf{m}_c\xi^2 & 4\mathbf{1} & 4\xi\mathbf{1} \\ 4\xi\mathbf{1} & 2\xi^2\left(2+\gamma\xi\right)\mathbf{1} & 2\mathbf{m}_c\xi^3 & 4\xi\mathbf{1} & 4\xi^2\mathbf{1} \end{pmatrix} \cdot j_0[\xi]\,\mathrm{d}\xi \tag{B.50}$$

and

$$\hat{\mathbf{M}}^{\text{con}} = \int_{-\frac{h}{2}}^{\frac{h}{2}} \rho_0 \begin{pmatrix} \xi^2\mathbf{1} \\ \frac{1}{2}\xi^3\left(2+\gamma\xi\right)\mathbf{1} \\ \frac{1}{2}\xi^4\mathbf{m}_c^t \\ \xi^2\mathbf{1} \\ \xi^3\mathbf{1} \end{pmatrix} \dot{\mathbf{m}}_c\dot{\gamma}\, j_0[\xi]\,\mathrm{d}\xi. \tag{B.51}$$

It turns out that the mass contributions can be integrated explicitly in the thickness direction, whereby in view of Eq. (3.57) it is noted that the volume measure $j_0[\xi]$ (relating to the undeformed configuration) can to be developed in terms of the covariant vectors as

$$j_0 = \frac{b_0}{\omega_0} = a_1\xi^2 + a_2\xi + a_3 \tag{B.52}$$

where

$$a_1 = \frac{|\mathbf{M}_{\Phi,1}\times\mathbf{M}_{\Phi,2}|}{|\mathbf{\Phi}_{,1}\times\mathbf{\Phi}_{,2}|}, a_2 = \frac{\mathbf{M}_\Phi\cdot\left(\mathbf{\Phi}_1\times\mathbf{M}_{\Phi,2}+\mathbf{M}_{\Phi,1}\times\mathbf{\Phi}_2\right)}{|\mathbf{\Phi}_{,1}\times\mathbf{\Phi}_{,2}|}\,,\ a_3 = 1 \tag{B.53}$$

Hence, the explicit integrated result of the consistent mass matrix $\hat{\mathbf{M}}$ in Eq. (B.50) is in view of (B.52) obtained as

$$\hat{\mathbf{M}} = \begin{pmatrix} \mathbf{M}_{11} & \mathbf{M}_{12} & \mathbf{M}_{13} & \mathbf{M}_{14} & \mathbf{M}_{15} \\ \mathbf{M}_{21} & \mathbf{M}_{22} & \mathbf{M}_{23} & \mathbf{M}_{24} & \mathbf{M}_{25} \\ \mathbf{M}_{31} & \mathbf{M}_{32} & \mathbf{M}_{33} & \mathbf{M}_{34} & \mathbf{M}_{35} \\ \mathbf{M}_{41} & \mathbf{M}_{42} & \mathbf{M}_{43} & \mathbf{M}_{44} & \mathbf{M}_{45} \\ \mathbf{M}_{51} & \mathbf{M}_{52} & \mathbf{M}_{53} & \mathbf{M}_{54} & \mathbf{M}_{55} \end{pmatrix} \tag{B.54}$$

where one obtains e.g. the components

$$\begin{pmatrix} \mathbf{M}_{11} & \mathbf{M}_{12} \\ \mathbf{M}_{21} & \mathbf{M}_{22} \end{pmatrix} = \rho_0 \begin{pmatrix} \left(\frac{1}{12}h^3a_1 + ha_3\right)\mathbf{1} & \frac{1}{480}h^3\left(3h^2\gamma a_1 + 40a_2 + 20\gamma a_3\right)\mathbf{1} \\ \frac{1}{480}h^3\left(3h^2\gamma a_1 + 40a_2 + 20\gamma a_3\right)\mathbf{1} & \frac{h^3\left(3h^2\left(\left(112+5h^2\gamma^2\right)a_1 + 112\gamma a_2\right) + 28\left(80+3h^2\gamma^2\right)a_3\right)}{26880}\mathbf{1} \end{pmatrix} \tag{B.55}$$

We also obtain the integrated result for the convective contribution $\hat{\mathbf{M}}^{\text{con}}$ in Eq. (B.51) as

$$\hat{\mathbf{M}}^{\text{con}} = \rho_0 \begin{pmatrix} \frac{1}{240} h^3 \left(3h^2 a_1 + 20 a_3\right) \\ \frac{h^5 \left(5h^2 \gamma a_1 + 56 a_2 + 28 \gamma a_3\right)}{4480} \\ \frac{h^5 \left(5h^2 a_1 + 28 a_3\right)}{4480} \mathbf{m}_c^t \\ \frac{1}{240} h^3 \left(3h^2 a_1 + 20 a_3\right) \\ \frac{1}{80} h^5 a_2 \end{pmatrix} \dot{\mathbf{m}}_c \dot{\gamma} \tag{B.56}$$

C

APPENDIX C

C.1. WEAK FORM OF MOMENTUM BALANCE

In this section the weak form of the momentum balance based on the employed shell formulation is discussed. To avoid unnecessary elaboration, it is assumed the domain under consideration is cracked and completely refined on the subscale level using the proposed approach. We begin from the momentum balance in Eq. (4.7) and extend it in terms of the shell formulation kinematics employed Eq. (4.41) as follows

Find: $[\bar{\boldsymbol{\varphi}}, \mathbf{m}, \gamma]$

$$
\begin{aligned}
&G^{\text{ine}}[\ddot{\bar{\boldsymbol{\varphi}}}, \ddot{\mathbf{m}}, \ddot{\gamma}; \delta\bar{\boldsymbol{\varphi}}, \delta\mathbf{m}, \delta\gamma] + G^{\text{int}}[\bar{\boldsymbol{\varphi}}, \mathbf{m}, \gamma; \delta\bar{\boldsymbol{\varphi}}, \delta\mathbf{m}, \delta\gamma] - \\
&G^{\text{ext}}[\delta\bar{\boldsymbol{\varphi}}, \delta\mathbf{m}, \delta\gamma] = 0 \quad \forall\ \delta\bar{\boldsymbol{\varphi}}, \delta\mathbf{m}, \delta\gamma
\end{aligned} \tag{C.1}
$$

Introducing the deformation vector $\hat{\mathbf{n}}^t = [\bar{\boldsymbol{\varphi}}, \mathbf{m}, \gamma]$ and the stress resultant vectors (cf. Appendix C.2) we arrive at the inertia, internal, and external virtual work contributions as

$$
G^{\text{ine}} = \int_{\Omega_0} \rho_0\, \delta\hat{\mathbf{n}}^t (\hat{\mathbf{M}}\ddot{\hat{\mathbf{n}}} + \hat{\mathbf{M}}_{\text{con}})\, \omega_0\, \mathrm{d}\xi_1 \mathrm{d}\xi_2 \tag{C.2}
$$

$$
G^{\text{int}} = \int_{\Omega_0} \delta\hat{\mathbf{n}}_c^t \hat{\mathbf{N}}_c \omega_0\, \mathrm{d}\xi_1 \mathrm{d}\xi_2 + \int_{\mathscr{L}_{\Gamma_S}} \delta\hat{\mathbf{n}}_{\text{coh}}^t \hat{\mathbf{N}}_{\text{coh}}\, \mathrm{d}\mathscr{L} \tag{C.3}
$$

$$
G^{\text{ext}} = \int_{\mathscr{L}_{\partial\Omega_0}} \left(\delta\bar{\boldsymbol{\varphi}} \cdot \mathbf{n}_0 + \delta\mathbf{m} \cdot \tilde{\mathbf{m}}_0 + \delta\gamma\, m_s\right) \mathrm{d}\mathscr{L} - \int_{\Omega} p\, \delta\bar{\boldsymbol{\varphi}} \cdot \mathbf{g}_{b_1} \times \mathbf{g}_{b_2}\, \mathrm{d}\Omega \tag{C.4}
$$

where $\delta\hat{\mathbf{n}}_c^t$, $\delta\hat{\mathbf{n}}_{\text{coh}}^t$, $\hat{\mathbf{N}}_c^t$ and $\hat{\mathbf{N}}_{\text{coh}}^t$ are defined as

$$
\delta\hat{\mathbf{n}}_c^t = \left[\delta\bar{\boldsymbol{\varphi}}_{,\alpha}, \delta\mathbf{m}_{,\alpha}, \delta\mathbf{m}, \delta\gamma_{,\alpha}, \delta\gamma\right], \delta\hat{\mathbf{n}}_{\text{coh}}^t = \left[\delta[\![\bar{\boldsymbol{\varphi}}]\!], \delta[\![\mathbf{m}]\!], \delta[\![\gamma]\!]\right] \tag{C.5}
$$

$$
\hat{\mathbf{N}}_c^t = \left[\mathbf{N}^\alpha, \mathbf{M}^\alpha, \mathbf{T}, M_s^\alpha, T_s\right], \hat{\mathbf{N}}_{\text{coh}}^t = \left[\mathbf{n}_S, \mathbf{m}_S, \mathbf{t}_S\right], \tag{C.6}
$$

Therein, p and $\hat{\mathbf{M}}$ denotes external pressure and consistent mass matrix. As in [1], the contributions from the first order time derivative of the director and thickness inhomogeneous

strain fields are represented by, $\hat{\mathbf{M}}_{\text{con}}$, convective mass force per unit area (cf. Appendix C.3). The boundary along the shell midsurface over which traction acts is also considered as $\mathscr{L}$. In order to carry out integration of Eqs. (C.2)-(C.4), domain of integration is changed from B_0 (3D) to Ω_0 (2D) via $j_0[\xi] = b_0/\omega_0$ as

$$\mathrm{d}B_0 = j_0 \mathrm{d}\xi \mathrm{d}\Omega_0 \text{ with } \mathrm{d}\Omega_0 = \omega_0 \mathrm{d}\xi_1 \mathrm{d}\xi_2 \text{ and } \omega_0 = |\mathbf{\Phi}_{,1} \times \mathbf{\Phi}_{,2}| \tag{C.7}$$

C.2. STRESS RESULTANTS

The through-thickness integrated stress resultants referred to in Eq. (C.3) are defined as:

$$\mathbf{N}^{\alpha} = \int_{-h_0/2}^{h_0/2} S^{\alpha k} \mathbf{g}_{b_k} j_0 \mathrm{d}\xi \tag{C.8}$$

$$\mathbf{M}^{\alpha} = \int_{-h_0/2}^{h_0/2} \left(1 + \frac{1}{2}\gamma\xi\right) \xi S^{\alpha k} \mathbf{g}_{c_k} j_0 \mathrm{d}\xi \tag{C.9}$$

$$\mathbf{T} = \int_{-h_0/2}^{h_0/2} \left(\left(1 + \gamma\xi\right) S^{3k} \mathbf{g}_{b_k} + \frac{1}{2}\xi^2 S^{\alpha k} \cdot \mathbf{g}_{b_k} \gamma_{,\alpha} \right) \mathrm{j}_0 \mathrm{d}\xi \tag{C.10}$$

$$M_s^{\alpha} = \int_{-h_0/2}^{h_0/2} \frac{1}{2}\xi^2 S^{\alpha k} \mathbf{m} \cdot \mathbf{g}_{b_k} j_0 \mathrm{d}\xi \tag{C.11}$$

$$T_s = \int_{-h_0/2}^{h_0/2} \left(\frac{1}{2}\xi^2 S^{\alpha k} \mathbf{m}_{,\alpha} \cdot \mathbf{g}_{b_k} + \xi S^{3k} \mathbf{m} \cdot \mathbf{g}_{b_k} \right) j_0 \mathrm{d}\xi \tag{C.12}$$

$$\mathbf{n}_0 = \int_{-h_0/2}^{h_0/2} \bar{\mathbf{t}}_1 \mathrm{d}\xi \tag{C.13}$$

$$\tilde{\mathbf{m}}_0 = \int_{-h_0/2}^{h_0/2} \xi \left(1 + \frac{1}{2}\xi\gamma\right) \bar{\mathbf{t}}_1 \mathrm{d}\xi \tag{C.14}$$

$$m_s = \int_{-h_0/2}^{h_0/2} \frac{1}{2}\xi^2 \mathbf{m} \cdot \bar{\mathbf{t}}_1 \mathrm{d}\xi \tag{C.15}$$

$$\mathbf{m}_0 = \int_{-h_0/2}^{h_0/2} \xi \bar{\mathbf{t}}_1 \mathrm{d}\xi \tag{C.16}$$

$$\mathbf{n}_S = \int_{-h_0/2}^{h_0/2} \mathbf{t}_1 \mathrm{d}\xi \tag{C.17}$$

$$\mathbf{m}_S = \int_{-h_0/2}^{h_0/2} \xi \mathbf{t}_1 \mathrm{d}\xi \tag{C.18}$$

where $S^{\alpha k}$ are the contra-variant components of the second Piola Kirchhoff stress tensor $\mathbf{S}$, $\mathbf{g}_{b_k}$ the spatial co-variant basis vectors defined in Eq. (4.43), j_0 the relation between area and volumetric measures of the shell defined in Eq. (C.7) and $\mathbf{t}_1$ is the nominal traction vector of the cohesive zone defined by $\mathbf{t}_1 = \mathbf{P}^t \cdot \mathbf{N}_S$.

C.3. MASS MATRIX

The consistent mass matrix $\hat{\mathbf{M}}$ and the convective mass (force) $\hat{\mathbf{M}}^{\text{con}}$ introduced in Eq. (C.2) have, for the current kinematical representation, the explicit forms

$$\hat{\mathbf{M}} = \int_{-\frac{h_0}{2}}^{\frac{h_0}{2}} \frac{\rho_0}{4} \cdot \begin{pmatrix} 4\mathbf{1} & 2\xi\left(2+\gamma\xi\right)\mathbf{1} & 2\mathbf{m}\xi^2 & 4\mathbf{1} & 4\xi\mathbf{1} \\ 2\xi\left(2+\gamma\xi\right)\mathbf{1} & \xi^2\left(2+\gamma\xi\right)^2\mathbf{1} & \xi^3\left(2+\gamma\xi\right)\mathbf{m} & 2\xi\left(2+\gamma\xi\right)\mathbf{1} & 2\xi^2\left(2+\gamma\xi\right)\mathbf{1} \\ 2\xi^2\mathbf{m} & \xi^3\left(2+\gamma\xi\right)\mathbf{m} & \xi^4\mathbf{m}\cdot\mathbf{m} & 2\xi^2\mathbf{m} & 2\xi^3\mathbf{m} \\ 4\mathbf{1} & 2\xi\left(2+\gamma\xi\right)\mathbf{1} & 2\mathbf{m}\xi^2 & 4\mathbf{1} & 4\xi\mathbf{1} \\ 4\xi\mathbf{1} & 2\xi^2\left(2+\gamma\xi\right)\mathbf{1} & 2\mathbf{m}\xi^3 & 4\xi\mathbf{1} & 4\xi^2\mathbf{1} \end{pmatrix} \cdot j_0[\xi]\,\mathrm{d}\xi \tag{C.19}$$

and

$$\hat{\mathbf{M}}^{\text{con}} = \int_{-\frac{h}{2}}^{\frac{h}{2}} \rho_0 \begin{pmatrix} \xi^2\mathbf{1} \\ \frac{1}{2}\xi^3\left(2+\gamma\xi\right)\mathbf{1} \\ \frac{1}{2}\xi^4\mathbf{m}^t \\ \xi^2\mathbf{1} \\ \xi^3\mathbf{1} \end{pmatrix} \dot{\mathbf{m}\gamma}\, j_0[\xi]\,\mathrm{d}\xi. \tag{C.20}$$

It turns out that the mass contributions can be integrated explicitly in the thickness direction, whereby in view of Eq. (C.7) it is noted that the volume measure $j_0[\xi]$ (relating to the undeformed configuration) can to be developed in terms of the covariant vectors as

$$j_0 = \frac{b_0}{\omega_0} = a_1\xi^2 + a_2\xi + a_3 \tag{C.21}$$

where

$$a_1 = \frac{|\mathbf{M}_{\Phi,1}\times\mathbf{M}_{\Phi,2}|}{|\mathbf{\Phi}_{,1}\times\mathbf{\Phi}_{,2}|}, a_2 = \frac{\mathbf{M}_\Phi\cdot\left(\mathbf{\Phi}_1\times\mathbf{M}_{\Phi,2}+\mathbf{M}_{\Phi,1}\times\mathbf{\Phi}_2\right)}{|\mathbf{\Phi}_{,1}\times\mathbf{\Phi}_{,2}|}\,, a_3 = 1 \tag{C.22}$$

Hence, the explicit integrated result of the consistent mass matrix $\hat{\mathbf{M}}$ in Eq. (C.19) is in view of (C.21) obtained as

$$\hat{\mathbf{M}} = \begin{pmatrix} \mathbf{M}_{11} & \mathbf{M}_{12} & \mathbf{M}_{13} & \mathbf{M}_{14} & \mathbf{M}_{15} \\ \mathbf{M}_{21} & \mathbf{M}_{22} & \mathbf{M}_{23} & \mathbf{M}_{24} & \mathbf{M}_{25} \\ \mathbf{M}_{31} & \mathbf{M}_{32} & \mathbf{M}_{33} & \mathbf{M}_{34} & \mathbf{M}_{35} \\ \mathbf{M}_{41} & \mathbf{M}_{42} & \mathbf{M}_{43} & \mathbf{M}_{44} & \mathbf{M}_{45} \\ \mathbf{M}_{51} & \mathbf{M}_{52} & \mathbf{M}_{53} & \mathbf{M}_{54} & \mathbf{M}_{55} \end{pmatrix} \tag{C.23}$$

where one obtains e.g. the components

$$\begin{pmatrix} \mathbf{M}_{11} & \mathbf{M}_{12} \\ \mathbf{M}_{21} & \mathbf{M}_{22} \end{pmatrix} = \\ = \rho_0 \begin{pmatrix} \left(\frac{1}{12}h^3a_1 + ha_3\right)\mathbf{1} & \frac{1}{480}h^3\left(3h^2\gamma a_1 + 40a_2 + 20\gamma a_3\right)\mathbf{1} \\ \frac{1}{480}h^3\left(3h^2\gamma a_1 + 40a_2 + 20\gamma a_3\right)\mathbf{1} & \frac{h^3\left(3h^2\left(\left(112+5h^2\gamma^2\right)a_1+112\gamma a_2\right)+28\left(80+3h^2\gamma^2\right)a_3\right)}{26880}\mathbf{1} \end{pmatrix} \tag{C.24}$$

We also obtain the integrated result for the convective contribution $\hat{\mathbf{M}}^{\text{con}}$ in Eq. (C.20) as

$$\hat{\mathbf{M}}^{\text{con}} = \rho_0 \begin{pmatrix} \frac{1}{240} h^3 \left(3h^2 a_1 + 20 a_3\right) \\ \frac{h^5 \left(5h^2 \gamma a_1 + 56 a_2 + 28 \gamma a_3\right)}{4480} \\ \frac{h^5 \left(5h^2 a_1 + 28 a_3\right)}{4480} \mathbf{m}^t \\ \frac{1}{240} h^3 \left(3h^2 a_1 + 20 a_3\right) \\ \frac{1}{80} h^5 a_2 \end{pmatrix} \dot{\mathbf{m}} \dot{\gamma} \tag{C.25}$$

REFERENCES

[1] R. Larsson, J. Mediavilla, and M. Fagerström, *Dynamic fracture modeling in shell structures based on XFEM,* International Journal for Numerical Methods in Engineering **86**, 499 (2010).

D

APPENDIX D

D.1. STRESS RESULTANTS

The stress resultants terms referred to in Eq. (5.14) and Eq. (5.15) are expressed as:

$$\mathbf{N}^{\alpha} = \int_{-h_0/2}^{h_0/2} S^{\alpha k}\mathbf{g}_{b_k} j_0 \mathrm{d}\xi \tag{D.1}$$

$$\mathbf{M}^{\alpha} = \int_{-h_0/2}^{h_0/2} \left(1+\frac{1}{2}\gamma\xi\right)\xi S^{\alpha k}\mathbf{g}_{c_k} j_0 \mathrm{d}\xi \tag{D.2}$$

$$\mathbf{T} = \int_{-h_0/2}^{h_0/2} \left(\left(1+\gamma\xi\right) S^{3k}\mathbf{g}_{b_k} + \frac{1}{2}\xi^2 S^{\alpha k}\cdot\mathbf{g}_{b_k}\gamma_{,\alpha}\right) \mathrm{j}_0 \mathrm{d}\xi \tag{D.3}$$

$$M_s^{\alpha} = \int_{-h_0/2}^{h_0/2} \frac{1}{2}\xi^2 S^{\alpha k}\mathbf{m}\cdot\mathbf{g}_{b_k} j_0 \mathrm{d}\xi \tag{D.4}$$

$$T_s = \int_{-h_0/2}^{h_0/2} \left(\frac{1}{2}\xi^2 S^{\alpha k}\mathbf{m}_{,\alpha}\cdot\mathbf{g}_{b_k} + \xi S^{3k}\mathbf{m}\cdot\mathbf{g}_{b_k}\right) j_0 \mathrm{d}\xi \tag{D.5}$$

$$\mathbf{n}_0 = \int_{-h_0/2}^{h_0/2} \bar{\mathbf{t}}_1 \mathrm{d}\xi \tag{D.6}$$

$$\tilde{\mathbf{m}}_0 = \int_{-h_0/2}^{h_0/2} \xi\left(1+\frac{1}{2}\xi\gamma\right)\bar{\mathbf{t}}_1 \mathrm{d}\xi \tag{D.7}$$

$$m_s = \int_{-h_0/2}^{h_0/2} \frac{1}{2}\xi^2\mathbf{m}\cdot\bar{\mathbf{t}}_1 \mathrm{d}\xi \tag{D.8}$$

$$\mathbf{m}_0 = \int_{-h_0/2}^{h_0/2} \xi\bar{\mathbf{t}}_1 \mathrm{d}\xi \tag{D.9}$$

in the equations above $S^{\alpha k}$ is the contra-variant component of the second Piola Kirchhoff stress tensor $\mathbf{S}$, $\mathbf{g}_{b_k}$ is the spatial co-variant basis vectors defined in Eq. (5.8), and j_0 is the relation between area and volumetric measures of the shell defined in Eq. (5.18).

D.2. MASS MATRIX

To elaborate on consistent mass matrix $\hat{\mathbf{M}}$ and the convective mass $\hat{\mathbf{M}}^{\text{con}}$ employed in Eq. (5.13), based on the current configuration we have

$$\hat{\mathbf{M}} = \int_{-\frac{h_0}{2}}^{\frac{h_0}{2}} \frac{\rho_0}{4} \cdot \begin{pmatrix} 4\mathbf{1} & 2\xi\left(2+\gamma\xi\right)\mathbf{1} & 2\mathbf{m}\xi^2 & 4\mathbf{1} & 4\xi\mathbf{1} \\ 2\xi\left(2+\gamma\xi\right)\mathbf{1} & \xi^2\left(2+\gamma\xi\right)^2\mathbf{1} & \xi^3\left(2+\gamma\xi\right)\mathbf{m} & 2\xi\left(2+\gamma\xi\right)\mathbf{1} & 2\xi^2\left(2+\gamma\xi\right)\mathbf{1} \\ 2\xi^2\mathbf{m} & \xi^3\left(2+\gamma\xi\right)\mathbf{m} & \xi^4\mathbf{m}\cdot\mathbf{m} & 2\xi^2\mathbf{m} & 2\xi^3\mathbf{m} \\ 4\mathbf{1} & 2\xi\left(2+\gamma\xi\right)\mathbf{1} & 2\mathbf{m}\xi^2 & 4\mathbf{1} & 4\xi\mathbf{1} \\ 4\xi\mathbf{1} & 2\xi^2\left(2+\gamma\xi\right)\mathbf{1} & 2\mathbf{m}\xi^3 & 4\xi\mathbf{1} & 4\xi^2\mathbf{1} \end{pmatrix} \cdot j_0[\xi]\mathrm{d}\xi \tag{D.10}$$

and

$$\hat{\mathbf{M}}^{\text{con}} = \int_{-\frac{h}{2}}^{\frac{h}{2}} \rho_0 \begin{pmatrix} \xi^2\mathbf{1} \\ \frac{1}{2}\xi^3\left(2+\gamma\xi\right)\mathbf{1} \\ \frac{1}{2}\xi^4\mathbf{m}^t \\ \xi^2\mathbf{1} \\ \xi^3\mathbf{1} \end{pmatrix} \dot{\mathbf{m}}\dot{\gamma}\, j_0[\xi]\mathrm{d}\xi. \tag{D.11}$$

where mass contributions can be integrated in the thickness direction by employing the volume measure $j_0[\xi]$ (cf. Eq. (5.18)) that can be formulated in terms of the covariant vectors as

$$j_0 = \frac{b_0}{\omega_0} = a_1\xi^2 + a_2\xi + a_3 \tag{D.12}$$

where

$$a_1 = \frac{|\mathbf{M}_{\Phi,1}\times\mathbf{M}_{\Phi,2}|}{|\mathbf{\Phi}_{,1}\times\mathbf{\Phi}_{,2}|}, a_2 = \frac{\mathbf{M}_\Phi\cdot\left(\mathbf{\Phi}_1\times\mathbf{M}_{\Phi,2}+\mathbf{M}_{\Phi,1}\times\mathbf{\Phi}_2\right)}{|\mathbf{\Phi}_{,1}\times\mathbf{\Phi}_{,2}|}\,,\ a_3 = 1 \tag{D.13}$$

Integrating the mass matrix $\hat{\mathbf{M}}$ in Eq. (D.10) considering the (D.12) it becomes

$$\hat{\mathbf{M}} = \begin{pmatrix} \mathbf{M}_{11} & \mathbf{M}_{12} & \mathbf{M}_{13} & \mathbf{M}_{14} & \mathbf{M}_{15} \\ \mathbf{M}_{21} & \mathbf{M}_{22} & \mathbf{M}_{23} & \mathbf{M}_{24} & \mathbf{M}_{25} \\ \mathbf{M}_{31} & \mathbf{M}_{32} & \mathbf{M}_{33} & \mathbf{M}_{34} & \mathbf{M}_{35} \\ \mathbf{M}_{41} & \mathbf{M}_{42} & \mathbf{M}_{43} & \mathbf{M}_{44} & \mathbf{M}_{45} \\ \mathbf{M}_{51} & \mathbf{M}_{52} & \mathbf{M}_{53} & \mathbf{M}_{54} & \mathbf{M}_{55} \end{pmatrix} \tag{D.14}$$

where it results in e.g. the components

$$\begin{pmatrix} \mathbf{M}_{11} & \mathbf{M}_{12} \\ \mathbf{M}_{21} & \mathbf{M}_{22} \end{pmatrix} = \\ = \rho_0 \begin{pmatrix} \left(\frac{1}{12}h^3a_1 + ha_3\right)\mathbf{1} & \frac{1}{480}h^3\left(3h^2\gamma a_1 + 40a_2 + 20\gamma a_3\right)\mathbf{1} \\ \frac{1}{480}h^3\left(3h^2\gamma a_1 + 40a_2 + 20\gamma a_3\right)\mathbf{1} & \frac{h^3\left(3h^2\left(\left(112+5h^2\gamma^2\right)a_1+112\gamma a_2\right)+28\left(80+3h^2\gamma^2\right)a_3\right)}{26880}\mathbf{1} \end{pmatrix} \tag{D.15}$$

Also integrating the convective mass contribution $\hat{\mathbf{M}}^{\text{con}}$ in Eq. (D.11) results in

$$\hat{\mathbf{M}}^{\text{con}} = \rho_0 \begin{pmatrix} \frac{1}{240} h^3 \left(3h^2 a_1 + 20 a_3\right) \\ \frac{h^5 \left(5h^2 \gamma a_1 + 56 a_2 + 28 \gamma a_3\right)}{4480} \\ \frac{h^5 \left(5h^2 a_1 + 28 a_3\right)}{4480} \mathbf{m}^t \\ \frac{1}{240} h^3 \left(3h^2 a_1 + 20 a_3\right) \\ \frac{1}{80} h^5 a_2 \end{pmatrix} \dot{\mathbf{m}} \dot{\gamma} \tag{D.16}$$

CURRICULUM VITÆ

21-03-1984 Born in Tehran, Iran.

EDUCATION

2002–2007 B.Sc. in Mechanical Engineering
Faculty of Mechanical Engineering, Azad University (Central Branch of Tehran)
Tehran, Iran

2008–2010 M.Sc. in Mechanical Engineering
Linköping University, Department of Management and Engineering
Linköping, Sweden

2011–2015 Ph.D. candidate
Faculty of Civil Engineering and Geosciences, Delft University of Technology
Delft, the Netherlands

2011–2015 Ph.D. candidate
Department of Industrial and Materials Science, Chalmers University of Technology
Göteborg, Sweden

WORK EXPERIENCE

2015–2017 CAE Engineer
Vinngroup (Case5)
Göteborg, Sweden

2017–2019 CAE Engineer at Body/Interior/Crash group
NEVS
Trollhättan, Sweden

2019–Present CAE Engineer at Solidity group
Volvo Car Group
Göteborg, Sweden

LIST OF PUBLICATIONS

Journal papers

1. **S. Mostofizadeh, M. Fagerström, and R. Larsson**, *Dynamic crack propagation in elasto-plastic thin-walled structures: Modelling and validation*, International Journal for Numerical Methods in Engineering **96**, 63-86 (2013).
2. **S. Mostofizadeh, M. Fagerström, and R. Larsson**, *XFEM based element subscale refinement for detailed representation of crack propagation in large scale analyses*, International Journal for Numerical Methods in Engineering **10**, 549-572 (2016).
3. **S. Mostofizadeh, F. P. van der Meer, M. Fagerström, R. Larsson, and B. Sluys**, *An element subscale refinement for representation of the progressive fracture based on the phantom node approach*, Computers and Structures **196**, 134-145 (2018).
4. **S. Mostofizadeh, S. Razanica, R. Larsson and M. Fagerström**, *A continuum damage failure model for thin-walled structures*, To be submitted for international publications.

Conferences

1. **R. Larsson, S. Mostofizadeh, J. Mediavilla, and M. Fagerström**, *Dynamic Ductile Fracture in Thin-walled Structures based on XFEM*, CFRAC (2011).
2. **S. Mostofizadeh, M. Fagerström, R. Larsson, B. Sluys and J. Mediavilla**, *Dynamic ductile fracture in shells*, ECCOMAS (2012).
3. **M. Fagerström, S. Mostofizadeh, and R. Larsson**, *Subscale enrichment of discontinuity for XFEM crack tip element*, Third International Conference on Computational Modeling of Fracture and Failure of Materials and Structures (2013).
4. **M. Fagerström, S. Mostofizadeh, and J. Brouzoulis**, *Utilising the eXtended Finite Element Method (XFEM) to model failure of thin-walled structures*, Svenska mekanikdagar (2013).
5. **S. Mostofizadeh, B. Sluys, and R. Larsson**, *On the subscale enrichment of crack tip element in XFEM and the phantom node method*, 11th World Congress on Computational Mechanics (2014).